

Faculty of Engineering

Department of Mechanical, Materials and Manufacturing Engineering

Analytical and Experimental Investigation of Incremental Sheet Forming of Thermoplastics

Hui Zhu, BEng, MSc

Thesis submitted to the University of Nottingham

for the degree of Doctor of Philosophy

September 2022

Abstract

Incremental sheet forming (ISF) is a promising flexible manufacturing process and has drawn increasing attention in the past decades. The final shape of ISF formed part is accumulated by localised deformation under the forming tool. Extensive research has shown that it is especially advantageous in manufacturing small-batch and customised sheet parts because of its distinctive features of flexibility, adaptability, applicability, improved material formability and associated benefits in energy efficiency and reduced costs. Apart from metals, thermoplastics are also widely used engineering materials in different fields as they have great advantages in resistance to impact, temperature and load carrying capability. As a result, ISF of thermoplastics has been noticed in recent years.

This thesis reports the findings of analytical and experimental investigations on ISF and its application in thermoplastics. By revealing the mechanical behaviour of thermoplastics and the deformation mechanism of ISF, a new constitutive model for thermoplastics, and new analytical models for ISF force and contact pressure prediction are developed. Focus is also given to the experimental study of thermoplastic-based ISF process and the application in manufacture of customised cranial plates.

A new phenomenological constitutive model is proposed to predict the mechanical behaviour of thermoplastics. The new constitutive model and the method to determine the parameters of the model are introduced. In the new model, a transition function is proposed to enable a smooth transition of the flow stress behaviours under both small-strain and large-strain conditions. In validating the model with testing data of Polyether ether ketone (PEEK) and Polycarbonate (PC), it is found that this new model is able to predict different phases of the flow stress behaviour of thermoplastics in consideration

of the effect of strain, strain rate and temperature. Although the basic trends of tensile and compressive behaviours of PEEK and PC materials are different, the new constitutive model can be used to represent these behaviours effectively. In addition, the results show that the new model gives a favourable prediction of the PC material at high strain rate conditions. Compared with Johnson-Cook, Nasraoui et al., Duan-Saigal-Greif-Zimmerman (DSGZ) and Mulliken-Boyce models, the new model presents an improved level of accuracy on the mechanical behaviour of thermoplastics in a wide range of deformation conditions.

A new analytical model for forming force prediction in the ISF process is presented. The modelling of contact region, thickness distribution and strain components are carried out as the basis for the prediction of vertical and horizontal forces. The effect of local contact behaviour, material deformation and stretching, as well as the less investigated behaviours of global elastic bending, change of deformation mode and contact condition change are considered in the derivation. The force prediction model at both plane strain and biaxial tension condition area is developed based on the differences in contact region and thickness distribution between these two different deformation states. Validated by ISF tests for a truncated cone and pyramid part with varying drawing angles, the prediction of force history captures well the fluctuation of different force components due to the change of deformation conditions and provides an insight into the material deformation mechanisms and the correlation to forming force characteristics of the whole ISF process. In a practical case, the developed model is successfully applied to the force prediction in ISF-based cranial plate manufacture. The developed model is also validated by a series of ISF tests with different process parameters. Compared with other models, the developed analytical model has the capability to predict both peak and stabilised forces and is more accurate in most cases

of the whole ISF process.

An analytical model is developed to predict the contact pressure distribution in ISF for the first time. Referring to the contact mechanics of sheet indentation, the size of contact area, maximum contact pressure and pressure distribution are predicted by the analytical method based on the revealing of the local tool-sheet contact behaviour in ISF. Point based method is used to implement and visualise the analytical model. The validity of the developed analytical model is confirmed by comparison with FE simulation for ISF of titanium grade 1 (TA1) sheet and heat-assisted ISF of PEEK sheet in different aspects. The effect of mesh size in FE simulation is analysed to have an influence on the discrepancy between analytical and simulation results.

Experimental study is carried out to test the feasibility of ISF of PEEK and polymethyl methacrylate (PMMA) sheets at elevated temperature. Heat-assisted ISF setup, force and temperature measurement systems are developed and tested to investigate the effect of spindle speed, feed rate and geometry on temperature distribution, forming force variation, thickness distribution, formed geometry and formability. Results show that spindle speed has the most significant influence on temperature distribution and forming accuracy in ISF of PEEK and PMMA. For ISF of PEEK, preheating temperature of 130 °C and spindle speed of 100 rpm is recommended compared to 1000 rpm, while for ISF of PMMA, 100 °C and 100 rpm can be useful. Based on the experimental tests, ISF-based manufacture of PEEK and PMMA cranial plates is presented and regarded as an effective alternative to cranial reconstruction. Apart from experimental observations, the fracture mechanism, geometric inaccuracy, and twist behaviour are discussed and considered as challenging issues in ISF of thermoplastics.

List of Publications

[1] Hui Zhu, Hengan Ou, Atanas Popov, Incremental sheet forming of thermoplastics: a review, The International Journal of Advanced Manufacturing Technology, 111(1) (2020) 565-587.

[2] Hui Zhu, Hengan Ou, Atanas Popov, A new phenomenological constitutive model for thermoplastics, Mechanics of Materials, 157 (2021) 103817.

[3] Hui Zhu, Hengan Ou, Constitutive modelling of hot deformation behaviour of metallic materials, Materials Science and Engineering: A, 832 (2022) 142473.

[4] Hui Zhu, Hengan Ou, A new analytical model for force prediction in incremental sheet forming. (To be submitted)

[5] Hui Zhu, Zhenyuan Qin, Hengan Ou, Effect of stress triaxiality and temperature on the fracture strain of PEEK. (To be submitted)

[6] Hui Zhu, Hengan Ou, Yixin Wang, Zhenyuan Qin, Peter Kendall, Heat-assisted incremental sheet forming of PEEK and PMMA: experimental investigation and application in cranial reconstruction. (To be submitted)

[7] Hui Zhu, Hengan Ou, Analytical modelling and validation of local contact pressure distribution in incremental sheet forming. (To be submitted)

Acknowledgements

I would like to acknowledge my supervisors Dr Hengan Ou and Prof Atanas Popov for their supervision and guidance on my way towards PhD. Special thanks go to Dr Ou, who always gives me warm encouragement, full support, timely help, and invaluable advice.

I would like to express my gratitude to the financial support of Faculty of Engineering Research Excellence PhD Scholarship awarded by the University of Nottingham.

I would like to thank my internal examiner, Dr Xin Dong, and my external examiner, Dr Zhusheng Shi of Department of Mechanical Engineering, Imperial College London, for their feedback and suggestions to the thesis.

Sincere thanks are given to Mr Geoffrey Bexon and Dr Peter Kendall of Rolls Royce UTC Advanced Manufacturing Group for their help on my ISF tests. Special thanks go to Mr Andy Plummer and Mr Ken Wilson of Central Engineering Workshop for their support in preparation of ISF tooling.

I would like to thank Dr Shakir Gatea of Faculty of Engineering, University of Kufa for discussions on the literature review of thermoplastic-based ISF, and Dr Lars Korner of SO REAL Digital Twins for his help in preparation of temperature measurement system.

Special thanks are given to Dr Wenxuan Peng, Ms Xuelei Zhao, Mr Zhenyuan Qin and other colleagues for all they have done to help me in both work and life. I wish all of them will have a bright future.

Finally, I would like to give my most sincere gratitude to my parents, Mr Yanjun Zhu and Ms Cuiyun Wu for their continuous support behind me. Without them, I will never be who I am today. My love and thanks also go to my fiancée, Dr Yixin Wang, who

always raises me up during the past four years. What we have experienced together in the UK will be precious memories when we get old.

List of Abbreviations

3D	Three dimensional
C3D8R	8-node brick element with reduced integration
C3D8RT	8-node thermally coupled brick element with reduced integration
CD	Corner deformation
CNC	Computer numerical control
CT	Computed tomography
DSGZ	Duan-Saigal-Greif-Zimmerman
DSIF	Double side incremental forming
ER	Elastic recovery
ERL	Left part of elastic recovery
ERR	Right part of elastic recovery
FE	Finite element
FFL	Fracture forming line
FLC	Forming limit curve
FLD	Forming limit diagram
ISF	Incremental sheet forming
ND	Non-overlapping deformation
OD	Overlapping deformation

PA	Polyamide
PA 6	Polyamide-6
PC	Polycarbonate
PCL	Polycaprolactone
PEEK	Polyether ether ketone
PEK	Polyether ketone
PET	Polyethylene terephthalate
PMMA	Polymethyl methacrylate
POM	Polyoxymethylene
PP	Polypropylene
PVC	Polyvinylchloride
R^2	R squared, coefficient of determination
$RMSE$	Root mean square error
SPIF	Single point incremental forming
TA1	Titanium grade 1
TPIF	Two-point incremental forming
UHMWPE	Ultrahigh molecular weight polyethylene
ZOP	Zhu-Ou-Popov

Table of Contents

Abstract.....I

List of Publications.....IV

Acknowledgements V

List of Abbreviations.....VII

Table of Contents IX

List of Figures.....XVII

List of Tables..... XXX

Chapter 1 Introduction..... 1

1.1 Overview of incremental sheet forming (ISF) and its application in thermoplastics 1

1.1.1 Overview of ISF..... 1

1.1.2 Overview of ISF of thermoplastics 3

1.2 Research challenges..... 4

1.2.1 Material constitutive modelling 4

1.2.2 Process analytical modelling..... 4

1.2.3 Forming and testing method..... 5

1.3 Aim and objectives 5

1.4 Research methodology..... 6

1.5 Thesis contributions..... 9

1.6 Thesis structure 10

Chapter 2 Literature Review 13

2.1 Introduction 13

2.2 ISF of thermoplastics 13

2.2.1 ISF Processing conditions 13

2.2.2 Deformation and failure mechanism 21

2.2.3 Formability of thermoplastic materials 34

2.2.4 Forming quality 44

2.2.5 Discussions 50

2.3 Constitutive modelling of thermoplastics 57

2.3.1 Deformation behaviour of thermoplastics 57

2.3.2 Constitutive modelling of thermoplastics 60

2.4 Analytical modelling of ISF 64

2.4.1 Analytical modelling of forming force 64

2.4.2 Analytical modelling of other aspects in ISF 67

2.5 Research challenges and future directions 70

2.5.1 Research challenges 70

2.5.2 Future directions 71

Chapter 3 A New Phenomenological Constitutive Model for Thermoplastics 75

Nomenclature 75

3.1 Introduction 76

3.2 Formulation of the new constitutive model 76

3.2.1 Effect of strain rate and temperature 78

3.2.2 Linear elastic, non-linear elastic, yield, and strain softening behaviours 79

3.2.3 Strain hardening behaviour 80

3.2.4 Transition functions 81

3.3 Validation of the constitutive model 82

3.3.1 Validation with PEEK material 83

3.3.2 Validation with PC material 87

3.3.3 Validation with PC material at high strain rate conditions 92

3.4 Comparison with other constitutive models 96

3.4.1 Prediction of Johnson-Cook model 97

3.4.2 Prediction of Nasraoui et al. model 98

3.4.3 Prediction of DSGZ model 100

3.4.4 Comparison and quantitative evaluation of studied phenomenological constitutive models 102

3.4.5 Comparison with Mulliken-Boyce model 106

3.5 Conclusions 108

Chapter 4 A New Analytical Model for Force Prediction in Incremental Sheet Forming 110

Nomenclature 110

4.1 Introduction 114

4.2 Analytical model of forming force 115

4.2.1 Contact region 115

4.2.2 Thickness distribution under tool-sheet contact 122

4.2.3 Indentation and drawing angles 126

4.2.4 Strain components 129

4.2.5 Forming force 131

4.2.6 Forming force in biaxial tension condition area 136

4.2.7 Implementation 139

4.3 Force prediction and validation 140

4.3.1 Model validation from ISF of TA1 sheet 140

4.3.2 Model validation from ISF of PEEK sheet 148

4.3.3 Model validation in a practical application 151

4.3.4 Model validation from ISF of AA1003-O sheet 153

4.3.5 Model validation of force components 157

4.3.6 Comparison among the analytical model and other models 159

4.4 Discussions 162

4.4.1 Effect of lubrication condition 162

4.4.2 Effect of the tool-sheet interaction on prediction accuracy 163

4.5 Conclusions 165

Chapter 5 Analytical Modelling and Validation of Local Contact Pressure Distribution in Incremental Sheet Forming 167

Nomenclature 167

5.1 Introduction 170

5.2 Analytical model of the contact pressure distribution 170

5.2.1 Modelling of contact region 170

5.2.2 Modelling of contact pressure distribution 173

5.2.3 Implementation method 177

5.3 Finite element simulation 180

5.3.1 ISF of TA1 sheet 180

5.3.2 Heat-assisted ISF of PEEK sheet 182

5.4 Validation of analytical model with ISF of TA1 and PEEK 186

5.4.1 Comparison of forming force between analytical model and FE simulation 186

5.4.2 Validation of the size of contact area 189

5.4.3 Validation of the maximum contact pressure 191

5.4.4 Validation of contact pressure distribution 192

5.5 Discussions 197

5.5.1 Effect of element size on the FE simulation results 197

5.5.2 Potential improvement of the analytical model 198

5.6 Conclusions 199

Chapter 6 Heat-assisted Incremental Sheet Forming of PEEK and PMMA 200

Nomenclature 200

6.1 Introduction 203

6.2 Materials and methods 204

6.2.1 Material 204

6.2.2 Heat-assisted ISF setup 205

6.2.3 ISF experimental design 206

6.2.4 Model of cranial plate for ISF manufacture 209

6.2.5 Geometric and thickness measurement 210

6.3 Results and discussions of heat-assisted ISF of PEEK 211

6.3.1 ISF formed parts 211

6.3.2 Forming temperature 212

6.3.3 Forming force 217

6.3.4 Geometric accuracy 220

6.3.5 Thickness distribution 224

6.4 Results and discussion of heat-assisted ISF of PMMA 226

6.4.1 ISF formed parts 227

6.4.2 Forming temperature 227

6.4.3 Forming force 230

6.4.4 Geometric accuracy 231

6.4.5 Thickness distribution 234

6.5 ISF-based manufacture of cranial plate 236

6.6 Discussions on the challenging issues in ISF of PEEK and PMMA 242

6.6.1 Forming accuracy 243

6.6.2 Fracture mechanism 247

6.6.3 Twist behaviour 255

6.7 Conclusions 261

Chapter 7 Conclusions and Future Work 263

7.1 Introduction 263

7.2 Conclusions 263

7.3 Future work 265

References 268

Appendix A Identification of material parameters in the new constitutive model 296

Appendix B Constitutive modelling of hot deformation behaviour of metallic materials 301

B.1 Introduction 301

B.2 Constitutive modelling of hot deformation behaviour 303

B.2.1 ZOP model 303

B.2.2 Modified model I 306

B.2.3 Modified model II 307

B.2.4 Modified model III 309

B.3 Identification of model parameters 310

B.3.1 ZOP model 311

B.3.2 Modified model I 314

B.3.3 Modified model II 315

B.3.4 Modified model III 319

B.4 Validation of the developed constitutive models 321

B.4.1 Prediction and validation of ZOP model 322

B.4.2 Prediction and validation of Modified model I 323

B.4.3 Prediction and validation of Modified model II 325

B.4.4 Prediction and validation of Modified model III 327

B.4.5 Prediction of peak and yield stresses 328

B.4.6 Evaluation and comparison of prediction accuracy 331

B.5 Discussion 333

B.5.1 Applicability of developed constitutive models 333

B.5.2 Physical meanings of the developed constitutive models 335

B.6 Conclusions 340

List of Figures

Figure 1.1 The basic principle of ISF. 1

Figure 1.2 Different variants of the ISF process. (a) TPIF with a partial die, (b) TPIF with a full die and (c) DSIF. 2

Figure 1.3 Formed thermoplastic parts by ISF [11]. 3

Figure 2.1 (a) Schematic representation of a cross-section view [8] and (b) experimental setup of SPIF [19]. 14

Figure 2.2 Essentials for the theoretical framework based on membrane analysis [37]. (a) Schematic representation of the local contact area (shell element) between the tool and sheet placed immediately ahead. (b) Instantaneous deformation zones and evidence of the extreme modes of deformation obtained from circle grid analysis. 23

Figure 2.3 Membrane analysis of SPIF [18]. (a) Schematic representation of the local contact area between the tool and sheet placed immediately ahead. (b) Approximation of the local contact area by a shell element. (c) Cross-section view showing the acting stresses in meridional, circumferential and thickness directions. 24

Figure 2.4 SEM micrographs of PLA funnel part [45]: (a) original material and (b) formed part. 30

Figure 2.5 Schematic representation of the orientation of polymer chains reorientation during SPIF. 30

Figure 2.6 Schematic illustration (a) and (b) and experimental observation (c) and (d) [8] of Failure Mode 1, 2 and 3 in the rotational symmetric SPIF of thermoplastics. 32

Figure 2.7 Fracture of (a), (b), (c) and (d) PVC and (e), (f), (g) and (h) PC sheet in ISF with spindle non-rotating. (a), (c), (e) and (f) Fracture under plane strain state; (b), (d), (f) and (h) Fracture under biaxial strain state [69]. 33

Figure 2.8 Illustration of the forming limits of SPIF (labelled FFL) against that of the conventional forming process (labelled FLC) in the principal strain space (ε_1, ε_2) [29]. 35

Figure 2.9 FFL of PVC obtained by Martins et al. [10]. 36

Figure 2.10 FFL for PVC sheet with spindle non-rotating [69]. 37

Figure 2.11 Formability (indicated by maximum drawing angle at failure) as a function of the initial drawing angle for sheet blanks with 2 mm thickness (5 mm tool radius) [11]. In the legend, PVC (1): the shiny (smooth) surface of the sheet blank placed facing the forming tool; PVC (2): the rough surface of the sheet blank placed facing the forming tool. 40

Figure 2.12 Effect of step size on formability and failure modes for funnel-shaped PLA parts with radius of curvature (a) 10 mm, (b) 12 mm, (c) 14 mm and (d) 16 mm [45]. 42

Figure 2.13 Typical deformation behaviour of a thermoplastic. 59

Figure 2.14 One-dimensional schematic of Mulliken-Boyce model [97]. 61

Figure 2.15 Mechanism of torsion in ISF of thermoplastics [65]. 70

Figure 3.1 Effects of Terms A and B to normalised function value and Term C to a proportional function value according to the normalisation of Terms A and B. 77

Figure 3.2 Mathematic representation of (a) $f(\varepsilon, \dot{\varepsilon}, T)$ and $g(\varepsilon, \dot{\varepsilon}, T)$ and (b) $u(\varepsilon, \dot{\varepsilon}, T)$ and $v(\varepsilon, \dot{\varepsilon}, T)$. 80

Figure 3.3 Experimental true stress – strain curves from Joseph [136] and predicted results for tensile behaviour of PEEK material (a) and (b) under different strain rates at constant temperature of 296 K and (c) and (d) under different temperatures at constant strain rate of 4.96×10^{-4} s^{-1}. 84

Figure 3.4 Experimental compressive true stress – strain curves from Joseph [136] and predicted results of PEEK (a) and (b) under different strain rates at constant temperature of 296 K and (c) and (d) under different temperatures at constant strain rate of 1.04×10^{-3} s^{-1}..... 86

Figure 3.5 Experimental tensile true stress – strain curves from Cao et al. [87] and predicted results of PC (a) and (b) under different strain rates at constant temperature of 293 K and (c) and (d) under different temperatures at constant strain rate of 10^{-3} s^{-1}. 89

Figure 3.6 Experimental compressive true stress – strain curves from Yu et al. [88] and predicted results of PC (a) and (b) under different strain rates at constant temperature of 293 K and (c) and (d) under different temperatures at constant strain rate of 10^{-3} s^{-1}. 91

Figure 3.7 Experimental dynamic tensile true stress – strain curves from Cao et al. [87] and predicted results of PC (a) and (b) under different strain rates at constant temperature of 293 K and (c) and (d) under different temperatures at constant strain rate of 1700 s^{-1}. 93

Figure 3.8 Experimental dynamic compressive true stress – strain curves from Yu et al. [88] and predicted results of PC (a) and (b) under different strain rates at constant temperature of 293 K and (c) and (d) under different temperatures at constant strain rate of 5000 s^{-1}. 95

Figure 3.9 Comparison between experimental data for tensile tests of PEEK material from Joseph [136] and predicted results of Johnson-Cook model (a) and (b) at constant temperature of 296 K and (c) and (d) at constant strain rate of 4.96×10^{-4} s^{-1}. 98

Figure 3.10 Comparison between experimental data for tensile tests of PEEK material from Joseph [136] and predicted results of Nasraoui et al. model (a) and (b) at constant temperature of 296 K and (c) and (d) at constant strain rate of 4.96×10^{-4} s^{-1}. 100

Figure 3.11 Comparison between experimental data for tensile tests of PEEK material from Joseph [136] and predicted results of DSGZ model (a) and (b) at constant temperature of 296 K and (c) and (d) at constant strain rate of 4.96×10^{-4} s^{-1}. 102

Figure 3.12 Comparison of predicted results provided by Johnson-Cook, Nasraoui et al., DSGZ and the new model in the conditions of (a) 296 K and 1.04×10^{-4} s^{-1}, (b) 296 K and 4.96×10^{-4} s^{-1}, (c) 296 K and 1.54×10^{-3} s^{-1}, (d) 343 K and 4.96×10^{-4} s^{-1} and (e) 373 K and 4.96×10^{-4} s^{-1}. 104

Figure 3.13 Comparison between Mulliken-Boyce and the new models. (a) Experimental data for compressive tests of PC material at constant temperature from Mulliken and Boyce [97] and predicted results and (b) calculated R^2 and $RMSE$. ... 107

Figure 4.1 Boolean subtraction of a ball tool from (a), (b) truncated cone shape, (c), (d) linear part and (e), (f) corner of truncated pyramid shape. 117

Figure 4.2 Illustration of contact region in ISF and the coordinate system. 118

Figure 4.3 Illustration of contact region from top view in (a) plane strain condition area and (b) biaxial tension condition area at corner of ISF. 120

Figure 4.4 ISF illustration of (a) meridional and (b) circumferential cross-sections of workpiece. 123

Figure 4.5 (a) Comparison of indentation angle between simulation and analytical results. (b) Illustration of tool-sheet relationship at the beginning of ISF..... 128

Figure 4.6 Decomposition of forming force in ISF. 131

Figure 4.7 Illustration of the workpiece circumferential cross-section. 135

Figure 4.8 Flow chart to solve and implement the analytical model of forming force prediction in ISF. 140

Figure 4.9 Designed ISF parts in (a), (b) truncated cone shape, and (c), (d) truncated pyramid shape with varying drawing angle..... 141

Figure 4.10 Experimental setup for ISF of TA1..... 142

Figure 4.11 Analytically predicted results of (a) total force, (b) z force, (c) x force and (d) y force of different tool position in ISF of truncated cone part of TA1. 144

Figure 4.12 Comparison between experimental and analytically predicted force components in ISF of truncated cone part of TA1: (a) whole process comparison and (b) detailed comparison in an enlarged time range. 145

Figure 4.13 Analytically predicted results of (a) total force, (b) z force, (c) x force and (d) y force of different tool position in ISF of truncated pyramid part of TA1..... 146

Figure 4.14 Comparison between experimental and analytically predicted force components in ISF of truncated pyramid part of TA1: (a) whole process comparison, (b) detailed comparison in an enlarged time range and (c) prediction with and without consideration of biaxial tension condition..... 147

Figure 4.15 Comparison between experimental and analytically predicted force components in ISF of truncated cone part of PEEK: (a) whole process comparison and (b) detailed comparison in an enlarged time range. 150

Figure 4.16 Application of the analytical model in ISF-based manufacture of cranial plate: (a) Head and cranial models, (b) prediction of total force, (c) prediction of vertical force, (d) prediction of horizontal force and (e) comparison between the experimentally measured vertical force F_v and horizontal force F_h from Lu et al. [141] and analytically predicted results. 152

Figure 4.17 Experimentally measured total forces from Duflou et al. [117] and predicted results in ISF of AA3003-O with different (a) step size, (b) tool radius, (c) drawing angle and (d) sheet thickness 154

Figure 4.18 Comparison of peak F_p and stabilised forces F_s between experimentally measured results from Duflou et al. [117] and analytically predicted results in ISF of AA3003-O with different (a) step size, (b) tool radius, (c) drawing angle and (d) sheet thickness. 156

Figure 4.19 Comparison of force components between experimentally measured results from Aerens et al. [119] and analytically predicted results in ISF of AA3003-O with different (a) step size, (b) tool radius, (c) drawing angle and (d) sheet thickness. 158

Figure 4.20 Comparisons of vertical forming force predicted by different models at different (a), (b) step size, (c), (d) tool radius, (e), (f) drawing angle and (g), (h) sheet thickness based on testing results in ISF of AA3003-O by Aerens et al. [119]. 160

Figure 4.21 Effect of friction coefficient on (a) forming force history and (b) stabilised total force and force components. 163

Figure 4.22 Effect of ratio r_{tool}/t_0 on (a) comparison between predicted stabilised force F_{s} and peak force F_{p} and experimental results from Duflou et al. [117] and (b) prediction errors of peak and stabilised forces. 165

Figure 5.1 Contact region and maximum pressure position in ISF. 171

Figure 5.2 Illustration of contact between a rigid hemispherical tool and an elastic/ elastic-plastic half space. 174

Figure 5.3 Illustration of elastic-plastic contact between forming tool and sheet material in ISF. 176

Figure 5.4 Illustration of implementation method of contact pressure distribution. .. 177

Figure 5.5 MATLAB visualization of contact pressure distribution on the forming tool in ISF of (a) TA1 sheet and (b) PEEK sheet. 180

Figure 5.6 FE model and element mesh strategy of ISF of TA1 sheet. 182

Figure 5.7 Data of quasi-static uniaxial tension and Johnson-Cook model for the plasticity definition in FE simulation. 182

Figure 5.8 (a) Thermal conductivity [149], (b) specific heat capacity [150] and (c) Young's modulus of PEEK [151] at different temperatures. 184

Figure 5.9 Flow stress data and constitutive prediction of PEEK at different high temperatures. 184

Figure 5.10 Temperature distribution in FE simulation of heat-assisted ISF of PEEK sheet. 186

Figure 5.11 Comparison of forming force between FE simulation and analytical prediction in ISF of TA1. (a) Whole process comparison and (b) detailed comparison in an enlarged time range..... 188

Figure 5.12 Comparison of forming force between FE simulation and analytical prediction in ISF of PEEK. (a) Whole process comparison and (b) detailed comparison in an enlarged time range. 189

Figure 5.13 Comparison of the size of contact area between FE simulation and analytical prediction in ISF of (a) TA1 and (b) PEEK. 190

Figure 5.14 Comparison of the maximum contact pressure between FE simulation and analytical prediction in ISF of (a) TA1 and (b) PEEK. 191

Figure 5.15 Comparison of contact pressure distribution between FE simulation (a), (c) and (e) and analytical prediction (b), (d) and (f) with different drawing angles in ISF of TA1. (a) and (b) 40°, (c) and (d) 50°, (e) and (f) 60°. 193

Figure 5.16 Quantitative comparison of (a) contact area and (b) maximum contact pressure between FE simulation and analytical prediction with drawing angles of 40°, 50° and 60° in ISF of TA1..... 194

Figure 5.17 Comparison of contact pressure distribution between FE simulation (a), (c) and (e) and analytical prediction (b), (d) and (f) with different drawing angles in ISF of PEEK. (a) and (b) 40°, (c) and (d) 50°, (e) and (f) 60°. 196

Figure 5.18 Quantitative comparison of (a) contact area and (b) maximum contact pressure between FE simulation and analytical prediction with drawing angles of 40°, 50° and 60° in ISF of PEEK. 197

Figure 5.19 Effect of element size in ISF simulation of TA1 sheet on the comparison between FE simulation and analytical results. (a) Size of contact area and (b) the maximum contact pressure. 198

Figure 6.1 Experimental setup of heat-assisted ISF. (a) CNC milling machine, (b) ISF fixture, heating and measurement systems, and (c) schematic of the ISF test rig..... 206

Figure 6.2 Designed shape of ISF tests: (a) Profile with varying drawing angles, (b) model truncated cone part and (c) model of truncated pyramid part. 207

Figure 6.3 Preliminary ISF testing results of PMMA at (a) 90 °C and (b) 100 °C. ... 209

Figure 6.4 (a) Head model and (b) customised cranial plate for ISF manufacture. ... 210

Figure 6.5 Laser scanning system for geometric shape measurement. 210

Figure 6.6 ISF formed parts of (a) PEEK I, (b) PEEK II, (c) PEEK III, (d) PEEK IV and (e) PEEK V. 212

Figure 6.7 Temperature distribution during ISF of PEEK truncated cone part PEEK I. 213

Figure 6.8 Temperature distribution during ISF of PEEK truncated pyramid part PEEK V. 214

Figure 6.9 Comparison of temperature variation during ISF of PEEK. (a) Effect of spindle speed, (b) effect of feed rate, (c) effect of step size and (d) effect of forming shape. 215

Figure 6.10 Comparison of vertical and horizontal forming forces in ISF of PEEK sheet. (a) Effect of spindle speed, (b) effect of feed rate, (c) effect of step size and (d) effect of forming shape. 218

Figure 6.11 Comparison among experimental, analytical and simulation force components in ISF of truncated cone part of PEEK: (a) whole process comparison and (b) detailed comparison in an enlarged time range. 220

Figure 6.12 Deviation map of the formed PEEK parts as compared with the designed model: (a) PEEK I, (b) PEEK II, (c) PEEK III, (d) PEEK IV and (e) PEEK V..... 221

Figure 6.13 Profile comparison of formed truncated cone parts by heat-assisted ISF of PEEK sheet. (a) Effect of spindle speed, (b) effect of feed rate and (c) effect of step size. 223

Figure 6.14 Profile comparison of formed truncated pyramid part by heat-assisted ISF of PEEK sheet from different cross-sections..... 224

Figure 6.15 Thickness distribution of the formed PEEK parts: (a) PEEK I, (b) PEEK II, (c) PEEK III, (d) PEEK IV and (e) PEEK V..... 225

Figure 6.16 Thickness distribution from cross-section of formed PEEK truncated cone parts: (a) PEEK I, (b) PEEK II, (c) PEEK III and (d) PEEK IV. 226

Figure 6.17 Thickness distribution from cross-section of formed PEEK truncated pyramid par: (a) From x-z plane and (b) from diagonal cross-section..... 226

Figure 6.18 ISF formed parts of (a) PMMA I, (b) PMMA II, (c) PMMA III and (d) PMMA IV..... 227

Figure 6.19 Temperature distribution during ISF of PMMA truncated cone part PMMA I..... 228

Figure 6.20 Temperature distribution during ISF of PMMA truncated pyramid part PMMA IV..... 229

Figure 6.21 Comparison of temperature variation during ISF of PMMA sheet. (a) Effect of preheating temperature, (b) effect of spindle speed and (c) effect of forming shape. 230

Figure 6.22 Comparison of vertical and horizontal forming forces in ISF of PMMA sheet. (a) Effect of preheating temperature, (b) effect of spindle speed and (c) effect of forming shape. 231

Figure 6.23 Deviation map of the formed PMMA parts as compared with the designed model: (a) PMMA I, (b) PMMA II, (c) PMMA III and (d) PMMA IV. 232

Figure 6.24 Profile comparison of formed truncated cone parts by heat-assisted ISF of PMMA sheet. (a) Effect of preheating temperature and (b) effect of spindle speed.. 233

Figure 6.25 Profile comparison of formed truncated pyramid part by heat-assisted ISF of PMMA sheet from different cross-sections. 234

Figure 6.26 Thickness distribution of the formed PMMA parts: (a) PMMA I, (b) PMMA II, (c) PMMA III and (d) PMMA IV. 235

Figure 6.27 Thickness distribution from cross-section of formed PMMA truncated cone parts: (a) PMMA I, (b) PMMA II and (c) PMMA III. 236

Figure 6.28 Thickness distribution from cross-section of formed PMMA truncated pyramid part: (a) From x-z plane and (b) from diagonal cross-section..... 236

Figure 6.29 Heat-assisted ISF parts of (a) PEEK cranial plate and (b) PMMA cranial plate. 237

Figure 6.30 Temperature distribution during ISF-based manufacture of PEEK cranial plate. 238

Figure 6.31 Temperature distribution during ISF-based manufacture of PMMA cranial plate. 238

Figure 6.32 Temperature variation during ISF-based manufacture of (a) PEEK cranial plate and (b) PMMA cranial plate. 239

Figure 6.33 Vertical and horizontal forming forces in ISF-based manufacture of (a) PEEK cranial plate and (b) PMMA cranial plate. 240

Figure 6.34 Deviation map of the formed cranial plate as compared with the designed model: (a) PEEK part and (b) PMMA part. 241

Figure 6.35 Profile comparison of formed cranial plates by heat-assisted ISF of PEEK and PMMA in cross-sections of (a) y-z plane and (b) x-z plane. 241

Figure 6.36 Thickness distribution of the formed cranial plate: (a) PEEK part and (b) PMMA part. 242

Figure 6.37 Illustration of the initial bending condition in ISF. 244

Figure 6.38 Illustration of the theoretical ISF formed profile with consideration of bending and distortion behaviours 245

Figure 6.39 Comparison of the formed profile between the analytically prediction result and the experimental result. 247

Figure 6.40 Illustration of stress components in a small element. (a) Stress components on a small element, (b) φ direction view and (c) θ direction view. 248

Figure 6.41 Illustration of the predicted results of (a) stress triaxiality distribution and (b) equivalent strain distribution in ISF with drawing angle of 60°, tool radius of 5 mm and sheet thickness of 3 mm. 251

Figure 6.42 Simulation result of the stress triaxiality distribution of different regions under tool-sheet contact. 253

Figure 6.43 Fracture observation of ISF formed PMMA truncated cone part: (a) From the front view, (b) from the left view and (c) from the right view. 254

Figure 6.44 Observation of twist behaviour in ISF formed truncated cone parts: (a) PEEK part and (b) PMMA part. 255

Figure 6.45 Definition of the twist angle and the shear stain/ angle of ISF formed truncated cone part: (a) Overview of the twisted PEEK part and (b) detailed definition. 256

Figure 6.46 Global coordinate system and the principal stresses in ISF. 257

Figure 6.47 Illustration of the change of twist angel and shear strain/ angle in a small element. 259

Figure 6.48 Comparison of the shear strain/ angle between analytically predicted result and experimental result. 260

List of Tables

Table 2.1 State of stress and strain in the small localised plastic zone of the SPIF of thermoplastics and metals [37]. 27

Table 2.2 Effects of process parameters on different aspects of ISF of thermoplastics. 54

Table 2.3 Differences between ISF of thermoplastic and metallic materials. 55

Table 3.1 Material parameters of the new model for the tensile behaviour of PEEK.. 84

Table 3.2 Material parameters of the new model for the compressive behaviour of PEEK. 87

Table 3.3 Material parameters of the new model for the tensile behaviour of PC. 89

Table 3.4 Material parameters of the new model for the compressive behaviour of PC. 91

Table 3.5 Material parameters of the new model for the dynamic tensile behaviour of PC. 93

Table 3.6 Material parameters of the new model for the dynamic compressive behaviour of PC. 95

Table 3.7 Material parameters of Johnson-Cook model for the tensile behaviour of PEEK. 97

Table 3.8 Material parameters of Nasraoui et al. model for the tensile behaviour of PEEK. 99

Table 3.9 Material parameters of DSGZ model for the tensile behaviour of PEEK.. 100

Table 3.10 A comparison of Johnson-Cook, Nasraoui et al., DSGZ and the new model at different strain rates and a constant temperature of 296 K. 105

Table 3.11 A comparison of Johnson-Cook, Nasraoui et al., DSGZ and the new model at different temperatures and a constant strain rate of 4.96×10^{-4} s^{-1}. 105

Table 3.12 Material parameters of the new model for the compressive behaviour of PC tested by Mulliken and Boyce. 107

Table 4.1 Johnson-Cook parameters of TA1 and AA3003-O sheet. 142

Table 4.2 Horizontal force conversion in ISF of truncated cone and pyramid parts.. 143

Table 4.3 Model parameters of Modified ZOP model I for PEEK at 130 °C. 149

Table 5.1 Parameters used in the FE simulation for ISF of TA1 and PEEK sheets... 181

Table 5.2 Parameters in FE simulation of ISF of TA1 sheet. 182

Table 5.3 Model parameters of Modified ZOP model I for PEEK at high temperatures. 185

Table 5.4 Parameters in FE simulation of ISF of PEEK sheet. 185

Table 6.1 Experimental parameters for ISF of PEEK and PMMA. 208

Chapter 1 Introduction

1.1 Overview of incremental sheet forming (ISF) and its application in thermoplastics

1.1.1 Overview of ISF

Incremental sheet forming (ISF) is a relatively new flexible sheet forming process, which has drawn increasing attention in recent years. As shown in Figure 1.1, its principal concept is to progressively enable localized deformations by moving a hemispherical tool along a tool path to gradually deform the blank sheet to its designed shape. In the early stage of ISF research, researchers mostly focused on single point incremental forming (SPIF, one commonly used type of ISF), during which the flange of the sheet is clamped without further support and the sheet is maintained at a fixed position. In most cases, the sheet is deformed from the outside to the inside, and the centre of sheet is moved downwards gradually.

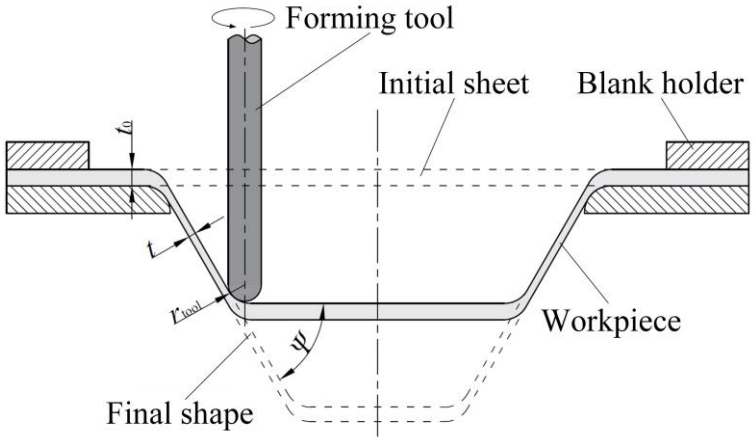


Figure 1.1 The basic principle of ISF.

In the past decade, variants of ISF have been developed from SPIF including two-point incremental forming (TPIF) and double side incremental forming (DSIF), as shown in Fig. 2. During the process of TPIF, the sheet is supported by a partial die or a full die at

the other side and is deformed from the inside to outside with the flange moving downwards. During the process of DSIF, a second tool is used on the other side, serving as local support for the forming tool. The sheet is deformed under the cooperative effect of the forming tool and the supporting tool.

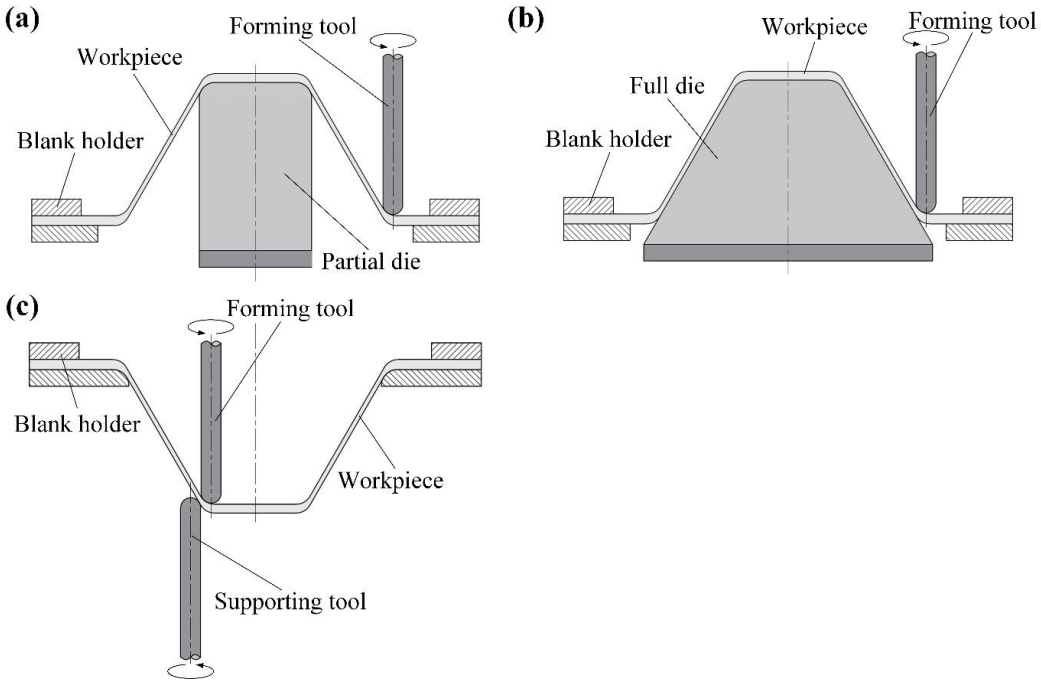


Figure 1.2 Different variants of the ISF process. (a) TPIF with a partial die, (b) TPIF with a full die and (c) DSIF.

Comparing with traditional sheet forming processes, ISF is especially advantageous in manufacturing small-batch and customised sheet parts because of its distinctive features of flexibility, adaptability, applicability [1], improved material formability [2] and associated benefits in energy efficiency and reduced costs [3]. It has shown the potential in practical applications in aerospace [4], automotive industries [5] and medical engineering [6]. Therefore, ISF has been studied and tested to shape metal sheet parts since its inception. Most studies about ISF are focused on the deformation and fracture mechanism, formability improvement, different variants of ISF and their applicability to different metallic materials such as steel, aluminium, and titanium alloys, as well as some thermoplastics.

1.1.2 Overview of ISF of thermoplastics

The early research works are mainly focused on ISF in metallic system, while Le et al. [7] and Franzen et al. [8], for the first time, attempted to use ISF to form thermoplastics. Since then, ISF of thermoplastic materials has attracted increasing attention for possible applications mainly because of the materials' advantages including good resistance to impact and to temperature and bearing capacity [7, 9]. In recent years, many researchers extend the scope to investigate the use of ISF to process different kinds of thermoplastics such as polypropylene (PP), polyoxymethylene (POM), polyamide (PA), polycarbonate (PC), polyvinylchloride (PVC) and polyethylene terephthalate (PET) [10-13], as shown in Figure 1.3. Yonan et al. [14] compared the main thermoplastic materials processing technologies from the technical and economic aspects. From their summarisation, the benefits of using ISF process to form thermoplastics appear to include low cost, low production rate, rapid prototype, and small-batch production, compared with traditional moulding and forming technologies.

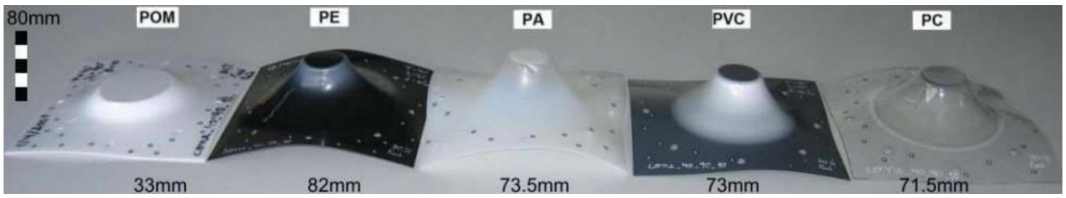


Figure 1.3 Formed thermoplastic parts by ISF [11].

Most researchers investigated ISF of thermoplastics with consideration of the basic process mechanism [8, 14-19], while considerable interest has been made especially for such as customised cranial implant applications [20-24]. Centeno et al. [20, 22] put forward a methodology to manufacture cranial implants by using ISF of thermoplastic sheets as the ISF-based cranioplasty implant processing gives an excellent demonstration of the aforementioned advantages in manufacturing customised parts for medical applications. Following the similar approach, Bagudanch et al. [25, 26]

achieved the manufacture of cranial plates with biocompatible thermoplastics, polycaprolactone (PCL) and ultrahigh molecular weight polyethylene (UHMWPE).

From the above overview, it can be summarised that the advantages of both ISF processing technology and thermoplastic materials promote their combination, and there is an increasing interest of transferring the research focus to ISF of thermoplastics in recent years because of the extensive application prospects.

1.2 Research challenges

Although advances have been made in the process design and implementation of ISF of metals and thermoplastics, the deformation behaviour in the ISF process is still less understood, especially the localised interaction between the forming tool and sheet material. This leads to the current PhD research project to investigate the local tool-sheet contact behaviour and deformation mechanism in ISF of metals and thermoplastics. The research challenges can be given from the following three aspects.

1.2.1 Material constitutive modelling

The complexity of constitutive response of thermoplastic materials has been acknowledged. Five phases can be usually found in the deformation process: linear elasticity, non-linear elasticity, yield, strain softening and hardening [27], while the strain rate and temperature also have an influence on the stress evolution. This makes the material flow of thermoplastic in ISF much more difficult to describe and predict than metals. To overcome this challenge, a vigorous constitutive model is needed to be developed for the use in further analytical modelling and finite element (FE) simulation.

1.2.2 Process analytical modelling

The appropriate solutions of modelling for different aspects can promote the

understanding of the deformation and fracture mechanism in ISF. Although some studies have been done following the framework of membrane analysis developed by Silva et al. [28], the process modelling focused on the local deformation and contact region is less involved. As challenging aspects to the research community, the analytical modelling of forming force and contact pressure distribution can help develop more in-depth understanding of the deformation behaviour and the interaction between forming tool and sheet material.

1.2.3 Forming and testing method

Different from metals, ISF of thermoplastics may be conducted at elevated temperatures with the use of external heating source and forming tool rotation. This leads to the complexity of the ISF testing and measurement setup, which involves the ISF fixture, the force measurement system, the temperature measurement and recording system. Besides, it also would be a challenge for heat-assisted ISF of thermoplastics to determine proper process parameters for successfully forming of thermoplastics without obvious defects, which is essential to the further applications of ISF-based manufacture of thermoplastics.

1.3 Aim and objectives

The core aim of this PhD project is to investigate the deformation mechanism and localised contact behaviour in ISF of metals and thermoplastics. By looking into the insight of material deformation and tool-sheet contact, theoretical analysis is carried out and analytical models are developed to predict the material constitutive response, forming force history, contact pressure distribution in ISF of polyether ether ketone (PEEK) and other materials. This PhD research study also aims to test the feasibility of heat-assisted ISF on PEEK and polymethyl methacrylate (PMMA, acrylic), and to

investigate some challenging issues in ISF of PEEK and PMMA such as forming inaccuracy, fracture, and twist. The following objectives are supportive to achieve these aims:

(1) A constitutive model is aimed to be developed and validated to predict the stress – strain relationship of PEEK and other thermoplastics at elevated temperatures and different strain rates.

(2) A new analytical model is aimed to be developed and validated to predict the forming force history by looking into the material deformation and local contact behaviour in ISF.

(3) A new analytical model is aimed to be developed and validated to predict the contact area and pressure distribution under local tool-sheet contact.

(4) The possibility and feasibility of ISF in forming high-performance PEEK and brittle PMMA sheets at elevated temperature and the application in cranial plate manufacture are aimed to be tested.

(5) Theoretical analysis is aimed to be carried out and validated to reveal the forming accuracy, fracture and twist behaviour in ISF of PEEK and PMMA.

1.4 Research methodology

The following tasks are planned to achieve the research aim and objectives:

(1) A new constitutive model is developed with phenomenological method to predict the constitutive response of PEEK and other thermoplastics with consideration of the linear elastic, non-linear elastic, yield, strain softening, hardening behaviours, the effect of temperature and strain rate. Tensile and compressive behaviours of semi-crystalline (such as PEEK) and glassy thermoplastics (such as polycarbonate, PC) are used to

validate the new model. A comparison is made between the new model and some other models from literature. The constitutive model is fundamental for the development of analytical models of forming force prediction in Task (2), contact pressure prediction in Task (3) and the mechanism discussion of challenging issues in heat-assisted ISF tests of thermoplastics in Tasks (4) and (5).

(2) A new force prediction model is developed with analytical method to predict the forming force history in ISF by considering localised shear and indentation, material thinning, instant elastic recovery and global elastic bending. In the modelling process, the constitutive model developed in Task (1) is used to calculate the equivalent of the sheet material. The analytical model is implemented and visualised in MATLAB. Experimental validations are conducted to test the prediction results of the analytical model at different deformation conditions including heat-assisted ISF of PEEK in Task (4). The analytical model for force prediction is the key to the modelling of contact pressure distribution in Task (3) and the mechanism understanding of the experimentally observed fracture and twist in Tasks (4) and (5).

(3) A new contact pressure prediction model is proposed with analytical method by considering the local interaction between the forming tool and sheet material. The contact theory in elastic plastic regime is adopted to develop the analytical model in ISF. In the modelling process, the constitutive model developed in Task (1) and force prediction model developed in Task (2) are used to calculate the maximum contact pressure and derive the pressure distribution equation. The implementation and visualisation are accomplished in MATLAB. A thermomechanical coupled FE simulation method for heat-assisted ISF is developed, and the results is used to validate the analytically predicted size of contact area, maximum contact pressure and pressure distribution. The analytical model for contact pressure distribution is used in the

evaluation of fracture behaviour in heat-assisted ISF tests of thermoplastics in Tasks (4) and (5).

(4) The heat-assisted ISF of PEEK and PMMA is set up, and the force and temperature measurement systems are developed. The ISF tests with different process parameters, such as spindle speed, feed rate and geometric shape, are carried out to investigate their effect on the forming temperature, forming force, geometric accuracy, and thickness distribution. From the tests, a proper set of process parameters is obtained and used for ISF-based manufacture of PEEK and PMMA cranial plates. The experimental results in this task lead to the observation of challenging issues including insufficient forming accuracy, fracture and twist in heat-assisted ISF of thermoplastics, which are analysed in Task (5). In addition, the forming force measurement in heat-assisted ISF of PEEK is used to validate the analytical model and FE simulation for force prediction in Tasks (3) and (4).

(5) Based on the experimental observations of formed parts by heat-assisted ISF in Task (4), a theoretical model is developed and validated for forming accuracy prediction by considering the global bending and elastic springback behaviour. In the modelling process, the constitutive model developed in Task (1) is used to calculate the equivalent stress of sheet material in bending and springback. Analytical models of stress triaxiality and equivalent strain distribution are developed to discuss the fracture mechanism in ISF. In the modelling of stress triaxiality distribution, the analytical models for forming force prediction in Task (2) and contact pressure prediction in Task (3) are used. By considering the torque, shear strain energy and twist accumulation along tool path, a theoretical analysis is developed and validated for prediction of the twist behaviour during ISF process. The equivalent stress in the modelling process is calculated by the constitutive model developed in Task (1), while the torque is calculated based on the

analytical model for force prediction in Task (2). The modelling and evaluation of results in this task help to explain and understand the forming inaccuracy, fracture and twist, which are observed from experiments of heat-assisted ISF of PEEK and PMMA in Task (4).

1.5 Thesis contributions

The contributions of the PhD thesis can be concluded as follows:

(1) A piecewise based method is proposed for construction of constitutive model. The use of a transition function enables a smooth shifting of the flow stress behaviours under small and large strain conditions.

(2) The new phenomenological model can be used to predict the complicated effect of strain, strain rate and temperature on the flow stress. The new model is applicable for both tensile and compressive behaviours of crystalline and glassy thermoplastics in low and high strain rate conditions.

(3) A localised coordinate system is proposed for the analytical modelling of the local tool-sheet contact behaviour. For the first time, the local contact region, thickness distribution and strain components are modelled in the proposed coordinate system.

(4) For the first time, an analytical model for force prediction in ISF is derived by comprehensively considering the deformation condition, localised shear and indentation, stretching, as well as the effects of instant elastic recovery, tool-sheet friction, localised and global bending.

(5) The prediction of force history captures well the forming force fluctuation due to the change of deformation condition and provides an insight into the material deformation conditions and its correlation to forming force characteristics of the whole ISF process.

(6) For the first time, the developed analytical model for force prediction has the capability to predict both peak and stabilised forces and is more accurate in most cases, compared with other models.

(7) For the first time, the contact pressure prediction model is developed for ISF-based on the elastic plastic contact theory. The size of contact area, maximum contact pressure and pressure distribution is validated by the FE simulation results. This promotes the understanding of local tool-sheet contact problem in ISF.

(8) The feasibility of using ISF to form high-performance PEEK and hard-to-form PMMA by a heat-assisted ISF setup with heating, force and temperature measurement systems is confirmed by the study.

(9) The effect of process parameters on the forming temperature, force history, geometric accuracy and thickness distribution is revealed. The study results guide the achievement of ISF-based manufacture of PEEK and PMMA cranial plates.

(10) Better understanding is made in terms of the forming accuracy, fracture mechanism and twist behaviour. The forming inaccuracy may be caused by the global banding, springback behaviour and thermal distortion. The stress triaxiality and equivalent strain distribution influence the fracture position. The twist behaviour may be analysed with consideration of the torque, shear strain energy and twist accumulation along tool path.

1.6 Thesis structure

Seven chapters are included in the thesis as follows:

Chapter 1 gives an introduction of the thesis. The overview of ISF and the application in thermoplastics are introduced firstly. This leads to the research challenges, the aims and objectives of the thesis. Accordingly, the methodology is introduced, and thesis

contributions are given.

Chapter 2 reviews the concurrent research progress on the emerging trend of thermoplastics focused ISF processes. Attention is given to the processing conditions, the deformation mechanism and failure behaviour. This leads to detailed discussions on the formability, effect of different process parameters and the forming quality. A comparison of important similarities and differences between ISF of thermoplastic and metallic materials is made. A brief discussion is provided on the technical challenges and research directions for ISF of thermoplastic materials in the future.

Chapter 3 proposed a new phenomenological constitutive model to predict the mechanical behaviour of thermoplastics. The new constitutive model and the method to determine the parameters of the model are introduced. Piecewise and transition functions are proposed to enable a smooth transition of the flow stress behaviours under both small-strain and large-strain conditions. The new model is validated by tensile and compressive behaviours of PEEK and PC in low and high strain rate conditions. A comparison between the new model and other others is given to present the improved level of prediction accuracy.

Chapter 4 presents a new analytical model for the prediction of forming force during the ISF process by looking into an insight of deformation mechanism and local tool-sheet contact behaviour. The modelling of contact region, thickness distribution and strain components are carried out firstly, and the effect of deformation condition, localised shear and indentation, stretching, as well as the effects of instant elastic recovery, tool-sheet friction, localised and global bending are fully considered in the modelling process. The analytical model is validated by a series of ISF tests and comparison with other models.

Chapter 5 follows the framework of ISF force prediction established in Chapter 4 and develops an analytical model for the prediction of contact pressure distribution in ISF. A thermomechanical FE simulation method for heat-assisted ISF is also developed in this chapter. The contact pressure prediction model is then validated by the FE simulation results in terms of the size of contact area, the maximum contact pressure, and the pressure distribution. A discussion is given on the aspects affecting the validation results and potential improvement of the analytical model.

Chapter 6 is focused on the experimental aspect of the heat-assisted ISF of PEEK and PMMA sheet. The ISF setup, temperature and force measurement systems are tested in this chapter. The effect of different process parameters on the forming temperature, force history, forming accuracy and thickness distribution is revealed. Based on the testing results, PEEK and PMMA cranial plates are manufactured by heat-assisted ISF. Finally, discussions are given on the understanding of some challenging issues in ISF, including forming inaccuracy, fracture mechanism and twist behaviour.

Chapter 7 summarises the conclusions of the thesis and gives some recommended directions for future studies.

Chapter 2 Literature Review

2.1 Introduction

ISF is a promising flexible manufacturing process, which has been used in sheet forming of various metallic materials. Although ISF-based forming of thermoplastics is relatively new, it has drawn considerable interests and significant progress has been made in recent years. This section presents a review of concurrent research on the emerging trend of thermoplastics focused ISF processes. Attention is given to the processing conditions including process setup, process parameters and forming forces. The deformation mechanism and failure behaviour during ISF of thermoplastics are evaluated, which leads to detailed discussions on the formability, effect of different process parameters and the forming quality such as geometric accuracy, surface finish and other consideration factors in ISF of thermoplastics. A comparison of important similarities and differences between ISF of thermoplastic and metallic materials is made. Besides, the constitutive modelling of thermoplastics and analytical modelling of different aspects in ISF are reviewed. Finally, a brief discussion is provided on the technical challenges and research directions for ISF of thermoplastic materials in the future.

2.2 ISF of thermoplastics

2.2.1 ISF Processing conditions

ISF is performed by progressive localised deformations along a tool path to form the whole shape of the part. The process conditions are fundamental to ISF processing. Many researchers have investigated the process setup (Section 2.2.1.1) and process parameters (Section 2.2.1.2) of ISF of thermoplastic materials. During the ISF process,

the forming force (Section 2.2.1.3) is also a significant factor because of its importance in selection of ISF forming tool.

2.2.1.1 Process setup

The setup of metallic ISF processing is generally comprised of four different parts: (1) positioning system; (2) forming tool; (3) clamping fixture; (4) support structure [29]. It is the same case for the ISF of thermoplastic materials. Franzen et al. [8], Silva et al. [30] and Yonan et al. [19] equipped a computer numerical control (CNC) machining centre with an experimental set-up to perform ISF on PVC, PET and PC sheets, as shown in Figure 2.1. In Figure 2.1(a), t_0 and t_f are the initial and formed sheet thickness, Ψ is the drawing angle and λ is complementary angle of the drawing angle. The equipment consisted of the thermoplastic sheet blank, the blank holder, the backing plate and the rotating forming tool controlled by CNC machining programme. Medina-Sanchez et al. [16] developed an in-house fixing system to conduct SPIF on a milling machine to shape PVC sheet with a thickness of 3 mm.

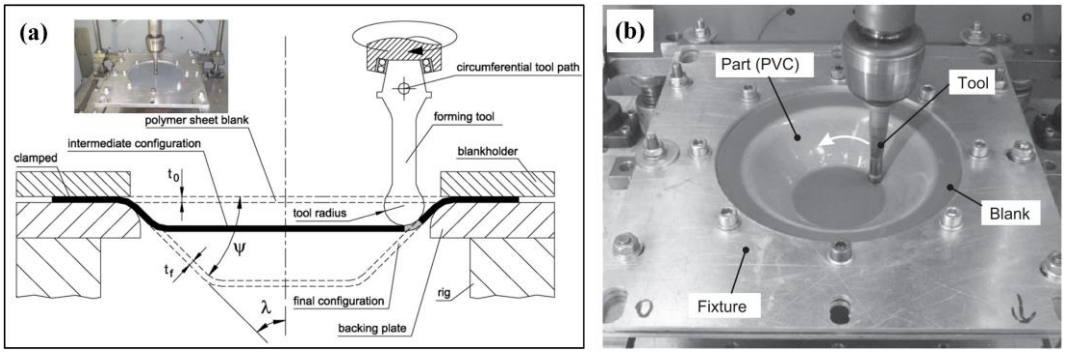


Figure 2.1 (a) Schematic representation of a cross-section view [8] and (b) experimental setup of SPIF [19].

For polymeric materials, reduced strength and increased ductility can be obtained with the rise of forming temperature. During ISF, temperature elevation is useful to improve the formability of some hard-to-form polymeric materials. Therefore, ISF of thermoplastics is often assisted by using a heating system in the setup [31, 32]. Some

researchers have developed different heating methods used in ISF process to elevate the forming temperature of thermoplastic sheets. When forming PMMA sheet and a composite material sheet made of polyamide-6 (PA 6) and short glass fibres, Conte et al. [33, 34] designed a heating system using an electric resistance of 2 kW as the heating source. In the system, a thermal isolated chamber was constructed inside of the metallic structure coated with refractory material. And then, the thermal power produced by electrical resistance heated up the air inside to enable heat transfer between the air and the thermoplastic materials. The temperature of upper face of the sheet was monitored and controlled by a thermos-camera and a control unit. Ambrigio et al. [31] inherited the same heating system when they tried to form PMMA sheets using ISF. Okada et al. [35] realised local heating using a halogen lamp on the one side of the carbon fibre reinforced thermoplastic sheet and formed on the opposite side of the sheet using a hemispherical forming punch with a reciprocating motion. In the research of Sridhar and Rajenthirakumar [36], a heating coil is fixed and placed below the part to achieve the temperature elevation during SPIF process of PC sheet. It can be concluded that different heating methods have been attempted to conduct warm/hot incremental sheet forming of thermoplastic materials.

However, a heating system is not always essential in the ISF process of thermoplastics, especially when the given material has excellent formability, or the friction heat is sufficient to soften the material. Moreover, cold ISF could produce thermoplastic parts with higher strength and save energy and cost [19]. In the studies of Franzen et al. [8] Silva et al. [18], PVC sheet parts were proved to be successfully formed with large drawing angle and forming depths at room temperature. Martins et al. [10], Marques et al. [37], Hussain et al. [38] and some other researchers found that cold ISF is a viable option for thermoplastics, which is an attractive and promising research aspect. On the

other hand, in the study of Bagudanch et al. [15] the temperature rise resulting from the friction heat could reach about 50 ºC above the room temperature at the tool tip using a spindle speed of 2000 rpm. This temperature rise was also presented by many other researchers, e.g. Medina-Sanchez et al. [16]. This leads to the relatively good material formability without pre-set temperature rise by external heating system.

2.2.1.2 Process parameters

The ISF process parameters include forming temperature, drawing angle (Ψ), step size (Δz), spindle speed (ω), feed rate (v), tool radius (r_{tool}), initial sheet thickness (t_0), tool shape and tool path. Among them, forming temperature, drawing angle, tool radius, step size, spindle speed and initial sheet thickness are important to the formability, failure and forming quality in ISF processing of thermoplastics. Therefore, these parameters are discussed below.

(1) Forming temperature

Forming temperature can significantly influence material properties and thus exhibits non-negligible effects on the ISF process of thermoplastics. In general, the material formability can be improved at elevated temperature. The forming geometric accuracy and surface roughness would also be affected. The temperature elevation can be reached by not only external heating sources but also the heat of friction between sheet blanks and ISF tool during the forming process [39]. Both have been studied by researchers on their influence on the ISF forming quality.

Conte et al. [34] studied the effects of process temperature on the SPIF of PMMA sheet with a thickness of 2 mm. According to their research results, the initial temperature arisen from external heating and the spindle speed was adjustable parameters to achieve an appropriate forming temperature without brittle fracture and excessive springback

during the process. However, the surface quality of the part was damaged when a high spindle speed was applied. Therefore, adjusting the initial temperature before forming without increasing the spindle speed was an effective method to realise better forming quality of thermoplastic materials. In another research [33], the same authors investigated the effects of forming temperature on material formability, thickness distribution and the forming accuracy of a composite material sheet part made of PA 6 and short glass fibres. The authors found that better performance could be achieved at a higher temperature in ISF of thermoplastics. To maximise the effect of process temperature, Formisano et al. [40] observed that a reasonable localised temperature should be produced below the glass transition temperature, which was ideal to soften the thermoplastic sheet and keep the stiffness at a proper level. The similar conclusion was also reported by Kulkarni et al. [41].

(2) Drawing angle (wall angle)

During the ISF process, a constant or varying drawing angle may be defined to form a specific geometry. The maximum drawing angle $\Psi_{\max}$ and the initial drawing angle Ψ_0 are considered as two important parameters in ISF of thermoplastics. For metallic materials, the maximum drawing angle $\Psi_{\max}$ is used as a parameter to determine the formability [42]. However, for thermoplastic materials, in addition to the maximum drawing angle $\Psi_{\max}$ used as a significant parameter of material formability [43], researchers also consider initial drawing angle Ψ_0 as a parameter with an effect to the material formability. Therefore, as a parameter in ISF of thermoplastic materials, the initial drawing angle Ψ_0 has been studied widely and is believed to have a significant influence on the formability and forming quality of ISF.

As reported by Marques et al. [37], the initial drawing angle Ψ_0 has an influence on the formability of thermoplastic materials only varying from 30º to 60 º. It is noteworthy that with the increase of Ψ_0, the tendency of formability is different for different thermoplastics [11]. More detailed discussion is given in Section 2.2.3.2. Apart from material formability, the forming accuracy is also influenced by the initial drawing angle. The springback rises with the increase of the initial drawing angle, according to the study of Martins et al. [10].

(3) Tool radius

Tool radius is an important parameter in the ISF process of thermoplastic materials in terms of both formability and forming quality. According to studies by Bagudanch et al. [39] and Hussain et al. [38], the increase of the tool radius leads to the elevation of local temperature due to increased friction heat resulting from the increased tool-sheet contact zone. Besides, the surface finish can be significantly influenced by the tool radius. Better surface quality can be produced by a tool with a smaller radius [8, 12]. Apart from causing the change of forming temperature and surface finish, the variation of tool radius can also have an influence on the material forming limit. In general, the material formability can be increased with the decrease of tool radius, according to the studies of Martins et al. [10] and Marques et al. [37]. The influence of tool radius on the formability of thermoplastic materials in ISF is discussed in detail in Section 2.2.3.2.

(4) Step size

The step size is an important parameter related to the formability and forming quality for both metallic and thermoplastic materials. Edwards et al. [44] found that, in ISF of PC sheet, reduced springback can be realised via increasing the step size due to the increased forming force. Also, a smaller step size can lead to reduced thinning in ISF of

composite materials, according to Conte et al. [33]. In another study, Bagudanch et al [15] found out that the step size only has less influence on the maximum vertical force than on the surface roughness of the formed parts. From the micro aspect, the larger step size can cause greater void densities and thus the thermoplastic material formed using SPIF exhibits greater crystallinity than unformed material [45]. This may provide an explanation for the macro influence of step size on thermoplastic in ISF.

(5) Spindle speed

Spindle speed plays an important role in the formability and surface finish and needs to be taken into consideration in the ISF process of thermoplastic materials. Medina-Sanchez et al. [16] and Bagudanch et al. [39] found that the increased spindle speed can lead to the temperature rise during the forming process resulting from more friction between sheet blanks and tools compared with a free rotating tool. Bagudanch et al. [15] also observed that the spindle rotation and higher spindle speed were found to not only decrease the maximum forming force but also help to improve the formability of PVC sheets, as also shown in the study of Le et al. [7]. However, it can have negative effects on the surface roughness of sheet parts, as also revealed by Conte et al. [34]. Therefore, to find an optimum spindle speed considering both the formability and surface roughness is of significance to the forming process. Besides, an increase in the spindle speed can lead to an earlier occurrence of wrinkle [45] and an increase in energy consumption [46].

(6) Initial sheet thickness

Similar to the metallic system, the initial thickness of thermoplastic sheet was identified as one of the most important process parameters on the material formability in ISF of thermoplastics [10, 18, 37]. Apart from formability, the initial thickness can have an

influence on the forming forces [15], the forming accuracy [19] and the surface roughness [46]. In some cases, the initial sheet thickness has a positive influence on the ISF process, such as improved material formability as investigated by many researchers [10, 18, 37, 46]. However, in other cases, the increased initial thickness can cause an overestimated in-plane force and larger geometrical deviation, which may have a negative effect on the forming quality [19]. Therefore, care should be taken in the selection of a reasonable thickness to perform ISF of a thermoplastic sheet. The details of the influence of initial thickness on the material formability and the forming quality are presented in Sections 2.2.3 and 2.2.4.

2.2.1.3 Forming force

Forming force, especially the maximum forming force, is an important parameter in ISF processing and in selecting a suitable machine and forming tool. Forming force is a reaction to the material deformation in the process [47] and the adjustments of different parameters such as drawing angle, spindle speed, tool radius, step size. These parameters could have an influence on the formability, failure, forming accuracy and surface finish during the process. Bagudanch et al. [15] studied the effects of some main process parameters including step size, tool radius, feed rate and spindle speed, as well as sheet thickness on the maximum forming force in ISF process of PVC. The authors found the maximum forming force increased with the rise of tool radius, step size and initial thickness. It is worth noting that the increased spindle speed leads to a decrease in the maximum forming force due to the material softening resulting from temperature increase. Davarpanah et al. [45] presented the same finding that the forming force increased with the increase of step size and decrease of spindle speed when forming PVC and PCL sheets. Also, the authors hypothesised the increased in-plane forces could cause the sheet wrinkle because of the drag of sheet in pace with tool moving. Apart

from the parameters mentioned above, the types and materials of forming tool and the tool path can also influence the forming forces. According to the study of Durante et al. [48], in ISF process of PC sheet with thickness of 1.9 mm, the forming force produced by a rotating tool was a little higher than that produced by a fixed tool, and the toolpath strategy had an influence as well. In the study of Medina-Sanchez et al. [16], the aluminium tool produced slightly higher forming force than the steel tool due to the lower temperature rise when using aluminium tool to form 3 mm PVC. In a recent study of Lozano-Sánchez et al. [49] and Sabater et al. [50], spindle speed and tool radius were found to be most influential on the maximum forming force for UHMWPE and PCL sheets. As demonstrated, the maximum forming force is decreased with the increased spindle speed and the decreased tool radius. To predict axial force in SPIF of thermoplastic sheets, two procedures were proposed by Medina-Sanchez et al. [51], the first of which is based on the finite element simulation, the other is a simple semi-analytical model. The results showed reasonable agreement with the experimental measurements with a relative error of less than 10%. Garcia-Collado et al. [52] developed thermomechanical coupled FE simulation to predict the forming force, which took the effect of friction heat generation into consideration. With the use of classical isotropic hardening models, the developed simulation method can accurately capture the force variation during ISF of different thermoplastics. Apart from FE simulation, analytical models are also developed for force prediction in ISF of different materials, which is reviewed in Section 2.4.2.

2.2.2 Deformation and failure mechanism

It was found that ISF can effectively increase the formability of not only metals but also thermoplastics. The reasons for the improved formability of metallic materials in ISF have been studied and reviewed widely, but for thermoplastics, there is still a lack of

review to bring previous research findings together. This section firstly introduces the deformation mechanism of polymeric materials to analyse the fundamentals for the enhanced formability. Then the discussion is focused on failure, which is the limitation for the material formability in ISF processing of thermoplastic materials.

2.2.2.1 Deformation mechanism

For metallic materials, ISF can improve materials formability compared with other traditional sheet plastic forming process such as bulging and deep drawing [53, 54] because of the highly localised plastic deformation. This is the same for thermoplastic materials. As the use of ISF to form thermoplastic materials claims further improved formability, better forming accuracy and acceptable surface finish, the understanding of the material deformation mechanism is of great significance for further investigation. The deformation mechanism of thermoplastics in ISF is being studied by many researchers.

(1) Deformation mechanics

It has been widely acknowledged that stretching leading to membrane strain is the dominant deformation mode in the ISF process. In SPIF of not only metallic but also thermoplastic materials, there are three basic deformation modes including (A) plane strain stretching on flat surfaces, (B) plane strain stretching on rotational symmetric surfaces and (C) equi-biaxial stretching at corners by Marques et al. [37] as illustrated in Figure 2.2.

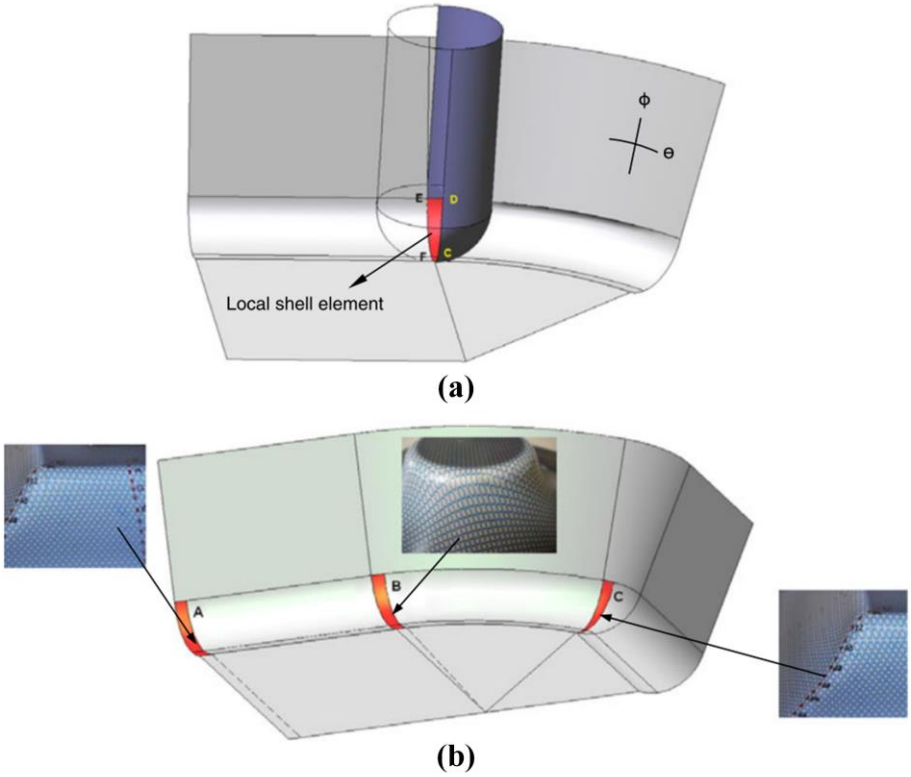


Figure 2.2 Essentials for the theoretical framework based on membrane analysis [37]. (a) Schematic representation of the local contact area (shell element) between the tool and sheet placed immediately ahead. (b) Instantaneous deformation zones and evidence of the extreme modes of deformation obtained from circle grid analysis.

For the deformation mode of plane strain stretching conditions, Silva et al. [55] proposed a theoretical framework of membrane analysis on the deformation mechanism of sheet metal in rotational symmetric SPIF. In subsequent research, the authors innovatively extended the membrane approach developed before to model the cold plastic deformation of thermoplastic materials with the typical pressure-sensitive yield surfaces [18]. In their derivation, some assumptions were set up to simplify the model: (1) bending moments were neglected and circumferential, meridional and thickness stresses are principal stresses; (2) the material is rigid-perfectly plastic and strain hardening effects are ignored; (3) the utilised yield criteria was the pressure-modified Tresca and von-Mises criteria; (4) no material anisotropic effects are taken into account; (5) rate effects are neglected; (6) the frictional stress at the contact surface between tool and

sheet is just made of in-plane meridional and circumferential components. The local shell element utilized in their research to analyse the membrane equilibrium conditions and the stresses acting on the element are illustrated in Figure 2.3.

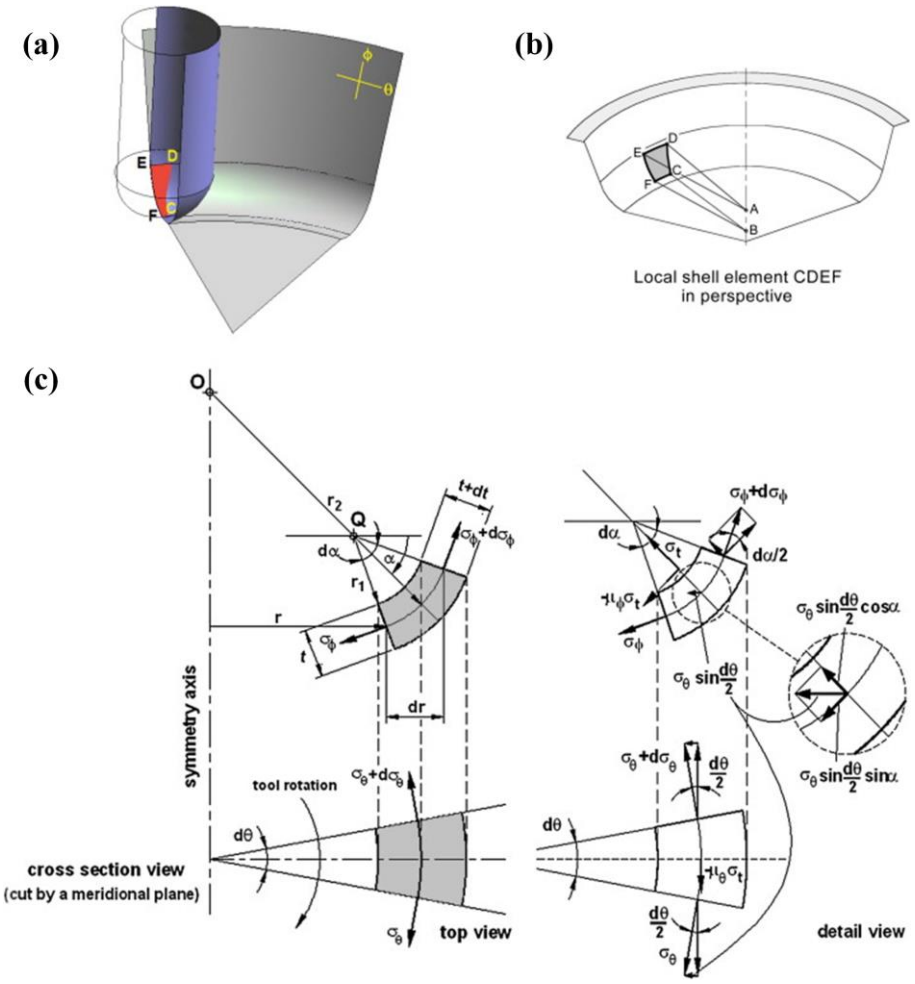


Figure 2.3 Membrane analysis of SPIF [18]. (a) Schematic representation of the local contact area between the tool and sheet placed immediately ahead. (b) Approximation of the local contact area by a shell element. (c) Cross-section view showing the acting stresses in meridional, circumferential and thickness directions.

Three analytical equations are used to express force equilibrium along circumferential, meridional and thickness directions and can be deduced and simplified as follows:

$$\mathrm{d}\sigma_\theta = -\mu_\theta \cdot \sigma_\mathrm{t} \cdot \frac{r\mathrm{d}\theta}{t} \cong -\mu_\theta \cdot \sigma_\mathrm{t} \tag{2.1}$$

$$\frac{\sigma_\mathrm{t}}{t} + \frac{\sigma_\varphi}{r_1} + \frac{\sigma_\theta}{r_2} = 0 \tag{2.2}$$

$$\frac{\mathrm{d}\sigma_{\varphi}}{\mathrm{d}r}+\frac{\sigma_{\varphi}-\sigma_{\theta}}{r}+\frac{\mu_{\varphi}\cdot\sigma_{\mathrm{t}}}{t\cdot\sin\alpha}+\frac{\sigma_{\varphi}}{t}\cdot\frac{\mathrm{d}t}{\mathrm{d}r}=0 \tag{2.3}$$

where, σ_{θ}, σ_{t} and σ_{φ} are the circumferential, thickness and meridional stress, respectively, α is the drawing angle, μ_{θ} is the coefficient of friction in circumferential direction, μ_{φ} is the coefficient of friction in meridional direction, t is the thickness of the sheet, r is the radial coordinate of the element, r_1 is the radius of curvature of meridian at the element (radius of the tool, $r_1 = r_{\mathrm{tool}}$), r_2 is the radius of the element normal where it cuts the z-axis.

After deriving the stress state of the local shell element 'CDEF' by taking into account the rigid-plastic constitutive equations derived according to the modified version of Tresca and von-Mises criteria, the authors drew the conclusion that the principal stresses distribution of the shell element is always identified as follows, regardless of what constitutive equations applied on the thermoplastic sheet:

$$\sigma_{\varphi}=\sigma_1>0 \tag{2.4}$$

$$\sigma_{\theta}=\sigma_2 \tag{2.5}$$

$$\sigma_{\mathrm{t}}=\sigma_3<0 \tag{2.6}$$

where, $|\sigma_{\mathrm{t}}|<|\sigma_{\varphi}|$. In detail, the stress state can be described using the following expressions:

$$\sigma_{\varphi}=\frac{\left(\sigma_{\mathrm{Y}}\cdot\sqrt{1-\beta\cdot\sigma_{\mathrm{kk}}}\right)}{\left(1+\frac{t}{r_{\mathrm{tool}}}\right)}>0 \tag{2.7}$$

$$\sigma_{\theta}=\frac{1}{2\left(\sigma_{\phi}+\sigma_{\mathrm{t}}-\beta\cdot\sigma_{\mathrm{Y}}\right)} \tag{2.8}$$

$$\sigma_{\mathrm{t}}=-\frac{\left(\sigma_{\mathrm{Y}}\cdot\sqrt{1-\beta\cdot\sigma_{\mathrm{kk}}}\right)}{\left(\frac{t}{r_{\mathrm{tool}}}+t\right)}<0 \tag{2.9}$$

where, σ_Y is the geometric mean of the tensile and compressive yield strengths ($\sigma_Y = \sqrt{\sigma_{YC} \cdot \sigma_{YT}}$, $\sigma_{YC} > 0$, $\sigma_{YT} > 0$) and β is the normalised form of the strength-differential effect of the cold deformation of thermoplastic materials ($\beta = (\sigma_{YC} - \sigma_{YT})/\sigma_Y^2$).

In terms of the deformation mode of equi-biaxial stretching conditions, Marques et al. [37] extended the analytical framework for the condition of rotational symmetry to the corner of the formed part to make both these two extreme and special deformation modes focused on in SPIF of thermoplastic materials. The authors followed the analytical procedures used by Silva et al [18] and obtained the stress distribution under the condition of equi-biaxial stretching. Based on previous study results and their derivation, the authors summarised the stress and strain state in the small localised plastic zone of SPIF of thermoplastic and metallic materials under both plane strain conditions and equi-biaxial stretching conditions, as shown in Table 2.1.

Table 2.1 State of stress and strain in the small localised plastic zone of the SPIF of thermoplastics and metals [37].

		State of strain	State of stress	Hydrostatic stress
SPIF of thermoplastics	Plane strain conditions [18]	$d\varepsilon_{\varphi} = -d\varepsilon_{t} > 0$	$\sigma_{\varphi} = \sigma_1 = \left(\sigma_Y \cdot \sqrt{1-\beta\cdot\sigma_{kk}}\right)/(1+t/r_{tool}) > 0$	$\sigma_m = \left(\sigma_Y \cdot \sqrt{1-\beta\cdot\sigma_{kk}}/2\right)\cdot[(r_{tool}-t)/(r_{tool}+t)] - 1/6\cdot\beta\cdot\sigma_Y$
		$d\varepsilon_{\theta} = 0$	$\sigma_{\theta} = \sigma_2 = 1/2\cdot(\sigma_1+\sigma_3-\beta\cdot\sigma_Y)$	
		$d\varepsilon_{t} < 0$	$\sigma_t = \sigma_3 = -\left(\sigma_Y \cdot \sqrt{1-\beta\cdot\sigma_{kk}}\right)/(t/r_{tool}+t) < 0$	
	Equi-biaxial stretching	$d\varepsilon_{\varphi} = d\varepsilon_{\theta} > 0$	$\sigma_{\varphi} = \sigma_{\theta} = \sigma_1 = \left(\sigma_Y \cdot \sqrt{1-\beta\cdot\sigma_{kk}}\right)/(1+2\cdot t/r_{tool}) > 0$	$\sigma_m = \left(2\cdot\sigma_Y\cdot\sqrt{1-\beta\cdot\sigma_{kk}}/3\right)\cdot[(r_{tool}-t)/(r_{tool}+2\cdot t)]$
		$d\varepsilon_{t} < 0$	$\sigma_t = \sigma_3 = -2\cdot\left(\sigma_Y \cdot \sqrt{1-\beta\cdot\sigma_{kk}}\right)/(t/r_{tool}+2\cdot t) < 0$	
SPIF of metals [56]	Plane strain conditions	$d\varepsilon_{\varphi} = -d\varepsilon_{t} > 0$	$\sigma_{\varphi} = \sigma_1 = \sigma_Y/(1+t/r_{tool}) > 0$	$\sigma_m = 1/2\cdot\sigma_Y\cdot[(r_{tool}-t)/(r_{tool}+t)]$
		$d\varepsilon_{\theta} = 0$	$\sigma_{\theta} = \sigma_2 = 1/2\cdot(\sigma_1+\sigma_3)$	
		$d\varepsilon_{t} < 0$	$\sigma_t = \sigma_3 = -\sigma_Y\cdot(t/r_{tool}+t) < 0$	
	Equi-biaxial stretching	$d\varepsilon_{\varphi} = d\varepsilon_{\theta} > 0$	$\sigma_{\varphi} = \sigma_{\theta} = \sigma_1 = \sigma_Y/(1+2\cdot t/r_{tool}) > 0$	$\sigma_m = 2/3\cdot\sigma_Y\cdot[(r_{tool}-t)/(r_{tool}+2\cdot t)]$
		$d\varepsilon_{t} < 0$	$\sigma_t = \sigma_3 = -2\cdot\sigma_Y\cdot(t/r_{tool}+2\cdot t) < 0$	

In Table 2.1, β is the normalised form of the strength-differential effect due to the difference between yield strengths in tension σ_{YT} and compression σ_{YC} ($\beta = \sigma_Y \cdot (\sigma_{YC} - \sigma_{YT})/2$). In the metallic system, the strength-differential effect is null, but for thermoplastic materials, the strength-differential effect exists. This leads to the above difference between the SPIF of thermoplastics and metals in Table 2.1.

Apart from the above membrane analysis, Bagudanch et al. [57, 58] attempted to find a suitable material constitutive model to describe the stress-versus-strain states of PVC and PC sheet and further to be used in FE simulation of ISF. Sy et al. [59] selected a modified viscoelasticity theory based on overstress and the simulation and experimental results showed good agreement for the prediction of the thickness and the forming accuracy. Furthermore, Yonan et al. [19, 60] developed a non-linear visco-plastic material model used in ISF of thermoplastics and extended it to the FE simulation of PVC parts shaped by SPIF. However, this material model has limited applicability only with small deformations, making it difficult to analyse the plastic flow and the stress states for large strain. To solve this problem, the authors subsequently proposed an alternative and effective method, focusing on the characterisation of plastic flow and failure in SPIF of thermoplastic materials [14]. In their methodology, the constitutive equations relating the in-plane strain increments ($d\varepsilon_1$ and $d\varepsilon_2$) with the applied stresses (σ_1 and σ_2) is expressed by the following equations:

$$d\varepsilon_1 = \frac{d\bar{\varepsilon}}{\bar{\sigma}} \cdot \left(\sigma_1 - \frac{1}{2} \cdot \sigma_2\right) \tag{2.10}$$

$$d\varepsilon_2 = \frac{d\bar{\varepsilon}}{\bar{\sigma}} \cdot \left(\sigma_2 - \frac{1}{2} \cdot \sigma_1\right) \tag{2.11}$$

where $\bar{\sigma}$ and $\bar{\varepsilon}$ are the effective stress and strain, respectively. In the above equations, the principal in-plane stresses can be calculated using the following equations:

$$\sigma_1 = \frac{\bar{\sigma}}{\sqrt{(1-\alpha+\alpha^2)}} \tag{2.12}$$

$$\sigma_2 = \frac{\alpha \cdot \bar{\sigma}}{\sqrt{(1-\alpha+\alpha^2)}} \tag{2.13}$$

where α is the stress ratio, $\alpha = \sigma_2/\sigma_1 = (2 \cdot \beta + 1)/(2 + \beta)$ and $\beta = \mathrm{d}\varepsilon_2/\mathrm{d}\varepsilon_1 = \varepsilon_2/\varepsilon_1$.

The above deformation mechanics plays an important role in revealing the strain and stress distribution in the small contact area between the forming tool and the thermoplastic sheet, where plastic deformation occurs. Consequently, it helps understand the mechanism behind the fracture of thermoplastic materials in ISF and the improved formability and can help to explain the relevant experimental observation.

(2) Microstructure evolution under deformation

The microstructure evolution of thermoplastics during the ISF process is relatively complicated and of significance to the deformation behaviour. In general, the microstructure has an interaction effect with the deformation in the forming process.

Under the deformation of ISF, voids or pores may occur in the thermoplastic materials during the process [45, 61], as shown in Figure 2.4. Davarpanah et al. [45] found the increase of void density in the formed PLA material can lead to the enhanced formability. In other studies [62, 63], the authors observed there is a change in orientation of crystalline lamella and molecular chain orientation in thermoplastics due to the deformation of ISF process with a slight change in the total degree of crystallinity. The schematic for the orientation change in ISF could be presented as Figure 2.5. The authors thought this change may have an influence on sheet failure and forming forces. Further, Lozano-Sanchez et al. [49] found that polymer chains prefer to be oriented in different directions on the inner and outer surfaces of the shaped parts with a geometry of pyramid.

On the inner surface, the horizontal orientation of chains is caused by the tool path, while on the other surface, the polymer chains are mainly pulled downwards, and the orientation of chains is vertical. Also, it was found that there may be an alpha star transition ($T_\alpha{}^*$) occurring in PCL and UHMWPE materials during ISF process, which is associated with the slippage between crystallites, when the process temperature is able to drive the transition.

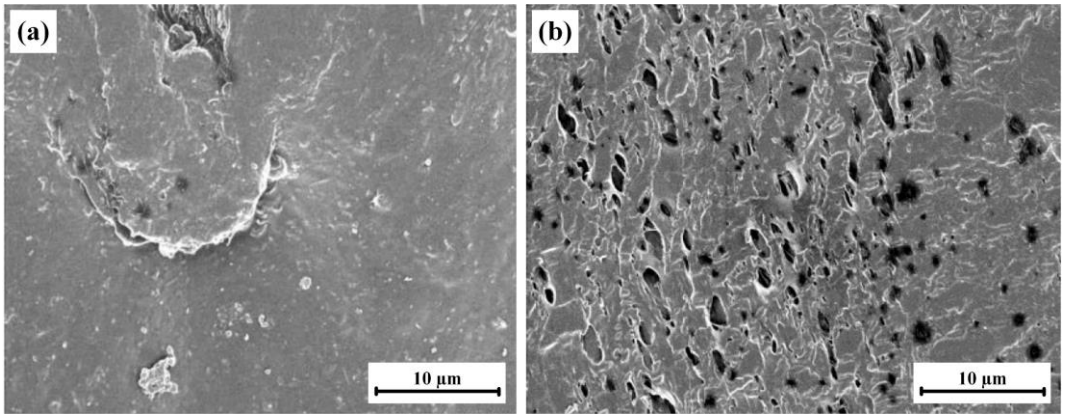


Figure 2.4 SEM micrographs of PLA funnel part [45]: (a) original material and (b) formed part.

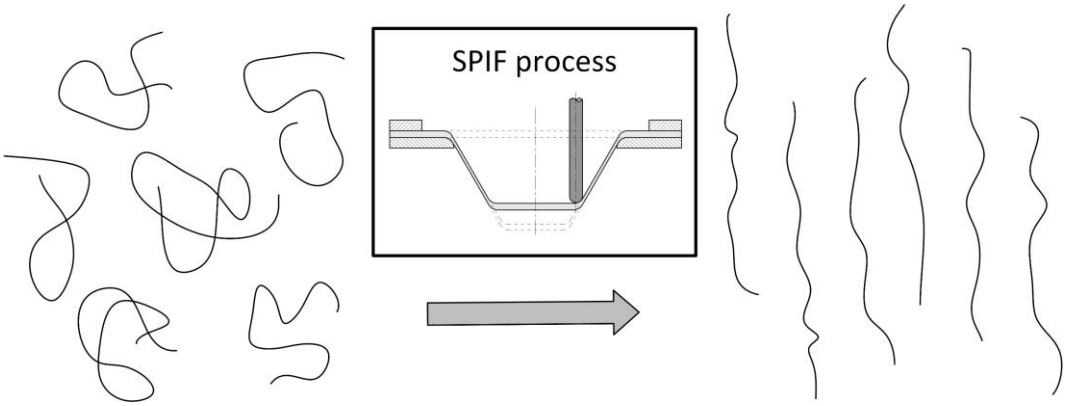


Figure 2.5 Schematic representation of the orientation of polymer chains reorientation during SPIF.

2.2.2.2 Failure behaviour

It is well acknowledged that the failure behaviour of thermoplastic materials in ISF depends on the stress and strain state of material under the effect of forming tool [64]. As demonstrated in Section 2.2.2.1, the deformation mechanics, which play a significant

role in the failure mechanism of thermoplastics in ISF, has been summarised. Therefore, this section is mainly focused on how to characterise the failures of thermoplastic materials in ISF-based on the above-summarised deformation mechanics.

In ISF of thermoplastics, there are three failure modes proposed by Franzen et al. [8], i.e., in-plane fracture, wrinkle and oblique fracture, which limit the material formability during the forming process. The three modes are described as follows:

Mode 1: In-plane fracture by ductile tearing along the circumferential direction, at the transition area between the inclined wall and the corner of formed parts, as seen in Figure 2.6(a) and (c). This failure mode is caused by stretching mechanisms owing to meridional tensile stress σ_{φ};

Mode 2: Wrinkle of the sheet along the inclined wall of the part from the immediate proximity of the corner, as illustrated in Figure 2.6(a) and (c). This failure mode is related to the twist [65] of radial cross-sectional planes caused by the movement of the forming tool along the spiral path, and is expected to occur at thinner sheet parts;

Mode 3: Oblique fracture of the sheet in the bisector direction of the $\theta - \varphi$ surface on the wall of the shaped part, as shown in Figure 2.6(b) and (d). This failure mode always arises from the redundant straining because of simultaneous straining by shearing on the $\theta - \varphi$ surface and by bending, followed by additional unbending, along the θ direction.

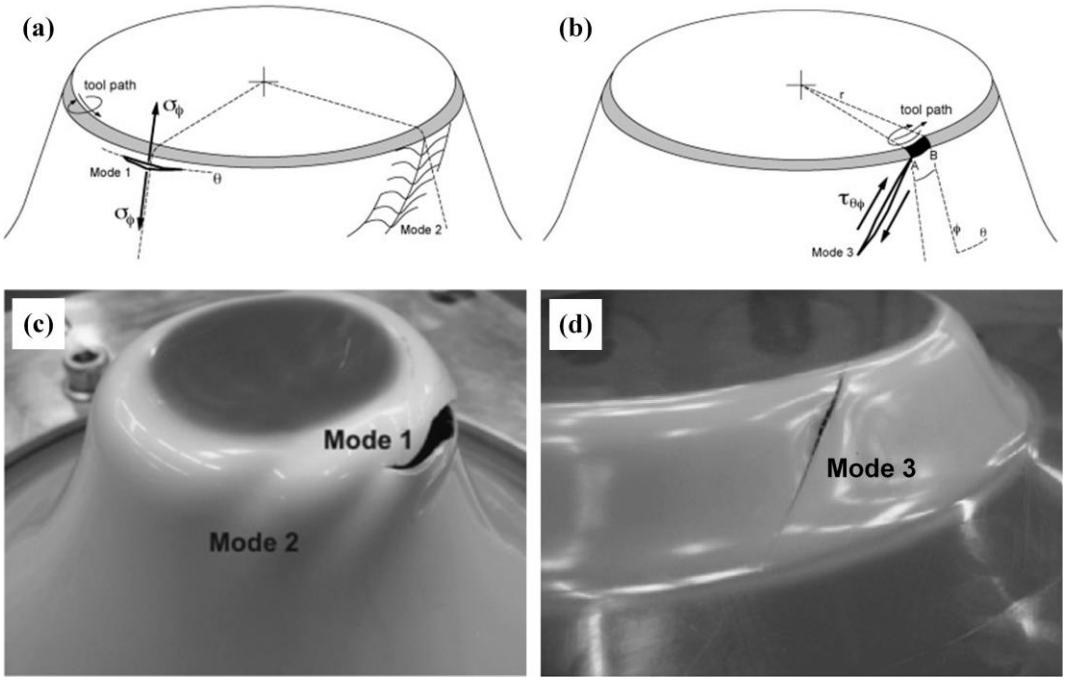


Figure 2.6 Schematic illustration (a) and (b) and experimental observation (c) and (d) [8] of Failure Mode 1, 2 and 3 in the rotational symmetric SPIF of thermoplastics.

Among the above-described failure modes, Failure Mode 1, i.e., in-plane fracture, is generally observed in ISF of metal sheet parts as well, while Failure Mode 2 and 3, i.e., wrinkle and oblique fracture, are unique failure behaviours in ISF of thermoplastic sheet parts.

Apart from the above failure modes, a significant phenomenon observed in ISF of thermoplastic materials is there is no obvious necking before fracture. For metallic system, fracture with gradual necking or without necking depends on the material [66-68] although in most cases there is no necking observed. Marques et al. described the phenomenon of the fracture without necking before as necking seems to be postponed or even suppressed [37]. Many researchers also verified the phenomenon in thermoplastic system either using the method of comparing the experimental strain of formed parts with the fracture forming lines (FFLs) [10, 18] or through observing the fracture surface after crack [69]. Bagudanch et al. [69] investigated the fracture morphologies of thermoplastic materials in ISF along different strain path. As shown in

Figure 2.7, the suppression of necking before fracture can be observed both on the flat surface under plane strain state and at the corner under biaxial strain state, which are two extreme strain distributions in ISF.

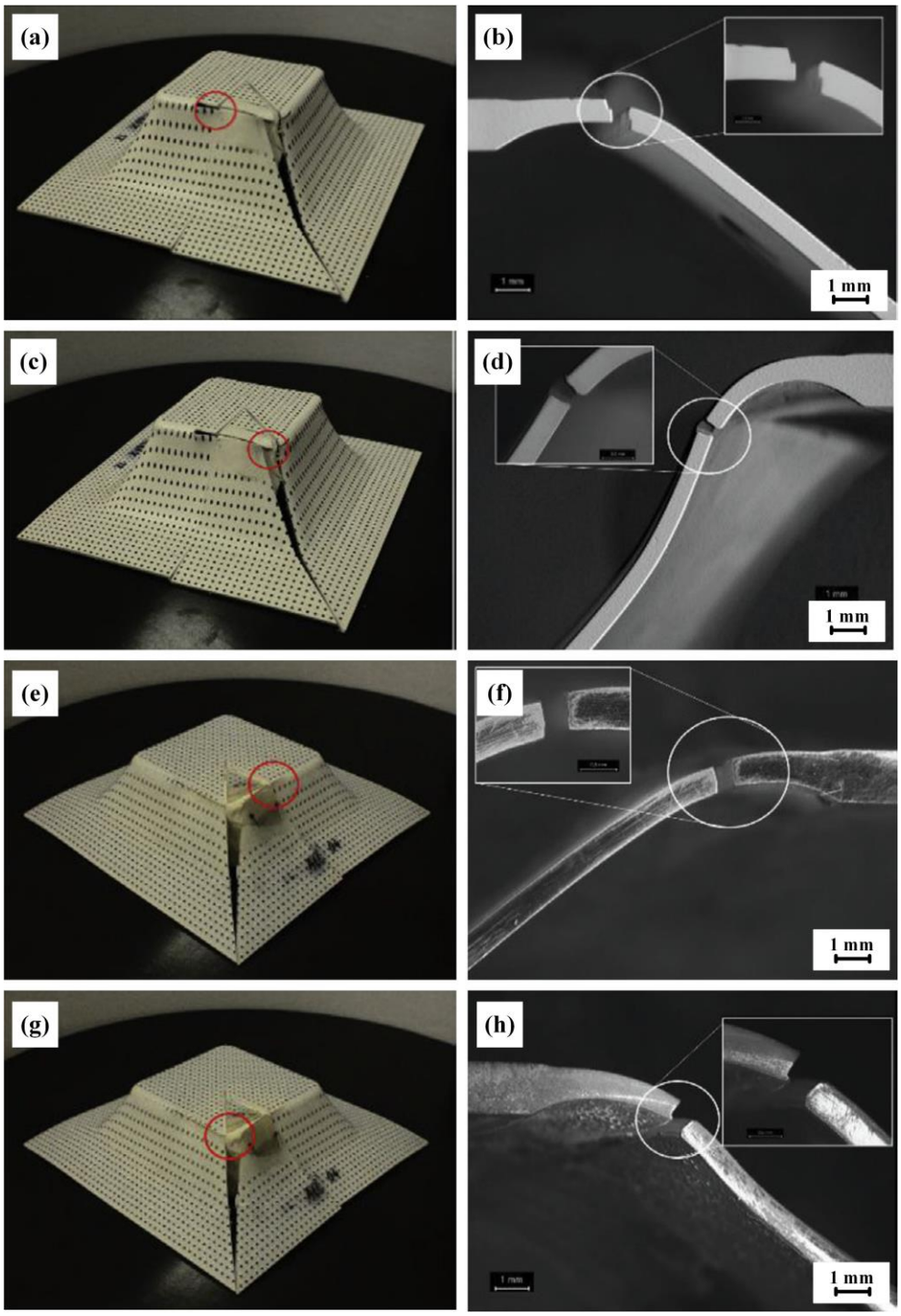


Figure 2.7 Fracture of (a), (b), (c) and (d) PVC and (e), (f), (g) and (h) PC sheet in ISF with spindle non-rotating. (a), (c), (e) and (f) Fracture under plane strain state; (b), (d), (f) and (h) Fracture under biaxial strain state [69].

2.2.3 Formability of thermoplastic materials

It was reported that in ISF with a certain range of parameters, materials are deformed locally with a stable straining and uniform thinning, which directly contributes to the suppression of necking and thus enhances the material formability in ISF [2, 18]. While some other authors stated the improved formability results from the through-thickness shear [70]. This section aims to discuss the strategies to evaluate material formability in ISF of thermoplastics and the effects of different parameters mentioned in Section 2.2.1.2 on the formability.

2.2.3.1 Formability evaluation

Material formability in ISF is often characterised using forming limit diagrams (FLDs), following the same method as the traditional sheet forming technologies. The limit strains at the area where failures occur are important components of an FLD. As a result, there are two curves in FLDs to describe the formability in the sheet forming process determined by different beginning modes of fracture: (1) local necking, i.e., forming limit curve (FLC); (2) direct ductile fracture, i.e., fracture forming line (FFL). In ISF of thermoplastic materials, there is no obvious necking occurring before fracture. Taking this usually observed behaviour into consideration, FLC, i.e., the FLD at necking, is not applicable to characterise the formability of thermoplastics in ISF. On the contrary, FFL, i.e., the FLD at fracture, is usually applied to describe the formability of thermoplastic materials in ISF. FLDs for ISF (FFL) and traditional forming technologies (FLC) are shown in Figure 2.8 and FFL is always shaped like a straight line with a negative slope in the first quadrant of the FLD.

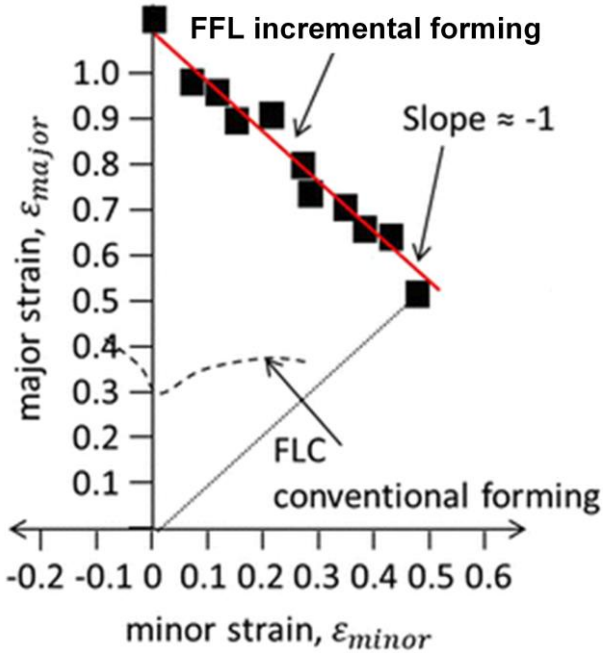


Figure 2.8 Illustration of the forming limits of SPIF (labelled FFL) against that of the conventional forming process (labelled FLC) in the principal strain space (ε_1, ε_2) [29].

Martins et al. [10] attempted, for the first time, to employ FFL on the assessment of formability of thermoplastic materials in ISF. The authors did experiments in different strain paths through the tensile test, circular bulge and elliptical bulge to approach uniaxial, equi-biaxial and biaxial strain, respectively, to obtain the FFL of PVC, which is approximately a straight line with an analytical expression of $\varepsilon_1 + 0.28\varepsilon_2 = 0.74$, as shown in Figure 2.9. In the process of extracting FFL, the thickness at fracture is required to measure so that the 'gauge length' strains (major true strain ε_1 and the minor true strain ε_2) can be obtained. Afterwards, the FFLs of PC, PVC, PA and PET were tested and obtained by Marques et al. [37], by using the methods described in detail in the publication of Silva et al. [56]. Subsequently, researchers found plane strain state, equi-biaxial strain state and biaxial strain state can be approached along different meridional paths of cone frustum and pyramid frustum with varying wall angle in ISF and thus Bagudanch et al. [69] conducted SPIF tests to obtain the FFLs for PVC, PC and PCL without spindle rotation, as shown in Figure 2.10. The details are as follows:

(1) the strain distribution on the outer surface of the formed thermoplastic sheet parts was measured off-line with the assistance of a three dimensional (3D) deformation digital measurement system via circle grid analysis; (2) the labelled Section S_0 is at the corner of the pyramid and closed to the equi-biaxial strain state; (3) Section S_1 is near the corner and refers to the biaxial strain state; (4) Section S_2 is on the flat surface and corresponds to the plane strain state. It is noteworthy that in Figure 2.10, the fracture only takes place at the equi-biaxial strain (S_0) and plane strain (S_2) states rather than the biaxial strain state (S_1) which is close to S_0. The material thinning is severe at the corner and there is a sudden change of the tool moving direction, so the fracture directly happens at S_0 instead of S_1. The FFL can be obtained as the straight line through the two average fracture points at plane strain and equi-biaxial strain states, respectively.

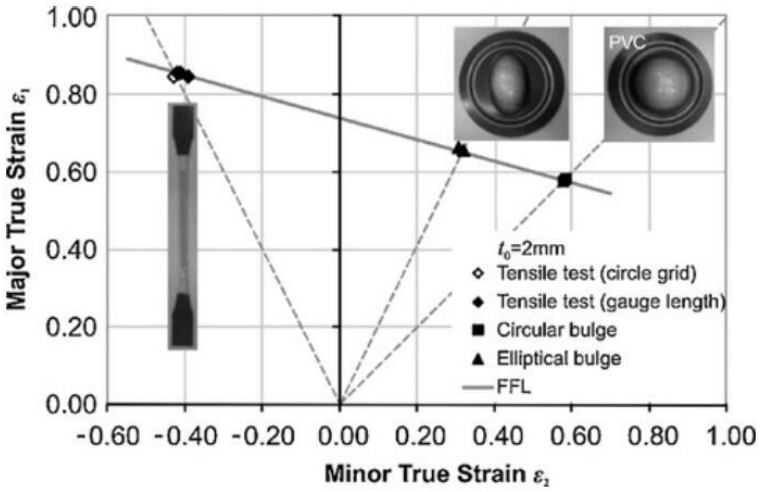


Figure 2.9 FFL of PVC obtained by Martins et al. [10].

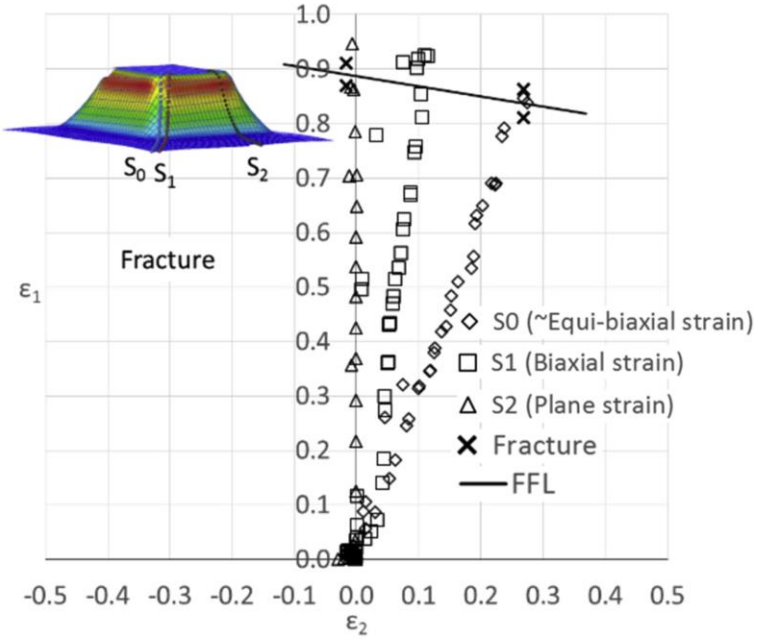


Figure 2.10 FFL for PVC sheet with spindle non-rotating [69].

Apart from FFL, the formability of thermoplastic materials in ISF can also be characterised or indicated by the maximum forming depth [15] and the maximum drawing angle [45, 71]. When the maximum forming depth is used as a metric to describe the formability, as conducted by Bagudanch et al. [15], the part geometry, which is a pyramidal frustum with circular generatrix and changing wall angle, is always fixed in aspects of the length of pyramidal edges, initial wall angle, final wall angle, and generatrix radius, while the parameters are variable to investigate their effects on the maximum forming depth, i.e., formability, of the thermoplastic materials in ISF. When the maximum drawing angle acts as an indication of the formability, the selected geometry of the part is fixed as well [45], except the condition in which the effect of initial drawing angle on the formability is focused on [10, 18].

2.2.3.2 Effects of process parameters on formability

As mentioned in Section 2.2.1.2, forming temperature, drawing angle, tool radius, step size and spindle speed are important process parameters, which affect the formability of thermoplastics in ISF.

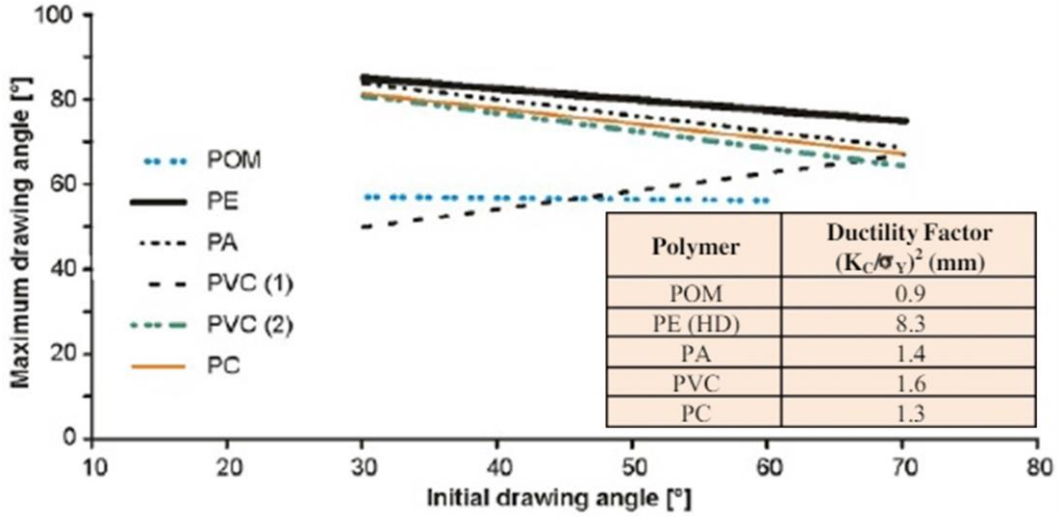
(1) Forming temperature

During the ISF process of thermoplastic materials, the material properties can be changed depending on the forming temperature because of its fundamental role in the material microstructure evolution and flow characteristics. Conte et al. [33] revealed the positive influence of process temperature on material formability in ISF of a thermoplastic-based composite reinforced by glass fibre. In their research, the formability, which is indicated by the final depth of shaped parts, is improved with the increase of forming temperature, no matter what combination of wall angle and step size. For the specific reason, Ambrogio et al. [31] found the thermoplastic sheets exhibit a super-plastic behaviour under elevated forming temperature, which allows significant strains improving the material formability. Apart from the preset forming temperature, the friction heat can also lead to the temperature rise, which has an influence on the material formability of thermoplastics as well. Although several process parameters, such as tool radius and feed rate, could have influence on the friction between the tool and the workpiece, the major friction heat increase is generated from the spindle rotation and higher spindle speed.

(2) Initial drawing angle

As a significant process parameter in ISF of thermoplastic materials, initial drawing angle Ψ_0 has been studied with important findings. In research of Martins et al. [10], with the increase of initial drawing angle, the formability (indicated by the maximum drawing angle) was decreased in ISF of PVC sheet. In another study of Silva et al. [18],

for different thickness (2 mm and 3 mm) of PVC sheets, the trends of formability with the variation of initial drawing angle were the same as previous research. Other researchers found the above-mentioned influence of initial drawing angle on the formability of thermoplastics is not always applicable for all conditions. Marques et al. [37] drew a conclusion that the initial drawing angle Ψ_0 has an influence on the formability of thermoplastic materials only when varying from 30º to 60º. Frazen et al. [11] revealed that with the increase of Ψ_0, the tendency of formability is different for different thermoplastics, even for different forming surface, as shown in Figure 2.11. As observed by the authors, all thermoplastics, except POM, exhibited a significant variation in formability as initial drawing angle increases. For the majority of thermoplastic sheets investigated, the formability was decreased by the increased initial drawing angle. While for PVC sheet, the formability was improved with the increase of initial drawing angle when the rough surface with poor surface finish of the sheet was placed in contact with the forming tool. The trend is consistent with other thermoplastic sheets. However, when the shiny or smooth surface with good surface finish of the sheet was placed in contact with the forming tool, the formability was increased with the rise of initial drawing angle.



Polymer	Ductility Factor $(K_C/\sigma_Y)^2$ (mm)
POM	0.9
PE (HD)	8.3
PA	1.4
PVC	1.6
PC	1.3

Figure 2.11 Formability (indicated by maximum drawing angle at failure) as a function of the initial drawing angle for sheet blanks with 2 mm thickness (5 mm tool radius) [11]. In the legend, PVC (1): the shiny (smooth) surface of the sheet blank placed facing the forming tool; PVC (2): the rough surface of the sheet blank placed facing the forming tool.

(3) Tool radius

The formability of thermoplastic materials can be influenced by the shape of the forming tool [40], and more importantly by the tool radius. According to the studies by Marques et al. [37] and Martins et al. [10], it was found that the formability of thermoplastics in ISF is decreased with the increase of tool radius in ISF, which is consistent with the case of metallic material. However, in the research of Le et al. [7], the material formability exhibited a significant decrease when smaller tool radius was applied in the ISF of PP sheet with a thickness of 3 mm. Similarly, when Silva et al. [18] investigated the influence of some important parameters, including tool radius, on the formability of PVC sheets in SPIF performed with benchmark cones with varying wall angle, the authors found the formability of PVC sheets with 3 mm initial thickness was increased with the increase of tool radius. It was an atypical behaviour shown by PVC sheets with 3 mm initial thickness but could be possibly explained by the reduced average level of meridional stress σ_φ. In other studies by Formisano et al. [72] and Lambiase et al. [64],

the formability of PC sheet with thickness of 1.4 mm and 1.9 mm was improved with the increase of the tool radius in tests of both a varying wall angle conical frusta and a pyramid frustum, and the same conclusion was obtained by Zhang et al. [71]. It can be concluded that the effect of tool radius is still debatable; some studies claim that large tool radius has a positive effect on the formability of thermoplastics, while other publications reveal that large tool radius has a negative effect.

(4) Step size

In ISF of metallic materials, the increased step size has a negative effect on the material formability [73]. For the cases of thermoplastic materials in ISF, the trend is not always the same. Le et al. [7] found the larger step size may lead to the increased formability of PP sheet in SPIF, which is the same with the metallic sheet. However, in the study of Bagudanch et al. [15], a larger step size leads to the increased formability in ISF process of PVC sheet, which is opposite from the regular behaviour of metals and other thermoplastics in ISF process. As the authors explained, the difference results from the rheological properties of thermoplastic materials [74]. Davarpanah et al. [45] found the above-mentioned positive influence of step size on formability of thermoplastics shows a limitation by the occurrence of wrinkle at excessively high step size, as indicated in Figure 2.12.

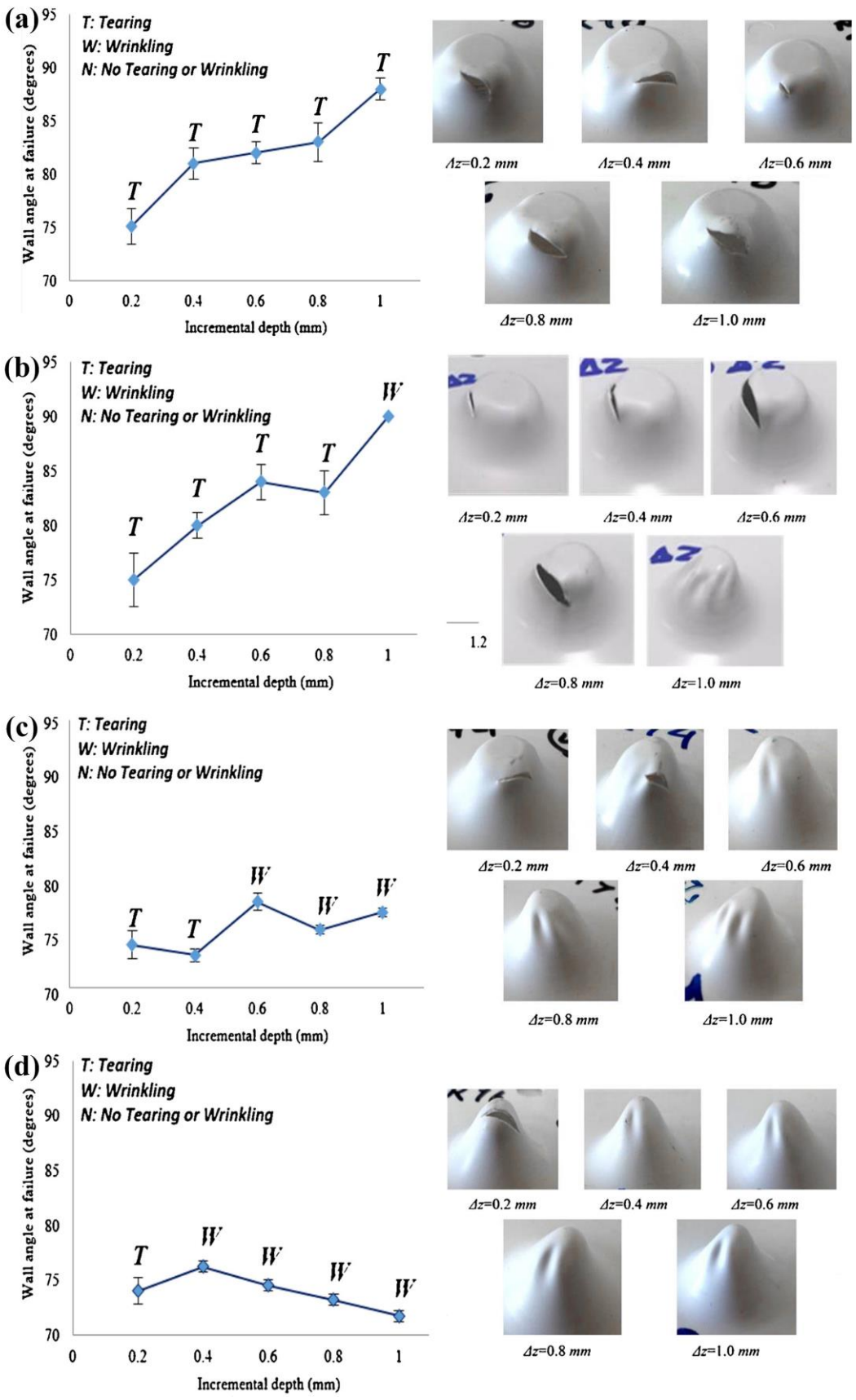


Figure 2.12 Effect of step size on formability and failure modes for funnel-shaped PLA parts with radius of curvature (a) 10 mm, (b) 12 mm, (c) 14 mm and (d) 16 mm [45].

(5) Spindle speed

Spindle speed has a significant influence on the formability of thermoplastic materials in ISF. Many studies have been carried out to investigate the effects. Le et al. [7] indicated that the increased spindle speed can lead to improved formability of thermoplastics in ISF only when large tool radius, small step size or large feed rate is applied, which is the same with the major researches in the metallic system [53, 75, 76]. Bagudanch et al. [15, 69] also found the rise of spindle speed can contribute to the improvement of material formability, which is indicated by the maximum forming depth and the limit major strain, while the formability becomes worse in the condition of free rotation. The influence results from the more generated friction heat on the contact tool-sheet surface and the temperature rise during the forming process. In detail, considering the failure modes, Davarpanah et al. [45] found the spindle speed has little influence on the formability with Mode 1 of failure but can drive the occurrence of wrinkle, which is consistent with the study findings of Le et al. [7].

(6) Initial sheet thickness

As one of the significant parameters related to the formability in ISF of thermoplastic sheet, the initial thickness has been investigated in many studies. Most researchers believe that the material formability can be improved with the increase of the initial thickness, which is the same as the result in ISF of metallic sheet parts. In the studies of Martins et al. [10], Silva et al. [18], Marques et al. [37] and Bagudanch et al. [15], the thicker thermoplastic sheet was used, the higher formability was obtained, no matter what indication (maximum drawing angle, with or without wrinkle) was used. Marques et al. [37] considered that the reason for the positive influence is the reduced stress triaxiality. However, some other researchers found the formability could be decreased

with the increased initial sheet thickness, such as Franzen et al. [8] and Formisano et al. [72]. In terms of this issue, a final conclusion has not been made up to now and more in-depth investigations should be carried out in the future.

(7) Combined effects of different parameters on formability

As investigated by Le et al. [7], the decreased formability of PP sheet (indicated by the maximum drawing angle) can be caused by the increase of step size and feed rate. Particularly, when a larger step size was applied, its influence on the formability became extremely significant. The effect of interaction between tool radius and step size on the formability of thermoplastic materials were also found in this research. The combination of smaller tool radius and larger step size can lead to a decrease of formability. In another research by Hussain et al. [38], the formability of polymer is increased with the rising ratio between tool radius and initial sheet thickness, tool radius and step size, or spindle speed and feed rate.

2.2.4 Forming quality

As ISF technology is application-oriented in such as medical fields, the forming quality plays an important role. Many researchers have investigated the forming qualities, including forming accuracy, surface finish and other factors, in ISF process of thermoplastic materials.

2.2.4.1 Accuracy

Forming accuracy refers to the geometrical/dimensional difference between the expected/set geometry and the formed thermoplastics part after ISF. In many cases, the reduction of forming accuracy results from the springback, thermal distortion and twist.

Different methods to measure forming accuracy have been developed and the influential factors of forming accuracy have been investigated in previous literature. In the study of Durante et al. [48], the springback after the forming process was calculated by measuring the upward movement of the forming tool from the last region of the shaped part in contact with the tool until the vertical force became zero. The difference between the two vertical coordinates of the tool was considered as the springback. The authors found the springback is significantly influenced by the tool type but negligibly influenced by toolpath strategy: the springback of the part shaped by the forming tool with a fixed end is lower than that in the condition of the rotating one because the rotating tool generates lower friction force and smaller plastic strain in consequence. Besides, correction of the toolpath to overbend the thermoplastic sheet is also an effective method to reduce the springback and improve the forming accuracy, as revealed by Maaß et al. [77]. Bagudanch et al. [21] used a portable 3D scanning system to obtain the real dimensions of the shaped parts after ISF of biocompatible PLC with thickness of 2 mm and compared with the designed CAD file. The authors found the sheet part would recover once it was taken off from the clamping system because of the springback, but the accuracy was still in an acceptable degree. However, this problem could be eliminated to a certain degree by heating the workpiece after forming without removal of the clamp, as investigated by Edwards et al. [44]. The authors also found increased step size can lead to reduced springback. Apart from the parameter step size, the study of Martins et al. [10] indicates that with the decrease of initial drawing angle Ψ_0 and increase of initial thickness of the sheet blanks, springback can be reduced, leading to the increased accuracy of the shaped parts. In the hot incremental sheet forming process of PC sheet, as investigated by Sridhar and Rajenthirakumar [36], the springback can be reduced to only 2% but the thinning of shaped parts are increased by

20%. Further, the difference of springback between ISF of metallic and thermoplastic sheets was revealed by Al-Ghamdi [78]. In his study, besides the immediate elastic recovery as observed in ISF of metallic sheets, in ISF of thermoplastics there is pronounced springback after an extended time. This results from the significant "an-elasticity", i.e., elastic recovery over a wider time span, due to inherent phenomenal molecular processes [78]. Lately, Yang and Chen et al. [65] argued that the twist has a critical effect on the geometric accuracy and more severe twist occurs in ISF of polymers than that of metals. The authors revealed the mechanism of twist experimentally and analytically and proposed a new alternate spiral trajectory to restrain twist and eliminate wrinkle. Apart from springback and twist, thermal distortion may be another reason for the forming inaccuracy in heat-assisted ISF. However, in the research field of ISF, there are rare studies about the thermal distortion. This may be a possible direction of future investigation.

2.2.4.2 Surface finish

Compared with other responses, the study of the surface finish in ISF is scarce, for both metallic and thermoplastic parts, while it is quite important to ensure that the surface finish of final part manufactured by ISF is able to meet the requirements. The surface finish in ISF mainly refers to the surface roughness. In general, the quantitative measurement of the surface roughness is obtained with a profilometer by measuring the texture and topography of the surface. Only few researchers have studied the surface finish of final parts after ISF.

In general, the use of lubricant can improve the surface finish because the friction between the tool and the workpiece can be reduced. Commonly used types of lubricants in ISF of thermoplastics include grease [45, 62] and liquid lubricant [14, 21, 34, 38, 48,

61, 69, 72, 79]. Even water-soap emulsion can be used as lubricant [8, 10, 18, 30, 37]. Apart from appropriate lubricant, some forming parameters also have an influence on the surface roughness. In the study of Sabater et al. [50], the increased spindle speed and tool radius can lead to worse surface roughness because of the temperature rise due to the friction and the increased surface contact area and time period between the tool and the thermoplastic sheets. Thangavel et al. [12] also found a smaller roller ball tool with a diameter of 10 mm produces better surface finish compared with a larger one with a diameter of 16 mm. According to the study of Bagudanch et al. [15], for the surface roughness of shaped parts, the most significantly influential parameters are the step size and the spindle speed. Besides, the interactions between the step size with the feed rate, the tool radius with the sheet thickness and the feed rate with the spindle speed play an important role as well. Among the above parameters, the negative influence of increased step size is expected because at a larger step down the generated tool path will slightly differ from the geometry profile due to the interpolation. For example, in using a tool diameter of 6 mm at a feet rate of 1500 mm/min without spindle rotation, a surface roughness (R_a) of 0.422 μm was achieved with a step size of 0.5 mm. This is compared to a surface roughness of 0.321 μm with a step size of 0.2 mm in ISF of a 2 mm thick sheet. Also, as the increase of spindle speeds, the surface roughness increases due to the temperature rise resulting from the friction heat when the forming temperature is close to the glass transition temperature. However, in the study of Medina-Sanchez et al. [16], the roughness of parts formed with the steel tool decreases as the increase of the spindle speed, mainly because the forming temperature is lower than the glass transition temperature. The authors also found that, for parts formed using the aluminium tool, surface roughness is significantly lower than those obtained with the steel tool. Using an aluminium tool to form a thermoplastic part can lead to almost changeless roughness

compared with the original sheet. Besides the tool material, surface roughness can also be influenced by tool types and tool paths. High surface quality can be guaranteed by both tool types and tool paths [48].

2.2.4.3 Other consideration factors

Environmental and sustainability issues have become an important consideration in the whole field of manufacturing research. For ISF technology, it is important to consider economic cost and energy consumption during the manufacturing process.

(1) Economic cost

Bagudanch et al. [46] studied the effects of different parameters on the cost in ISF and gave the relationships between them. Apart from this, a complete and accurate method to estimate the cost during ISF was proposed by Branker et al. [80]. This method is suitable for both metal parts and thermoplastic parts, taking the forming costs (C_{f}), the setup costs (C_{s}), the workpiece handling costs (C_1), the tooling costs (C_{t}), the direct material costs (C_{MD}), the indirect material costs (C_{MID}), the energy consumed during the process (C_{ED}), the ancillary energy (C_{EA}) and the environmental burden (C_{env}), into consideration. For simple geometries, the above method is effective to calculate the cost of ISF because it considers not only the raw materials and manufacturing time but also the environmental impact, but for a customized shape, an additional design cost (C_{design}) should be included. Also, the trimming cost (C_{cut}) and the cost for biomodel fabrication (C_{bm}) also need to be considered [23]. Therefore, the cost for a customised part manufactured by SPIF (C_{SPIF}) may be estimated by the following equation:

$$C_{\mathrm{SPIF}} = \mathrm{C_f} + \mathrm{C_s} + \mathrm{C_1} + C_{\mathrm{t}} + C_{\mathrm{MD}} + C_{\mathrm{MID}} + C_{\mathrm{ED}} + C_{\mathrm{EA}} + C_{\mathrm{env}} + C_{\mathrm{design}} + C_{\mathrm{cut}} + C_{\mathrm{bm}} \quad (2.14)$$

If TPIF is used to manufacture the customized part, the die manufacturing cost (C_{die}) should be included to estimate the cost for TPIF (C_{TPIF}), as shown in the following equation:

$$C_{\mathrm{TPIF}} = C_{\mathrm{SPIF}} + C_{\mathrm{die}} \tag{2.15}$$

The above-mentioned approach is mainly about the total cost used in the manufacturing process of a certain shape.

(2) Energy consumption

In addition to the economic cost, energy consumption can be reduced by optimising the process parameters. Bagudanch et al. [46] investigated the effects of some process parameters on energy consumption in SPIF of PC and PVC. According to their research, the increase of step down and the feed rate and the decrease in the spindle speed lead to decreased energy consumption. An empirical equation to estimate the energy consumption used in SPIF was proposed in the following equation, specifically for the Kondia HS1000 3-axis milling machine used in the research.

$$E = (2854.6 + 0.592 \cdot \omega) \cdot S \tag{2.16}$$

where E is the energy consumption in kilojoule, ω is the spindle speed in rpm and S is the forming time in second. The error of energy consumption estimated by the proposed empirical equation is always less than 10% compared with the value measured in experiments. Another important influence factor on energy consumption is the external heating sources used in heat-assisted ISF. The use of the external heating device, i.e., the pre-set forming temperature, can raise the cost, which is the same as that in the metallic system [81]. Therefore, to avoid using external heat to conduct ISF of thermoplastics at room temperature is an effective way to reduce the energy consumption of the process, but this should be based on the premise that the satisfactory

parts can be obtained. To summarise, the cost and energy consumption can be obtained by using analytical or empirical equations. More importantly, the cost and energy consumption can be reduced by optimising the process parameters.

2.2.5 Discussions

ISF technology has been studied to form thermoplastic materials for over 10 years and gained increasing attention in recent years. The rapid development of this research field mainly results from the combined advantages of the technology itself (improved material formability, good geometric accuracy and other benefits in manufacturing small-batch and customised non-axisymmetric sheet parts) and promising thermoplastic materials. A number of key areas in ISF of thermoplastics are discussed in the following sections.

2.2.5.1 Processing conditions

The process setup for ISF of thermoplastic materials is almost the same as the setup used in the metallic system. The elevated temperature is effective to improve the formability of thermoplastic sheets in ISF, and a heating system, using a heating source such as electric resistance, a halogen lamp or a heating coil, can be embedded into the ISF machine to form workpieces with higher forming accuracy. However, an external heating source is not definitely necessary given the condition that the thermoplastics have good material formability, and the friction heat could be used to soften the material, although the effect of friction heat is still debatable because it may damage the surface quality of workpiece. Therefore, both the pre-set heat and the friction heat have their own advantages and shortcomings. The external heat could greatly improve the material formability and forming quality in ISF but cause lower strength of the formed part and

more energy use and cost, while the friction heat could help save energy and increase the formability to a certain extent but affect the surface finish of the formed part.

Apart from forming temperature, initial drawing angle, tool radius, step size, spindle speed and initial sheet thickness are important parameters in ISF of thermoplastics. All these parameters have considerable influence on the formability and other aspects of forming quality. Higher forming temperature and spindle speed can cause reduced surface quality, and larger step size can lead to excessive thinning and high surface roughness. In addition, the above parameters have an influence on the forming force, which gives an indication in selecting a suitable machine and using a specific tool.

2.2.5.2 Deformation and failure mechanism

The highly localised plastic forming is a distinctive feature of ISF compared with other traditional sheet plastic forming processes and stretching leading to membrane strain is the dominant deformation mode. For ISF of thermoplastic materials, there are three basic deformation modes including plane strain stretching on flat surfaces, plane strain stretching on rotational symmetric surfaces and equi-biaxial stretching at corners. Currently, a theoretical framework of membrane analysis is mainly used to investigate the deformation mechanism in ISF of thermoplastics although some material constitutive models have been developed. In ISF, the stress and strain states in the small-localised plastic zone of thermoplastics show a significant difference from that of metals. The microstructure evolution under deformation is also complicated with the changes of micro void density, degree of crystallinity, crystal and chain orientation.

Under the ISF deformation, there are three proposed failure modes in ISF of thermoplastic materials, including in-plane fracture by ductile tearing along the circumferential direction at the transition area between the inclined wall and the corner,

wrinkle along the inclined wall in the proximity of the corner and oblique fracture in the bisector direction of the circumferential – meridional surface on the wall. Among the above failure modes, the last two are unique to the ISF of thermoplastics. During the fracture process, no obvious necking i.e., suppressed necking, is considered as an important feature.

2.2.5.3 Formability

The formability of thermoplastic sheets in ISF exhibits significant improvement compared with other plastic forming technologies. Basically, FFL, i.e., the FLD at fracture, is utilised to characterise the formability of thermoplastic sheet in ISF. FFL is comprised of a straight line with a negative slope in the first quadrant of the FLD. The uniaxial, equi-biaxial, biaxial strain and plane strain can be obtained by some traditional tests including tensile test, circular bulge and elliptical bulge, or in different meridional paths of cone and pyramid frustums with varying wall angle in ISF under the above-mentioned three deformation modes. Besides FFL, the maximum forming depth and the maximum drawing angle can also be used as metrics of formability.

In general, for the majority of thermoplastics, the increased formability in ISF can be approached with the higher forming temperature and spindle speed (leading to more friction heat), while there remains controversy about the effect of initial drawing angle, tool radius, step size and initial sheet thickness on the formability. For the majority of thermoplastic materials, with the increase of initial drawing angle, the formability is increased, but there are some exceptions such as POM, and PVC sheet with the smooth surface placed facing the forming tool [11]. The positive effect of decreased tool radius, step size and increased initial sheet thickness on the improvement of formability is not always suitable as well. An appropriate combination of different parameters is also

important to the formability. The combination of larger step size and larger feed rate and the combination of smaller tool radius and larger step size can lead to the decreased formability, while the combination of larger tool radius and smaller initial sheet thickness and the combination of larger spindle speed and smaller feed rate can improve the formability.

2.2.5.4 Forming quality

The forming accuracy can be measured by using a portable 3D scanning system, coordinate measuring machine to calculate the moving distance of forming tool. The main reason for the poor forming accuracy is springback, including immediate elastic recovery and an-elastic recovery after an extended time span. The springback can be reduced by appropriate tool type, toolpath strategy, decreased initial drawing angle, increased initial sheet thickness or elevated forming temperature.

The surface roughness of shaped thermoplastic workpieces can be quantitatively obtained with a profilometer by measuring the texture and topography. In general, the better surface finish can be approached with slower spindle speed, tool radius, step size as well as suitable tool material, type, and path.

2.2.5.5 Effects of process parameters on ISF of thermoplastics

The effects of different parameters on the formability of thermoplastic materials are summarised based on the above literature review in order to provide readers with clearer information to refer to. The detailed results are given in Table 2.2 with the effects of process parameters and corresponding publications.

Table 2.2 Effects of process parameters on different aspects of ISF of thermoplastics.

Process parameters	**Resulting effects**				
	Forming force	Formability	Accuracy	Surface finish	Energy and cost
Forming temperature ↑	⇩ [15]	⇧ [15, 69]	⇧ [16, 36]	⇩ [16]	
Initial drawing angle ↓		⇧ [10, 18]	⇧ [10]		
Tool radius ↓	⇩ [15, 46, 50]	⇧ [10, 37] ⇩ [7, 8, 15, 18, 46, 64, 72]		⇧ [8, 12] ⟊ [46]	⟊ [46]
Step size ↑	⇧ [15, 45, 46]	⇧ [15, 45, 46] ⇩ [7]	⇧ [44]	⇩ [15, 46]	⇩ [46]
Spindle speed ↑	⇩ [15, 16, 45, 50]	⇧ [7, 15, 46, 69]	⇧ [22, 23] ⟊ [44]	⇩ [15, 16, 34, 46]	⇧ [46]
Initial sheet thickness ↑	⇧ [15, 19, 46]	⇧ [10, 15, 18, 37, 46] ⇩ [8, 64, 72]	⇧ [10]	⇩ [46]	⟊ [46]

Table 2.2 is comprised of the parameters, forming temperature, initial drawing angle, tool radius, step size, spindle speed and initial sheet thickness, and their effects on the forming force, formability, forming accuracy, surface finish and energy and cost. The up arrow (↑) or down arrow (↓) behind the parameters means the increase or decrease of this parameter. Similarly, the up arrow (⇧), down arrow (⇩) or horizontal bar (⟊) in the cells for resulting effects represents the positive, negative or no influence on them.

From Table 2.2, although most process parameters are reported to have the same effect in ISF of thermoplastics from referenced publications, it is still debatable on the effect of tool radius, step size, initial sheet thickness on the formability as introduced above. The effect of spindle speed on the forming accuracy and the effect of tool radius on the surface finish are not commonly acknowledged. Although a possible explanation is the difference in mechanical and physical properties among different thermoplastics, further work should be done to understand the detailed reasons.

2.2.5.6 Comparison between ISF of thermoplastic and metallic materials

Although ISF of thermoplastic materials is similar with the condition in the metallic system in aspects of process setup, formability evaluation methods and the influence of different parameters on forming quality, the material behaviour is quite different from thermoplastics to metals. Therefore, there is a particular need to identify and understand important differences between ISF of thermoplastic and metallic materials. Based on the review of published work, the main differences are summarised in Table 2.3.

Table 2.3 Differences between ISF of thermoplastic and metallic materials.

Research aspect	Thermoplastics	Metals
Process parameters	Initial drawing angle acts as a parameter. Maximum drawing angle acts as a metric of formability	Maximum drawing angle is a parameter to determine the formability
Effects of process parameters on formability	(1) Majority exhibits decreased formability with increased tool radius while there are some exceptions.	(1) Formability decreases with increased tool radius. (2) Formability decreases with an increased step size.

	(2) The effect of step size on formability depends on the material.	
Deformation mechanism	(1) Membrane analysis with pressure-sensitive yield surface is mainly investigated.	(1) Membrane analysis, through-thickness shear deformation and tension under bending are widely investigated
	(2) Stress and strain states in the small localised plastic zone are different. Details are shown in Table 2.1.	
Failure behaviour	(1) Failure Mode 2 and 3, i.e., wrinkle and oblique fracture, are unique to thermoplastic materials. (2) No obvious necking occurs before fracture.	(1) Failure Mode 1, i.e., in-plane fracture, is generally observed. (2) Fracture with or without necking depends on the material.
Forming accuracy	(1) The springback results from not only immediate elastic recovery but also an-elastic recovery after an extended time span.	(1) The springback is only caused by immediate elastic recovery.
	(2) More severe twist occurs in ISF of thermoplastics than that of metals.	

In thermoplastic system, the initial drawing angle, of which the effect on formability has never been studied in the metallic system, is considered as a parameter and has an important influence on the formability of thermoplastic sheet in ISF. Also, the influence of tool radius and step size on the formability of different thermoplastics are not the same. Some of them are identical to metals while there remain some exceptions. In terms

of the deformation mechanism, the relevant investigation is mainly focused on the membrane analysis with pressure-sensitive yield surface in ISF of thermoplastics, but other mechanisms including through-thickness shear deformation and bending under tension have been widely studied in metallic system. Even only for the membrane analysis, the stress and strain states in the small localised plastic zone are different in these two systems. In terms of failure behaviour, in-plane fracture is generally observed in ISF of both thermoplastics and metals, while wrinkle and oblique fracture are unique failure modes for thermoplastic sheets. For forming accuracy, immediate elastic recovery causes springback and poor forming accuracy in both these two systems, but there is additional an-elastic recovery after a long time after ISF of thermoplastic sheets. Finally, in ISF of thermoplastics, the twist is more serious compared with that in ISF of metals.

2.3 Constitutive modelling of thermoplastics

2.3.1 Deformation behaviour of thermoplastics

As a kind of polymer, thermoplastics have advantages in resistance to impact, temperature and load carrying capability [27, 82, 83]. In particular, they may be repeatedly heated and cooled without severe damage because of their property of softening by heating and solidification in cooling, and hence commonly used for reprocessing and recycling [84]. The mechanical behaviours of thermoplastics have been investigated and characterized in numerous studies. Boyce et al. [85, 86] were dedicated on the compression, tension and simple shear of PC material at large strains under room temperature and low strain rate. They revealed that the strain hardening is caused by the axial movement of molecules at necking area during cold stretching under tension, while under compression, it results from the plane orientation movement of

molecules. Cao et al. [87] and Yu et al. [88] studied the tensile and compressive behaviour of PC at different strain rates and different temperatures. Besides the effects of strain rate and temperature, both presented the non-linear characteristics of the mechanical behaviour of PC such as obvious yielding and strain softening. Hamdan and Swallown [89] investigated the strain rate and temperature dependence of the mechanical properties of polyether ketone (PEK) material and PEEK. At temperature below the glass transition temperature (T_g), the dependence of strain rate of both polymers is almost independent of temperature, while at temperature above T_g, increasing temperature leads to an increase in yield stress due to the cold-crystallization phenomena. Also, the crystallization was found with high strain-rate sensitivity for both PEK and PEEK material. Rae et al. [90] studied the compressive and tensile behaviour of PEEK material with large ranges of strain rate and temperature. In their study, a strong dependence on strain rate and temperature was found as with all semi-crystalline thermoplastics. At large compressive strain, the phenomenon of darkening previous observed in Taylor impacted samples [91, 92] results from reduced crystallinity. Nasraoui et al. [93] conducted a series of uniaxial compression tests under quasi-static loading at room and lower temperature and under dynamic loading at room temperature to study the strain-rate and temperature sensitivity of PMMA.

To summarize from previous research, in most cases, the mechanical behaviour of thermoplastics, whether is in tension or compression, exhibits great strain-rate and temperature dependence. The deformation behaviour of a thermoplastic can be generally described by the flow stress curve as shown in Figure 2.13.

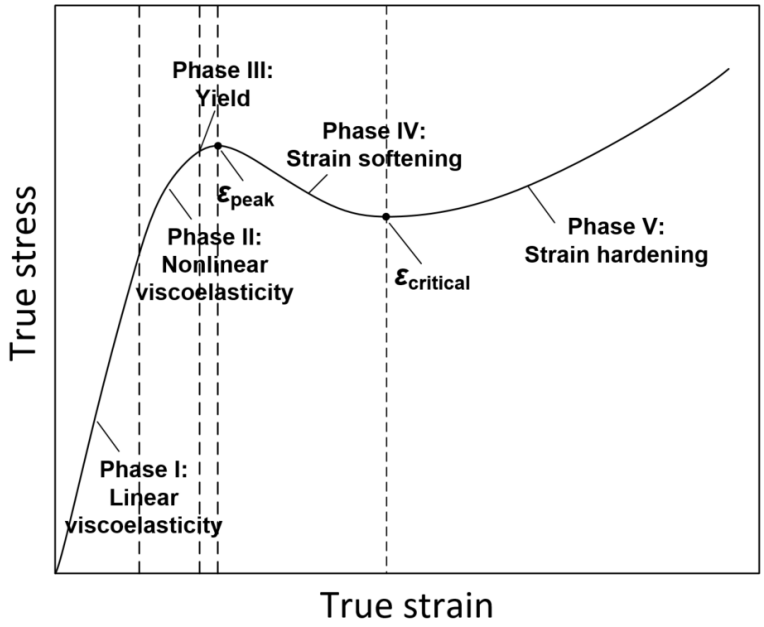


Figure 2.13 Typical deformation behaviour of a thermoplastic.

As shown in Figure 2.13, there are five phases in the deformation process [27]. Phase I is linear viscoelastic deformation, in which the deformation is fully reversible. Phase II is non-linear viscoelastic deformation under increasing loading, followed by Phase III – yield, after which the deformation becomes irrecoverable (while the plastic deformation can be fully recovered at a temperature above T_g [94, 95]). Phase IV is strain softening and finally Phase V – strain hardening is obvious at large deformations. Among them, the strain softening refers to that the flow stress decreases with increased strain and the strain hardening refers to the rise of flow stress along with a further increase of strain. For glassy thermoplastics, the strain softening behaviour is governed by the relationship between the relaxation time of molecular chains movement and the deformation speed. The strain hardening behaviour is due to enhanced orientation of molecular chains, second-order phase transition [96] or other microstructure evolution at large deformation. For semi-crystalline thermoplastics, the strain softening behaviour is related to the broken crystallization and the strain hardening behaviour is also related to the recrystallization at large strains, which are different from glassy thermoplastics. No

matter what mechanisms are involved in deformation, they generally follow the aforementioned trend.

2.3.2 Constitutive modelling of thermoplastics

Since the deformation behaviour of thermoplastics is more complex than metallic materials, it is more difficult to develop constitutive models to predict the flow stress of thermoplastics. As reviewed in Section 2.2.2.1, Bagudanch et al. [57, 58] and Yonan et al. [19, 60] showed the attempts to find or develop a suitable constitutive model for thermoplastics in ISF. Apart from this, there are also some constitutive models proposed to describe the tensile and compressive behaviour of thermoplastics, which is the basis for the use in ISF. Generally, they can be classified into two types: physical and phenomenological constitutive models. Physical constitutive models are constructed based on the physical mechanism under deformation and have a complex form whilst phenomenological constitutive models are constructed by fitting experimental data and have a relatively simple form as long as the flow stress behaviour can be represented.

Among many constitutive models developed to predict the mechanical behaviour of thermoplastics, Mulliken-Boyce model [97] is a physically based model with wide acceptance. This model was developed based on Ree-Eyring theory [98] and is composed of three basic components including a linear elastic spring, a viscoplastic dashpot and a non-linear Langevin spring, as shown in Figure 2.14. To characterize the interactions between molecules in stretching and rearranging process of molecular sections, two parts are included in the model: A and B, in which A is used to describe the intermolecular resistance to chain-segment rotation and B is used to describe the entropic resistance to chain alignment. Part A consists of section α and section β, both of which can be decomposed into a linear elastic spring and a viscoplastic dashpot. α

and β present the different degrees of thermal activation of molecules during motion. In detail, α is relevant to the rotation of main molecular chains, whilst β is related to the local rotation and can only be activated at low temperature and high strain rate. As A_α, A_β and B are parallel, the total stress (T) in the polymer reads as the tensor sum of the α intermolecular stress (T_{A_α}) and β intermolecular stress (T_{A_β}) and the network (back) stress (T_B) as shown in Equation (2.17).

$$T = T_{A_\alpha} + T_{A_\beta} + T_B \tag{2.17}$$

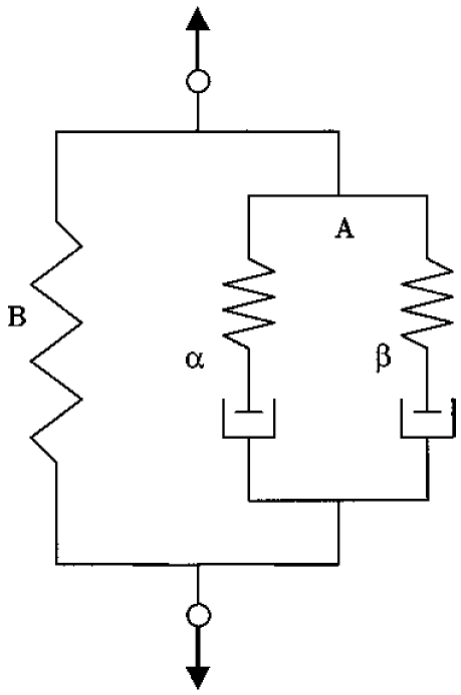


Figure 2.14 One-dimensional schematic of Mulliken-Boyce model [97].

Therefore, Mulliken-Boyce model was developed to successfully predict the mechanical behaviour of thermoplastics in high strain rate and low temperature cases, as compared with the original model proposed by Boyce et al. [99] and Arruda and Boyce [100], which can only be used in plane strain compression, simple shear, uniaxial tension and uniaxial compression at high temperature and low strain rate.

Different from Mulliken-Boyce model [97], Johnson-Cook [101], Nasraoui et al. [93] and Duan-Saigal-Greif-Zimmerman (DSGZ) [102] models are well recognized phenomenological models and commonly used to predict the flow stress with relatively high precision.

Johnson-Cook model was proposed by Johnson and Cook [101] with the following expression:

$$\sigma(\varepsilon^{\mathrm{p}}, \dot{\varepsilon}, T) = [A + B \cdot (\varepsilon^{\mathrm{p}})^{n}] \cdot \left[1 + C \cdot \ln\left(\frac{\dot{\varepsilon}}{\dot{\varepsilon}_{\mathrm{ref}}}\right)\right] \cdot \left[1 - \left(\frac{T - T_{\mathrm{ref}}}{T_{\mathrm{melting}} - T_{\mathrm{ref}}}\right)^{m}\right] \tag{2.18}$$

where, σ is the flow stress, A is the yield stress at reference strain rate and reference temperature, B is the strain hardening coefficient, n is the strain hardening exponent, ε^{p} is the true plastic strain, $\dot{\varepsilon}$ is the strain rate, $\dot{\varepsilon}_{\mathrm{ref}}$ is the reference strain rate, T is the temperature in Kelvin or K, T_{ref} is the reference temperature, T_{melting} is the melting temperature, C and m are material parameters. In this model, there are five parameters, i.e., A, B, n, C and m [101].

This model takes the strain rate and temperature into consideration, which makes it popular in the metallic system. Apart from metals, Johnson-Cook model and its variations have been used to describe the tensile and compressive behaviour of PEEK material in the research of Chen et al. [103, 104] and Garcia-Gonzalez et al. [105], although the prediction may deviate from the testing results to a considerable degree. Meanwhile, Johnson-Cook model can only be used to predict the plastic deformation part. Other model or parameters are needed to describe the whole deformation process from elastic to plastic deformation parts.

Nasraoui et al. [93] proposed a model to predict the flow stress of PMMA based on the previous work of G'sell and Jonas [106]. It is expressed as a combination of an additive and a multiplicative formulation as follows:

$$\sigma_{\mathrm{eq}}(\varepsilon,\dot{\varepsilon},T)=\left(1-\frac{T}{T_{\mathrm{g}}}\right)\cdot[1-\exp(-w\cdot\varepsilon)]\cdot\left\{\sigma_1\cdot\exp(-b\cdot\varepsilon)\cdot\left(\frac{\dot{\varepsilon}}{\dot{\varepsilon}_{\mathrm{ref}}}\right)^{m_1}+\sigma_2\cdot\right.$$

$$\left.\exp\left[\left(h_0+h_1\cdot\frac{T-T_{\mathrm{ref}}}{T_{\mathrm{ref}}}\right)\cdot\varepsilon^2\right]\cdot\left[1+\left(\frac{\dot{\varepsilon}}{\dot{\varepsilon}_{\mathrm{ref}}}\right)^{-1}\right]^{-m_2}\right\} \tag{2.19}$$

where, T_{g} is the glass transition temperature in K. There are eight parameters in this model: w, b, σ_1, σ_2, m_1, m_2, h_0 and h_1. In this model, the term $\sigma_1\cdot\exp(-b\cdot\varepsilon)\cdot\left(\frac{\dot{\varepsilon}}{\dot{\varepsilon}_{\mathrm{ref}}}\right)^{m_1}$ is used to describe the yield and strain softening behaviour and the term $\sigma_2\cdot\exp\left[\left(h_0+h_1\cdot\frac{T-T_{\mathrm{ref}}}{T_{\mathrm{ref}}}\right)\cdot\varepsilon^2\right]\cdot\left(1+\left(\frac{\dot{\varepsilon}}{\dot{\varepsilon}_{\mathrm{ref}}}\right)^{-1}\right)^{-m_2}$ is used to describe the strain hardening behaviour at large strains [93]. In their research, this model was observed to precisely predict the quasi-static and dynamic compressive behaviour of PMMA under room temperature and the plastic deformation under different low temperatures at low strain rates. However, Nasraoui et al. model has yet to be proved to be effective in high temperature conditions [93].

DSGZ model is a uniform phenomenological constitutive model proposed by Duan et al. for not only glassy but also semi-crystalline thermoplastics [102]. It can be expressed in the following form:

$$\sigma(\varepsilon,\dot{\varepsilon},T)=K\cdot\left\{f(\varepsilon)+\left[\frac{\varepsilon\cdot e^{\left(1-\frac{\varepsilon}{C_3\cdot h(\dot{\varepsilon},T)}\right)}}{C_3\cdot h(\dot{\varepsilon},T)}-f(\varepsilon)\right]\cdot e^{[\ln(g(\dot{\varepsilon},T))-C_4]\cdot\varepsilon}\right\}\cdot h(\dot{\varepsilon},T) \tag{2.20}$$

where,

$$f(\varepsilon)=(e^{-C_1\cdot\varepsilon}+\varepsilon^{C_2})\cdot(1-e^{-\alpha\cdot\varepsilon}) \tag{2.21}$$

$$h(\dot{\varepsilon}, T) = \dot{\varepsilon}^m \cdot e^{\frac{a}{T}} \tag{2.22}$$

and $g(\dot{\varepsilon}, T)$ is the dimensionless form of $h(\dot{\varepsilon}, T)$ by omitting the unit in calculation. There are eight material parameters in DSGZ model: K, C_1, C_2, C_3, C_4, a, m and α.

DSGZ model is proposed based on several phenomenological constitutive models including Johnson-Cook model [101], G'Sell-Jonas model [106] (Equation (2.22)), Matsuoka model and Brooks model [107]. It has been used to predict the flow stress of PMMA [102], PC [102, 108] and other thermoplastics, but its applicability has not been proved comprehensively. For example, in the research of Duan et al. [102], the results of DSGZ model at large strains under the conditions of moderate strain rate were not clear and the trends show a degree of deviation of the predicted results as compared to experimental data. Therefore, although DSGZ model is an effective model for thermoplastics, there remains a scope for improvements.

2.4 Analytical modelling of ISF

In Section 2.2.2.1, some analytical solutions of stress state in ISF of thermoplastics and metals are reviewed, which reflect the deformation state of ISF. This section is concentrated on the analytical modelling of specific issues in ISF such as forming force and other aspects.

2.4.1 Analytical modelling of forming force

In ISF, the designed shape is achieved by local deformation in steps, which is driven by often a hemispheric forming tool following a contour path [29, 109]. The contact between the forming tool and the sheet material is important to the deformation, formability and fracture in ISF [110-112], and the forming force in ISF directly reflects the tool-sheet contact relationship, as revealed by Lu et al. [113] on the friction-related

effect, by Li et al. [114] on the bending, shearing and stretching effect and by Obikawa et al. [115] on the tool rotational effect.

The forming force in ISF is influenced by process parameters including step size, forming tool dimension, drawing angle, sheet thickness, feed rate, spindle speed, temperature, lubricant condition and material property. Filice et al. [116] observed the force trend in ISF and clarified that the initial bending leads to the peak force. After the peak, the stretching begins and there are three distinguished force trends: steady-state, polynomial and monotonically decreasing trends. Duflou et al. [117] presented a sudden change when the tool starts to enter each contour or deforms corner positions of a pyramid part although there was no significant difference of mean total forces in ISF of cones and pyramids. These indicate the effect of initial bending and geometric shape on the force variations in ISF.

Accurate prediction of forming force provides an insight into the material deformation, presents the interaction to ISF parameters and even captures fracture failure [118]. To predict forming force in ISF, finite element simulation is commonly used. However, a satisfactory FE simulation is affected by multiple factors and often takes considerable time to complete. To save computing resources, it is highly desirable to develop analytical models for force prediction with sufficient accuracy and efficiency.

Analytical models could be developed in experimental or theoretical based methods. The experimental based model requires a large number of testing results to establish the relationship equation between forming force and process parameters. Aerens et al. [119] attempted to predict ISF forces by analysing testing results under different parameters and fitting the regression equations with power functions. As a function of sheet thickness, drawing angle, tool diameter, step size and material tensile strength, Aerens

et al. model was capable to predict three force components for five different sheet materials in the studied forming conditions. However, this kind of model was developed using specific materials and under specific ISF conditions, which may limit the use for extensive materials and forming conditions.

On the other hand, theoretical based models could be developed by looking into the intrinsic relationships among ISF parameters, material deformation, stress and strain states. Allwood et al. [120] estimated the vertical force by assuming that the vertical motion punches through the sheet material with a resistance of shear stress. The horizontal force was calculated by assuming the horizontal motion is resisted by the compressive stress of the material ahead. This provides a quick calculation of the forming force for ISF machine design, but the assumption of the above two extreme cases makes the prediction equations a rough approximation. Li et al. [114, 121] developed models based on the energy method, and took the deformation modes of shear, bending and stretching into account. The prediction results showed a good agreement with experimental data. However, only considering the prediction of horizontal force components and the use of an empirical coefficient for combined shear and bending deformation, require Li et al. model further adjustment for a wider range of process conditions. Bansal et al. [122] presented equations for axial, radial and tangential forces, and the prediction of axial force was validated by comparing with experimental results although the modelling assumed a rectangle contact region and uniform stress distribution. Chang et al. [123] developed an analytical model to predict forming force in ISF and adjusted the model for several variants. This model calculates the forming force and components by multiplying the through-thickness stress on neutral surface with contact area and projection areas. For different parameters and workpiece shapes, the prediction accuracy of the model was validated. However, without consideration of

the force caused by elastic bending of unsupported sidewall makes this model more suitable to predict stabilised force with given process parameters.

2.4.2 Analytical modelling of other aspects in ISF

Apart from analytical modelling of forming force in ISF, some other aspects also draw increasing interest such as forming precision, surface finish, fracture, and twist.

Ambrogio et al. [124] evaluated the distance from the formed profile to the ideal surface in different ISF tests and proposed equations to predict the forming precision at the corner (K_1) and the centre (K_2) as following:

$$K_1 = -1.23 + 0.022 \cdot D_\mathrm{p} + 2.55 \cdot p + 0.98 \cdot s - 0.02 \cdot H + 0.04 \cdot \alpha - 0.045 \cdot p \cdot \alpha - 0.29 \cdot s^2 \quad (2.23)$$

$$K_2 = 2.57 + 1.35 \cdot D_\mathrm{p} - 13.76 \cdot p - 6.47 \cdot s + 0.27 \cdot H - 0.19 \cdot \alpha - 0.008 \cdot D_\mathrm{p} \cdot H + 3.03 \cdot p \cdot s + 0.193 \cdot p \cdot \alpha + 0.11 s \cdot \alpha - 0.0034 \cdot H \cdot \alpha - 0.035 \cdot D_\mathrm{p}^2 - 0.92 \cdot s^2 \quad (2.24)$$

where D_p is the tool diameter, p is the step size, s is the sheet thickness, H is the final depth of forming part, α is the drawing angle. The developed model can be used to select proper parameters for reduction of geometrical error and helps to generate "over-depth" tool path for compensation of sheet elastic springback.

For the same purpose, Asghar et al. [125] referred to the method for a circular shell part and calculated the elastic deflection γ at the studied position as the following equation:

$$\gamma = \frac{F_\mathrm{v}}{8 \cdot \pi \cdot D} \cdot \left[-(r^2 + b^2) \cdot \ln\left(\frac{a}{b}\right) + (r^2 - b^2) + \frac{1}{2} \cdot \left(1 + \frac{b^2}{a^2}\right) \cdot (a^2 - r^2) \right] \quad (2.25)$$

where, F_v is the vertical/ axial force, D is the flexural rigidity of sheet material, a is the distance from the clamped edge to the part centre, b is the distance from the part centre

to the tool position, and r is the distance from the part centre to the studied position. The elastic deflection is considered as the main reason for the forming inaccuracy in ISF, and with the above analytical equation, the authors proposed a tool path design strategy to improve forming accuracy by compensating the deflection.

Durante et al. [126] provided an analytical model to predict the average surface roughness (R_a) and the maximum roughness (R_z) by considering the envelope effect of the subsequent tool position. This model indicated that the surface roughness is influenced by three process parameters: tool radius, step size and drawing angle. Chang et al. [127] also developed an analytical model to predict the surface finish after ISF, and proposed that R_z can be calculated as the thickness difference between the contact region and the proximity of contact region. While, R_a can be obtained as the mean thickness difference in the measuring range and is approximated as $R_a = 0.268 \cdot R_z$, which is consistent with the measured relationship by Durante et al. [126]. This model considered both elastic deflection and plastic deformation, and indicated that tool radius, drawing angle, step size, sheet thickness and material properties have an influence on the surface finish.

In terms of the analytical modelling of fracture in ISF, Huang et al. [128] considered the effects of sheet thickness, tool dimension and step size, and gave an analytical solution for the maximum forming angle without fracture in ISF. The model indicated that later fracture and higher formability can be achieved by smaller tool dimension and step size. However, this model made an assumption that the stress distribution is uniform in the contact area, and the detailed variation of fracture initiation cannot be reflected. Differently, Fang et al. [129] derived the stress triaxiality distribution of different contact regions under forming tool and claimed that the fracture initiates on the outer surface of the region immediately above the contact region. Chang et al. [130] developed

an analytical model to predict the fracture strain under two different deformation states in ISF. In this model, the fracture strain was mainly influenced by the stress triaxiality and the material properties, between which the stress triaxiality was obtained by the stress state derivation with membrane analysis. In the derivation, the effect of bending, shearing and cyclic loading was considered, making the model effective in different ISF conditions.

The twist behaviour in ISF has also drawn increasing attention in recent years. A large number of experimental studies demonstrate that twist does exist and cause geometric inaccuracy in ISF. Duflou et al. [131] and Vanhove et al. [132] found that apart from conventional twist at low drawing angle, reverse twist exists when the drawing angle is large. Following this, Chang et al. [133] proposed an analytical model to predict the twist angle by assuming that the twist is caused by the unevenly distributed circumferential friction stress in meridional direction, and virtual work method was used to calculate the twisting angle. The developed model was validated by a series of experiments with different parameters. Yang et al. [65] also investigated the twist mechanism and developed an analytical model to calculate the twisting angle in ISF of PEEK. Different from the model developed by Chang et al. [133], Yang et al. [65] considered the effect of material flow on twist behaviour, as shown in Figure 2.16. Experiments showed that the developed model was valid to predict the twist angle at different wall angles.

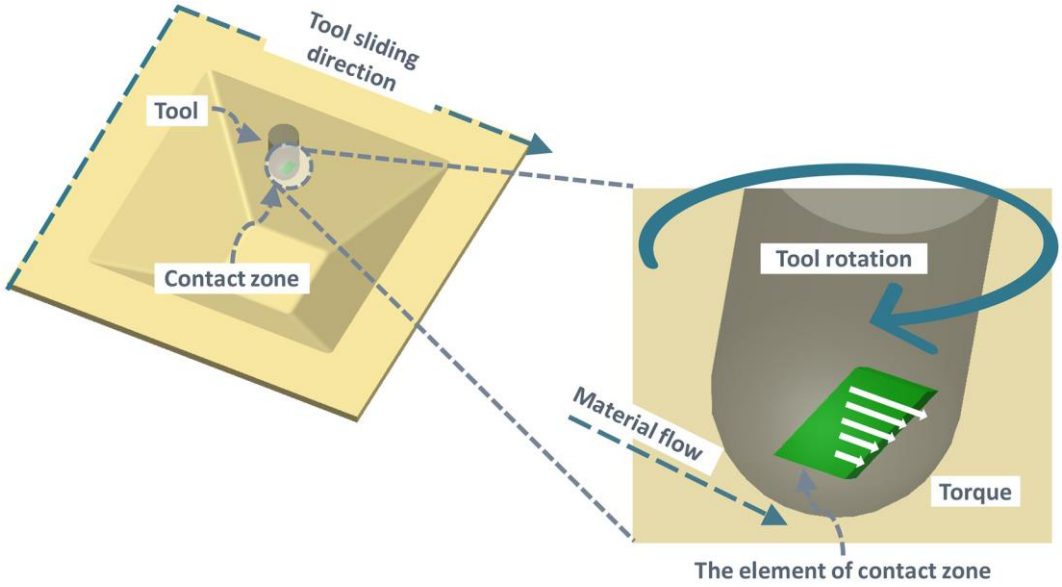


Figure 2.15 Mechanism of torsion in ISF of thermoplastics [65].

At last, after reviewing the analytical studies of ISF, a lack of attention on the contact pressure between forming tool and sheet material is found, but only a few investigations were carried out by FE simulation [119, 134, 135]. However, the contact pressure reflects the tool-sheet interaction, has an influence on the deformation and fracture, and governs the friction behaviour between forming tool and sheet. This leads to the research interest of the analytical solution of contact pressure distribution, which is in urgent demand and can be of great significance on the development of ISF.

2.5 Research challenges and future directions

Although ISF has been extensively researched to form metal sheet parts, the application of ISF on thermoplastic sheets is still at an early stage. In this section, attempt is given to provide a summary of the recent advances, discussions on the key scientific issues in ISF of thermoplastic materials. This provides a basis for observation of research challenges and future directions.

2.5.1 Research challenges

(1) There is little research on phenomenological or physical constitutive and damage models to describe and predict the material behaviour of thermoplastics in the ISF process with relatively high precision. The physical mechanism behind the material behaviour of thermoplastics, such as strain softening and strain hardening, has not been fully understood particularly under the ISF deformation conditions.

(2) The analytical mechanics are relatively complicated when membrane analysis with pressure-sensitive yield surface is used. If other mechanisms, such as through-thickness shear deformation, bending under tension and indentation effect, are taken into consideration, the case is even much more complicated, especially for thermoplastic materials.

(3) The current analytical framework of ISF of thermoplastic materials is mainly focused on the deformation mechanics associated with Failure Mode 1. It is difficult to apply this analytical framework to develop and investigate the deformation mechanics behind Failure Modes 2 and 3.

(4) In heat-assisted ISF of thermoplastics, the heat source is normally set under the sheet, leading to a higher temperature on the bottom surface than the top surface of the sheet. It would be a challenge to achieve a uniform temperature distribution through the thickness.

(5) Apart from springback and twist, thermal distortion may be another reason for the reduced forming accuracy in heat-assisted ISF of thermoplastics. Although the explanation of thermal distortion is clear, it is difficult and challenging to quantify the mechanism and model the influence on forming accuracy.

2.5.2 Future directions

(1) So far, little attention has been paid in numerical simulation for ISF of thermoplastic materials, which is an important research aspect. The thermomechanical FE simulation should be carried out to investigate the deformation mechanism, fracture behaviour and forming quality in ISF of thermoplastic materials.

(2) The capability for failure prediction of thermoplastic materials in ISF using either simulation or analytical method is of considerable benefits. Future work should be focused on the development of numerical simulation and analytical method to predict failure of thermoplastics in ISF.

(3) It is highly desirable to develop a new constitutive model to capture the effect of temperature, strain rate and deformation during SPIF of thermoplastics. This could be employed to evaluate the stresses in heat-assisted ISF of thermoplastics.

(4) There is a need to construct the FLC at fracture for some important types of biocompatible thermoplastics, e.g., PEEK and PMMA sheets by using such as Nakajima test so as to apply different strain paths in stretching. The constructed FLC would be beneficial in predicting fracture in SPIF of these biocompatible thermoplastics.

(5) The effect of strain softening and strain hardening in thermoplastics on the deformation and fracture mechanisms is yet to be fully established. Future research should take strain softening and strain hardening effects into consideration in looking into the deformation and fracture behaviour of thermoplastics in ISF.

(6) Through-thickness shear deformation and bending under tension in ISF of thermoplastic materials are lack of investigation. Future work should be carried out in taking through-thickness shear deformation and bending under tension of thermoplastics into consideration in either simple deformation or ISF.

(7) The fracture mode of thermoplastic materials in ISF is different from that under quasi-static tensile test: there is no significant necking before fracture. Future work should try to reveal the mechanism of the phenomenon.

(8) Little work has been reported on the mechanical properties and microstructural changes of thermoplastic materials in ISF. Future research should pay more attention to the mechanical properties and microstructural evolution of thermoplastics during ISF process.

(9) Future research should be devoted to exploring the possibility of ISF of other kinds of materials with application prospects, such as polymer-based composite materials, bilayer and multilayer sheets, and the optimised methods to form these types of materials using ISF.

(10) High temperature can improve the accuracy of the shaped part but may increase the surface wear, leading to increased surface roughness. The balance between temperature and surface roughness should be investigated.

(11) The influence of tool radius, step size and initial sheet thickness on the formability of thermoplastic materials is not always identical for different thermoplastics with some exceptions. Future work should be carried out to study such exceptional conditions.

(12) A more comprehensive parametric study can be beneficial to investigate the interdependence and interaction between these parameters and to achieve the optimum outcomes of formability and other aspects of forming quality.

(13) Forming force is a direct result and reflection of the complicated deformation behaviour in ISF. An analytical model for force prediction by comprehensively considering different factors in ISF is needed to overcome the shortcomings of the current models.

(14) Contact behaviour under the interaction between forming tool and sheet material can be helpful to reveal the deformation mechanism and investigate the friction behaviour. Effort should be made to develop the analytical model for reflection of localised contact.

(15) Thermal distortion clearly exists in heat-assisted ISF, but there are rare studies about this topic. Future work may be needed to investigate the mechanism of thermal distortion and develop analytical model to reflect its effect on forming accuracy in heat-assisted ISF of thermoplastics.

Chapter 3 A New Phenomenological Constitutive Model for Thermoplastics

Nomenclature

Symbol	Term	Unit
σ	True stress	MPa
ε	True strain	
σ_{peak}	Peak stress	MPa
$\varepsilon_{\text{peak}}$	Peak strain	
$\dot{\varepsilon}$	Strain rate	s^{-1}
T	Temperature	K
$\dot{\varepsilon}_{\text{ref}}$	Reference strain rate	s^{-1}
T_{ref}	Reference temperature	K
$\varepsilon_{\text{critical}}$	Critical strain between strain softening and strain hardening	
m, a	Parameters related to the effect of strain rate and temperature in $h(\dot{\varepsilon}, T)$ of the new constitutive model	
K_1, n, μ	Parameters in $f(\varepsilon, \dot{\varepsilon}, T)$ of the new constitutive model	MPa for K_1

K_2, C_1, C_2, α	Parameters in $g(\varepsilon, \dot{\varepsilon}, T)$ of the new constitutive model	MPa for K_2
k, w, λ	Parameters in $u(\varepsilon, \dot{\varepsilon}, T)$ and $v(\varepsilon, \dot{\varepsilon}, T)$ of the new constitutive model	

3.1 Introduction

As this PhD project mainly deals with ISF of thermoplastics, the constitutive model of thermoplastics is the fundamental of the proposed analytical study and FE simulation. Based on the complicated mechanical behaviour of thermoplastics and the inadequacies of previously proposed phenomenological constitutive models, this chapter aims to develop a new phenomenological constitutive model to describe the mechanical behaviour of thermoplastics. It can be used to predict both the tensile behaviour and compressive behaviour of semi-crystalline and glassy thermoplastics. First, an introduction to the new constitutive model is given followed by a description of the procedure to determine the material parameters of the new model. The new model is named Zhu-Ou-Popov (ZOP) model. The new model is then used to predict the tensile and compressive behaviours of PEEK (semi-crystalline thermoplastic) and PC material (glassy thermoplastic) to validate the applicability of the new model. Also, the dynamic tensile and compressive behaviours of PC material at high strain rate conditions are used to validate the new model. Finally, a comparative study is carried out between the new model and a number of commonly used constitutive models including Johnson-Cook, Nasraoui et al., DSGZ and Mulliken-Boyce models.

3.2 Formulation of the new constitutive model

The new constitutive model is referred to that of DSGZ model. In the study by Duan et al. [102] as shown in Equation (2.20), they use the term $\frac{\varepsilon \cdot e^{\left(1-\frac{\varepsilon}{C_3 \cdot h(\dot{\varepsilon},T)}\right)}}{C_3 \cdot h(\dot{\varepsilon},T)}$ (Term A) to describe the shift and strain softening behaviours at small strains a function of strain rate and temperature. The term $f(\varepsilon) = (e^{-C_1 \cdot \varepsilon} + \varepsilon^{C_2}) \cdot (1 - e^{-\alpha \cdot \varepsilon})$ (Term B) is used to describe the strain hardening behaviour at large strains. The term $e^{[\ln(g(\dot{\varepsilon},T))-C_4] \cdot \varepsilon}$ (Term C) is used to correlate deformation behaviours at small and large strains. Finally, the term $h(\dot{\varepsilon},T) = \dot{\varepsilon}^m \cdot e^{\frac{a}{T}}$ (Term D) represents the value of stress dependence on strain rate and temperature. In the above-mentioned four terms, ε is the true strain, $\dot{\varepsilon}$ is the strain rate in s^{-1}, T is the temperature in K, m and a are two material parameters related to the effect of strain rate and temperature, respectively, C_1, C_2, C_3, C_4, α are model parameters of DSGZ model. The specific effects of Terms A and C to a normalised function value and Term B to a proportional function value according to the normalisation of Terms A and C are presented in Figure 3.1 based on the material parameters for PMMA in their work.

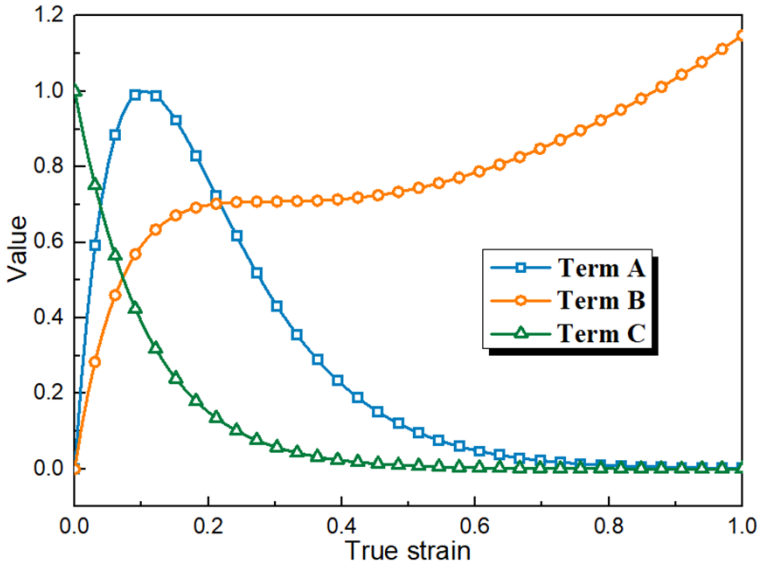


Figure 3.1 Effects of Terms A and C to normalised function value and Term B to a proportional function value according to the normalisation of Terms A and C.

As a result, DSGZ model can be used to provide a uniform representation of the flow stress behaviour for different types of thermoplastics (including glassy and semi-crystalline thermoplastics) and to describe the shift and strain softening behaviours at small strains and the strain hardening behaviours at large strains.

Inspired by the general concept of DSGZ model, a more effective constitutive method is proposed based on the method of piecewise function. In this method, the flow stress can be defined and presented in different expressions at small or large strains, and an effective term acts as a transition function to combine the two expressions smoothly into one equation for simplicity. The new model uses $h(\dot{\varepsilon}, T)$ to predict the effect of temperature and strain on the flow stress. $f(\varepsilon, \dot{\varepsilon}, T)$ is used to predict the linear elastic, non-linear elastic, yield, and strain softening behaviours at small strain range, while $g(\varepsilon, \dot{\varepsilon}, T)$ predicts the strain hardening behaviour at large strain range. $u(\varepsilon, \dot{\varepsilon}, T)$ and $v(\varepsilon, \dot{\varepsilon}, T)$ acts as the transition functions to enable the smooth shift of the stress prediction from small to large strain ranges for the connection between $f(\varepsilon, \dot{\varepsilon}, T)$ and $g(\varepsilon, \dot{\varepsilon}, T)$. The above gives the overall strategy for the new model, and details are presented in the next few sections.

3.2.1 Effect of strain rate and temperature

For thermoplastics, strain rate and temperature have a significant influence on the mechanical behaviour. In general, the flow stress would increase with the increase of strain rate and the reduction of temperature and vice versa. Therefore, to predict the mechanical behaviour of thermoplastics, the first step is to model the effect of strain rate and temperature on the flow stress. A term $h(\dot{\varepsilon}, T)$ is modified from the G'Sell-Jonas model [106] (Equation (2.22)) in the following:

$$h(\dot{\varepsilon}, T) = \left(\frac{\dot{\varepsilon}}{\dot{\varepsilon}_{\mathrm{ref}}}\right)^{m} \cdot e^{a\cdot\left(\frac{1}{T}-\frac{1}{T_{\mathrm{ref}}}\right)} \tag{3.1}$$

where, $\dot{\varepsilon}_{\mathrm{ref}}$ is the reference strain rate, and T_{ref} is the reference temperature in K. Different from the original term in G'Sell-Jonas model (Equation (2.22)), the modified term is rewritten to add a reference strain rate and temperature to have a clearer meaning that the value of $h(\dot{\varepsilon}, T)$ becomes larger than 1 at a higher strain rate and/or a lower temperature compared with the reference strain rate and temperature, while $h(\dot{\varepsilon}, T)$ is smaller than 1 at a smaller strain rate and/or a higher temperature compared with the reference strain rate and temperature. This makes $h(\dot{\varepsilon}, T)$ to have a starting value of 1 and to be more easily used in the following proposed functions $f(\varepsilon, \dot{\varepsilon}, T)$, $g(\varepsilon, \dot{\varepsilon}, T)$, $u(\varepsilon, \dot{\varepsilon}, T)$, and $v(\varepsilon, \dot{\varepsilon}, T)$ in the next few sections.

3.2.2 Linear elastic, non-linear elastic, yield, and strain softening behaviours

In order to describe the linear elastic, non-linear elastic, yield and strain softening behaviours of thermoplastics, a function, $f(\varepsilon, \dot{\varepsilon}, T)$, is proposed based on the function $y = x \cdot \exp(-x)$, which can ideally fit the above-mentioned variation trend. $f(\varepsilon, \dot{\varepsilon}, T)$ can be expressed as follows:

$$f(\varepsilon, \dot{\varepsilon}, T) = K_1 \cdot \varepsilon^n \cdot e^{-\frac{\varepsilon}{\mu \cdot h(\dot{\varepsilon}, T)}} \tag{3.2}$$

where, K_1, n and μ are material parameters, and the unit of K_1 is MPa. The mathematical representation of $f(\varepsilon, \dot{\varepsilon}, T)$ is shown in Figure 3.2(a), which can be used to capture the yield behaviour and the strain softening behaviour at small strains (smaller than $\varepsilon_{\mathrm{critical}}$, which is the critical strain between the strain softening and the strain hardening as illustrated in Figure 2.13). It is noteworthy that the value of n reflects the curve trend in elastic deformation. $n > 1$ implies a slight concave shape of the predicted curve in elastic deformation at the very beginning, while $n < 1$ implies a slight convex shape of the predicted curve.

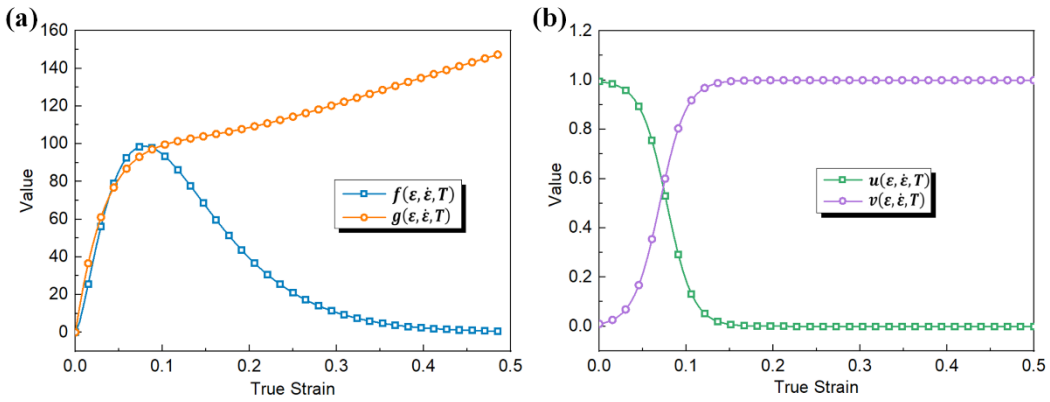


Figure 3.2 Mathematic representation of (a) $f(\varepsilon,\dot{\varepsilon},T)$ and $g(\varepsilon,\dot{\varepsilon},T)$ and (b) $u(\varepsilon,\dot{\varepsilon},T)$ and $v(\varepsilon,\dot{\varepsilon},T)$.

The partial derivative of $f(\varepsilon,\dot{\varepsilon},T)$ of ε can be derived as:

$$\frac{\partial f(\varepsilon,\dot{\varepsilon},T)}{\partial \varepsilon} = K_1 \cdot \varepsilon^{n-1} \cdot e^{-\frac{\varepsilon}{\mu \cdot h(\dot{\varepsilon},T)}} \cdot \left[n - \frac{\varepsilon}{\mu \cdot h(\dot{\varepsilon},T)}\right] \tag{3.3}$$

Therefore, when $\varepsilon = n \cdot \mu \cdot h(\dot{\varepsilon},T)$ (defined as a peak strain $\varepsilon_{\text{peak}}$, as illustrated in Figure 2.13), the flow stress reaches a peak value, $\sigma_{\text{peak}} = K_1 \cdot \left[\frac{n \cdot \mu \cdot h(\dot{\varepsilon},T)}{e}\right]^n$ which is obtained by putting the peak strain $\varepsilon_{\text{peak}}$ into Equation (3.2). As discussed earlier, the flow stress increases when a larger strain rate and/or lower temperature are applied. More discussions on the influence of the strain rate and temperature on the peak strain and peak stress are given in Section 3.4.

3.2.3 Strain hardening behaviour

The term $g(\varepsilon,\dot{\varepsilon},T)$ refers to the corresponding term in DSGZ model to predict the strain hardening behaviour at large strains (larger than $\varepsilon_{\text{critical}}$) after the strain softening behaviour at small strains. The expression of $g(\varepsilon,\dot{\varepsilon},T)$ is given as follows:

$$g(\varepsilon,\dot{\varepsilon},T) = K_2 \cdot (e^{-C_1 \cdot \varepsilon} + \varepsilon^{C_2}) \cdot (1 - e^{-\alpha \cdot \varepsilon}) \cdot h(\dot{\varepsilon},T) \tag{3.4}$$

where, K_2, C_1, C_2 and α are material parameters, and the unit of K_2 is MPa. The mathematical representation of $g(\varepsilon,\dot{\varepsilon},T)$ is given in Figure 3.2(a). The value of

$g(\varepsilon, \dot{\varepsilon}, T)$ rises with the increase of strain, which is consistent with the strain hardening behaviour at large strains.

3.2.4 Transition functions

The whole model is based on a transition function to effectively unify the flow stress behaviour under both small-strain, large-strain conditions with consideration of the effect of strain rate and temperature. To ensure a smooth transition between strain softening and strain hardening behaviours, two terms $u(\varepsilon, \dot{\varepsilon}, T)$ and $v(\varepsilon, \dot{\varepsilon}, T)$ are proposed in this new model as given below:

$$u(\varepsilon, \dot{\varepsilon}, T) = \frac{1}{1+k \cdot e^{w \cdot \varepsilon - \lambda \cdot h(\dot{\varepsilon}, T)}} \tag{3.5}$$

$$v(\varepsilon, \dot{\varepsilon}, T) = \frac{1}{1+e^{\lambda \cdot h(\dot{\varepsilon}, T) - w \cdot \varepsilon}} \tag{3.6}$$

where, k, w and λ are material parameters. These two terms are modified from $\frac{1}{1+e^{x}}$ and $\frac{1}{1+e^{-x}}$, which stabilise at '1' and '0' with different 'x' ranges. It acts as a function to enable a smooth transition between small strains and large strains. The mathematic representation of the terms $u(\varepsilon, \dot{\varepsilon}, T)$ and $v(\varepsilon, \dot{\varepsilon}, T)$ are presented in Figure 3.2(b) based on the material parameters worked out for PEEK in this section. By using them, the flow stress can be expressed in different equations at different strains. The new constitutive model approximately works like a piecewise function:

$$\sigma(\varepsilon, \dot{\varepsilon}, T) = \begin{cases} f(\varepsilon, \dot{\varepsilon}, T) = K_1 \cdot \varepsilon^{n} \cdot e^{-\frac{\varepsilon}{\mu \cdot h(\dot{\varepsilon}, T)}} & 0 \le \varepsilon < \varepsilon_{\text{critical}} \\ g(\varepsilon, \dot{\varepsilon}, T) = K_2 \cdot (e^{-C_1 \cdot \varepsilon} + \varepsilon^{C_2}) \cdot (1 - e^{-\alpha \cdot \varepsilon}) \cdot h(\dot{\varepsilon}, T) & \varepsilon > \varepsilon_{\text{critical}} \end{cases} \tag{3.7}$$

where, $\varepsilon_{\text{critical}}$ is the critical strain between the strain softening and the strain hardening behaviours. When the strain approaches a value close to $\varepsilon_{\text{critical}}$, the value of flow stress can be changed from small strain case to large strain case smoothly.

Following the above methodology, the proposed new phenomenological model may be given as follows:

$$\sigma(\varepsilon, \dot{\varepsilon}, T) = f(\varepsilon, \dot{\varepsilon}, T) \cdot u(\varepsilon, \dot{\varepsilon}, T) + g(\varepsilon, \dot{\varepsilon}, T) \cdot v(\varepsilon, \dot{\varepsilon}, T) \tag{3.8}$$

The twelve material parameters in this model are k, w, λ, n, μ, C_1, C_2, α, K_1, K_2, m and a. The procedure to derive these parameters is given in Appendix A.

3.3 Validation of the constitutive model

In this section, PEEK and PC materials, which are semi-crystalline and glassy thermoplastics respectively, are used to validate the new constitutive model and its applicability. The tensile and compressive behaviours used in the validation process were obtained by other researchers [87, 88, 136], and all the related temperatures and strain rates in the previous studies are used for model validation. In addition, it is noteworthy that from each experimental curve, 100 data points were extracted for the validation.

In order to evaluate the prediction precision of each model quantitatively the coefficient of determination (R^2) and root mean square error ($RMSE$) are used in the current research. A larger value of R^2 and a smaller value of $RMSE$ represent better prediction precision. Their calculation methods are as follows:

$$R^2 = \frac{\sum_{i=1}^{N}(E_i - \bar{E})^2 - \sum_{i=1}^{N}(E_i - P_i)^2}{\sum_{i=1}^{N}(E_i - \bar{E})^2} \tag{3.9}$$

$$RMSE = \sqrt{\frac{1}{N}\sum_{i=1}^{N}(E_i - P_i)^2} \tag{3.10}$$

where, E_i and P_i are the experimental and predicted values, respectively; $\bar{E}$ and $\bar{P}$ are the mean values of E_i and P_i, respectively; N is the number of data used in the evaluation process.

3.3.1 Validation with PEEK material

In the research of Joseph [136], unfilled PEEK was used to carry out the tensile and compressive tests. The tensile test samples were made from PEEK sheets and of dog-bone shape with a gauge length of 16 mm, width of 2 mm and thickness of 0.5 mm. The compressive test samples were manufactured from 450G extruded natural rod and of rod shape with 8 mm for both length and diameter. The tensile tests were conducted on a DEBEN MICROTEST 200N Extended Tester with Peltier Head, 10 mm maximum travel and the compressive tests were performed on an INSTRON servo hydraulic testing machine.

3.3.1.1 Tensile behaviour

The experimental tensile tests with strain rates of 1.04×10^{-4} s^{-1}, 4.96×10^{-4} s^{-1} and 1.54×10^{-3} s^{-1} and temperatures of 296 K, 343 K and 373 K are selected from the research of Joseph [136] to validate the new model. Figure 3.3(a) and (c) shows the true stress – strain curves for the tensile behaviour of the PEEK material, which shows clearly the five phases of tensile behaviour including linear viscoelastic deformation, non-linear viscoelastic deformation, yield behaviour, strain softening and hardening. As shown in Figure 3.3(a), at a temperature of 296 K, the flow stress including the peak stress is increased with the increase of strain rate. The peak point shifts to the right when a higher strain rate is applied, which indicates the yield behaviour appears later. As shown in Figure 3.3(c), at constant strain rate of 4.96×10^{-4} s^{-1}, the flow stress and the peak stress decreased with the increase of temperature. The peak point shifts to the left at a higher temperature, indicating the yield behaviour appears earlier.

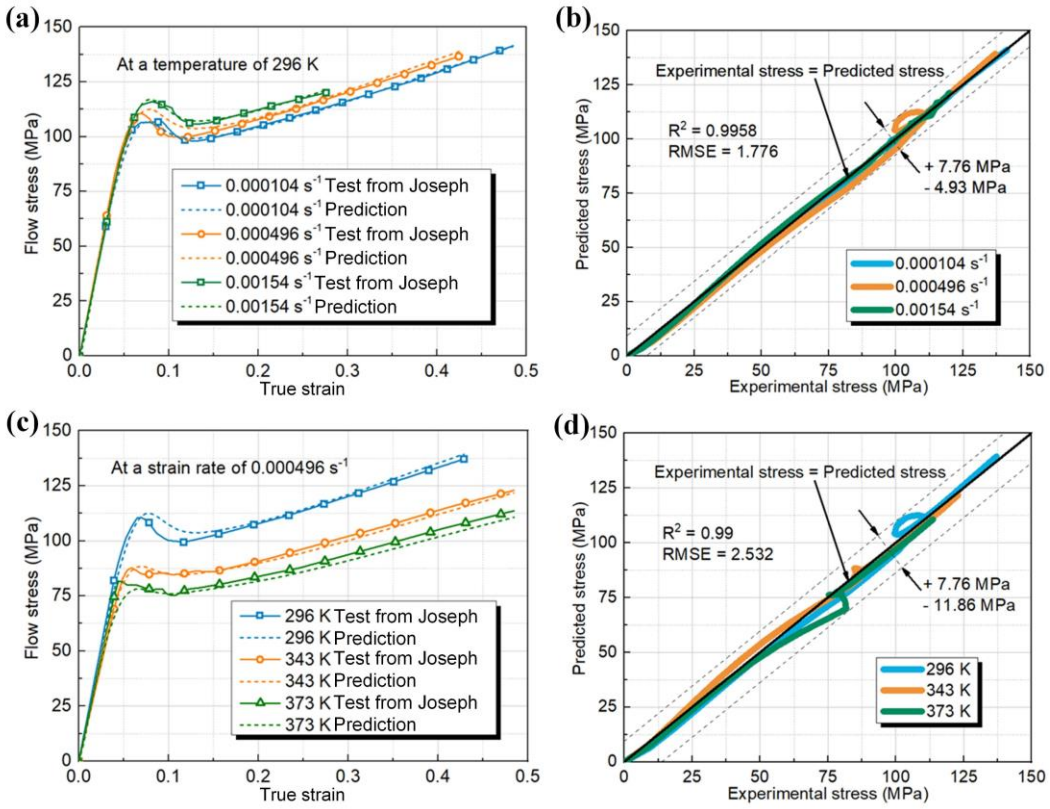


Figure 3.3 Experimental true stress – strain curves from Joseph [136] and predicted results for tensile behaviour of PEEK material (a) and (b) under different strain rates at constant temperature of 296 K and (c) and (d) under different temperatures at constant strain rate of 4.96×10^{-4} s^{-1}.

To validate the new constitutive model, the twelve material parameters in the new model were determined using the method stated in Appendix A and are presented in Table 3.1. For the identified parameters, the reference temperature is 296 K, and the reference strain rate is 4.96×10^{-4} s^{-1}.

Table 3.1 Material parameters of the new model for the tensile behaviour of PEEK.

k	w	λ	n	μ	C_1
0.4538	61.86	3.945	1.382	0.05976	11.77
C_2	α	K_1 (MPa)	K_2 (MPa)	m	a
0.4707	13.6	12020	206.2	0.0268	408.4

As shown in Figure 3.3, the predicted results by using the new model exhibit a good agreement with the experimental data, not only in the case at constant temperature but also in the case at constant strain rate. Overall, the prediction of experimental data shows the same trend, and their shapes are almost identical, indicating the new model can capture the effect of strain on the flow stress accurately. The fitting results at constant temperature are presented in Figure 3.3(a) and (b), which shows the effect of strain rate on the flow stress. In general, the new model is able to characterize the effect of strain rate on the flow stress. Also, the effect of strain rate on the appearance of the peak point is presented well from the prediction. The predicted results at constant strain rate are given in Figure 3.3(c) and (d), which shows the effect of temperature on the flow stress. The tested true stress – strain curves and the prediction indicate that the new model can describe the effect of temperature on the flow stress with good precision. The term corresponding to the temperature in the new model works well in the current case. Further, as shown in Figure 3.3(b) and (d), the R^2 values of the predicted results at constant temperature and strain rate are 0.9958 and 0.99, respectively. Therefore, the new model can be effectively used to predict the tensile behaviour of PEEK material.

3.3.1.2 Compressive behaviour

As shown in Figure 3.4(a) and (c), the experimental compressive tests with strain rates of 2.08×10^{-4} s^{-1}, 1.04×10^{-3} s^{-1} and 3.1×10^{-3} s^{-1} and the temperature of 296 K, 343 K and 373 K are selected to validate the new model. Figure 3.4(a) presents the effect of strain rate on the flow stress at constant temperature and Figure 3.4(c) shows the effect of temperature on the flow stress at constant strain rate. There are four phases observed in the flow stress curves including linear elastic deformation, non-linear elastic deformation, yield and strain hardening. Compared with the tensile test results, there is no obvious strain softening behaviour in the compressive testing process of PEEK

material. The same as tensile behaviour, at temperature of 296 K, the flow stress increased with the increase of strain rate, as shown in Figure 3.4(a), while the trend does not show obvious evidence for the yield point shifting to the right when higher strain rate applied. At constant strain rate of 10^{-3} s^{-1}, the flow stress decreased with the increase of temperature. However, the yield point shifts to the left obviously at a higher temperature, which means the yield behaviour appears earlier.

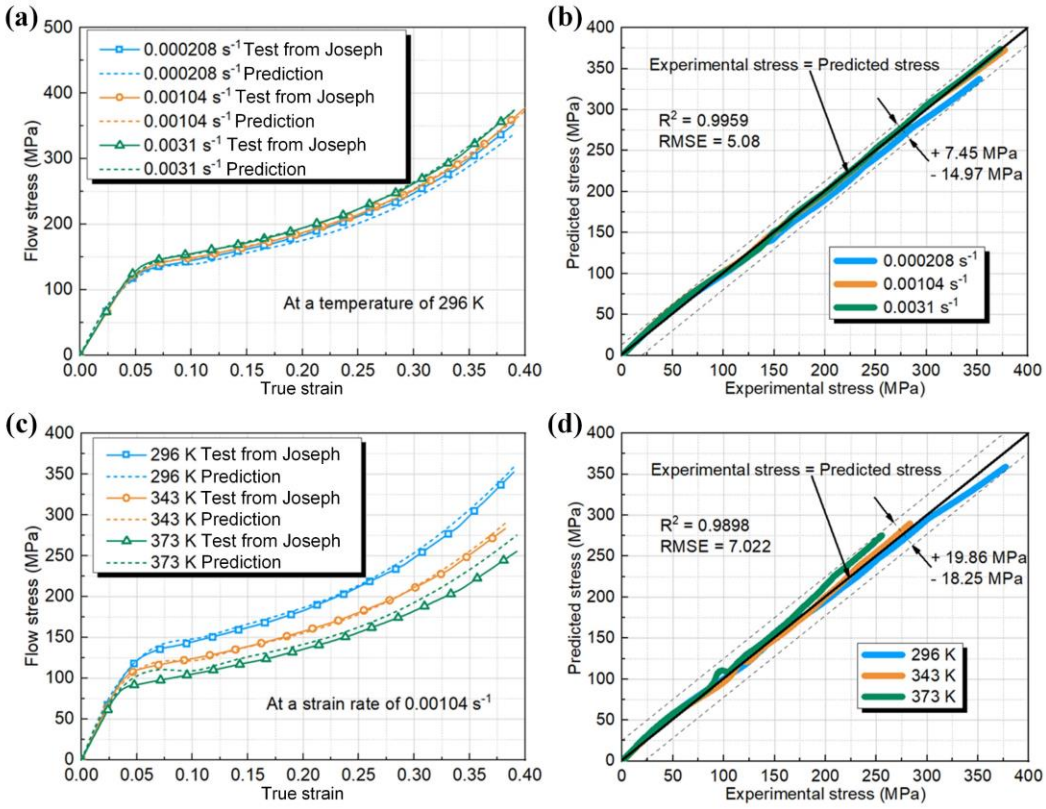


Figure 3.4 Experimental compressive true stress – strain curves from Joseph [136] and predicted results of PEEK (a) and (b) under different strain rates at constant temperature of 296 K and (c) and (d) under different temperatures at constant strain rate of 1.04×10^{-3} s^{-1}.

Following the identification method, the material parameters of the new model for the compressive behaviour of PEEK material were derived step by step with the selection of reference temperature of 296 K and reference strain rate of 1.04×10^{-3} s^{-1}. The details can be found in Table 3.2.

Table 3.2 Material parameters of the new model for the compressive behaviour of PEEK.

k	w	λ	n	μ	C_1
0.0002722	86.01	0.1481	1.063	0.03228	8.391
C_2	α	K_1 (MPa)	K_2 (MPa)	m	a
1.184	1.109	5010	955.1	0.0377	394.269

Using the material parameters given in Table 3.2, the prediction curves for the compressive behaviour of PEEK material were obtained by using the new constitutive model. As shown in Figure 3.4, the prediction matches the experimental results well. The new model is able to present the trend of compressive behaviour at different conditions, and the yield behaviour and strain hardening behaviour are included in the prediction curves. As observed from Figure 3.4(a), at a constant temperature, the predicted results for the strain rate of 2.08×10^{-4} s^{-1} and 1.04×10^{-3} s^{-1} show a good agreement with the experimental data although there is a degree of deviation of the prediction from the test data for the case of the strain rate of 3.1×10^{-3} s^{-1}. Meanwhile, at constant strain rate, as shown in Figure 3.4(b), the predicted results for the temperatures of 296 K and 343 K are almost identical to the experimental results, whilst there is an overestimation of the predicted results in the case for the temperature of 373 K.

3.3.2 Validation with PC material

3.3.2.1 Tensile behaviour

Performed on a MTS810 servo-hydraulic system, uniaxial tensile tests of 3 mm thickness PC sheet from Cao et al. [87] are used for validation in this section with a

selection of strain rate ranging from 10^{-3} s^{-1}, 10^{-2} s^{-1} to 0.5 s^{-1} and temperature from 293 K, 353 K to 393 K.

Figure 3.5(a) and (c) shows the experimental true stress – strain curves, which were derived from the engineering stress – strain curves in the paper of Cao et al. [87]. There are five phases in each curve as well: linear viscoelastic deformation, non-linear viscoelastic deformation, yield behaviour, strain softening and hardening. As shown in Figure 3.5(a), at temperature of 293 K, the flow stress including the peak stress increased with the increase of strain rate. The peak point shifts to the right when a higher strain rate applied, which indicates the yield behaviour appears later. As shown in Figure 3.5(c), at constant strain rate of 10^{-3} s^{-1}, the flow stress and the peak stress decrease with the elevation of temperature. The peak point shifts to the left at higher temperature, indicating the yield behaviour appears earlier.

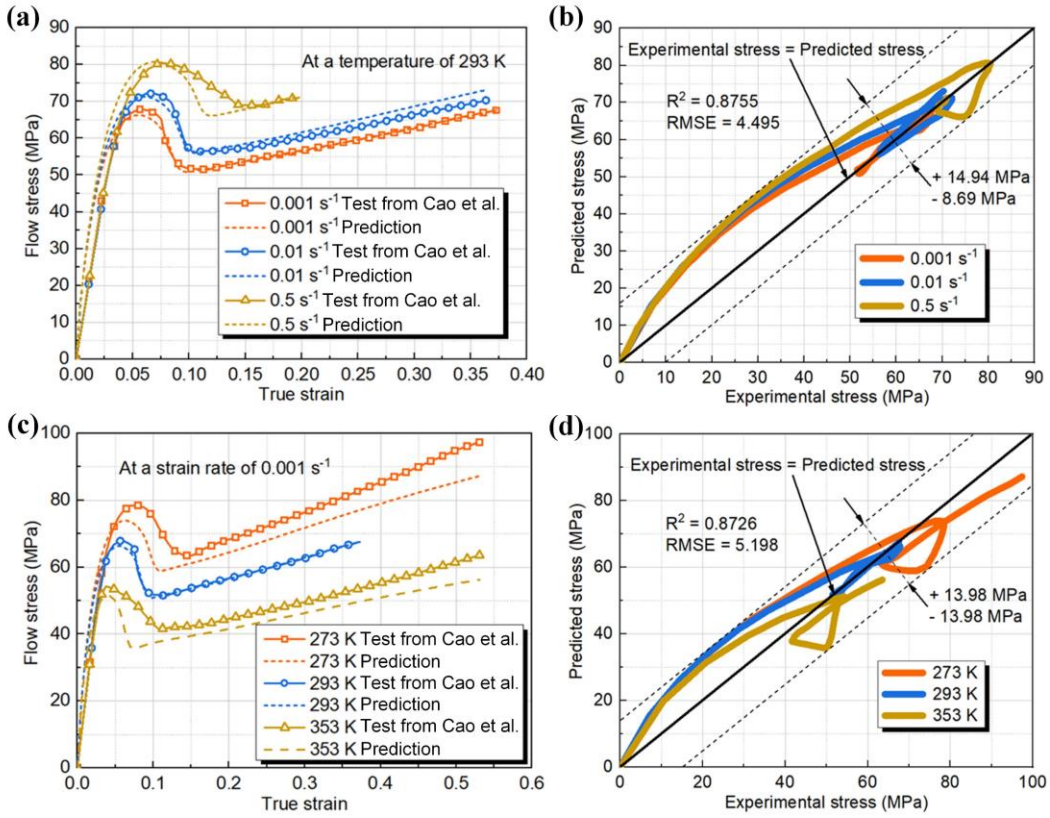


Figure 3.5 Experimental tensile true stress – strain curves from Cao et al. [87] and predicted results of PC (a) and (b) under different strain rates at constant temperature of 293 K and (c) and (d) under different temperatures at constant strain rate of 10^{-3} s^{-1}.

The twelve material parameters for the PC samples of the proposed model were determined using the procedure stated in Appendix A and are presented in Table 3.3. The reference temperature and strain rate were selected as 293 K and 10^{-3} s^{-1}, respectively.

Table 3.3 Material parameters of the new model for the tensile behaviour of PC.

k	w	λ	n	μ	C_1
0.9613	280.4	23.9	0.8307	0.06614	14.5
C_2	α	K_1 (MPa)	K_2 (MPa)	m	a
0.3592	15.48	1695	95.97	0.03796	528.4

Using the material parameters given in Table 3.3, the predicted results of the tensile behaviour of PC material are depicted in Figure 3.5. The results show that the new constitutive model is able to capture the experimental results at different strain rates and temperatures. As shown in Figure 3.5(a) and (b), at room temperature, the predicted and experimental results show acceptable agreement at different strain rates with R^2 of 0.8755. This indicates the new model is able to capture the effect of strain and strain rate on the flow stress at room temperature. As shown in Figure 3.5(c) and (d), the effect of temperature on the flow stress can also be predicted acceptably with R^2 of 0.8726, with certain deviation at both small and large strains. Generally, the new model can be used to predict the tensile behaviour of PC material.

3.3.2.2 Compressive behaviour

Compressive tests of PC selected for the current research were done by Yu et al. [88] on a servo-hydraulic machine with strain rates of 10^{-3} s^{-1}, 10^{-2} s^{-1} and 0.1 s^{-1} and temperatures at 293 K, 333 K and 373 K, respectively. The samples were of circular cylinder geometry with a length of 6 mm and diameter of 12 mm.

The experimental compressive true stress – strain curves of PC were obtained from the paper published by Yu et al. [88], and are shown in Figure 3.6(a) and (c). The trend of each curve is approximately the same as that of tensile true stress – strain curves. Besides, the influence of strain rate and temperature on the compressive behaviour is similar to that on tensile behaviour.

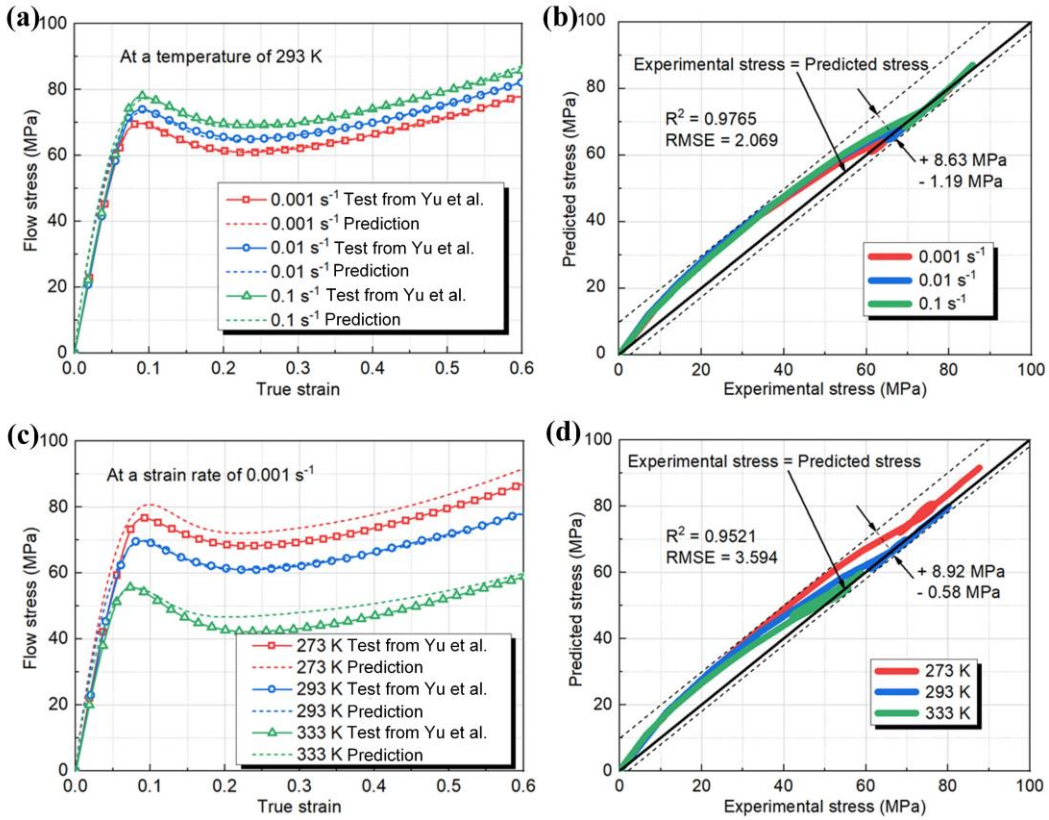


Figure 3.6 Experimental compressive true stress – strain curves from Yu et al. [88] and predicted results of PC (a) and (b) under different strain rates at constant temperature of 293 K and (c) and (d) under different temperatures at constant strain rate of 10^{-3} s^{-1}.

The material parameters in the new model for compressive behaviour of PC were derived as listed in Table 3.4. The selected reference temperature and strain rate are 293 K and 10^{-3} s^{-1}, respectively. Using the derived parameters, the predicted results are shown in Figure 3.6.

Table 3.4 Material parameters of the new model for the compressive behaviour of PC.

k	w	λ	n	μ	C_1
0.2488	28.57	0.8579	0.8345	0.2339	4.062
C_2	α	K_1 (MPa)	K_2 (MPa)	m	a
0.9424	7.972	646.4	111.5	0.02423	798.6

As shown in Figure 3.6(a) and (c), at room temperature of 293 K, the new model can predict the compressive behaviour of PC material precisely at different strain rates with R^2 of 0.9765. Not only can the general trend of each curve but also the effect of strain rate be predicted well. At lower and higher temperature, the prediction precision of the new model remains at a high level with R^2 of 0.9521. The predicted results show a good agreement with the experimental results although there are slight differences at 273 K and 333 K. Thus, an effective prediction is produced by the new model in the case of compressive behaviour of PC material.

3.3.3 Validation with PC material at high strain rate conditions

To explore the effectiveness of the new constitutive model for material behaviour at high strain rate conditions, both dynamic tensile and compressive behaviours of PC are used for further validation.

3.3.3.1 Dynamic tensile behaviour

The same as the tensile behaviour at low strain rate conditions, the experimental data obtained from the split Hopkinson tension bar (SHTB) technique by Cao et al. [87] are used to validate how effectively the new constitutive model can be used to predict the dynamic tensile behaviour. In this section, the engineering stress – strain relations were obtained from the split Hopkinson tension bar (SHTB) tests. Among them, three different strain rates (370 s^{-1}, 800 s^{-1} and 1700 s^{-1}) and three different temperatures (273 K, 293 K and 353 K) are selected to be used in the current research.

As shown in Figure 3.7(a) and (c), the experimental true stress – strain curves are converted from the engineering stress – strain curves. At high strain rate, the tensile true stress – strain curves have a similar shape to that at low strain rate conditions. The increase of strain rate leads to the increased flow stress and delayed yielding while the

elevated temperature causes the softening of PC material and the earlier occurrence of yielding. Following the procedures provided in Appendix A, the twelve material parameters for dynamic tensile behaviour were identified and are given in Table 3.5. For the given material parameters, the reference temperature is 293 K, and the reference strain rate is 1700 s^{-1}. Accordingly, the predicted results are shown in Figure 3.7.

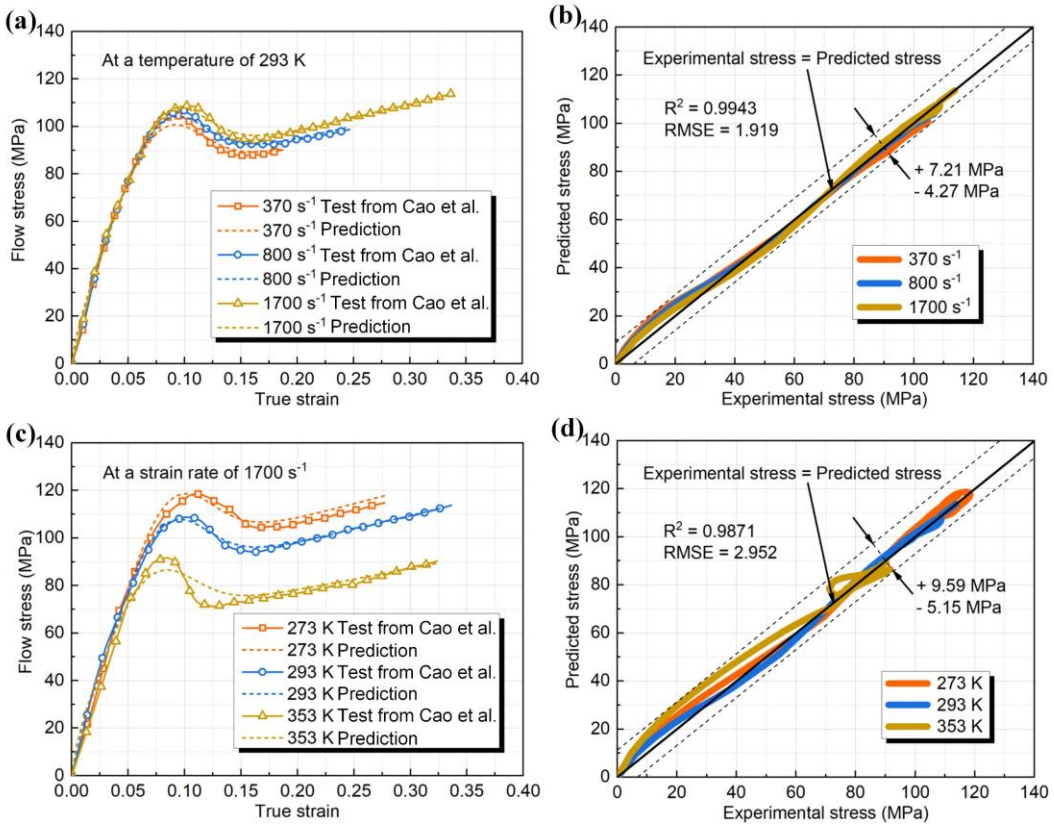


Figure 3.7 Experimental dynamic tensile true stress – strain curves from Cao et al. [87] and predicted results of PC (a) and (b) under different strain rates at constant temperature of 293 K and (c) and (d) under different temperatures at constant strain rate of 1700 s^{-1}.

Table 3.5 Material parameters of the new model for the dynamic tensile behaviour of PC.

k	w	λ	n	μ	C_1
0.02611	51.92	2.299	0.7065	0.1399	-1.31
C_2	α	K_1 (MPa)	K_2 (MPa)	m	a
0.1769	147.8	396	47.79	0.04651	391.5

As observed from Figure 3.7, the predicted curves show a good agreement with the experimental results. Meanwhile, the new constitutive model is able to predict the effect of strain rate and temperature on the tensile behaviour at high strain rate conditions. Generally, under different strain rates, the value of R^2 reaches 0.9943, while under different temperatures, a R^2 value of 0.9871 is obtained. In the comparison, only the predicted result at the strain rate of 1700 s^{-1} and the temperature of 353 K shows inaccuracy in yielding and strain softening phase compared with the true stress – strain curves in experiment. Nevertheless, it is feasible to use the new model to predict the dynamic tensile behaviour of PC.

3.3.3.2 Dynamic compressive behaviour

Validation of the new constitutive model for dynamic compressive behaviour is carried out using the experimental results obtained by Yu et al. [88]. The compressive behaviour at high strain rate conditions was obtained in compressive split Hopkinson pressure bar (SHPB) tests. Samples with circular cylinder geometry were designed for SHPB tests 6 mm of diameter and 3 mm of length, respectively. In the current research, strain rates of 3000 s^{-1}, 4000 s^{-1} and 5000 s^{-1} and temperature of 293 K, 323 K and 373K are used.

The extracted compressive true stress – strain curves in experiment at high strain rate condition can be found in Figure 3.8(a) and (b), and the identified parameters in the new constitutive model based on the experimental curves are given in Table 3.6. For this set of parameters, the reference temperature and strain rate were selected as 293 K and 5000 s^{-1}, respectively.

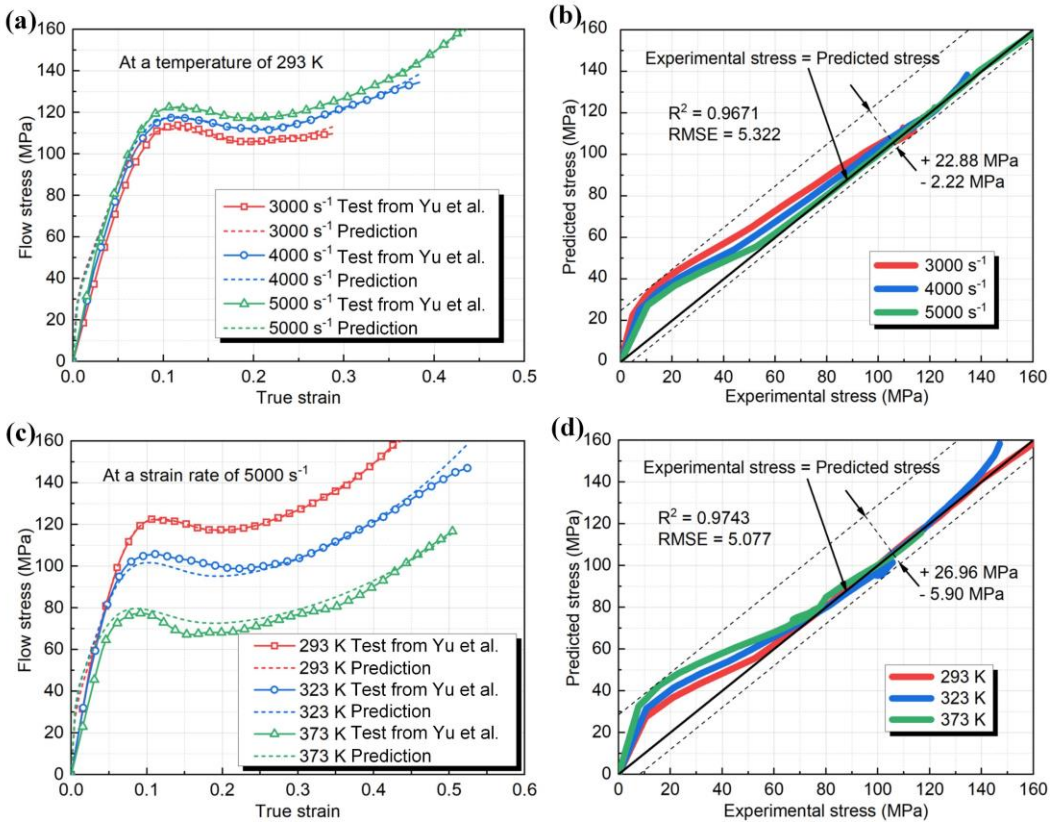


Figure 3.8 Experimental dynamic compressive true stress – strain curves from Yu et al. [88] and predicted results of PC (a) and (b) under different strain rates at constant temperature of 293 K and (c) and (d) under different temperatures at constant strain rate of 5000 s^{-1}.

Table 3.6 Material parameters of the new model for the dynamic compressive behaviour of PC.

k	w	λ	n	μ	C_1
0.006241	45.82	2.137	0.6523	0.1605	-3.164
C_2	α	K_1 (MPa)	K_2 (MPa)	m	a
-0.4483	163.2	71.47	29.5	0.1956	644.6

The comparison between the experimental results at high strain rate and the predicted results of the new constitutive model is presented in Figure 3.8, which shows a good agreement between them. As given in Figure 3.8(b) and (d), the values of R^2 reach 0.9671 and 0.9743, respectively, when the new model is used to predict the true stress

– strain relations at different high strain rates and different temperatures. This indicates the new model is able to provide a good prediction accuracy of the dynamic compressive behaviour of PC material.

It is noted that the material parameters identified for tensile/compressive behaviour of PC at high strain rate and low strain rate conditions are totally different. For example, in Section 3.3.2.1, the parameters were identified for tensile behaviours of PC based on the testing results at low strain rate conditions. However, another different set of parameters should be determined to predict the dynamic tensile behaviours of PC, and these parameter values were obtained upon the testing results at extremely high strain rate conditions. This means the quasi-static and dynamic deformation behaviours should be treated as two separate systems and their corresponding model parameters should be derived individually. The reason is that under different testing conditions, the material responses to quasi-static and dynamic loadings are different due to the strain rate effect, although the testing results come from the same published work. As a phenomenological model, the new constitutive model can be used to describe the trend of flow stress, but it has limitations to reflect the material responses to largely different loading conditions. A possible solution may be to add a functional term to describe the relationship and fill the gap between the low, moderate, and high behaviours. This would be a possible direction for the improvement of the new constitutive model.

3.4 Comparison with other constitutive models

By evaluating the above tensile and compressive behaviours of both PEEK (semi-crystalline thermoplastic) and PC (glassy thermoplastic), the tensile results of PEEK are found to be the behaviour more difficult to predict, as PEEK-like semi-crystalline thermoplastics show strain crystallization, which makes their mechanical behaviour

more complicated. Therefore, the ability to predict this behaviour gives a clear indication of the effectiveness and precision of a constitutive model. In this section, the experimental tensile test results of PEEK material by Joseph [136] are used to carry out the comparison among the new model with other phenomenological constitutive models including Johnson-Cook, Nasraoui et al. and DSGZ models. In addition, the compressive behaviour of PC material at low, moderate and high strain rates from the study of Mulliken and Boyce [97] is used to make the comparison between the new model and physically based Mulliken-Boyce model.

3.4.1 Prediction of Johnson-Cook model

The determination of the material parameters in Johnson-Cook model is presented in detail in the original paper of Johnson and Cook [101]. As shown in Equation (2.18), the material parameters in this model for the tensile behaviour of PEEK were calculated and given in Table 3.7. For the identified parameters, the reference temperature is 296 K, and the reference strain rate is 4.96×10^{-4} s^{-1}. The melting temperature of PEEK used in Johnson-Cook model is 616 K.

Table 3.7 Material parameters of Johnson-Cook model for the tensile behaviour of PEEK.

A (MPa)	B (MPa)	n	C	m
110.7	661.6	3.042	0.02168	0.9558

The comparison between experimental data for tensile tests of PEEK material and the predicted results of Johnson-Cook model is shown in Figure 3.9. As Johnson-Cook model can only be used to describe the part of plastic deformation, the prediction of elastic deformation is not included in the current research. Thus, all the prediction curves start from the peak points. As shown in Figure 3.9(a) and (c), the overall trend of the

prediction curves is upward, which means the flow stress increases with the increase of strain. This indicates that Johnson-Cook model can describe the strain hardening behaviour. In addition, Johnson-Cook model works well with the effect of strain rate on the flow stress at constant temperature (as shown in Figure 3.9(a)) and the effect of temperature on the flow stress at constant strain rate (as shown in Figure 3.9(c)). However, the shapes of prediction curves at different conditions are different from that of experimental curves and the value of R^2 is quite low. In addition, the strain softening behaviour cannot be observed. This is the main reason for the poor precision of Johnson-Cook model in the current case.

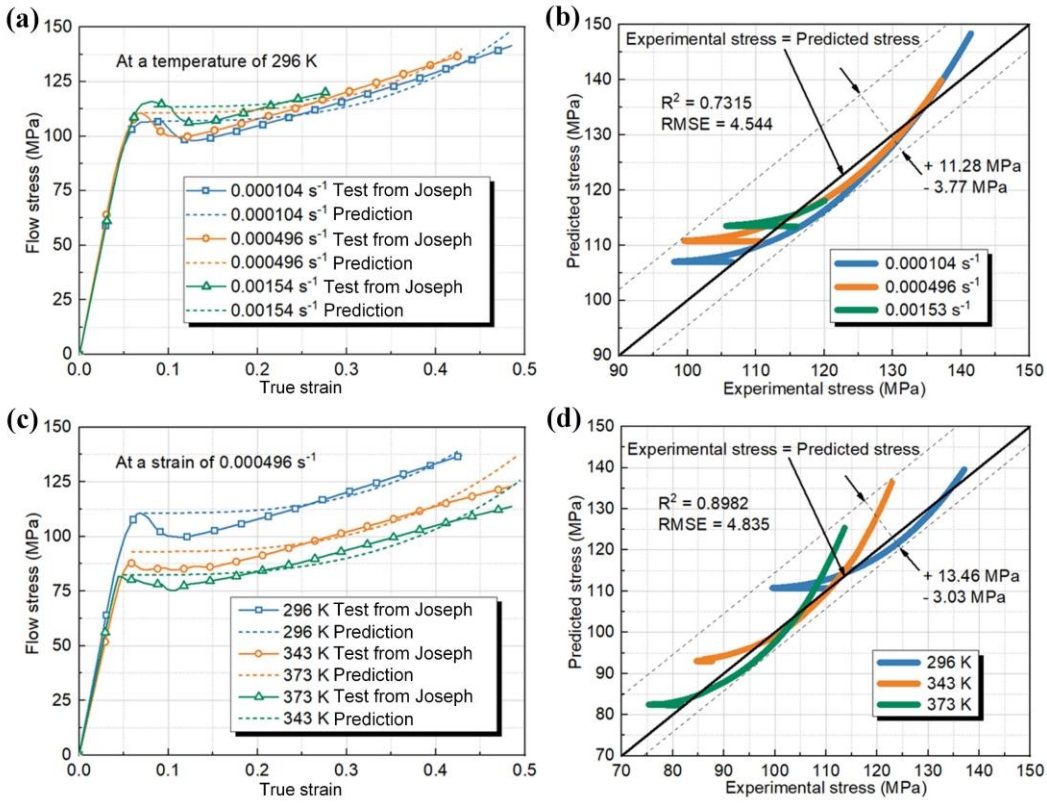


Figure 3.9 Comparison between experimental data for tensile tests of PEEK material from Joseph [136] and predicted results of Johnson-Cook model (a) and (b) at constant temperature of 296 K and (c) and (d) at constant strain rate of 4.96×10^{-4} s^{-1}.

3.4.2 Prediction of Nasraoui et al. model

In the research of Nasraoui et al. [93], the determination of materials parameters in Nasraoui et al. constitutive model is presented in details. As given in Equation (2.19), the material parameters in Nasraoui et al. model for the tensile behaviour of PEEK were obtained following their method and are shown in Table 3.8. The reference temperature and strain rate were selected as 296 K and 4.96×10^{-4} s^{-1}, respectively. It is noteworthy that to achieve better prediction, the glass transition temperature used in Nasraoui et al. model is replaced by the melting temperature of PEEK, which is 616 K.

Table 3.8 Material parameters of Nasraoui et al. model for the tensile behaviour of PEEK.

w	b	h_0	h_1	m_1	m_2	σ_1	σ_2
1.743	1.451	-125.9	-34.23	0.05509	0.02068	915.4	1861

As shown in Figure 3.10, for the tensile behaviour of PEEK material, the prediction curves of Nasraoui et al. model are able to show the basic trend of the flow stress and capture the yield behaviour, strain softening behaviour and strain hardening behaviour with the increase of the strain. However, the predicted results cannot follow the trend very well and there are obvious differences between the prediction and the experimental data. As shown in Figure 3.10(a), at constant temperature, with the increase of strain rate, the flow stress is increased as well, which is identical to the experimental observation. Meanwhile, as shown in Figure 3.10(c), at constant strain rate, with the increase of temperature, the flow stress is reduced conversely. The trend is also the same as the experimental results. However, the difference between two prediction curves is bigger than that between two experimental curves, as shown in both Figure 3.10(a) and (c), indicating an overestimation of the effect of the strain rate and temperature as given by Nasraoui et al. model. This leads to an observation that Nasraoui et al. model is able

to predict the general trend of the strain softening and hardening behaviours but, at the same time, it exhibits considerable deviations from the measured flow stress curves in the case of tensile behaviour of PEEK material.

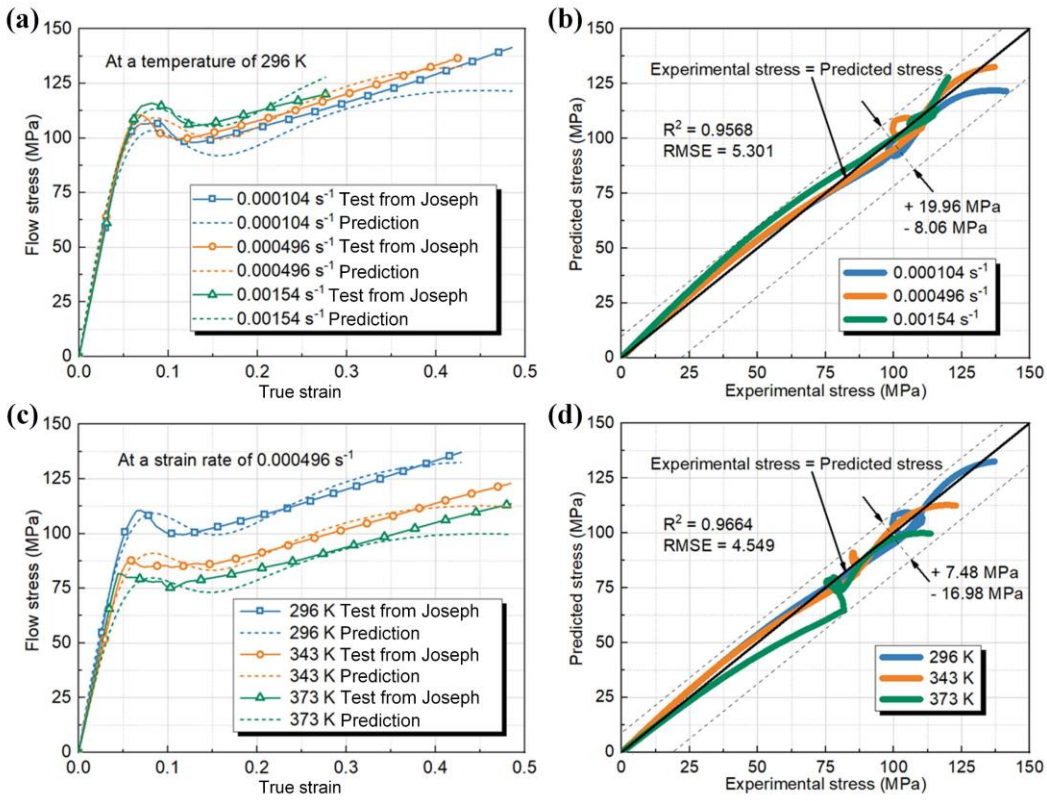


Figure 3.10 Comparison between experimental data for tensile tests of PEEK material from Joseph [136] and predicted results of Nasraoui et al. model (a) and (b) at constant temperature of 296 K and (c) and (d) at constant strain rate of 4.96×10^{-4} s^{-1}.

3.4.3 Prediction of DSGZ model

The determination of materials parameters in DSGZ model can be found in the original paper of Duan et al [102]. Following the same procedure, the material parameters in DSGZ model, as given in Equations (2.20) − (2.22), for the tensile behaviour of PEEK were derived as shown in Table 3.9.

Table 3.9 Material parameters of DSGZ model for the tensile behaviour of PEEK.

C_1	C_2	C_3	C_4	m	a	K	α

11.0733	0.5325	0.0296	743.1	0.0199	354.589	75.144	15.82

The comparison between the predictions of DSGZ model and the experimental data for the tensile test of PEEK material is given in Figure 3.11. At strains smaller than 0.05 and larger than 0.2, the predictions and experiments show good agreement. This means DSGZ model is able to describe the linear elastic deformation at small strains and the strain hardening behaviour at large strain with good precision. However, the shifting behaviour at the peak point and the strain softening behaviour after the peak point are not observed in the predicted results, which means DSGZ model is not sufficiently equipped to characterize the overall trend of the tensile behaviour of PEEK material, although it can be used to predict the compressive behaviour of PMMA and PC materials in the research of Duan et al. [102]. In terms of the effect of strain rate and temperature, although the effect of strain rate on the value of flow stress in DSGZ model is slightly different from the experimental data, the predicted results show a good trend to the hardening (strain rate) or softening (temperature) effect on the flow stress, especially the effect of temperature on it, as shown in Figure 3.11(c). Therefore, the results indicate a fewer degree of precision in using DSGZ model to predict the tensile behaviour of PEEK material, mainly because of the difficulty to capture the behaviour of strain softening behaviour after yielding.

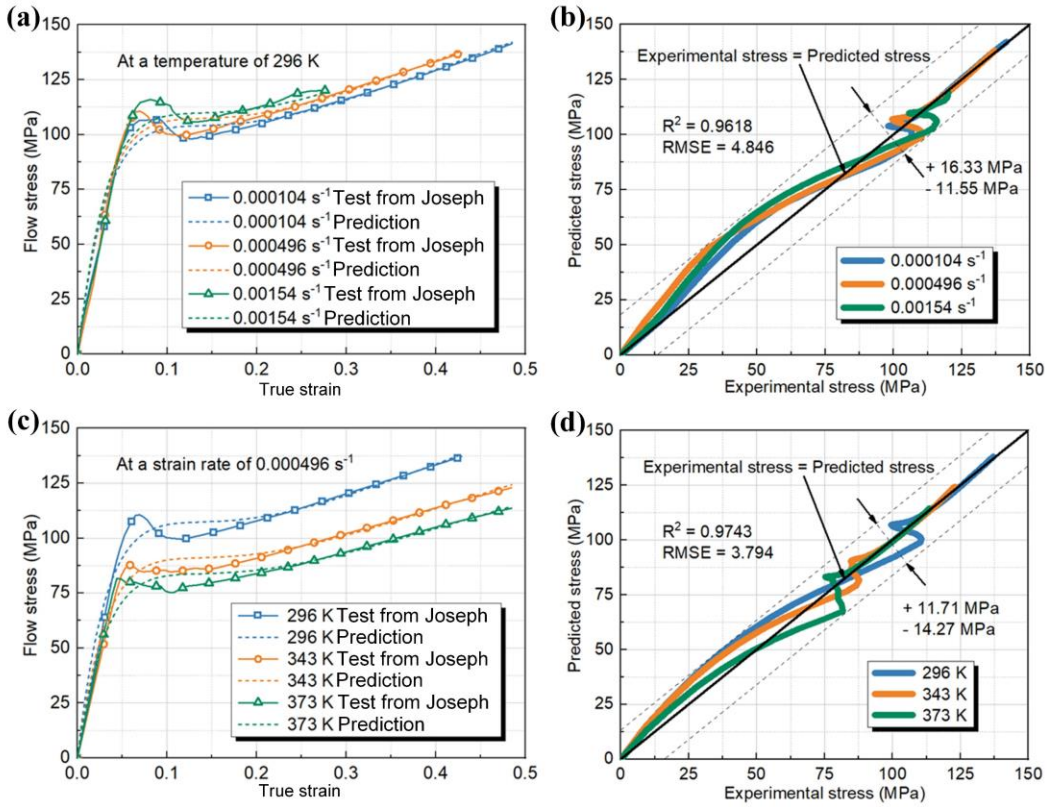


Figure 3.11 Comparison between experimental data for tensile tests of PEEK material from Joseph [136] and predicted results of DSGZ model (a) and (b) at constant temperature of 296 K and (c) and (d) at constant strain rate of 4.96×10^{-4} s^{-1}.

3.4.4 Comparison and quantitative evaluation of studied phenomenological constitutive models

To compare the prediction results of Johnson-Cook, Nasraoui et al., DSGZ and the new model developed in this paper, the tensile flow stress-true strain curves of PEEK material at specific temperature and strain rate conditions were shown in Figure 3.12. The experimental flow stress is given as black dots. The blue, green, purple and red lines represent the flow stress-strain curves predicted by Johnson-Cook, Nasraoui et al., DSGZ and the new models, respectively. As observed, Johnson-Cook model shows a poor precision at all the five conditions and can only predict the effect of temperature and strain rate. Although in recent years, some researchers have used Johnson-Cook model and its modified model to predict the mechanical behaviour of thermoplastics,

lack of precision in prediction seems to be inevitable because it was originally proposed for metals but not polymers. As shown in Figure 3.12(c), Nasraoui et al. model provides reasonable prediction in the condition of 296 K and 1.54×10^{-3} s^{-1} but less so in other cases. DSGZ model is only able to predict the section with strain hardening at large strains in all conditions but less capable of capturing the strain softening trend in all test conditions including the two at elevated temperatures of 343 K and 373 K. On the other hand, different from the above-mentioned four models, the predicted results of the new model show a good agreement with experimental results at all temperature and strain rate conditions. Therefore, the new model provides the best predicted results among the four constitutive models considered.

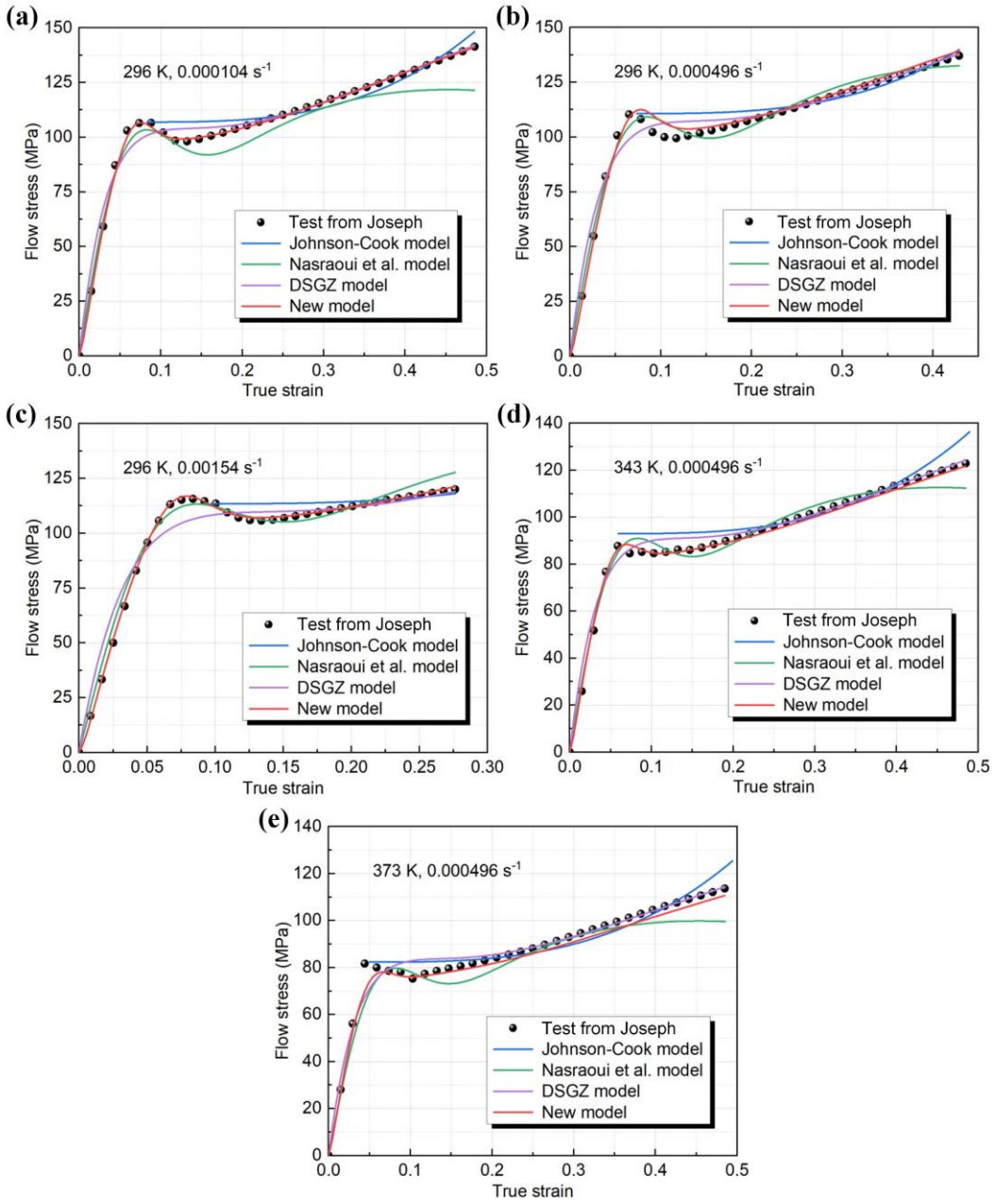


Figure 3.12 Comparison of predicted results provided by Johnson-Cook, Nasraoui et al., DSGZ and the new model in the conditions of (a) 296 K and 1.04×10^{-4} s^{-1}, (b) 296 K and 4.96×10^{-4} s^{-1}, (c) 296 K and 1.54×10^{-3} s^{-1}, (d) 343 K and 4.96×10^{-4} s^{-1} and (e) 373 K and 4.96×10^{-4} s^{-1}.

A quantitative evaluation of the prediction precision between Johnson-Cook, Nasraoui et al., DSGZ models and the new model was carried out and the results are presented in Tables 3.10 and 3.11 by using the R^2 and $RMSE$ values.

Table 3.10 A comparison of Johnson-Cook, Nasraoui et al., DSGZ and the new model at different strain rates and a constant temperature of 296 K.

Strain rate		**1.04×10^{-4} s^{-1}**				**4.96×10^{-4} s^{-1}**				**1.54×10^{-3} s^{-1}**		
Model	**Johnson-Cook**	**Nasraoui et al.**	**DSGZ**	**New model**	**Johnson-Cook**	**Nasraoui et al.**	**DSGZ**	**New model**	**Johnson-Cook**	**Nasraoui et al.**	**DSGZ**	**New model**
R^2	0.7732	0.9436	0.9649	0.9956	0.6534	0.9789	0.9534	0.9756	-0.06603	0.9882	0.9604	0.9986
***RMSE* (MPa)**	6.044	6.488	5.12	1.818	6.761	4.126	6.134	4.442	4.719	3.046	5.58	1.195

Table 3.11 A comparison of Johnson-Cook, Nasraoui et al., DSGZ and the new model at different temperatures and a constant strain rate of 4.96×10^{-4} s^{-1}.

Temperature		**296 K**				**343 K**				**373 K**		
Model	**Johnson-Cook**	**Nasraoui et al.**	**DSGZ**	**New model**	**Johnson-Cook**	**Nasraoui et al.**	**DSGZ**	**New model**	**Johnson-Cook**	**Nasraoui et al.**	**DSGZ**	**New model**
R^2	0.6534	0.9789	0.9534	0.9756	0.699	0.9717	0.971	0.9935	0.827	0.8704	0.9125	0.979
***RMSE* (MPa)**	6.761	4.126	6.134	4.442	6.742	4.072	4.127	1.947	4.65	7.757	6.373	3.123

As observed in Tables 3.10 and 3.11, at all strain rate and temperature conditions, the values of R^2 and $RMSE$ of the new constitutive model produced the best performance results as compared to Johnson-Cook, Nasraoui et al. and DSGZ models. This indicates that the prediction precision of the new model is the best among the four constitutive models and the new constitutive model developed in the current research is able to predict the tensile behaviour of PEEK materials used with good precision. First, the general shape of the prediction curves provided by the new model shows a better agreement with the experimental results among these four constitutive models. It can capture different phases of the flow stress curve including the linear elastic, non-linear elastic, the yield behaviour, strain softening and strain hardening behaviours. This is fundamental to the prediction accuracy of the material constitutive model. Moreover, the effect of strain rate and temperature on the flow stress can be well represented by using the new model, as compared to the other three constitutive models. It clearly shows the trend of the flow stress increase with increased strain rate and reduced temperature. Although there is slight inaccuracy such as the effect of strain rate on the value of flow stress, the new model presents a more precise and consistent prediction of the tensile behaviour of PEEK material as compared with other three commonly used constitutive phenomenological models. Compared with other phenomenological constitutive models, the new model has better flexibility to predict the complicated stress – strain curves because of the use of piecewise and transition functions. Piecewise functions show advantages for flow stress prediction in different strain ranges while transition functions work effectively to enable smooth and flexible shift between piecewise functions. The combination of the piecewise and transition functions is the key for the more accurate flow stress prediction than other phenomenological models.

3.4.5 Comparison with Mulliken-Boyce model

The compressive testing results of PC material from the study of Mulliken and Boyce [97] are used to make the comparison between physically based Mulliken-Boyce model and the new model. As there are no testing results and validations in a variety of temperatures, only compressive behaviour at different strain rates (10^{-3} s^{-1}, 1 s^{-1} and 5050 s^{-1}) are used in the current comparison. The testing curves and predicted results of Mulliken-Boyce model are shown in Figure 3.13(a). The material parameters of the new model were identified as given in Table 3.12 with the selection of reference strain rate of 1 s^{-1} and the predicted results of the new model are presented in Figure 3.13(a). It should be noted that the parameter a is inapplicable as the effect of temperature is not included in the comparison.

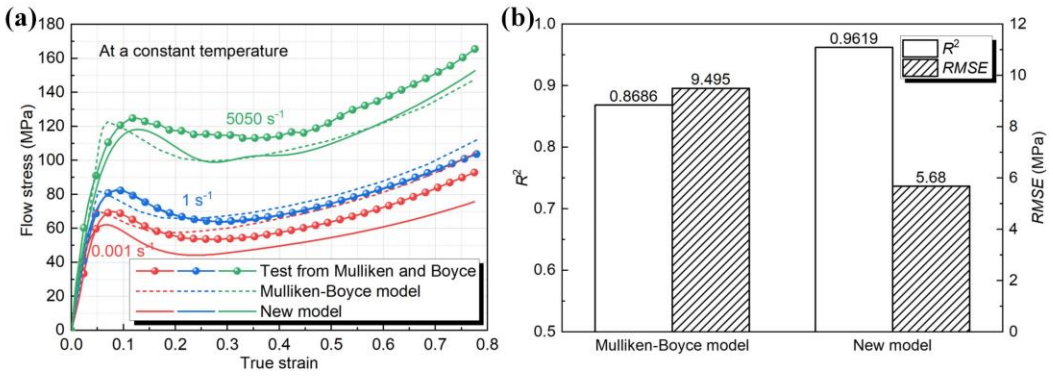


Figure 3.13 Comparison between Mulliken-Boyce and the new models. (a) Experimental data for compressive tests of PC material at constant temperature from Mulliken and Boyce [97] and predicted results and (b) calculated R^2 and $RMSE$.

Table 3.12 Material parameters of the new model for the compressive behaviour of PC tested by Mulliken and Boyce.

k	w	λ	n	μ	C_1
0.2599	23.11	4.855	0.9906	0.08601	-1.777
C_2	α	K_1 (MPa)	K_2 (MPa)	m	a
-0.267	146.8	2470	20.57	0.04542	–

As observed from Figure 3.13(a), both Mulliken-Boyce and the new models are able to predict the general trend of the compressive behaviour from low to high strain rates. However, the non-linear transition from the elastic phase to the yielding is not presented by Mulliken-Boyce model and the yield behaviour shows a sudden change [97]. Although the values of peak stress are predicted effectively, there are some differences from the experimental results in other parts of compressive curves. For the new model, the smooth transition to the yielding can be presented and the predicted curve at the strain rate of 1 s^{-1} fits the experimental curve perfectly, but the predicted results at strain rates of 10^{-3} s^{-1} and 5050 s^{-1} don't present a good agreement with the experimental ones. This happens because the new model has its limitation in representing the material responses to exceedingly different loading conditions as discussed in Section 3.3.3. In the current comparison, an extremely large range of strain rates from 10^{-3} s^{-1} to 5050 s^{-1} are used. Nevertheless, the new model presents a better prediction than Mulliken-Boyce model. As shown in Figure 3.13(b), a R^2 value of 0.9619 is achieved by the new model, while it is 0.8686 by Mulliken-Boyce model. In addition, the predicted results of the new model have a smaller $RMSE$ value as compared with that of Mulliken-Boyce model.

3.5 Conclusions

The main conclusions of this chapter can be drawn as follows:

(1) An effective method to construct a constitutive model is to use different mathematical functions to predict different phases of mechanical behaviours and to combine them with a new functional term. In the new constitutive model (ZOP model) proposed from this research, the deformation at small and large strains are expressed by

different functions. A new transition function is used to enable a smooth transition of the flow stress behaviours under both small and large strain conditions.

(2) The new model can be used to effectively represent different phases of mechanical behaviour of thermoplastics including the linear elastic and non-linear elastic deformation, the yield behaviour, strain softening and strain hardening behaviours. The effect of strain rate and temperature can be included in the new model.

(3) The new constitutive model can be used to predict both the tensile and the compressive behaviour of PEEK (semi-crystalline thermoplastic) and PC (glassy thermoplastic) with a good level of accuracy although the general trends of the two materials are different.

(4) Apart from low strain rate conditions, the new model is capable of predicting the dynamic tensile and compressive behaviours of PC at high strain rate conditions if the dynamic behaviours are treated as a separate system from the low strain rate conditions.

(5) Results show that better prediction and goodness of fit results of the tensile behaviour of PEEK material can be achieved as compared to that by Johnson-Cook, Nasraoui et al. and DSGZ models. Better precision is demonstrated by using the new model than that of Mulliken-Boyce model in the prediction of compressive behaviour of PC material from low to high strain rates.

Chapter 4 A New Analytical Model for Force Prediction in Incremental Sheet Forming

Nomenclature

Symbol	Term	Unit
r	Distance from studied position to tool centre	mm
φ	Angle from studied position to tool axis	rad
θ	Angle from workpiece meridional cross-section to studied position	rad
x, y, z	Coordinate of tool position in x, y, and z axes	mm
r_{tool}	Tool radius	mm
t_0	Initial sheet thickness	mm
Δz	Step size	mm
Ψ	Designed drawing angle	rad
α	Actual drawing angle	rad
α_{b}	Actual drawing angle at corner of pyramid part	rad
β, λ	Indentation angle in workpiece meridional and circumferential directions	rad
β_{b}	β angle at corner of pyramid part	rad
μ	Elastic recovery angle	rad

β_1	Angle induced by forming tool increment in workpiece meridional direction	rad
β_{1b}	β_1 angle at corner of pyramid part	rad
t	Thickness of sheet material below forming tool at different regions	mm
Δt	Sheet thickness reduction at different regions after contact	mm
t_b	Thickness in workpiece meridional direction at corner of pyramid part	mm
Δt_{er}	Maximum instant thickness recovery	mm
t_c	Sheet thickness below tool centre	mm
$\bar{\sigma}_c$	Mean equivalent stress of sheet material below tool centre	MPa
$\bar{\varepsilon}_c$	Mean equivalent strain of sheet material below tool centre	
w_{er}	Maximum width of elastic recovery region	mm
t_A, t_B	Thickness of sheet material in Parts A and B	mm
φ_p	φ angle of projection position on workpiece meridional cross-section	rad
t_p	Thickness of projection position on workpiece meridional cross-section	mm

ω	Arc angle from studied position to projection position on workpiece circumferential cross-section	rad
ρ_{d}, ρ_{er}	Thickness reduction rate of deformation and elastic recovery regions	mm
E	Young's modulus of sheet material	MPa
n	Strain hardening exponent of sheet material	
R_{b}, R_0, R	Distance from part centre/ symmetry axis to edge of backing plate, initial tool position and studied tool position	mm
r_{bending}	Global bending radius	mm
h	Depth of tool position	mm
$\varepsilon_{\mathrm{stretching}}$	Stretching strain of the neutral surface	
$\varepsilon_{\mathrm{bending}}$	Bending strain of sheet material	
ε_{φ}, ε_{θ}, ε_{r}	Strain in tool meridional, circumferential and radial directions	
$\bar{\sigma}$	Equivalent stress of sheet material	MPa
$\bar{\varepsilon}$	Equivalent strain of sheet material	
F, F_{v}, F_{h}, F_{r}, F_{t}	Total, vertical, horizontal, radial, and tangential forces	N

F_{ls}	Localised shear force	N
P1, P2	Boundaries of overlapping deformation region in plane strain condition	
P3	Boundary of non-overlapping deformation region in plane strain condition	
P4, P5	Boundaries of elastic recovery region in plane strain condition	
$F_{\mathrm{ls}}^{\mathrm{P1}}$, $F_{\mathrm{ls}}^{\mathrm{P2}}$, $F_{\mathrm{ls}}^{\mathrm{P3}}$, $F_{\mathrm{ls}}^{\mathrm{P4}}$, $F_{\mathrm{ls}}^{\mathrm{P5}}$	Localised shear force of P1, P2, P3, P4 and P5	N
Q1	Boundary of corner deformation region in biaxial tension condition	
Q2	Boundary of overlapping deformation region in biaxial tension condition	
Q3, Q4	Boundaries of elastic recovery region in biaxial tension condition	
$F_{\mathrm{ls}}^{\mathrm{Q1}}$, $F_{\mathrm{ls}}^{\mathrm{Q2}}$, $F_{\mathrm{ls}}^{\mathrm{Q3}}$, $F_{\mathrm{ls}}^{\mathrm{Q4}}$	Localised shear force of Q1, Q2, Q3 and Q4	N
$F_{\mathrm{v}}^{\mathrm{ls}}$	Vertical component of localised shear force	N
$F_{\mathrm{v}}^{\mathrm{ed}}$	Vertical force from global elastic bending	N
$F_{\mathrm{t}}^{\mathrm{ls}}$	Tangential component of localised shear force	N

$F_{\mathrm{t}}^{\mathrm{mt}}$	Tangential force leading to material thinning	N
$F_{\mathrm{t}}^{\mathrm{f}}$	Frictional force in tangential direction	N
F_{x}, F_{y}	Force along x and y axes	N
f	Frictional coefficient between forming tool and sheet	
σ_{s}	Yield stress of sheet material at different regions	MPa
ε_{s}	Yield strain of sheet material at different regions	
τ	Shear stress of sheet material	MPa
γ	Elastic deflection	mm
D	Flexural rigidity of sheet material	N·mm
ν	Poisson's ratio of sheet material	
$\bar{\varepsilon}_{\mathrm{ed}}$	Equivalent strain due to elastic bending of deflection	
$r_{\mathrm{bending}}^{\mathrm{critical}}$	Critical bending radius of maximum deflection	mm
h_{critical}	Critical depth of tool position for maximum deflection	mm

4.1 Introduction

In ISF, the forming force can reflect the tool-sheet contact, which drives the material deformation and the fracture occurrence. Traditionally, FE simulation is used to predict

the forming force in ISF, but the prediction result is usually sensitive to model settings, such as mesh density, time increment, and it often takes large amount of computing time. Differently, the analytical model provides an effective and efficient method to predict the forming force in ISF. By looking into the intrinsic relationship among ISF parameters, material deformation, stress and strain states, it can also help to reveal the deformation behaviour under the effect of tool-sheet interaction.

This section presents a new modelling strategy for force history prediction by looking into the material deformation in ISF. The modelling of contact region, thickness distribution and strain components are carried out as the basis for the prediction of vertical and horizontal forces. The effect of local contact behaviour, material deformation and stretching, as well as the less investigated behaviours of global elastic bending, change of deformation mode and contact condition change are considered in the derivation. The force prediction model at both plane strain and biaxial tension condition area is developed based on the differences in contact region and thickness distribution between these two different deformation states. Experimental validations are conducted to test the prediction results of the analytical model as well as comparison with other representative models. The developed model could help to reveal and understand the complicated and instable deformation behaviour from both local and global aspects.

4.2 Analytical model of forming force

4.2.1 Contact region

In ISF, larger contact area between forming tool and sheet material could contribute to larger forming force, while losing contact usually leads to smaller force. The first step of modelling is to identify the contact region. The similarity between ISF and milling

processes is that both obtain the final part through accumulation of localised deformation or cutting following a predefined tool path. The major difference is that the localised material under milling is subjected to cutting, while the localised sheet material undergoes plastic deformation in ISF followed by some elastic deformation. The ISF of rigid plastic materials may have the same contact region to the end milling process with a ball nose tool. As shown in Figure 4.1, Boolean operation is used to subtract a ball tool from parts with truncated cone and pyramid shapes. The blue area shows the cutting region in end milling process using a ball nose tool, which is the same as the contact region in ISF of materials only with rigid plastic deformation. However, the elastic deformation before full tool-sheet contact and the recovery after deformation should be considered in real ISF situation. A shrink of the front contact region and an expansion of the rear contact region may be applied, as shown by the white lines in Figure 4.1. The above analysis is the basis for the modelling of contact region in ISF.

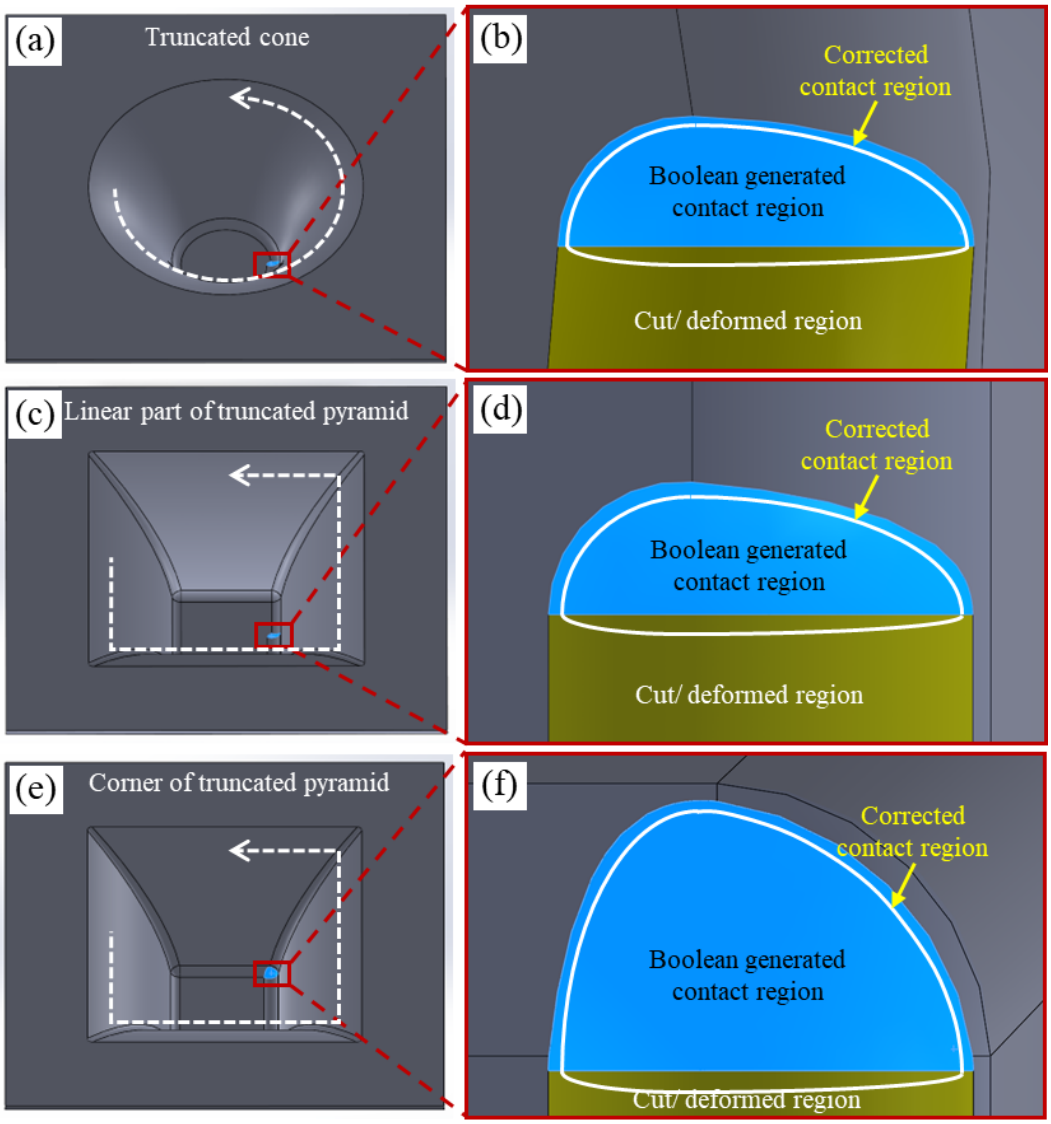


Figure 4.1 Boolean subtraction of a ball tool from (a), (b) truncated cone shape, (c), (d) linear part and (e), (f) corner of truncated pyramid shape.

Before analytical modelling, some assumptions are made below:

(1) The scallop height is neglected as it is relatively small compared to the sheet thickness.

(2) The thickness of localised contact region is assumed linearly distributed in the workpiece meridional and circumferential directions.

Under ISF condition, a localised 3D coordinate system is proposed with the origin at the tool centre. For a certain position or small element in the contact region, the coordinate

can be expressed as (r, φ, θ) as shown in Figure 4.2, where r is the distance from the studied position to the tool centre, φ is the angle between the position and the tool axis, and θ is the angle from the workpiece meridional cross-section to the position. r_{tool} is the tool radius, t_0 is the initial sheet thickness, α is the drawing angle, β and λ are the indentation angles in the workpiece meridional and circumferential directions, respectively, μ is the elastic recovery angle behind the tool resulting from the instant recovery after elastoplastic deformation, and β_1 is the angle induced by the increment of forming tool in workpiece meridional direction. The partition of Parts A and B is for the convenience of thickness derivation on workpiece meridional cross-section, and Parts A and B are at inner and outer sides of the tool, respectively.

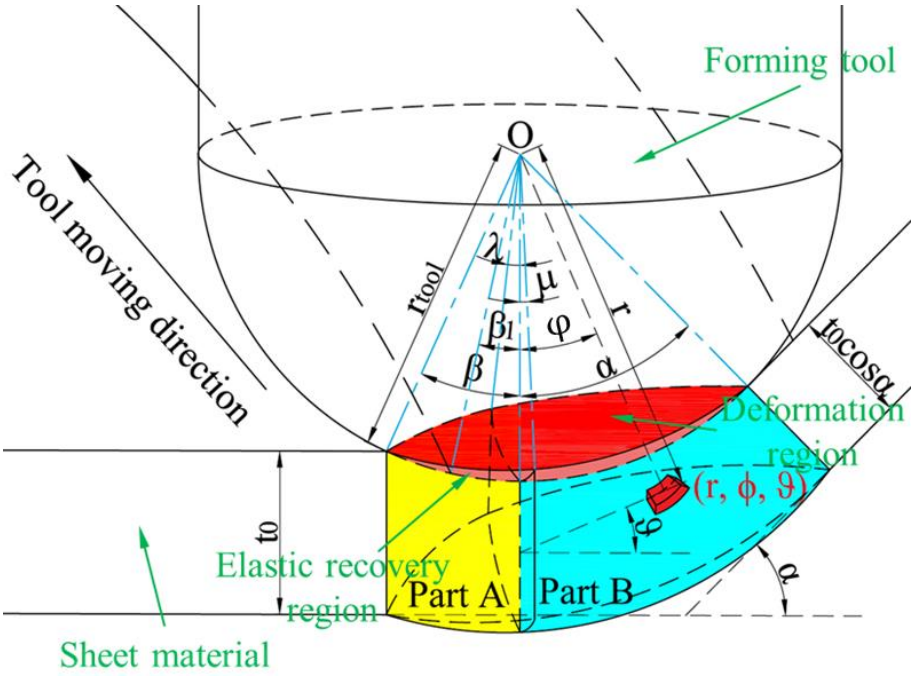


Figure 4.2 Illustration of contact region in ISF and the coordinate system.

As indicated by Park and Kim [137] and Martins et al. [138], the common state of ISF formed part is under plane strain condition. In this condition, the contact region may be comprised of three parts: non-overlapping deformation (ND), overlapping deformation (OD) and elastic recovery (ER) regions with a top view shown in Figure 4.3(a), which

can be seen as the combination of a part of a circular region and parts of three elliptical regions. The ND region covers the area where the sheet material is newly deformed under the tool, and P3 in Figure 4.3(a) is the border line of this region. The OD region defines the material that has already undergone at least one deformation cycle before this round of tool contact, and the border line is composed of P1 and P2. ER region represents the area where the sheet material undergoes the instant elastic recovery after deformation, and Parts A and B of the ER region have the boundaries as P4 and P5, respectively, as given in Figure 4.3(a). The definition of different regions is critical to the analytical modelling, as they are the key to derivation of the localised shear force, which may drive the material to move downwards.

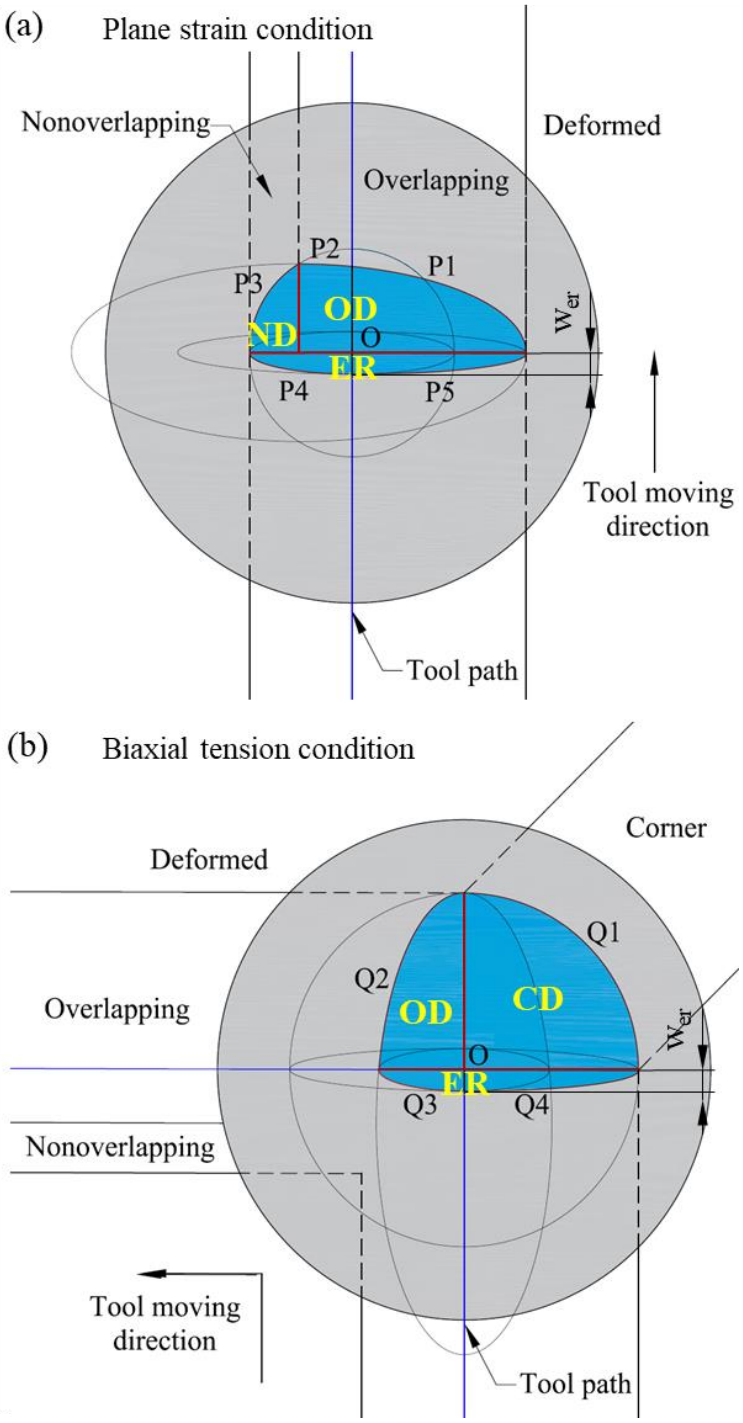


Figure 4.3 Illustration of contact region from top view in (a) plane strain condition area and (b) biaxial tension condition area at corner of ISF.

For the elliptical shape of OD region, the centre is located at (r_{tool}, β_1, π), the lengths of major and minor axes are ($r_{\text{tool}} \cdot \sin\alpha + r_{\text{tool}} \cdot \sin\beta_1$) and ($(r_{\text{tool}} \cdot \sin\beta)^2 - (r_{\text{tool}} \cdot \sin\beta_1)^2$), respectively. The expression of the ellipse can be written as following:

$$\frac{(\sin\varphi\cdot\cos\theta+\sin\beta_1)^2}{(\sin\alpha+\sin\beta_1)^2}+\frac{(\sin\varphi\cdot\sin\theta)^2}{(\sin\beta)^2-(\sin\beta_1)^2}=1 \tag{4.1}$$

where the relationship between β and β_1 can be given.

If the step size $\Delta z \le r_{\text{tool}}\cdot\sin\beta\cdot\tan\alpha$,

$$\beta_1=\arcsin\left(\sin\beta-\frac{\Delta z}{r_{\text{tool}}\cdot\tan\alpha}\right) \tag{4.2}$$

and if $\Delta z \ge r_{\text{tool}}\cdot\sin\beta\cdot\tan\alpha$,

$$\beta_1=\arcsin\left(\frac{\Delta z}{r_{\text{tool}}\cdot\tan\alpha}-\sin\beta\right) \tag{4.3}$$

The situation of $\Delta z \ge r_{\text{tool}}\cdot\sin\beta\cdot\tan\alpha$ leads to too small or even no overlapping region, which is uncommon in ISF design and would cause poor surface finish. Therefore, β_1 is calculated as Equation (4.2) throughout the modelling.

For the circular shape of ND region, the radius is $(r_{\text{tool}}\cdot\sin\beta)$. The contact boundary of this region can be expressed as following:

$$\varphi=\beta \tag{4.4}$$

Part A of ER region also has an elliptical shape with the tool tip as the centre and $(r_{\text{tool}}\cdot\sin\alpha+r_{\text{tool}}\cdot\sin\beta_1)$ as the length of long axis. The length of short axis can be calculated with consideration of the elastic recovery of the sheet thickness after deformation. The recovery Δt_{er} at the maximum elastic recovery position may be calculated with the following equation by considering the elastic strain recovery:

$$\Delta t_{\text{er}}=\left[\exp\left(\frac{1}{2}\cdot\frac{\bar{\sigma}_{\text{c}}}{E}\right)-1\right]\cdot(t_0-t_{\text{c}}) \tag{4.5}$$

where E is the Young's modulus, t_{c} and $\bar{\sigma}_{\text{c}}$ are the thickness and the mean equivalent stress of the sheet material below the tool centre position. The calculation methods for t_{c} and $\bar{\sigma}_{\text{c}}$ are given in Sections 4.2.2 and 4.2.4, respectively.

The maximum width of the ER region w_{er}, i.e., the length of short axis as shown in Figure 4.3, is given as the following expression:

$$w_{\mathrm{er}} = \sqrt{{r_{\mathrm{tool}}}^2 - (r_{\mathrm{tool}} - \Delta t_{\mathrm{er}})^2} \tag{4.6}$$

As a result, the boundary of the Part A is expressed as following:

$$\frac{(\sin\varphi\cdot\cos\theta)^2}{(\sin\beta)^2} + \frac{(r_{\mathrm{tool}}\cdot\sin\varphi\cdot\sin\theta)^2}{{w_{\mathrm{er}}}^2} = 1 \tag{4.7}$$

For Part B of ER region, expression of the boundary may be given similarly by the following expression:

$$\frac{(\sin\varphi\cdot\cos\theta)^2}{(\sin\alpha)^2} + \frac{(r_{\mathrm{tool}}\cdot\sin\varphi\cdot\sin\theta)^2}{{w_{\mathrm{er}}}^2} = 1 \tag{4.8}$$

4.2.2 Thickness distribution under tool-sheet contact

The thickness distribution on the workpiece meridional cross-section is firstly derived. According to the assumption of linear thickness distribution, the thickness along the workpiece meridional direction as shown in Figure 4.4(a) is linearly distributed from t_0 to $(t_0 \cdot \cos\alpha)$ following the cosine law [139]. So, the thickness t on the workpiece meridional cross-section at a proposed position with coordinates of $(r_{\mathrm{tool}}, \varphi, \theta)$ (on the workpiece meridional cross-section, $\theta = 0$ or $\theta = \pi$) can be expressed as the following equation:

$$t = t_0 - \frac{t_0\cdot(1-\cos\alpha)\cdot(\beta+\varphi\cdot\cos\theta)}{\alpha+\beta} \tag{4.9}$$

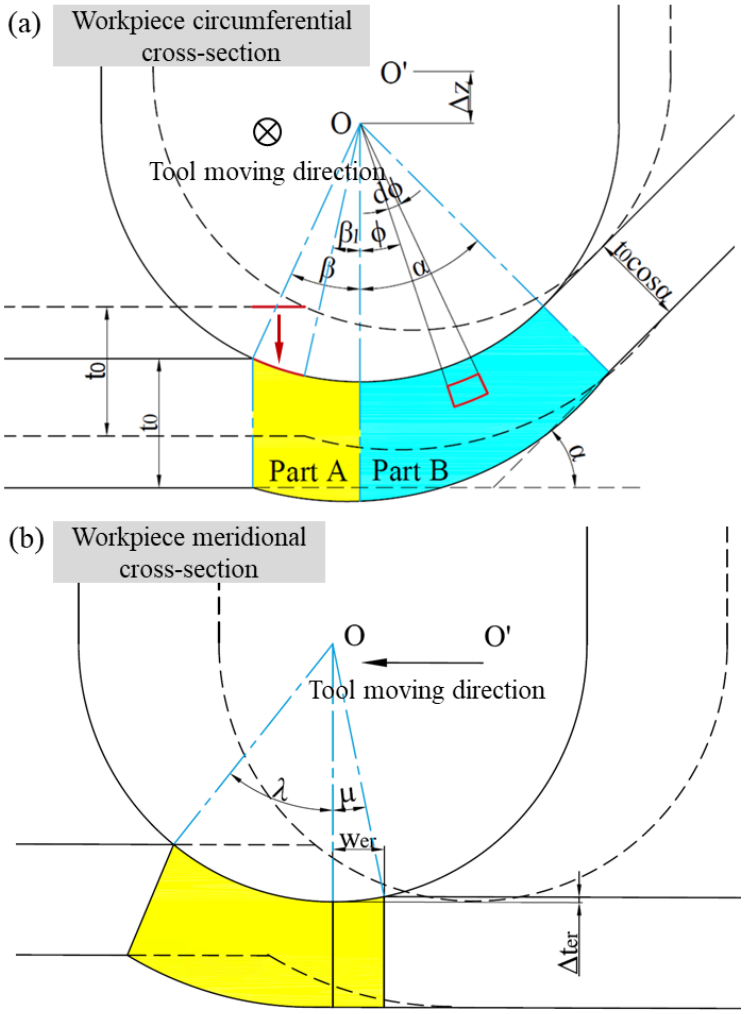


Figure 4.4 ISF illustration of (a) meridional and (b) circumferential cross-sections of workpiece.

On the cross-section of Parts A and B, Equation (4.9) can be written in the following formats:

$$t_{\mathrm{A}} = t_0 - \frac{t_0 \cdot (1-\cos\alpha) \cdot (\beta-\varphi)}{\alpha+\beta} \tag{4.10}$$

$$t_{\mathrm{B}} = t_0 - \frac{t_0 \cdot (1-\cos\alpha) \cdot (\beta+\varphi)}{\alpha+\beta} \tag{4.11}$$

The thickness at the tool centre position t_{c} can be calculated as following:

$$t_{\mathrm{c}} = t_0 - \frac{t_0 \cdot (1-\cos\alpha) \cdot \beta}{\alpha+\beta} \tag{4.12}$$

To derive the thickness distribution of the whole contact region, the 3D coordinate

system should be used. As mentioned above, for a proposed position on the top surface of the sheet, the spherical coordinates are $(r_{\mathrm{tool}}, \varphi, \theta)$.

If the selected position is in ND region, it must be in Part A. Through this position, the thickness along the circumferential direction would vary from t_0 at the position of $(r_{\mathrm{tool}}, \beta, \theta)$, to the thickness at the projection position on the workpiece meridional cross-section, the coordinates of which are supposed as $(r_{\mathrm{tool}}, \varphi_{\mathrm{p}}, \pi)$. The relationship between φ and φ_{p} can be expressed as following:

$$\varphi_{\mathrm{p}} = -\arcsin(\sin\varphi \cdot \cos\theta) \tag{4.13}$$

The thickness of the projection position $(r_{\mathrm{tool}}, \varphi_{\mathrm{p}}, \pi)$ can be obtained as below:

$$t_{\mathrm{p}} = t_0 - \frac{t_0 \cdot (1-\cos\alpha) \cdot [\beta + \arcsin(\sin\varphi \cdot \cos\theta)]}{\alpha+\beta} \tag{4.14}$$

According to the assumption, the thickness from $(r_{\mathrm{tool}}, \beta, \theta)$ to $(r_{\mathrm{tool}}, \varphi_{\mathrm{p}}, \pi)$ is linearly distributed along a circular arc, and the arc angle (ω) can be approximately expressed as following:

$$\omega = \frac{\sqrt{(r_{\mathrm{tool}}\cdot\beta)^2 - (r_{\mathrm{tool}}\cdot\beta_1)^2}}{\sqrt{{r_{\mathrm{tool}}}^2 - (r_{\mathrm{tool}}\cdot\sin\beta_1)^2}} = \frac{\sqrt{\beta^2 - {\beta_1}^2}}{\sqrt{1-(\sin\beta_1)^2}} \tag{4.15}$$

The thickness reduction rate ρ_{d} of ND region along workpiece circumferential direction may be calculated as following:

$$\rho_{\mathrm{d}} = \frac{t_0 - \left[t_0 - \frac{t_0\cdot(1-\cos\alpha)\cdot(\beta-\beta_1)}{\alpha+\beta}\right]}{\frac{\sqrt{\beta^2-{\beta_1}^2}}{\sqrt{1-(\sin\beta_1)^2}}} = \frac{t_0\cdot(1-\cos\alpha)\cdot(\beta-\beta_1)\cdot\sqrt{1-(\sin\beta_1)^2}}{(\alpha+\beta)\cdot\sqrt{\beta^2-{\beta_1}^2}} \tag{4.16}$$

As a result, the thickness at position $(r_{\mathrm{tool}}, \varphi, \theta)$ in ND region can be written as the expression below:

$$t = t_{\mathrm{p}} + \rho_{\mathrm{d}} \cdot \frac{r_{\mathrm{tool}} \cdot \varphi \cdot \sin\theta}{\sqrt{{r_{\mathrm{tool}}}^2 - (r_{\mathrm{tool}} \cdot \sin\varphi \cdot \cos\theta)^2}} \tag{4.17}$$

And the following expression can be obtained for the thickness distribution in ND region:

$$t = t_0 - \frac{t_0 \cdot (1-\cos\alpha)}{\alpha+\beta} \cdot \left[\beta + \arcsin(\sin\varphi \cdot \cos\theta) - \frac{(\beta-\beta_1) \cdot \sqrt{1-(\sin\beta_1)^2} \cdot \varphi \cdot \sin\theta}{\sqrt{{\beta^2-\beta_1}^2} \cdot \sqrt{1-(\sin\varphi \cdot \cos\theta)^2}} \right] \tag{4.18}$$

In OD region, the thickness increases from the projection position on the workpiece meridional cross-section along the circumferential direction with the same increase rate ρ_{d}. In Part A, the relationship between φ and φ_{p} is given as Equation (4.13), while in Part B, it can be calculated as following:

$$\varphi_{\mathrm{p}} = \arcsin(\sin\varphi \cdot \cos\theta) \tag{4.19}$$

Subsequently, no matter in Part A or B, the thickness of the projection position can be expressed as Equation (4.14) uniformly, and the thickness at position $(r_{\mathrm{tool}}, \varphi, \theta)$ in OD region is derived the same to Equation (4.18) in ND region.

In ER region, as the thickness increase Δt_{er} at the maximum elastic recovery position is given in Equation (4.5), combining the thickness expression t_{c} under the tool centre position in Equation (4.9), the increase rate ρ_{er} along the circular arc can be calculated using the following equation:

$$\rho_{\mathrm{er}} = \frac{\left[\exp\left(\frac{\sqrt{3}}{2} \cdot \frac{\sigma_{\mathrm{c}}}{E}\right) - 1\right] \cdot \frac{t_0 \cdot (1-\cos\alpha) \cdot \beta}{\alpha+\beta}}{\arccos\left\{1 - \left[\exp\left(\frac{\sqrt{3}}{2} \cdot \frac{\sigma_{\mathrm{c}}}{E}\right) - 1\right] \cdot \frac{t_0 \cdot (1-\cos\alpha) \cdot \beta}{r_{\mathrm{tool}} \cdot (\alpha+\beta)}\right\}} \tag{4.20}$$

For the proposed position $(r_{\mathrm{tool}}, \varphi, \theta)$, the φ_{p} coordinate of the projection position is derived as Equation (4.13) in Part A or Equation (4.19) in Part B of ER region. The thickness of the projection position is derived as Equation (4.14), the same as the ones in ND and OD regions. Therefore, in the workpiece circumferential direction, the

thickness in both Part A and B of ER region can be uniformly expressed as the below equation:

$$t = t_{\mathrm{p}} + \rho_{\mathrm{er}} \cdot \frac{-r_{\mathrm{tool}} \cdot \varphi \cdot \sin\theta}{\sqrt{{r_{\mathrm{tool}}}^2 - (r_{\mathrm{tool}} \cdot \sin\varphi \cdot \cos\theta)^2}} \tag{4.21}$$

Embedding Equations (4.14) and (4.20) in Equation (4.21), it gives the thickness expression in ER region as following:

$$t = t_0 - \frac{t_0 \cdot (1-\cos\alpha)}{\alpha+\beta} \cdot \left\{ \beta + \arcsin(\sin\varphi \cdot \cos\theta) + \frac{\left[\exp\left(\frac{\sqrt{3}}{2} \cdot \frac{\sigma_{\mathrm{c}}}{E}\right) - 1\right] \cdot \beta \cdot \varphi \cdot \sin\theta}{\arccos\left[1 - \left(\exp\left(\frac{\sqrt{3}}{2} \cdot \frac{\sigma_{\mathrm{c}}}{E}\right) - 1\right) \cdot \frac{t_0 \cdot (1-\cos\alpha) \cdot \beta}{r_{\mathrm{tool}} \cdot (\alpha+\beta)}\right] \cdot \sqrt{1-(\sin\varphi \cdot \cos\theta)^2}} \right\} \tag{4.22}$$

4.2.3 Indentation and drawing angles

In expressions of thickness distribution, Equation (4.18) and (4.22), there are two unknown parameters: equivalent stress $\bar{\sigma}_{\mathrm{c}}$ at the tool centre position and the indentation angle β in workpiece meridional direction. $\bar{\sigma}_{\mathrm{c}}$ can be calculated by using the equivalent strain in the constitutive equation, while β meets the condition given by the following expression:

$$r_{\mathrm{tool}} \cdot (1 - \cos\beta) > t_0 \cdot (1 - \cos\beta) \cdot \frac{\beta}{\alpha+\beta} \tag{4.23}$$

Considering the effect of material strain hardening exponent n on the indentation, the right half of Equation (4.23) needs to be modified with an additional term which is close to 0 with a large n and approaches $r_{\mathrm{tool}} \cdot (1 - \cos\beta)$ with a small n. The term $1/[1 + \exp(x)]$ stabilises at 1 and 0 with small and large x values, respectively, and can work well to capture the above-mentioned variation trend. Therefore, an equation is proposed as following by modifying Equation (4.23):

$$r_{\text{tool}} \cdot (1 - \cos\beta) = t_0 \cdot (1 - \cos\alpha) \cdot \frac{\beta}{\alpha+\beta} + \frac{1}{1+\exp(5 \cdot n-1)} \cdot r_{\text{tool}} \cdot (1 - \cos\beta) \quad (4.24)$$

Solving the above equation gives the expression of β:

$$\beta = \frac{1}{2} \cdot \left[\sqrt{\alpha^2 + \frac{8 \cdot t_0 \cdot (1-\cos\alpha) \cdot [1+\exp(5 \cdot n-1)]}{\exp(5 \cdot n-1)}} - \alpha \right] \quad (4.25)$$

To confirm the validity of Equation (4.25), FE simulation is used to obtain angle β of materials with different strain hardening exponent as it is difficult to observe in experiment. AA5052, PEEK, AA3003 and titanium grade 1 (TA1) are used in ISF simulation with drawing angle of 50° and sheet thickness of 1.2 mm. As shown in Figure 4.5(a), the comparison between the simulation and analytical results indicates that the proposed equation can predict angle β well. It is noteworthy that the term $(5 \cdot n)$ in Equations (4.24) and (4.25) is used to achieve a balance between effectiveness and simplicity of the analytical equation, although better agreement may be achieved if slight adjustment is made to the constant 5 in this term.

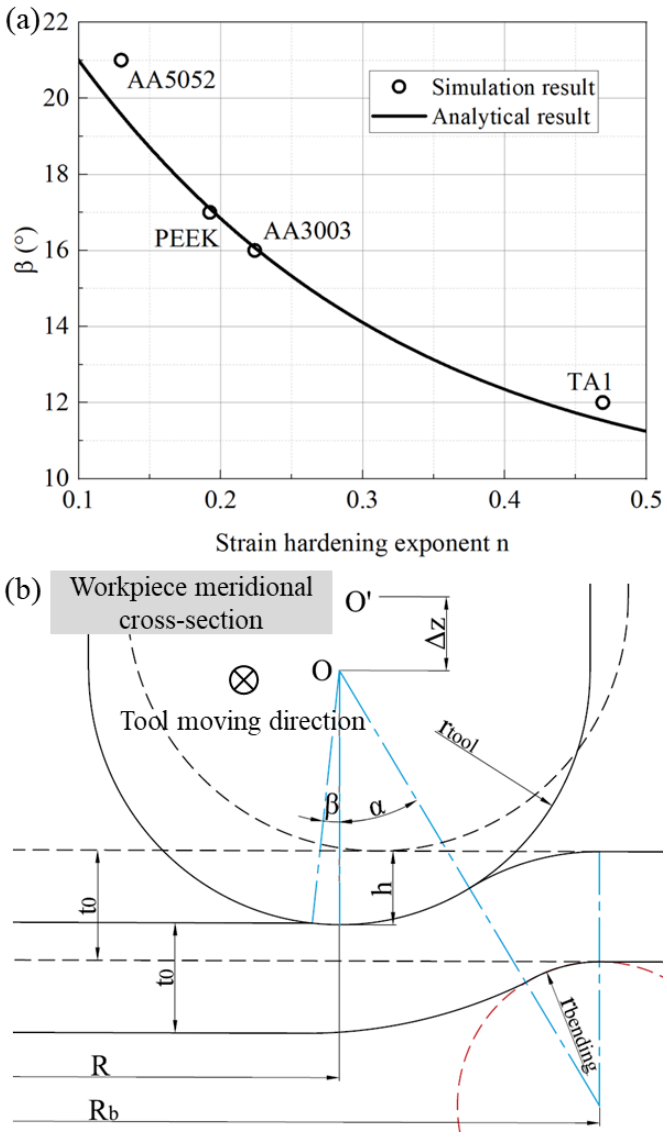


Figure 4.5 (a) Comparison of indentation angle between simulation and analytical results. (b) Illustration of tool-sheet relationship at the beginning of ISF.

Since the boundary expressions of different regions are derived in Equations (4.1), (4.4), (4.7) and (4.8), the indentation angle λ in workpiece circumferential direction and the elastic recovery angle μ as shown in Figure 4.4(b) can be approximately calculated as the following equations:

$$\lambda = \sqrt{\beta^2 - {\beta_1}^2} \tag{4.26}$$

$$\mu = \arcsin\frac{w_{er}}{r_{tool}} \tag{4.27}$$

Another important angle in the contact region is the drawing angle. At the initial stage of ISF, the actual drawing angle α is smaller than the designed drawing angle Ψ because the tool and the sheet are not in full contact. Figure 4.5(b) illustrates the contact relationship at the beginning of ISF, in which the initial bending effect is demonstrated. According to the geometric feature, following equations can be listed:

$$\left(r_{\text{bending}} + t_0 + r_{\text{tool}}\right) \cdot \sin\alpha = R_{\text{b}} - R \tag{4.28}$$

$$\left(r_{\text{bending}} + t_0\right) \cdot \cos\alpha + h - r_{\text{tool}} \cdot (1 - \cos\alpha) = r_{\text{bending}} + t_0 \tag{4.29}$$

where R_{b} is the distance from the part centre/ symmetry axis to the edge of backing plate (or clamping position if without backing plate), R is the distance from the part centre/ symmetry axis to the tool position, r_{bending} is the bending radius and h is the depth of tool position. By solving Equations (4.28) and (4.29), the actual drawing angle at the initial stage of ISF can be obtained as the following expression:

$$\alpha = 2 \cdot \tan^{-1}\left(\frac{h}{R_{\text{b}} - R}\right) \tag{4.30}$$

The actual drawing angle follows Equation (4.30) until the designed value Ψ is reached.

4.2.4 Strain components

In ISF, the strain distribution of the tool meridional cross-section may be calculated under the combined effect of stretching and local bending [129]. The strain caused by stretching and material thinning on the neutral surface can be calculated as following:

$$\varepsilon_{\text{stretching}} = \ln\frac{t + \Delta t}{t} \tag{4.31}$$

where t is the material thickness under contact, which is derived as Equation (4.18) and (4.22) for different contact regions. $\Delta t = t_0 \cdot (1 - \cos\alpha) \cdot (\beta - \beta_1)/(\alpha + \beta)$ for overlapping regions, while $\Delta t = t_0 - t$ for non-overlapping regions. The strain due to

pure bending has the following expression [140]:

$$\varepsilon_{\text{bending}} = \ln \frac{r}{\sqrt{r_{\text{tool}} \cdot (r_{\text{tool}} + t)}} \tag{4.32}$$

Combining the stretching and bending strain, the strain along the tool meridional direction can be calculated:

$$\varepsilon_{\varphi} = \varepsilon_{\text{stretching}} + \varepsilon_{\text{bending}} = \ln \frac{(t+\Delta t) \cdot r}{t \cdot \sqrt{r_{\text{tool}} \cdot (r_{\text{tool}} + t)}} \tag{4.33}$$

Although the final state of the ISF formed truncated cone part is in plane strain condition, the instant deformation state under the localised contact can be seen similar as stretch forming of thin sheet, which is typically in biaxial tension condition [140]. Therefore, ε_{θ} and ε_{r} in the tool meridional and radial directions may be given by the next equations:

$$\varepsilon_{\theta} = \ln \frac{(t+\Delta t) \cdot r}{t \cdot \sqrt{r_{\text{tool}} \cdot (r_{\text{tool}} + t)}} \tag{4.34}$$

$$\varepsilon_{\text{r}} = 2 \cdot \ln \frac{t \cdot \sqrt{r_{\text{tool}} \cdot (r_{\text{tool}} + t)}}{(t+\Delta t) \cdot r} \tag{4.35}$$

The equivalent strain $\bar{\varepsilon}$ can be derived as the following expression:

$$\bar{\varepsilon} = \frac{\sqrt{2}}{3} \cdot \sqrt{\left(\varepsilon_{\text{r}} - \varepsilon_{\varphi}\right)^2 + \left(\varepsilon_{\varphi} - \varepsilon_{\theta}\right)^2 + (\varepsilon_{\theta} - \varepsilon_{\text{r}})^2} = 2 \cdot \ln \frac{(t+\Delta t) \cdot r}{t \cdot \sqrt{r_{\text{tool}} \cdot (r_{\text{tool}} + t)}} \tag{4.36}$$

The equivalent stress $\bar{\sigma}$ can be calculated with a given material constitutive model and the equivalent strain. It is noteworthy that $\bar{\sigma}_{\text{c}}$ in Equation (4.5) can be obtained at the mean equivalent strain $\bar{\varepsilon}_{\text{c}}$, which may be calculated without consideration of bending strain:

$$\bar{\varepsilon}_{\text{c}} = 2 \cdot \ln \frac{t_{\text{c}} + \Delta t}{t_{\text{c}}} \tag{4.37}$$

where, $\Delta t = t_0 \cdot (1 - \cos \alpha) \cdot (\beta - \beta_1)/(\alpha + \beta)$ and t_{c} is derived as Equation (4.12).

4.2.5 Forming force

The forming force (F) is decomposed to the vertical force (F_{v}) and horizontal force (F_{h}), between which the horizontal force may be comprised of the force in radial direction (F_{r}) and the force in tangential direction (F_{t}). As shown in Figure 4.6, the vertical force may consist of the vertical component of localised shear force ($F_{\mathrm{v}}^{\mathrm{ls}}$) and the vertical force due to global bending ($F_{\mathrm{v}}^{\mathrm{ed}}$). The radial force F_{r} is perpendicular to the tool path and may come from the radial component of the localised shear force, while the tangential force F_{t} may be comprised of the localised shear force component in tangential direction ($F_{\mathrm{t}}^{\mathrm{ls}}$), the force leading to material thinning ($F_{\mathrm{t}}^{\mathrm{mt}}$) and the frictional force ($F_{\mathrm{t}}^{\mathrm{f}}$).

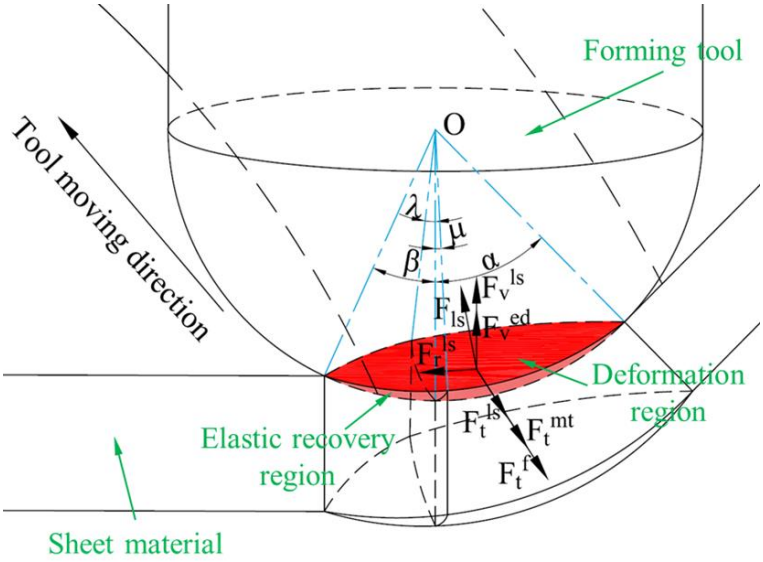


Figure 4.6 Decomposition of forming force in ISF.

4.2.5.1 Vertical forming force related to local shear deformation

In ISF, the downward movement of material is driven by the forming tool. The tool may be seen to punch the sheet along the normal direction of the contact region for deformation, and the sheet material gives the tool a reaction force to oppose the downward movement of forming tool and the material deformation. The vertical force

is a combination of the vertical component of reaction shear force provided by the sheet material and the force resulting from the global bending.

According to the von-Mises yield criteria, in biaxial tension condition of the localised deformation region as indicated above, the shear stress τ may be calculated using the following equation [140]:

$$\tau = \frac{1}{2} \cdot \sigma_{\mathrm{s}} \tag{4.38}$$

where the yield stress σ_{s} is represented by $\sigma_{\mathrm{s}}^{\mathrm{P1}}$, $\sigma_{\mathrm{s}}^{\mathrm{P2}}$, $\sigma_{\mathrm{s}}^{\mathrm{P3}}$, $\sigma_{\mathrm{s}}^{\mathrm{P4}}$ and $\sigma_{\mathrm{s}}^{\mathrm{P5}}$ for different parts and is calculated by the material constitutive model at the yield strain ε_{s} as given by Equation (4.39), which may only come from the material thinning Δt after contact and deformation.

$$\varepsilon_{\mathrm{s}} = 2 \cdot \ln\left[1 + \frac{\Delta t}{t_0 - \frac{t_0 \cdot (1-\cos\alpha) \cdot (\beta + \operatorname{asin}\delta \cdot \cos\theta)}{\alpha+\beta}}\right] \tag{4.39}$$

where $\Delta t = t_0 \cdot (1-\cos\alpha) \cdot (\beta - \beta_1)/(\alpha+\beta)$ for P1, P2 and P5, while $\Delta t = t_0 \cdot (1-\cos\alpha) \cdot (\beta + \operatorname{asin}\delta \cdot \cos\theta)/(\alpha+\beta)$ for P3 and P4. δ is represented by δ_{P1}, δ_{P2}, δ_{P3}, δ_{P4} and δ_{P5}, which are φ angles at boundaries of the five contact regions and are defined with different θ ranges by Equations (4.1), (4.4), (4.7) and (4.8).

The localised shear force (F_{ls}) in different contact regions may be calculated using the shear stress and through thickness area by the following expressions:

$$F_{\mathrm{ls}}^{\mathrm{P1}} = \int_0^{\frac{1}{2}\pi} \int_{r_{\mathrm{tool}}}^{r_{\mathrm{tool}}+t_{\mathrm{P1}}} \frac{\sigma_{\mathrm{s}}^{\mathrm{P1}} \cdot \sin\delta_{\mathrm{P1}} \cdot r_{\mathrm{tool}}}{2 \cdot \cos\left[\frac{\pi}{2} - \theta - \arctan\left(\frac{b^2 \cdot x}{a^2 \cdot y}\right)\right]} \,\mathrm{dr}\,\mathrm{d}\theta \tag{4.40}$$

$$F_{\mathrm{ls}}^{\mathrm{P2}} = \int_{\frac{1}{2}\pi}^{\arccos\left(-\frac{\sin\beta_1}{\sin\beta}\right)} \int_{r_{\mathrm{tool}}}^{r_{\mathrm{tool}}+t_{\mathrm{P2}}} \frac{\sigma_{\mathrm{s}}^{\mathrm{P2}} \cdot \sin\delta_{\mathrm{P2}} \cdot r_{\mathrm{tool}}}{2 \cdot \cos\left[\frac{\pi}{2} - \theta - \arctan\left(\frac{b^2 \cdot x}{a^2 \cdot y}\right)\right]} \,\mathrm{dr}\,\mathrm{d}\theta \tag{4.41}$$

$$F_{\mathrm{ls}}^{\mathrm{P3}} = \int_{\arccos\left(-\frac{\sin\beta_1}{\sin\beta}\right)}^{\pi} \int_{r_{\mathrm{tool}}}^{r_{\mathrm{tool}}+t_{\mathrm{P3}}} \frac{\sigma_{\mathrm{s}}^{\mathrm{P3}} \cdot \sin\delta_{\mathrm{P3}} \cdot r_{\mathrm{tool}}}{2} \mathrm{d}r\mathrm{d}\theta \tag{4.42}$$

$$F_{\mathrm{ls}}^{\mathrm{P4}} = \int_{\pi}^{\frac{3}{2}\pi} \int_{r_{\mathrm{tool}}}^{r_{\mathrm{tool}}+t_{\mathrm{P4}}} \frac{\sigma_{\mathrm{s}}^{\mathrm{P4}} \cdot \sin\delta_{\mathrm{P4}} \cdot r_{\mathrm{tool}}}{2 \cdot \cos\left[\frac{\pi}{2}+\theta+\arctan\left(\frac{b^2 \cdot x}{a^2 \cdot y}\right)\right]} \mathrm{d}r\mathrm{d}\theta \tag{4.43}$$

$$F_{\mathrm{ls}}^{\mathrm{P5}} = \int_{\frac{3}{2}\pi}^{2\pi} \int_{r_{\mathrm{tool}}}^{r_{\mathrm{tool}}+t_{\mathrm{P5}}} \frac{\sigma_{\mathrm{s}}^{\mathrm{P5}} \cdot \sin\delta_{\mathrm{P5}} \cdot r_{\mathrm{tool}}}{2 \cdot \cos\left[\frac{\pi}{2}+\theta+\arctan\left(\frac{b^2 \cdot x}{a^2 \cdot y}\right)\right]} \mathrm{d}r\mathrm{d}\theta \tag{4.44}$$

where $F_{\mathrm{ls}}^{\mathrm{P1}}$, $F_{\mathrm{ls}}^{\mathrm{P2}}$, $F_{\mathrm{ls}}^{\mathrm{P3}}$, $F_{\mathrm{ls}}^{\mathrm{P4}}$ and $F_{\mathrm{ls}}^{\mathrm{P5}}$ are localised shear forces of P1, P2, P3, P4 and P5, respectively; t_{P1}, t_{P2}, t_{P3}, t_{P4} and t_{P5} are the thickness at the boundary of the five regions by Equations (4.18) and (4.22); a and b in each equation are the length of long and short axes of corresponding boundary elliptical shapes.

The vertical forming force due to localised shear force may be calculated using the following equation:

$$F_{\mathrm{v}}^{\mathrm{ls}} = \cos\frac{\alpha-\beta}{2} \cdot \cos\frac{\lambda-\mu}{2} \cdot F_{\mathrm{ls}} = \cos\frac{\alpha-\beta}{2} \cdot \cos\frac{\lambda-\mu}{2} \cdot \left(F_{\mathrm{ls}}^{\mathrm{P1}} + F_{\mathrm{ls}}^{\mathrm{P2}} + F_{\mathrm{ls}}^{\mathrm{P3}} + F_{\mathrm{ls}}^{\mathrm{P4}} + F_{\mathrm{ls}}^{\mathrm{P5}}\right) \tag{4.45}$$

4.2.5.2 Vertical forming force from elastic bending

Referring to the case of a circular plate, elastic deflection γ and concentrated force $F_{\mathrm{v}}^{\mathrm{ed}}$ may have the following relationship:

$$\gamma = \frac{F_{\mathrm{v}}^{\mathrm{ed}} \cdot \left({R_{\mathrm{b}}}^2 - R^2\right)^2}{16 \cdot \pi \cdot D \cdot {R_{\mathrm{b}}}^2} \tag{4.46}$$

where D in N·mm is the flexural rigidity of sheet material:

$$D = \frac{E \cdot {t_0}^3}{12 \cdot (1-\nu^2)} \tag{4.47}$$

where ν is the material Poisson's ratio. The part of vertical force from elastic global bending can be expressed as follows:

$$F_{\mathrm{v}}^{\mathrm{ed}} = 16 \cdot \pi \cdot D \cdot \gamma \cdot \frac{{R_{\mathrm{b}}}^2}{\left({R_{\mathrm{b}}}^2 - R^2\right)^2} \tag{4.48}$$

The global bending of the sheet material between the forming tool and the backing plate is totally recovered until the equivalent strain due to bending (expressed as Equation (4.49)) equals to the yield strain ε_{s} of the sheet material.

$$\bar{\varepsilon}_{\mathrm{ed}} = \frac{2}{\sqrt{3}} \cdot \ln \frac{r_{\mathrm{bending}} + t_0}{\sqrt{r_{\mathrm{bending}} \cdot \left(r_{\mathrm{bending}} + t_0\right)}} = \frac{1}{\sqrt{3}} \cdot \ln \frac{r_{\mathrm{bending}} + t_0}{r_{\mathrm{bending}}} \tag{4.49}$$

Therefore, when the elastic deflection reaches the maximum value, the bending has a critical radius as expressed by Equation (4.50):

$$r_{\mathrm{bending}}^{\mathrm{critical}} = \frac{t_0}{\exp\left(\sqrt{3} \cdot \varepsilon_{\mathrm{s}}\right) - 1} \tag{4.50}$$

According to the relationships given by Equations (4.28) and (4.29), the critical depth of tool position, i.e., the maximum elastic deflection can be derived and calculated by the following equation:

$$h_{\mathrm{critical}} = \left[\frac{t_0}{\exp\left(\sqrt{3} \cdot \varepsilon_{\mathrm{s}}\right) - 1} + t_0 + r_{\mathrm{tool}}\right] \cdot \left\{1 - \cos\left[\arcsin \frac{R_{\mathrm{b}} - R}{\frac{t_0}{\exp\left(\sqrt{3} \cdot \varepsilon_{\mathrm{s}}\right) - 1} + t_0 + r_{\mathrm{tool}}}\right]\right\} \tag{4.51}$$

The elastic deflection γ equals to h until the tool position reaches a critical depth h_{critical}. After this position, the elastic deflection γ is treated as a constant value h_{critical}.

The vertical force is finally calculated as the superposition of $F_{\mathrm{v}}^{\mathrm{ls}}$ and $F_{\mathrm{v}}^{\mathrm{ed}}$ as following:

$$F_{\mathrm{v}} = F_{\mathrm{v}}^{\mathrm{ls}} + F_{\mathrm{v}}^{\mathrm{ed}} \tag{4.52}$$

4.2.5.3 Horizontal forming forces

The horizontal forces in radial and tangential directions due to local shear behaviour have expressions as follows:

$$F_{\mathrm{r}} = \sin\frac{\alpha-\beta}{2} \cdot (F_{\mathrm{s}}^{\mathrm{P1}} + F_{\mathrm{s}}^{\mathrm{P2}} + F_{\mathrm{s}}^{\mathrm{P3}} + F_{\mathrm{s}}^{\mathrm{P4}} + F_{\mathrm{s}}^{\mathrm{P5}}) \tag{4.53}$$

$$F_{\mathrm{t}}^{\mathrm{ls}} = \cos\frac{\alpha-\beta}{2} \cdot \sin\frac{\lambda-\mu}{2} \cdot (F_{\mathrm{s}}^{\mathrm{P1}} + F_{\mathrm{s}}^{\mathrm{P2}} + F_{\mathrm{s}}^{\mathrm{P3}} + F_{\mathrm{s}}^{\mathrm{P4}} + F_{\mathrm{s}}^{\mathrm{P5}}) \tag{4.54}$$

The derivation of the material thinning-related horizontal force is based on the energy method and the work done by the horizontal force in movement of l along the workpiece circumferential direction may lead to the thinning of the sheet, as shown in Figure 4.7.

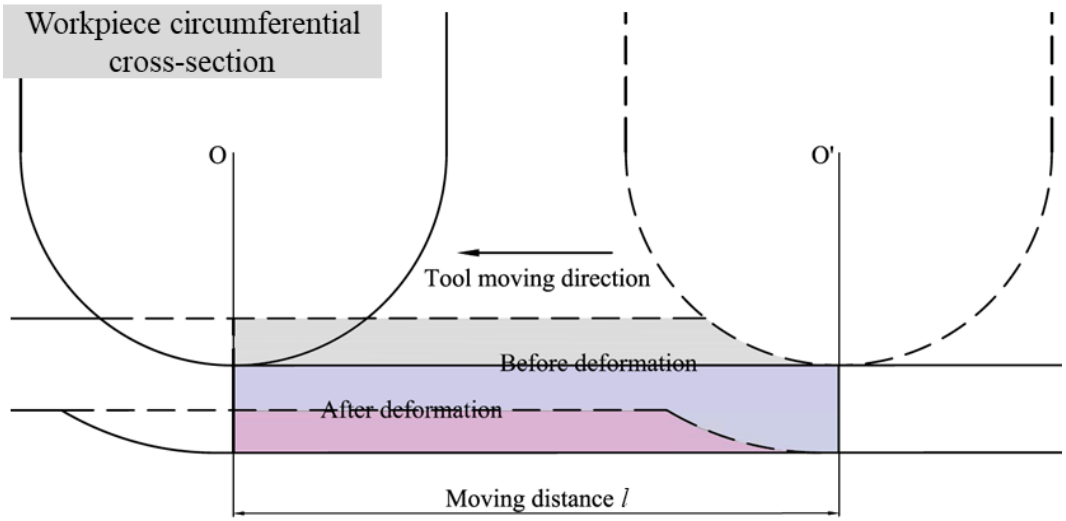


Figure 4.7 Illustration of the workpiece circumferential cross-section.

Energy balance equation along the workpiece circumferential direction is given as following:

$$F_{\mathrm{t}}^{\mathrm{mt}} \cdot l = \int_0^{\beta} \int_{r_{\mathrm{tool}}}^{r_{\mathrm{tool}}+t_{\mathrm{A}}} \bar{\sigma} \cdot r \cdot l \cdot \bar{\varepsilon}\, \mathrm{d}r\, \mathrm{d}\varphi + \int_0^{\alpha} \int_{r_{\mathrm{tool}}}^{r_{\mathrm{tool}}+t_{\mathrm{B}}} \bar{\sigma} \cdot r \cdot l \cdot \bar{\varepsilon}\, \mathrm{d}r\, \mathrm{d}\varphi \tag{4.55}$$

$F_{\mathrm{t}}^{\mathrm{mt}}$ has the following expression after solving Equation (4.55):

$$F_{\mathrm{t}}^{\mathrm{mt}} = \int_0^{\beta} \int_{r_{\mathrm{tool}}}^{r_{\mathrm{tool}}+t_{\mathrm{A}}} \bar{\sigma} \cdot r \cdot \bar{\varepsilon}\, \mathrm{d}r\, \mathrm{d}\varphi + \int_0^{\alpha} \int_{r_{\mathrm{tool}}}^{r_{\mathrm{tool}}+t_{\mathrm{B}}} \bar{\sigma} \cdot r \cdot \bar{\varepsilon}\, \mathrm{d}r\, \mathrm{d}\varphi \tag{4.56}$$

In ISF, the cross-section shape of workpiece after deformation is determined by the meridional cross-section, which has the minimum area. Therefore, in this equation, the volume of the deformed material and the strain distribution are utilised on the workpiece

meridional cross-section.

The frictional force $F_{\mathrm{t}}^{\mathrm{f}}$ approximately has the following relationship with the vertical forming force:

$$F_{\mathrm{t}}^{\mathrm{f}} = f \cdot \left(F_{\mathrm{ls}}^{\mathrm{P1}} + F_{\mathrm{ls}}^{\mathrm{P2}} + F_{\mathrm{ls}}^{\mathrm{P3}} + F_{\mathrm{ls}}^{\mathrm{P4}} + F_{\mathrm{ls}}^{\mathrm{P5}}\right) \tag{4.57}$$

where f is the frictional coefficient between the forming tool and the sheet. The tangential, horizontal and total forces, F_{t}, F_{h} and F can be calculated as following:

$$F_{\mathrm{t}} = F_{\mathrm{t}}^{\mathrm{ls}} + F_{\mathrm{t}}^{\mathrm{mt}} + F_{\mathrm{t}}^{\mathrm{f}} \tag{4.58}$$

$$F_{\mathrm{h}} = \sqrt{(F_{\mathrm{t}})^2 + (F_{\mathrm{r}})^2} \tag{4.59}$$

$$F = \sqrt{{F_{\mathrm{v}}}^2 + {F_{\mathrm{h}}}^2} \tag{4.60}$$

4.2.6 Forming force in biaxial tension condition area

4.2.6.1 Contact region

Although plane strain condition is the most common final state of ISF formed part, sometimes the material deformation presents biaxial tension condition at the corner [56, 137]. As shown in Figure 4.1(e) and (f), the blue area represents the contact region in end milling process or ISF process of a rigid plastic material. In consideration of the elastic deformation before contact and the recovery after contact in ISF, a shrink and an expansion are applied to the front and rear contact regions, respectively, as illustrated by the white borders.

In biaxial tension condition area, the contact region may be comprised of four different parts: corner deformation (CD) region, OD region and ER region, each of which can be assumed as a part of elliptical or super elliptical shape as shown in Figure 4.3(b). The boundaries of CD and OD regions are represented by Q1 and Q2, respectively, while

the boundary of ER region consists of Q3 and Q4.

The lateral edge of the pyramid is defined as the intersecting line between two lateral faces, and the drawing angle α_{b} becomes slightly smaller when the tool moves to the corner. Therefore, the super elliptical boundary of Q1 can be expressed as the following:

$$\left(\frac{r_{\mathrm{tool}}\cdot\sin\varphi\cdot\cos\theta}{r_{\mathrm{tool}}\cdot\sin\alpha}\right)^{\ln\frac{1}{2}/\ln\frac{\sin\alpha_{\mathrm{b}}}{\sqrt{2}\cdot\sin\alpha}}+\left(\frac{r_{\mathrm{tool}}\cdot\sin\varphi\cdot\sin\theta}{r_{\mathrm{tool}}\cdot\sin\alpha}\right)^{\ln\frac{1}{2}/\ln\frac{\sin\alpha_{\mathrm{b}}}{\sqrt{2}\cdot\sin\alpha}}=1 \tag{4.61}$$

The elliptical boundary of Q2 can be given by the following equation:

$$\frac{(r_{\mathrm{tool}}\cdot\sin\varphi\cdot cos\theta)^2}{(r_{\mathrm{tool}}\cdot\sin\beta)^2-(r_{\mathrm{tool}}\cdot\sin\beta_1)^2}+\frac{(r_{\mathrm{tool}}\cdot\sin\varphi\cdot\sin\theta+r_{\mathrm{tool}}\cdot\sin\beta_1)^2}{(r_{\mathrm{tool}}\cdot\sin\alpha+r_{\mathrm{tool}}\cdot\sin\beta_1)^2}=1 \tag{4.62}$$

Another elliptical boundary of Q3 can be expressed as:

$$\frac{(\sin\varphi\cdot\cos\theta)^2}{\left[1-\frac{(\sin\beta_1)^2}{(\sin\alpha+\sin\beta_1)^2}\right]\cdot[(\sin\beta)^2-(\sin\beta_1)^2]}+\frac{(r_{\mathrm{tool}}\cdot\sin\varphi\cdot\sin\theta)^2}{{w_{\mathrm{er}}}^2}=1 \tag{4.63}$$

Finally, the expression of the elliptical boundary of Q4 is derived as the following:

$$\frac{(\sin\varphi\cdot\cos\theta)^2}{(\sin\alpha)^2}+\frac{(r_{\mathrm{tool}}\cdot\sin\varphi\cdot\sin\theta)^2}{{w_{\mathrm{er}}}^2}=1 \tag{4.64}$$

4.2.6.2 Vertical forming force

Referring to plane strain condition area, the vertical force in biaxial tension condition area can be derived as in the following expression:

$$F_{\mathrm{v}}=\cos\frac{\alpha_{\mathrm{b}}}{2}\cdot\left(F_{\mathrm{ls}}^{\mathrm{Q1}}+F_{\mathrm{ls}}^{\mathrm{Q2}}+F_{\mathrm{ls}}^{\mathrm{Q3}}+F_{\mathrm{ls}}^{\mathrm{Q4}}\right)+F_{\mathrm{v}}^{\mathrm{ed}} \tag{4.65}$$

where $F_{\mathrm{ls}}^{\mathrm{Q2}}=F_{\mathrm{ls}}^{\mathrm{P1}}$, $F_{\mathrm{ls}}^{\mathrm{Q4}}=F_{\mathrm{ls}}^{\mathrm{P5}}$ and $F_{\mathrm{ls}}^{\mathrm{Q3}}$ can be approximated as $F_{\mathrm{ls}}^{\mathrm{P4}}$. $F_{\mathrm{ls}}^{\mathrm{Q1}}$ can be calculated by the following equation:

$$F_{\mathrm{ls}}^{\mathrm{Q1}}=\int_0^{\frac{1}{2}\pi}\int_{r_{\mathrm{tool}}}^{r_{\mathrm{tool}}+t_{\mathrm{Q1}}}\frac{\sigma_{\mathrm{s}}^{\mathrm{Q1}}\bar{\sigma}\cdot\sin\delta_{\mathrm{Q1}}\cdot r_{\mathrm{tool}}}{\sqrt{3}2\cdot\cos\left\{\frac{\pi}{2}-\theta-\arctan\left[(\cot\theta)^{\ln\frac{1}{2}/\ln\frac{\sin\alpha_{\mathrm{b}}}{\sqrt{2}\cdot\sin\alpha}-1}\right]\right\}}\mathrm{d}r\,\mathrm{d}\theta \tag{4.66}$$

where t_{Q1} and $\sigma_{\mathrm{s}}^{\mathrm{Q1}}$ are the sheet thickness and the yield stress of Q1, respectively. The sheet thickness at the immediate proximity near the contact region at the corner can be approximated as $(t_0 \cdot \cos\alpha_{\mathrm{b}})$. According to the assumption of linear distribution, when $0 \leq \theta \leq \frac{\pi}{4}$, the expression of t_{Q1} can be given by the following equation:

$$t_{\mathrm{Q1}} = t_0 \cdot \cos\alpha + t_0 \cdot (\cos\alpha_{\mathrm{b}} - \cos\alpha) \cdot \frac{4 \cdot \theta}{\pi} \tag{4.67}$$

When $\frac{\pi}{4} \leq \theta \leq \frac{\pi}{2}$, the thickness distribution along Q1 has the following expression:

$$t_{\mathrm{Q1}} = t_0 \cdot \cos\alpha_{\mathrm{b}} - t_0 \cdot (\cos\alpha_{\mathrm{b}} - \cos\alpha) \cdot \frac{4 \cdot \theta - \pi}{\pi} \tag{4.68}$$

$\sigma_{\mathrm{s}}^{\mathrm{Q1}}$ in Equation (4.66) may be calculated at the yield strain $\varepsilon_{\mathrm{s}}^{\mathrm{Q1}}$ as following by referring to Equation (4.39):

$$\varepsilon_{\mathrm{s}}^{\mathrm{Q1}} = 2 \cdot \ln\left(1 + \frac{\Delta t_{\mathrm{Q1}}}{t_{\mathrm{Q1}}}\right) \tag{4.69}$$

where Δt_{Q1} is the thickness reduction of Q1 after contact and $\Delta t_{\mathrm{Q1}} = t_0 \cdot (1 - \cos\alpha_{\mathrm{b}}) \cdot (\beta_{\mathrm{b}} - \beta_{1\mathrm{b}})/(\alpha_{\mathrm{b}} + \beta_{\mathrm{b}})$. β_{b} and $\beta_{1\mathrm{b}}$ are the β angle and β_1 angle at the corner, respectively, and $\beta_{\mathrm{b}} = \mathrm{asin}(\sin\beta/\cos 45^\circ)$, $\beta_{1\mathrm{b}} = \mathrm{asin}(\sin\beta_1/\cos 45^\circ)$.

Therefore, $F_{\mathrm{ls}}^{\mathrm{Q1}}$ can be calculated by putting Equation (4.67) – (4.69) in Equation (4.66) and the vertical forming force F_{v} can be calculated by Equation (4.65).

4.2.6.3 Horizontal forming force

In biaxial tension condition, the influence of ND region on the decomposition of localised shear force can be neglected as it is much smaller than CD region. Therefore, the tangential force is only comprised of the force related to material thinning and the frictional force. Referring to the calculation method in plane strain condition aera, the tangential horizontal force related to material thinning in biaxial tension condition can

be derived as in the following equation:

$$F_{\mathrm{t}}^{\mathrm{mt}} = \int_0^{\alpha_{\mathrm{b}}} \int_{r_{\mathrm{tool}}}^{r_{\mathrm{tool}}+t_{\mathrm{b}}} \bar{\sigma} \cdot r \cdot \bar{\varepsilon}\, \mathrm{d}r\, \mathrm{d}\varphi \tag{4.70}$$

where t_{b} is the thickness distribution along the workpiece meridional direction in biaxial tension condition at corner, and t_{b} has the following expression:

$$t_{\mathrm{b}} = t_0 - \frac{t_0 \cdot (1-\cos\alpha)\cdot\beta}{\alpha+\beta} + \left[t_0 - \frac{t_0 \cdot (1-\cos\alpha)\cdot\beta}{\alpha+\beta} - t_0 \cdot \cos\alpha_{\mathrm{b}}\right] \cdot \frac{\varphi}{\alpha_{\mathrm{b}}} \tag{4.71}$$

Besides, the frictional force $F_{\mathrm{t}}^{\mathrm{f}}$ and the horizontal force in the radial direction F_{r} can be derived and approximated as the following equations:

$$F_{\mathrm{t}}^{\mathrm{f}} = f \cdot \left(F_{\mathrm{s}}^{\mathrm{Q1}} + F_{\mathrm{s}}^{\mathrm{Q2}} + F_{\mathrm{s}}^{\mathrm{Q3}} + F_{\mathrm{s}}^{\mathrm{Q4}}\right) \tag{4.72}$$

$$F_{\mathrm{r}} = \sin\frac{\alpha_{\mathrm{b}}}{2} \cdot \left(F_{\mathrm{s}}^{\mathrm{Q1}} + F_{\mathrm{s}}^{\mathrm{Q2}} + F_{\mathrm{s}}^{\mathrm{Q3}} + F_{\mathrm{s}}^{\mathrm{Q4}}\right) \tag{4.73}$$

The horizontal force and total forming force in biaxial tension condition can be calculated by Equations (4.59) and (4.60), respectively.

4.2.7 Implementation

MATLAB software is used to implement and visualise the derived analytical model of force prediction, and the implementation steps are given in the flow chart as shown in Figure 4.8, where the calculation method for the plane strain condition area is introduced. In the flow chart shown in Figure 4.8, the equations used for each step are indicated for convenience.

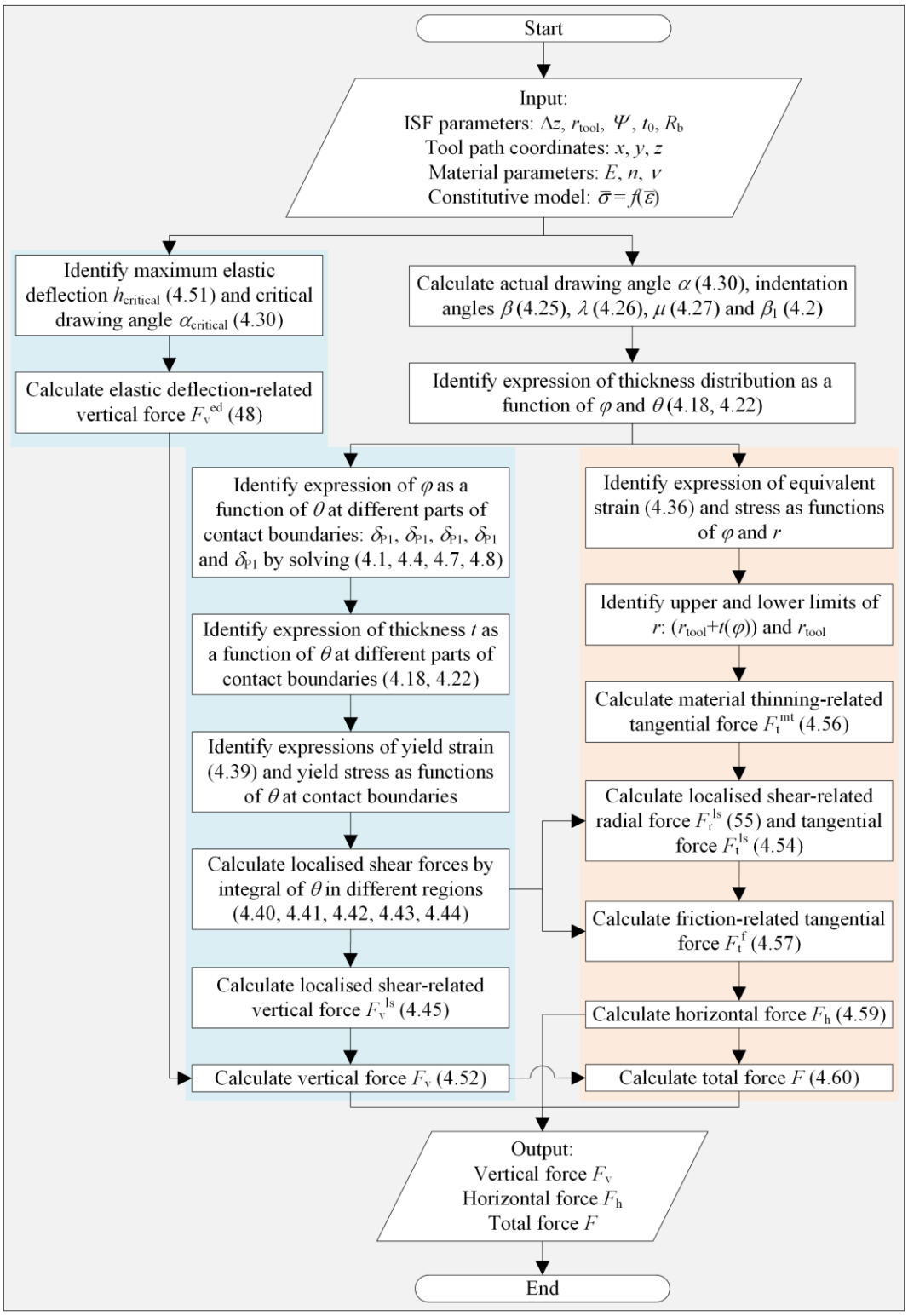


Figure 4.8 Flow chart to solve and implement the analytical model of forming force prediction in ISF.

4.3 Force prediction and validation

4.3.1 Model validation from ISF of TA1 sheet

In the developed analytical model, two different conditions are considered in ISF: plane strain condition on the flat surface and biaxial tension condition at the corner. To validate the analytical model, two different forming shapes were designed and formed as shown in Figure 4.9 with the assistance of a collaborator in the University of Sheffield under the author's instruction. The experimental setup is given as Figure 4.10. The drawing angles of the designed parts vary from 22° to 88° and the forming forces during ISF of 140 × 140 × 0.7 mm TA1 sheet were measured. Step size in ISF of the truncated cone is 0.28 mm, while for ISF of the truncated pyramid it is 0.44 mm. Other process parameters are the same: with tool radius of 5 mm, feed rate of 800 mm/min, no spindle rotation, and with use of RTD COMPOUND lubricant.

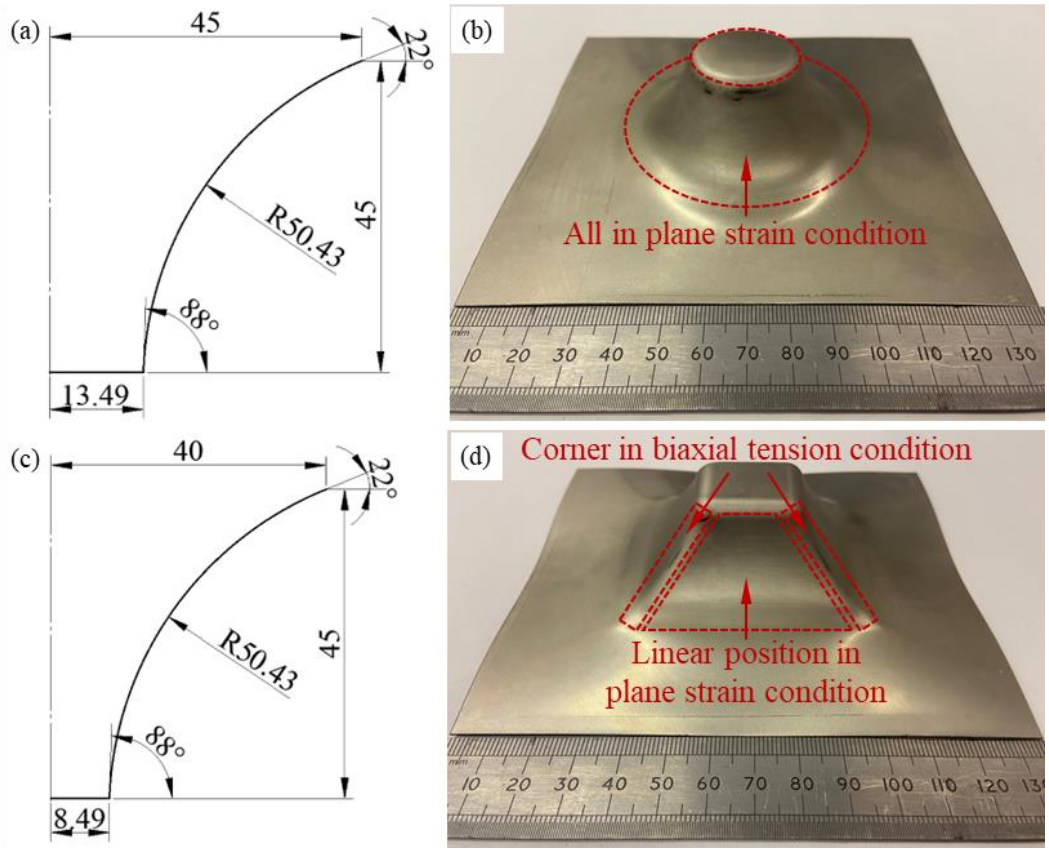


Figure 4.9 Designed ISF parts in (a), (b) truncated cone shape, and (c), (d) truncated pyramid shape with varying drawing angle.

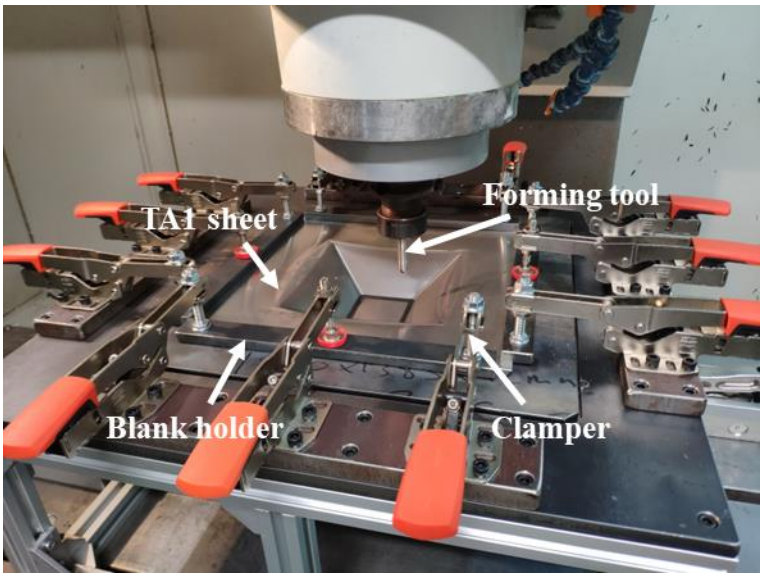


Figure 4.10 Experimental setup for ISF of TA1

Frictional coefficient of 0.25 is used, and Johnson-Cook model as given by Equation (4.74) is applied to describe the constitutive behaviour. The model parameters given in Table 4.1 were derived based on the quasi-static uniaxial tensile test. As the effects of strain rate and temperature are not considered in the current model, the constitutive model only has the part to predict the flow stress at different equivalent strain.

$$\bar{\sigma} = A + B * \bar{\varepsilon}^{n} \tag{4.74}$$

Table 4.1 Johnson-Cook parameters of TA1 and AA3003-O sheet.

Material parameters	$\boldsymbol{A}$ **(MPa)**	$\boldsymbol{B}$ **(MPa)**	$\boldsymbol{n}$	$\boldsymbol{E}$ **(MPa)**
TA1	220.6	341.3	0.4692	105000
AA3003-O	41.37	79.22	0.2244	68900

In ISF processing of the designed regular shapes, the prediction of forming force in x, y, and z axes of the ISF machine may be more convincing in the validation. Therefore, z force (F_z), x force (F_x) and y force (F_y) are predicted and compared with experimental results. F_z equals to F_v in the derivation, while F_x and F_y at different tool positions are

converted from the tangential (F_t) and radial forces (F_r) by the rules in Table 4.2.

Table 4.2 Horizontal force conversion in ISF of truncated cone and pyramid parts.

Tool position conditions		F_x	F_y
All positions of truncated cone part		$\frac{y}{\sqrt{x^2+y^2}} \cdot F_t$ $-\frac{x}{\sqrt{x^2+y^2}} \cdot F_r$	$-\frac{x}{\sqrt{x^2+y^2}} \cdot F_t$ $-\frac{y}{\sqrt{x^2+y^2}} \cdot F_r$
Linear positions of truncated pyramid part	$\left\|\frac{y}{x}\right\| < 1 \ \& \ x > 0$	$-F_r$	$-F_t$
	$\left\|\frac{y}{x}\right\| < 1 \ \& \ x < 0$	F_r	F_t
	$\left\|\frac{y}{x}\right\| > 1 \ \& \ y > 0$	F_t	$-F_r$
	$\left\|\frac{y}{x}\right\| > 1 \ \& \ y < 0$	$-F_t$	F_r
Corner positions of truncated pyramid part	$\frac{y}{x} = 1 \ \& \ x > 0$	$\frac{\sqrt{2}}{2} \cdot (F_t - F_r)$	$-\frac{\sqrt{2}}{2} \cdot (F_t + F_r)$
	$\frac{y}{x} = 1 \ \& \ x < 0$	$-\frac{\sqrt{2}}{2} \cdot (F_t - F_r)$	$\frac{\sqrt{2}}{2} \cdot (F_t + F_r)$
	$\frac{y}{x} = -1 \ \& \ y > 0$	$\frac{\sqrt{2}}{2} \cdot (F_t + F_r)$	$\frac{\sqrt{2}}{2} \cdot (F_t - F_r)$
	$\frac{y}{x} = -1 \ \& \ y < 0$	$-\frac{\sqrt{2}}{2} \cdot (F_t + F_r)$	$-\frac{\sqrt{2}}{2} \cdot (F_t - F_r)$

The prediction results of total force and force components with the change of tool position in ISF are presented in Figure 4.10. For convenience, the force variation with the change of tool position is given in a contour plot. Different colours indicate the predicted force levels when the tool moves to different positions. Figure 4.10(a) and (b) shows the nonuniform distribution of rising total and z forces with the increase of forming depth because of the change of drawing angle and the relatively uniform force

distribution in the same or adjacent tool path layers. Meanwhile, as given by Figure 4.10(c) and (d), horizontal forces in x and y axes are in regular alternant variation because of the approximate circular tool path.

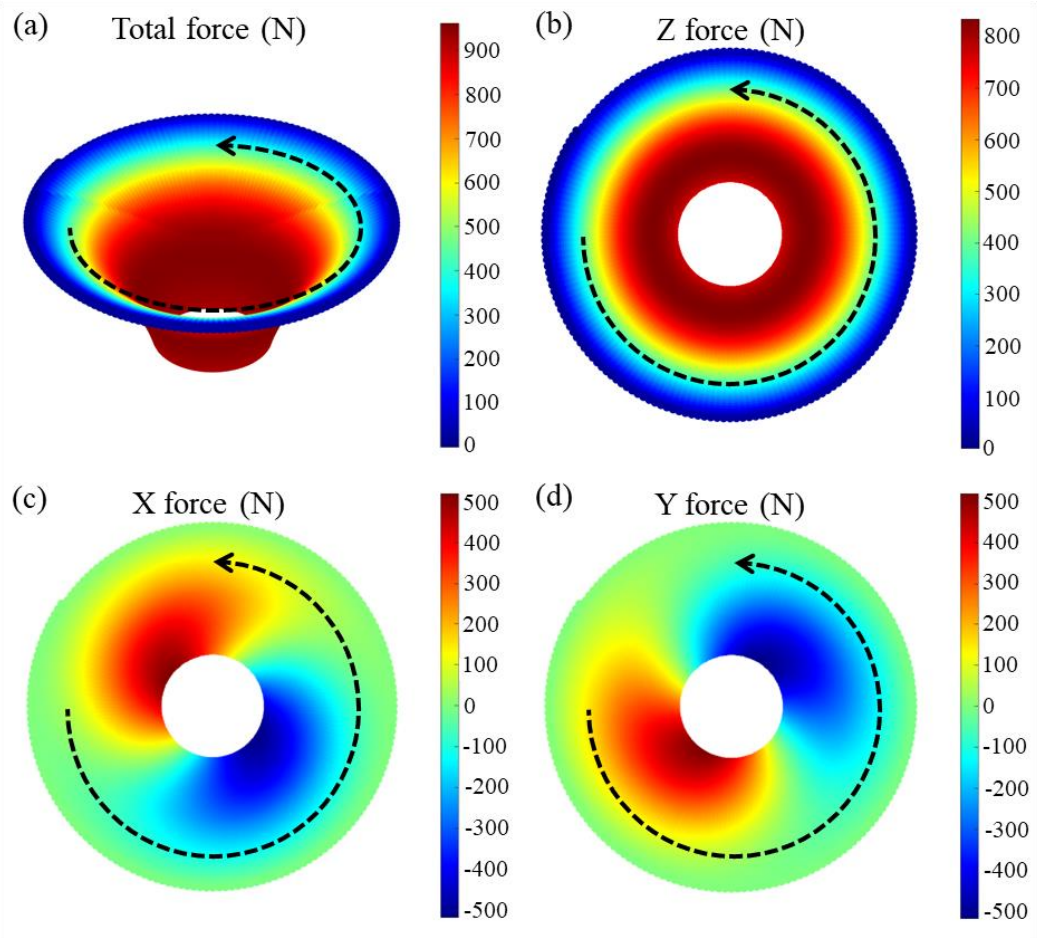


Figure 4.11 Analytically predicted results of (a) total force, (b) z force, (c) x force and (d) y force of different tool position in ISF of truncated cone part of TA1.

The comparison of force components between analytical prediction and experimental results is presented in Figure 4.12. Although the forming force in experiment shows a continuously changing trend, the variation is observed to be highly centrally distributed, which is an indication of identical deformation behaviour and contact condition in ISF of truncated cone part. The slight fluctuation may come from the non-horizontal placement of the ISF fixture or the stiffness change of sheet material [123]. The comparison shows that the prediction is in good agreement with experiment and the

predicted z force has a smooth variation trend because of the unchanged deformation behaviour and contact condition in the model implementation. As shown in Figure 4.12(b), the detailed force variation in an enlarged time range from 830 s to 860 s further indicates the prediction accuracy and confirms the regular alternant variation of x and y forces.

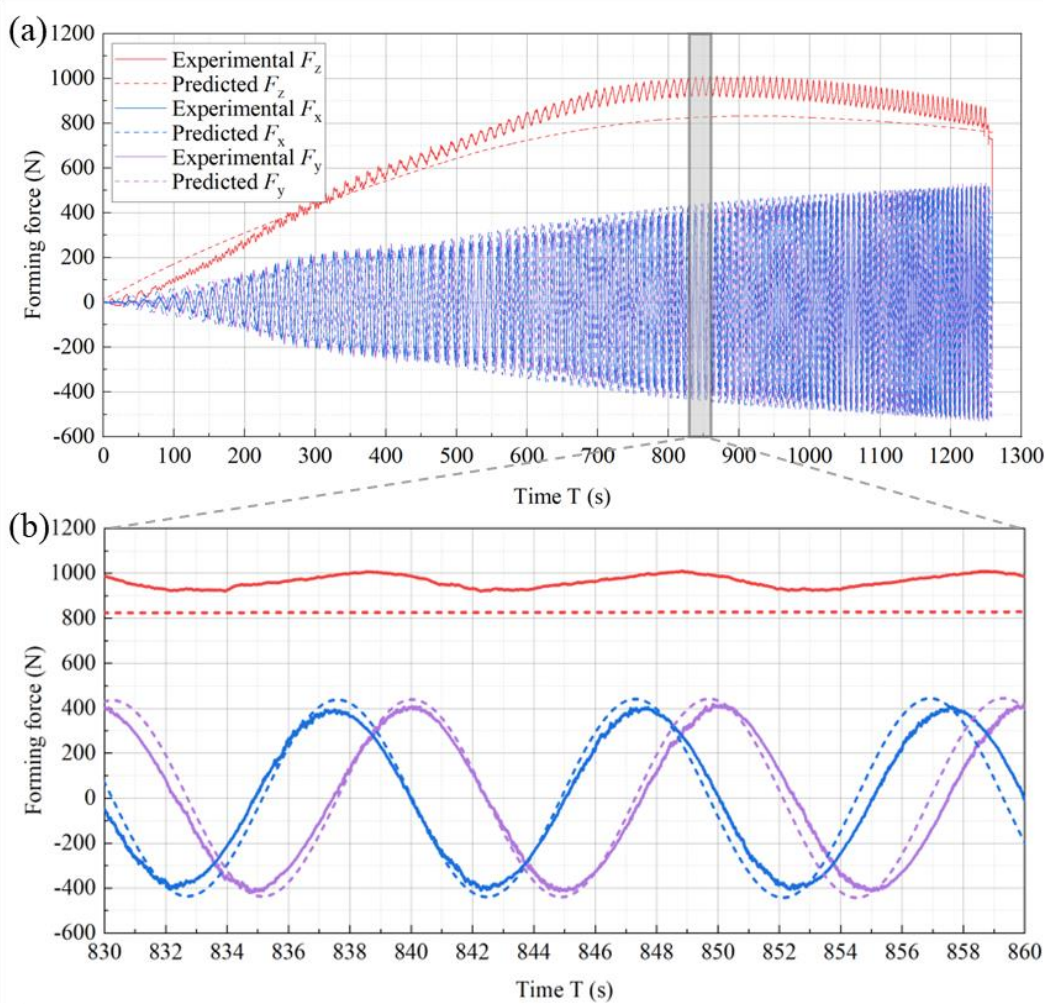


Figure 4.12 Comparison between experimental and analytically predicted force components in ISF of truncated cone part of TA1: (a) whole process comparison and (b) detailed comparison in an enlarged time range.

As shown in Figure 4.13, the predicted force distribution in ISF of truncated pyramid part shows that the force gradually increases if the tool moves from the middle position of linear part to the corner as well as with the increase of forming depth/ drawing angle. A sudden increase of total force and force components is presented at the corner, where

the calculation follows the analysis and equations for biaxial tension condition area. The alternant variation can also be predicted in the distribution of x and y forces.

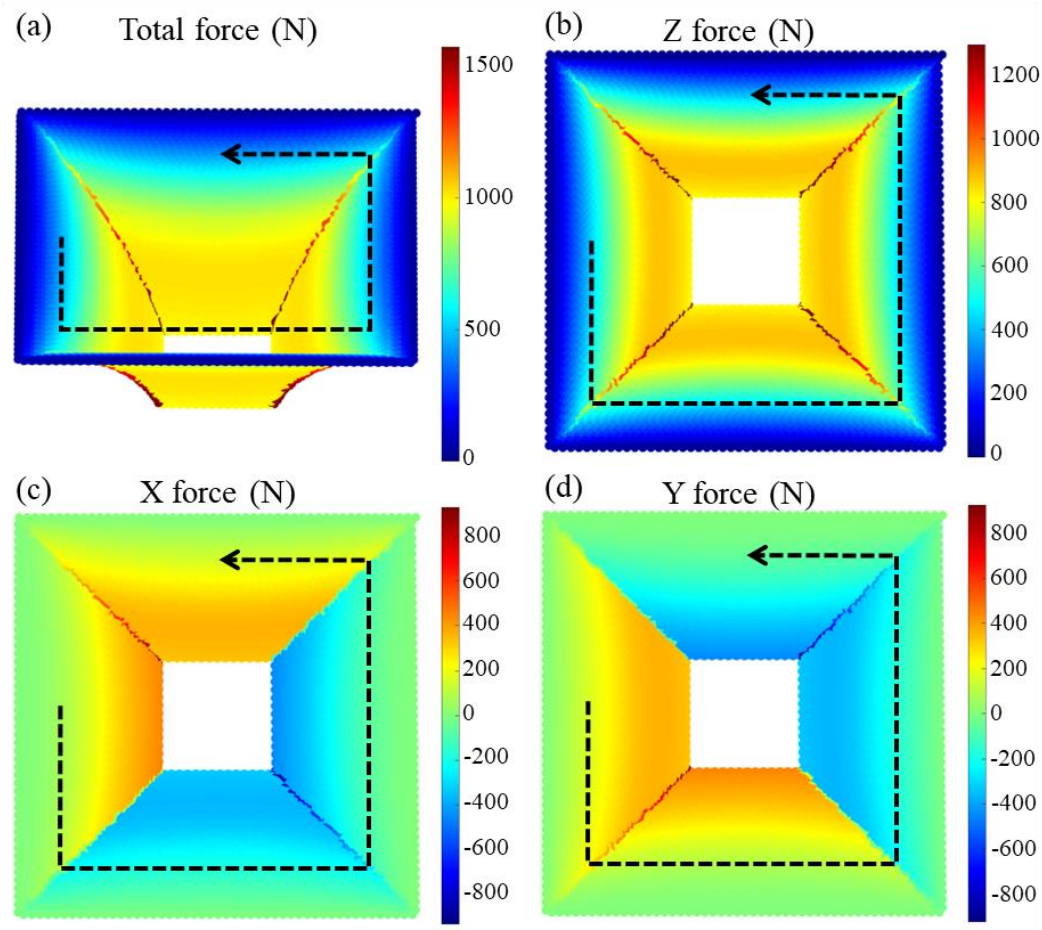


Figure 4.13 Analytically predicted results of (a) total force, (b) z force, (c) x force and (d) y force of different tool position in ISF of truncated pyramid part of TA1.

As shown by the solid curves in Figure 4.14, experimental z, x and y forces have significant fluctuation. Each time when the tool moves to the corner, the force would increase dramatically, which results from the change of deformation behaviour and the enhanced tool-sheet contact. However, at the linear part of pyramid, the force is comparable to that of truncated cone but only has some more frequent fluctuation. This clarifies that the deformation behaviour and contact condition at the linear part of the pyramid are the same as the truncated cone. The periodic fluctuation from the middle position of linear part to the position near the corner is a result of the change in bending

condition, which affects the actual drawing angle.

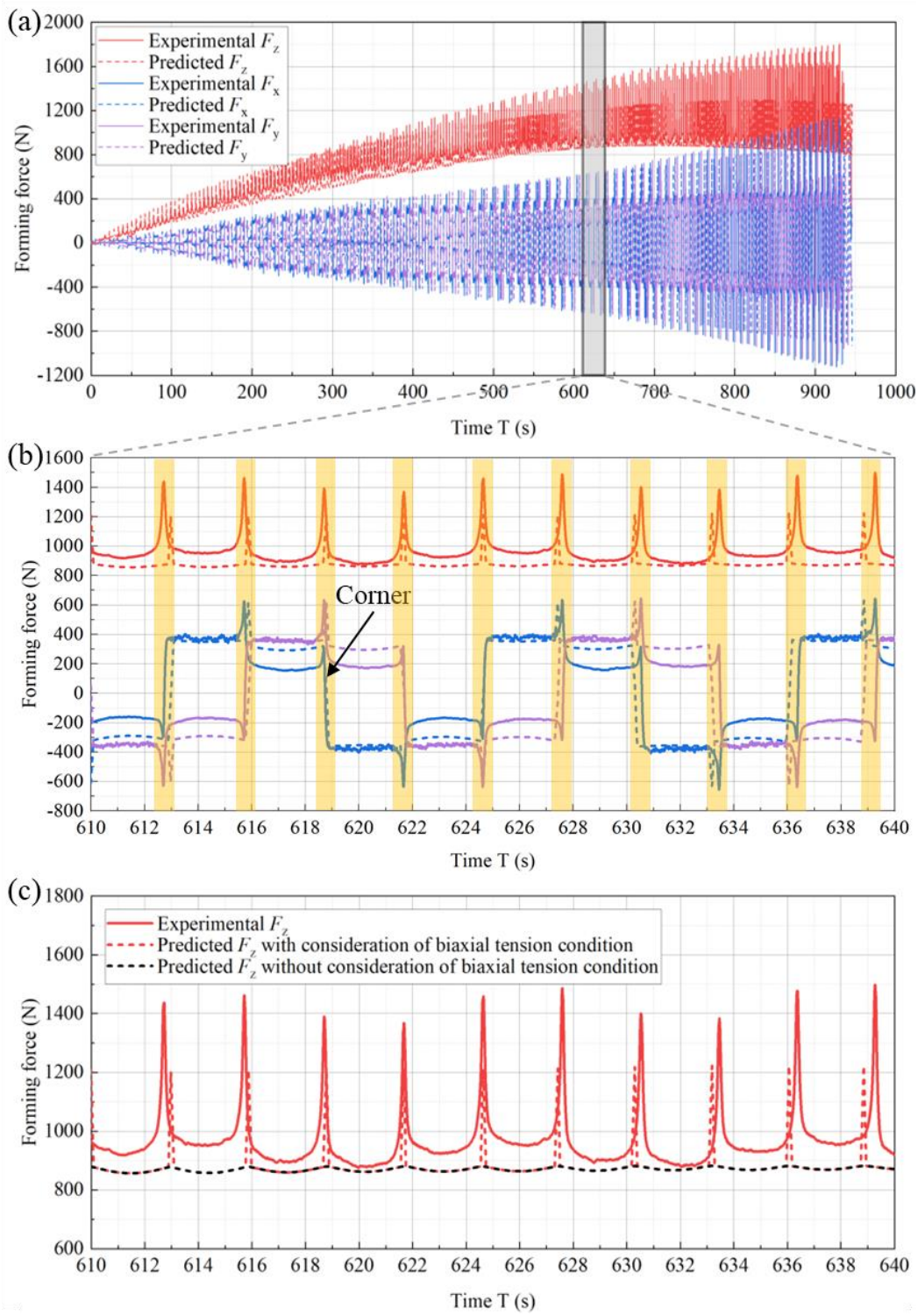


Figure 4.14 Comparison between experimental and analytically predicted force components in ISF of truncated pyramid part of TA1: (a) whole process comparison, (b) detailed comparison in an enlarged time range and (c) prediction with and without consideration of biaxial tension condition.

As shown in Figure 4.14(a) and (b), the comparison between predicted and experimental results shows a good correlation, no matter at linear or corner positions, in vertical or horizontal components. To further confirm the model validity and the prediction effect, only the model for plane strain condition area is used to predict the force in whole process. As presented by the dashed black curve in Figure 4.14(c), there is no sudden increase in z force but only slight fluctuation. This proves that if without the analytical modelling in biaxial tension condition area, the model is not able to predict the force change at the corner but can only describe the bending effect. This demonstrates that the analytical model successfully differentiates the force prediction for either plane strain or biaxial tension condition areas and clarifies that the severe fluctuation is mainly caused by the change of deformation mode and contact condition. By considering the effects of deformation condition, changed contact area and global bending, the analytical model shows the capability in predicting force variations and presenting the change characterisation of different force components.

4.3.2 Model validation from ISF of PEEK sheet

Different from metallic TA1 material, ISF of PEEK material is also used to confirm the validity of the developed analytical model. The experimental setup and process parameters for heat-assisted ISF of PEEK can be found in Sections 6.2.2 and 6.2.3 of Chapter 6. The drawing angles of the truncated cone shape vary from 22° to 88° and the dimension of PEEK sheet is 240 × 240 × 3 mm. The process parameters of ISF test of PEEK are preheating temperature 130 °C, tool radius 5 mm, spindle speed 100 rpm, feed rate 2350 mm/min and step size 1 mm. The coefficient of friction is assumed as 0.05. The Modified ZOP model I as given in Appendix B is used to describe the constitutive response of PEEK at 130 °C, the model parameters of which are given in Table 4.3. It is noteworthy that ZOP model is not used because it predicts the whole

deformation range including elastic and plastic deformation while the Modified ZOP model I omits the elastic deformation and can meet the requirement of stress calculation with plastic strain in the current analytical model. Besides, the change of strain rate and temperature is not considered within the developed analytical model, so the parameters related to strain rate and temperature change are also inapplicable in the constitutive relationship. The comparison between analytical and experimental results is shown in Figure 4.15.

Table 4.3 Model parameters of Modified ZOP model I for PEEK at 130 °C.

k	w	λ	n	μ	C_1	C_2
0.9473	68.75	11.99	0.8509	0.4458	-0.6403	1.771
α	K_1 (MPa)	K_2 (MPa)	m	a	B (MPa)	
167.4	78.65	42.18	—	—	39.24	

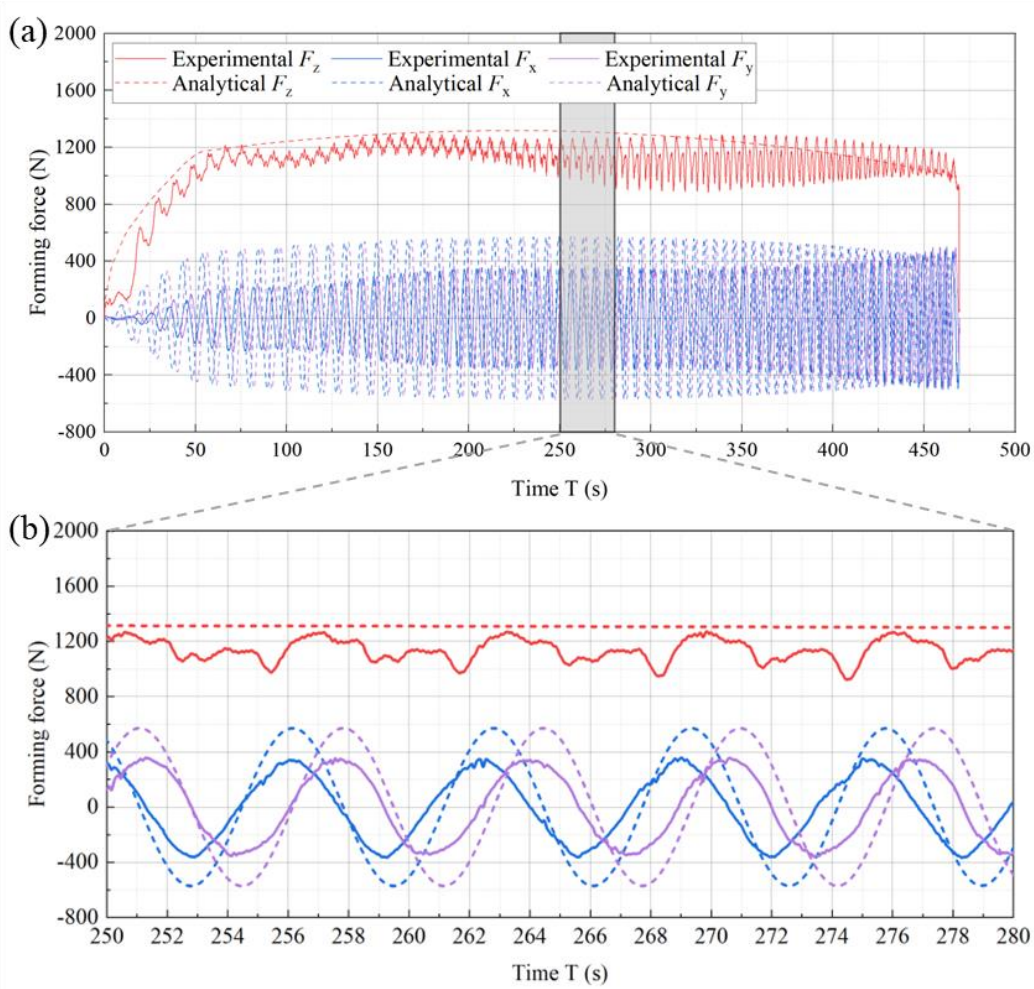


Figure 4.15 Comparison between experimental and analytically predicted force components in ISF of truncated cone part of PEEK: (a) whole process comparison and (b) detailed comparison in an enlarged time range.

Accurate prediction result is given by z force, while some discrepancy is observed in comparison of x and y forces. One reason may be the lack of consideration of local temperature rise due to friction heat generation and the effect on material softening. Another reason may be the inappropriate assumption of frictional coefficient, which plays an important role in calculation of horizontal forces as given by Equation (4.57) in Section 4.2.5.3. Besides, the analytical model may not have sufficient flexibility to effectively capture the slight change of deformation behaviour when thick PEEK sheet is formed in ISF. The effect of frictional coefficient on the prediction result is discussed in Section 4.4.1, and the effect of dimensional relationship between forming tool and

sheet thickness on the prediction accuracy is discussed in Section 4.4.2. Despite this, it may be concluded that the analytical model is applicable in z force prediction of heat-assisted ISF of PEEK material and would be more effective in x and y forces prediction if the local temperature rise is considered and accurate frictional coefficient is given.

4.3.3 Model validation in a practical application

To broaden the application of the analytical model, ISF-based manufacture of a cranial plate is used for further validation. As shown in Figure 4.16(a), the cranial plate, which is a customised asymmetric shape, was manufactured by ISF of 0.5 mm thickness TA1 sheet [141]. The experimental vertical and horizontal forces during the manufacture were measured by Lu et al. [141]. The analytical prediction and comparison with experimentally measured forces are given in Figure 4.16(b) – (e).

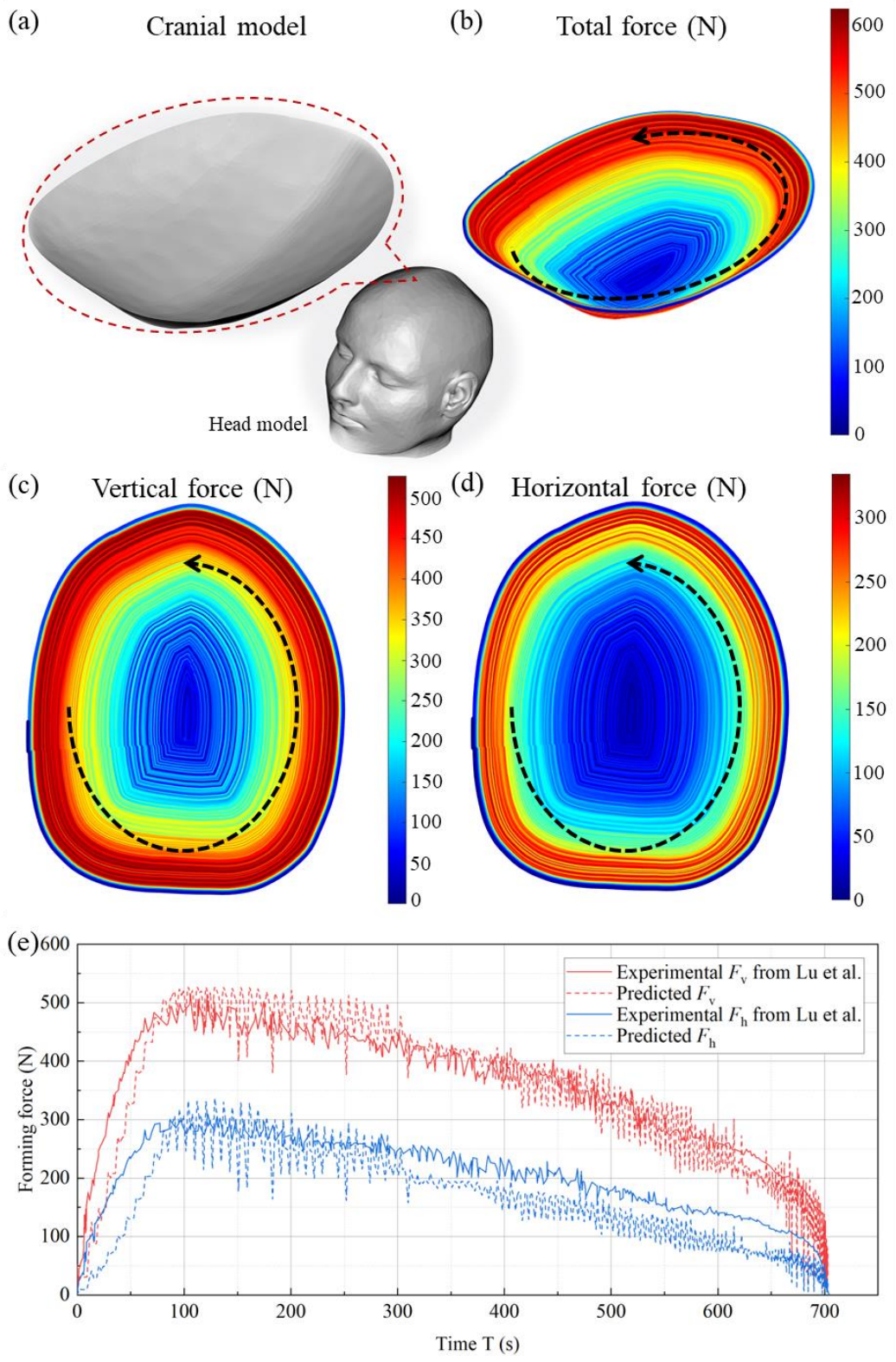


Figure 4.16 Application of the analytical model in ISF-based manufacture of cranial plate: (a) Head and cranial models, (b) prediction of total force, (c) prediction of vertical force, (d) prediction of horizontal force and (e) comparison between the experimentally measured vertical force F_v and horizontal force F_h from Lu et al. [141] and analytically predicted results.

Figure 4.16(b) – (d) presents the contour plot of the total, vertical and horizontal force variations, which has a sharp increase at the beginning and a gradual decreasing trend when the tool moves towards the part centre. This is also confirmed by Figure 4.16(e), where the solid and dashed curves represent experimental and analytical results, respectively. As shown by the red and blue dashed curves, the vertical and horizontal forces can be predicted with high accuracy. Moreover, the analytical model is effective to reflect the fluctuation, which is caused by drawing angle variation at the same layer and step size changes each layer due to the irregular cranial shape. It is noteworthy that the prediction of vertical force is totally determined with the predefined process parameters in tool path generation. However, the prediction accuracy of horizontal force partially depends on the coefficient of friction, which is an unknown factor even if the lubrication type is given. A value of 0.25 is used as the coefficient of friction in this analytical prediction. The effect of lubrication condition and friction coefficient on the prediction results is discussed in Section 4.4.1.

4.3.4 Model validation from ISF of AA1003-O sheet

The ISF testing results of AA3003-O by Duflou et al. [117] are used to validate the developed model. The tests of truncated cone parts were carried out with different parameters, and the base test had step size of 0.5 mm, tool radius of 5 mm, drawing angle of 50° and sheet thickness of 1.2 mm. The constitutive behaviour of AA3003-O is still described by Johnson-Cook model, parameters of which were derived based on the published test [142] and can be found in Table 4.1.

The predicted total force and the comparison with experimental results are given in Figure 4.17. The variation follows the same trend: at initial stage, the forming force continuously increases until a global bending induced peak force (F_p) is reached, and

after the peak, a reduction of forming force occurs followed by stable force afterwards. For different parameters, the predicted results of the analytical model can describe the varying trend well.

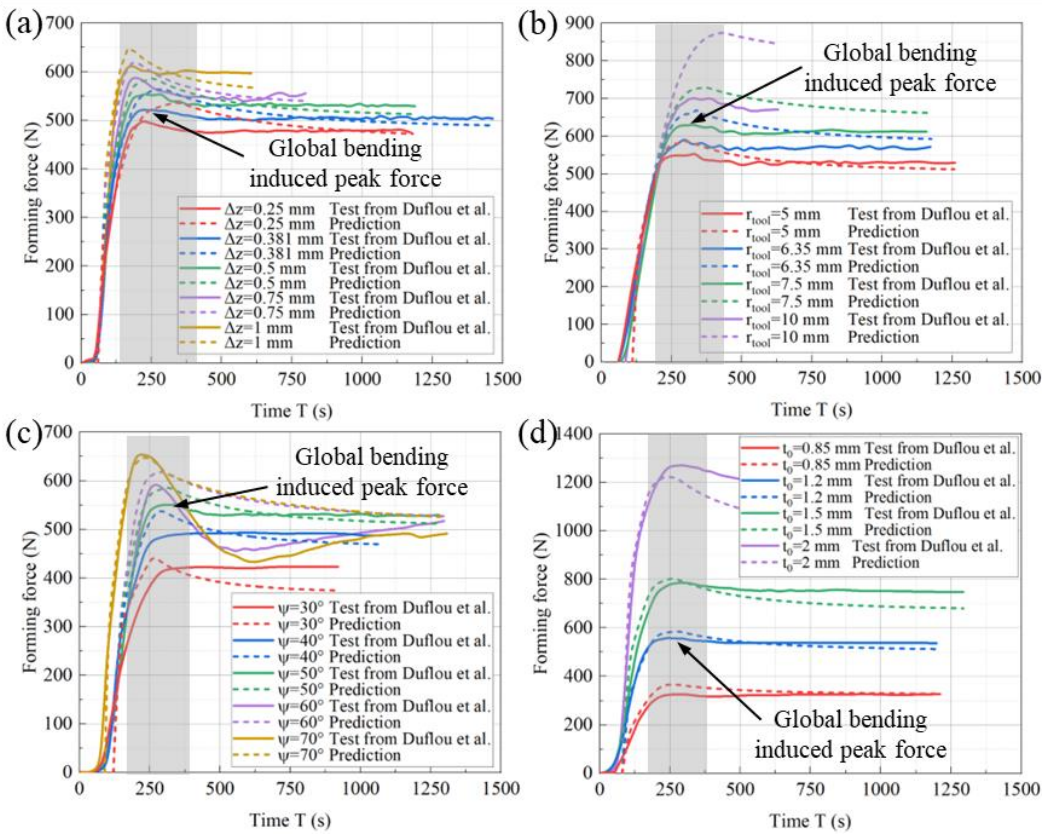


Figure 4.17 Experimentally measured total forces from Duflou et al. [117] and predicted results in ISF of AA3003-O with different (a) step size, (b) tool radius, (c) drawing angle and (d) sheet thickness.

As shown in Figure 4.17(a), both experimental and predicted results show that with the increase of step size, larger forming force are obtained. Figure 4.17(b) shows that larger tool radius increases forming force obviously, and with the increase of tool dimension, worse prediction effect is observed. In terms of different drawing angle, experimental results show that the peak force only appears when the drawing angle is larger than 50°. For the analytical results in dashed lines, the peak force exists at all drawing angles, but the peak becomes slightly less obvious at smaller drawing angles. It is noteworthy that at large drawing angles of 60° and 70°, the experimental curve presents an obvious

trough after peak. This may be caused by the sheet material wear [118], which is not involved in the current analytical model, so the predicted curve cannot reflect the corresponding effect. Finally, with the increase of sheet thickness, the forming force is increased dramatically, which is reflected by both the experimental and predicted results.

Figure 4.18 shows the comparison of peak and stabilised forces between experimental and prediction results. The effect of step size on both peak and stabilised forces are predicted effectively and the largest prediction error is 8.25% with step size of 1 mm. Among different tool radius, with values of 24.82% and 25.69%, the largest prediction errors of peak and stabilised forces appear when tool radius is 10 mm. While, with tool radius of 5 mm, the prediction errors are calculated as small as 5.96% and 3.27% for peak and stabilised forces, respectively. The effect of drawing angle on peak and stabilised forces is also predicted to have good agreement with experimental ones, with the largest error of 9.15% for the peak force and 11.45% for stabilised force. The peak force always rises with the increase of drawing angle, while there is a drop of stabilised force when larger drawing angles are used, which is reflected by the developed model. For different sheet thickness, the worst prediction accuracy of peak force appears at thickness of 0.85 mm with prediction error of 12.55%, while poor prediction of stabilised force is observed at 2 mm thickness with error of 15.24%. The above comparison demonstrates that the developed model has the capability to predict both stabilised and peak forces with high accuracy because of the consideration of both local deformation and global bending in ISF.

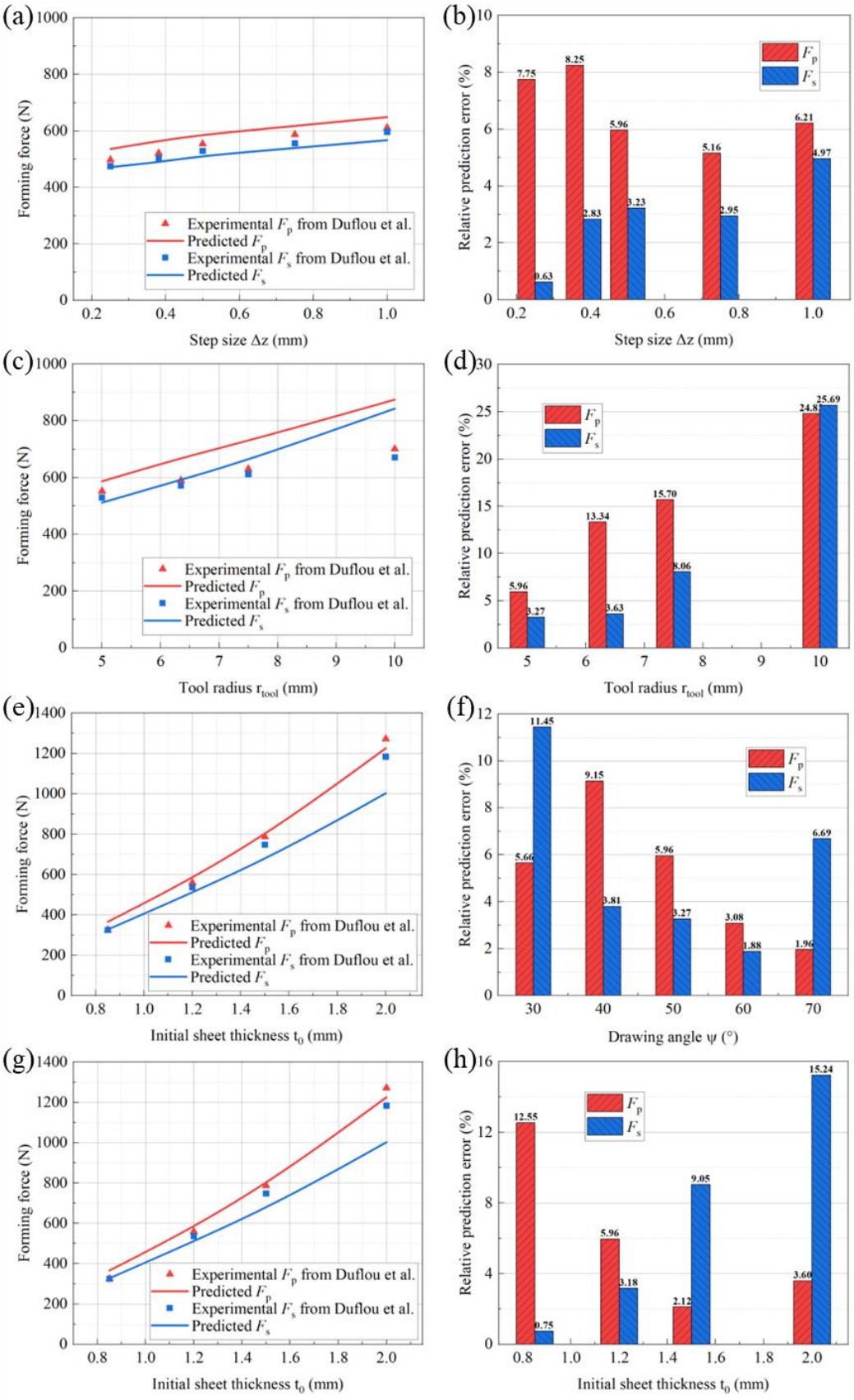


Figure 4.18 Comparison of peak F_p and stabilised forces F_s between experimentally measured results from Duflou et al. [117] and analytically predicted results in ISF of

AA3003-O with different (a) step size, (b) tool radius, (c) drawing angle and (d) sheet thickness.

4.3.5 Model validation of force components

The comparison between prediction and experimental results of the peak vertical (F_{v_p}), stabilized vertical (F_{v_s}) and horizontal forces is shown in Figure 4.19. The experimental data come from the study by Aerens et al. [119]. For different step size, the analytical model can predict the force components well, while the worst prediction results are given by the horizontal force, the largest error of which is 19.53%. As shown in Figure 4.19(c) and (d), when the tool radius is 10 mm, some discrepancy in peak and stabilised vertical forces is observed with prediction error of 25.77% and 27.19%. However, for smaller tool dimension, the prediction is more accurate. Figure 4.19(e) and (f) reveals that the tendency of force components with the increase of drawing angle is predicted well, especially the vertical component of peak force. While the prediction error of horizontal force shows large values at small drawing angles because of the low force level. As depicted in Figure 4.19(g) and (h), the analytical model exhibits higher accuracy with thinner sheet. ISF of 2 mm sheet shows the largest prediction deviation of peak vertical and horizontal forces, with error of 20.13% and 24.09%, respectively. The above analysis indicates that, the analytical model can predict the vertical and horizontal components of both peak and stabilised forces in different ISF conditions.

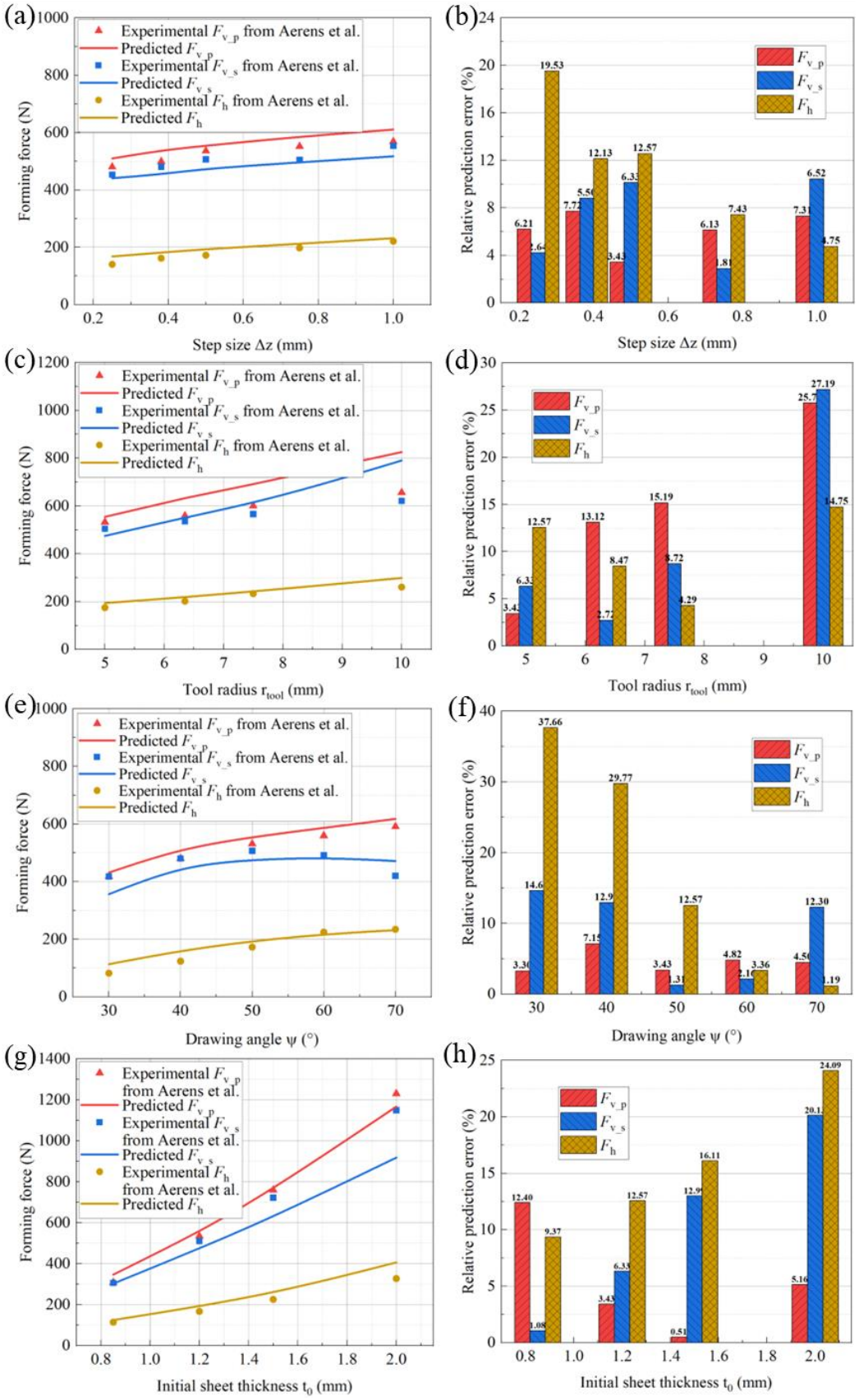


Figure 4.19 Comparison of force components between experimentally measured results from Aerens et al. [119] and analytically predicted results in ISF of AA3003-O with different (a) step size, (b) tool radius, (c) drawing angle and (d) sheet thickness.

4.3.6 Comparison among the analytical model and other models

As two of the representative studies for force prediction in ISF, Aerens et al. [119] model is experimental based, while Chang et al. [123] model were derived on the basis of theoretical analysis in ISF. In Aerens et al. model, the prediction equation of stabilized vertical force is expressed as following [119]:

$$F_{\mathrm{v_s}} = 0.0716 \cdot R_{\mathrm{m}} \cdot {t_0}^{1.57} \cdot {d_{\mathrm{tool}}}^{0.41} \cdot \Delta h^{0.09} \cdot \alpha \cdot \cos\alpha \tag{4.75}$$

where R_{m} is ultimate tensile strength, d_{tool} is tool diameter and Δh is scallop height.

Chang et al. model calculates the forming force as multiplication of the contact area and the through-thickness stress on neutral surface. The total force is decomposed to force components by projecting contact area in different directions on coordinate planes.

Distinctively, the new model is more focused on the deformation behaviour in ISF and decomposes the effect of different force components for separate calculation. The current model also considered the change of deformation condition, geometric feature, indentation effect, elastic recovery and global elastic bending effect, which are neglected in literature but important issues. The only similarity between Chang et al. model and this model is that both put the identification of contact region in an important position. Chang et al. model uses this to calculate the size of contact area, but the new model uses the defined region to calculate the localised shear force.

Adjusted coefficient of determination (R^2_{adj}) and root mean square error ($RMSE$) are used to evaluate and compare the models. Larger R^2_{adj} and smaller $RMSE$ indicate more accurate prediction. As shown in Figure 4.20, the evaluation and comparison are made based on vertical force results in ISF of AA3003-O by Aerens et al. [119].

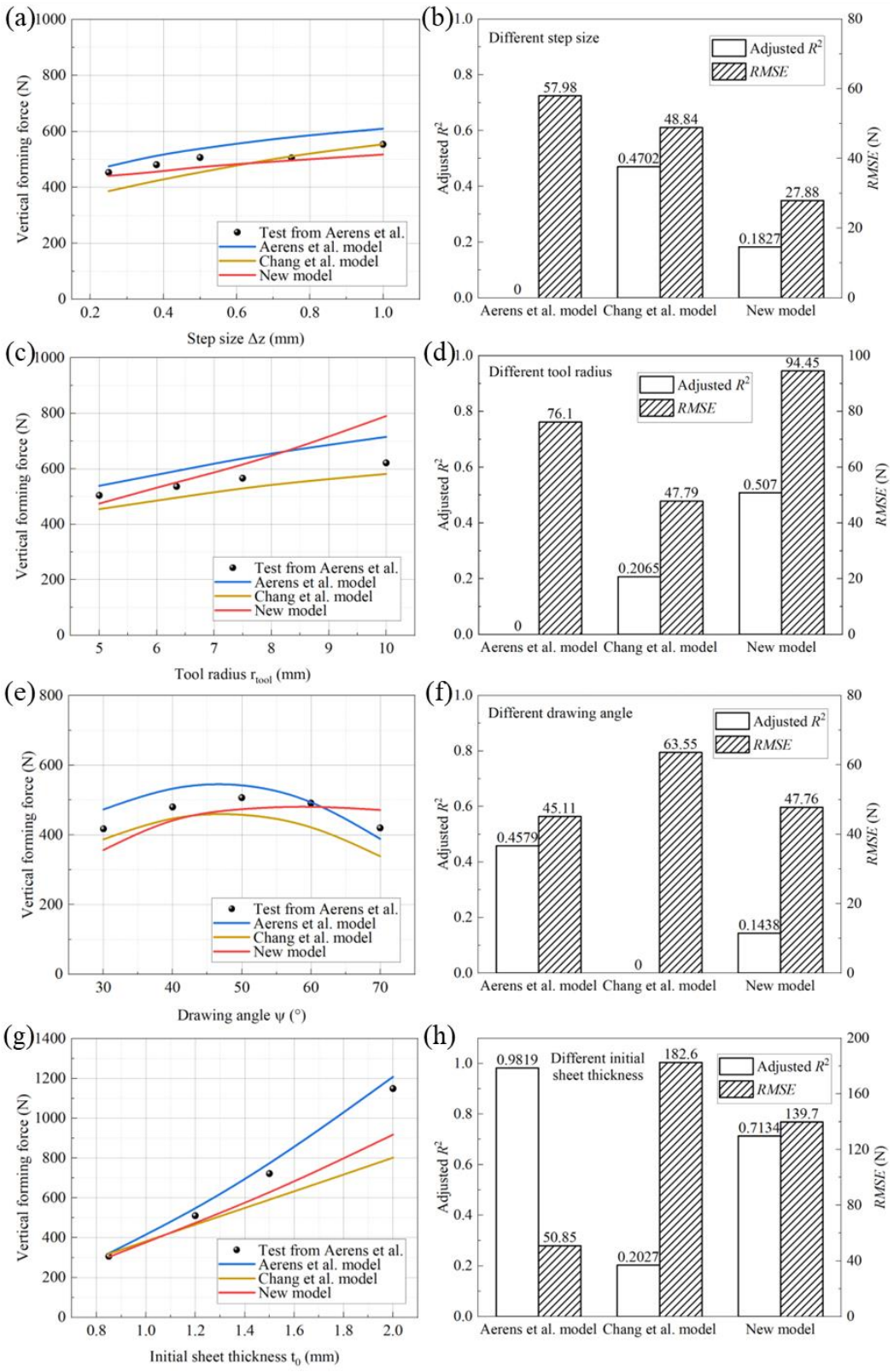


Figure 4.20 Comparisons of vertical forming force predicted by different models at different (a), (b) step size, (c), (d) tool radius, (e), (f) drawing angle and (g), (h) sheet thickness based on testing results in ISF of AA3003-O by Aerens et al. [119].

For different step size, the prediction results of the new model have better agreement

with experimental results than Aerens et al. and Chang et al. models when the step size is smaller than 0.75 mm, but shows worse accuracy with step size of 1 mm. The R^2_{adj} value of the new model is 0.1827, which is smaller than Chang et al. model, and this may be a result that the prediction results by the new model are always smaller than experimental results. However, the smallest $RMSE$ of 27.88 N indicates the good prediction effect of the new model. For different tool dimensions, the best prediction is provided by the new model at tool radius smaller than 7.5 mm. At a tool radius of 10 mm, the predicted force by the new model shows the largest deviation, which also leads to the largest $RMSE$. As presented in Figure 4.20(e), more accurate prediction is given by the new model at medium and high drawing angles, especially from 40° to 60°. The medium R^2_{adj} and $RMSE$ of the new model in Figure 4.20(f) indicate that the new model can give better prediction than Chang et al. model but is less accurate than Aerens et al. model for different drawing angles. For different sheet thickness, the best prediction is made by Aerens et al. model, while the new model could achieve the best prediction accuracy for ISF of thin sheet with thickness of 0.85 mm and 1.2 mm. It is noteworthy that in some cases the R^2_{adj} values of the compared models are 0, and this may be caused by that the prediction is always larger or smaller than experiment.

It could be concluded that in the current study the new model makes better prediction than Aerens et al. and Chang et al. models, especially in common ISF conditions, although these two models may perform better in a few ISF cases such as with step size of 1 mm, tool radius of 10 mm, drawing angle of 30° and sheet thickness of 2 mm. The discrepancy in prediction in the above uncommonly-used cases may be caused by the linear distribution assumption of the thickness in both meridional and circumferential directions and the insufficient flexibility in reflecting the dimensional relationship between the tool radius and sheet thickness, which causes the change of the deformation

mechanism in ISF as discussed in Section 4.4.2.

Different from Aerens et al. and Chang et al. models, the new analytical model provides a totally new modelling method, which is an important contribution to the ISF research. The new model could help to reveal and understand the complicated and instable deformation behaviour from both local and global aspects by comprehensively considering deformation state, contact condition, local plastic deformation and global elastic bending, which are previously neglected but important issues in ISF. The consideration of both local plastic deformation and global elastic bending makes the new model capable of reflecting the forming force history including the peak force, which is not involved in the comparison because the other two models are unable to do this. This is another contribution of the new analytical model compared with Aerens et al. and Chang et al. models.

4.4 Discussions

4.4.1 Effect of lubrication condition

In the developed analytical model, the friction coefficient between forming tool and sheet material also has an influence on the forming force. As there are only lubricant types but no definite friction coefficient given in previous publications, only a sensitivity analysis on the effect of friction coefficient is discussed without detailed validation. The analytical force history, stabilised total force, and force components with different friction coefficient can be found in Figure 4.21. Other process conditions of the studied cases are the same as the base test as given in Section 4.3.3.

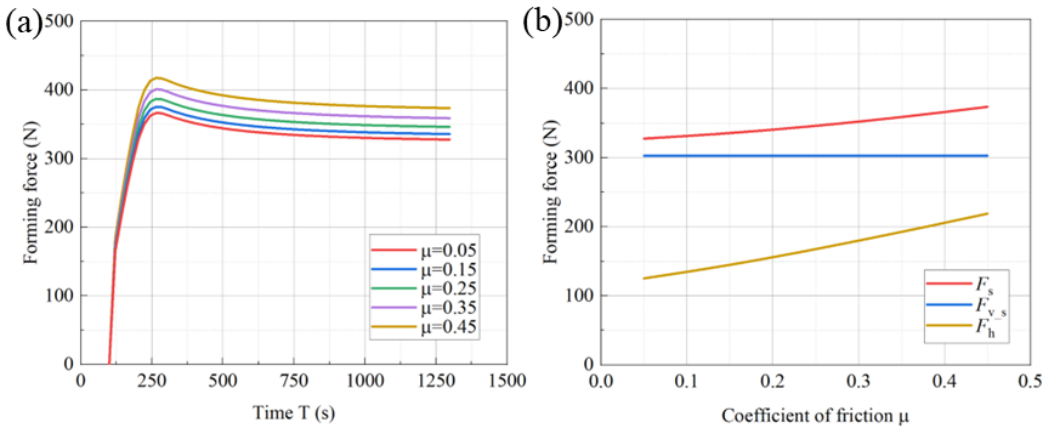


Figure 4.21 Effect of friction coefficient on (a) forming force history and (b) stabilised total force and force components.

As observed, the friction coefficient does not have any influence on the vertical force but has an obvious influence on the horizontal force. This is also indicated by the analytical modelling process. As the horizontal force is much smaller than the vertical force, the total force is not obviously influenced by friction coefficient, i.e., lubrication condition. In the analytical results, a wide range of friction coefficients are applied, only slight change of the total force is observed. This is consistent with the testing result from Duflou et al. [117], in which, with the use of lubricants, the peak force varied between 350 N and 365 N and the stabilised force was about 320 N in all cases. It is only in the case with no lubricant used that the peak force reached 375 N. Therefore, the lubrication condition may have a notable influence on the horizontal force and the accurate identification of friction coefficient between forming tool and sheet material in ISF plays an important role in the prediction of horizontal force, which may be beneficial to the improvement of the analytical model.

4.4.2 Effect of the tool-sheet interaction on prediction accuracy

As investigated by Silva et al. [66], the interaction between sheet thickness and tool radius has an influence on material formability, deformation, and fracture behaviour. In Section 4.3, the prediction accuracy of the developed analytical model is reduced with

the increase of the tool radius and the sheet thickness. When the sheet is relatively thin compared to the tool dimension, the local deformation may be close to the behaviour in stretch forming, where stretching, bending and through-thickness shearing dominate the material deformation. The indentation effect becomes more obvious when the sheet thickness is larger in ISF. This makes a slight change of deformation behaviour in ISF, which is essential to the analytical derivation of the model. Therefore, the ratio between the tool radius and the sheet thickness r_{tool}/t_0 should be considered as an important parameter in ISF. Figure 4.22 gives the effect of ratio r_{tool}/t_0 on the comparison between the analytical results and experimental stabilised force F_{s} and peak force F_{p} from Duflou et al. [117] in ISF of AA3003. With ratio r_{tool}/t_0 from 4.16 to 5.88, there are two prediction values for a certain r_{tool}/t_0. Although the ratio r_{tool}/t_0 is the same, the tool radius and sheet thickness are different and this leads to different predicted forces, which are obtained with the given tool radius and sheet thickness instead of the ratio r_{tool}/t_0. As shown in Figure 4.22, for ISF of AA3003-O, the most favourable prediction of the stabilised force F_{s} is given when the ratio r_{tool}/t_0 reaches 3.3, while the ratio of 5.88 gives the most accurate prediction of the peak force F_{p}. In the conditions of smaller or larger ratio r_{tool}/t_0, less accurate prediction is observed, which reflects that the developed model does not have enough flexibility to capture the change of local deformation behaviour due to the tool-sheet dimensional relationship. Therefore, further improvement is needed to make the analytical model more robust in more extensive range of tool dimension and sheet thickness.

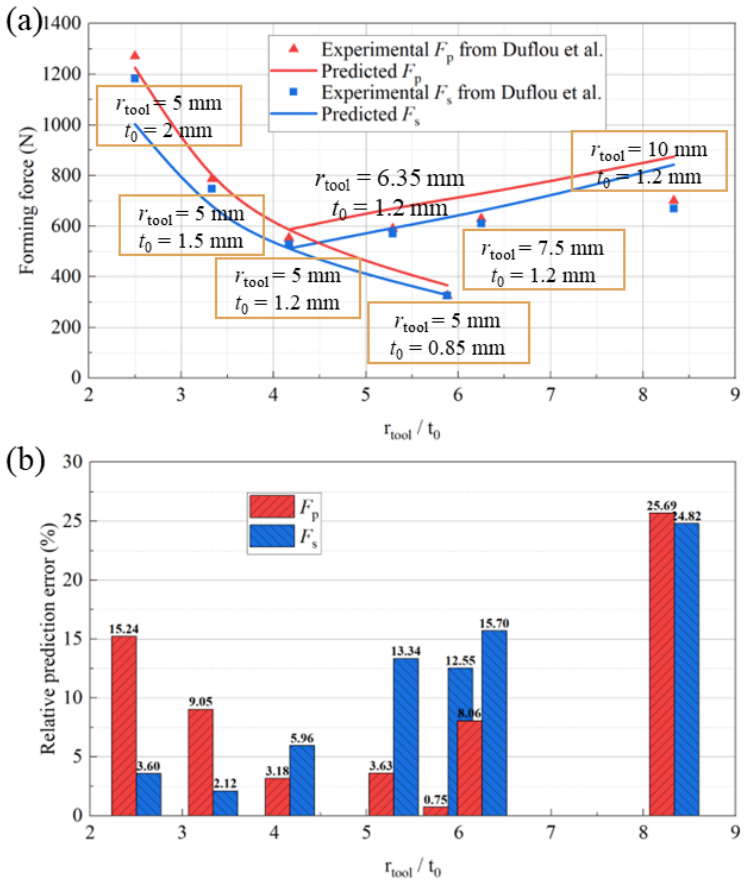


Figure 4.22 Effect of ratio r_{tool}/t_0 on (a) comparison between predicted stabilised force F_{s} and peak force F_{p} and experimental results from Duflou et al. [117] and (b) prediction errors of peak and stabilised forces.

4.5 Conclusions

The main conclusions of this chapter can be drawn as follows:

(1) A new force prediction model is developed and implemented for ISF with analytical method by revealing the deformation mechanism and localised tool-sheet contact. The validity is confirmed by a series of ISF tests with different shapes, materials, and process parameters.

(2) Deformation state, contact condition, thickness distribution under contact, local material deformation and global elastic bending/ deflection are cooperatively considered in the analytical model. The factors are proven to be essential in predicting forming

force history and force components in ISF. This work also presents the first attempt of the peak force prediction, which is well validated.

(3) The analytical model enables detailed prediction of forming force components and gives a direct correlation to different material deformation modes. The experimental data and prediction results show distinctive characterisations of both the vertical and horizontal forces in forming different geometries under plane strain and biaxial tension conditions.

(4) The selection of frictional coefficient and the interaction between tool dimension and sheet thickness may affect the prediction results. The prediction accuracy can be further improved by more precise measurement of frictional coefficient and more flexible reflection of tool-sheet dimensional relationship.

Chapter 5 Analytical Modelling and Validation of Local Contact Pressure Distribution in Incremental Sheet Forming

Nomenclature

Symbol	Term	Unit
r	Distance from studied position to tool centre	mm
φ	Angle from studied position to tool axis	rad
θ	Angle from workpiece meridional cross-section to studied	rad
r_{tool}	Radius of the forming tool	mm
t_0	Initial sheet thickness	mm
α	Actual drawing angle	rad
β	Indentation angle in the tool circumferential direction	rad
β_1	Angle induced by forming tool increment in workpiece meridional direction	rad
n	Material strain hardening exponent	
Δz	Step size	mm
$\varphi_{\text{OD}}(\theta)$	Expression of coordinate φ by coordinate θ in overlapping deformation region	rad
$\varphi_{\text{ND}}(\theta)$	Expression of coordinate φ by coordinate θ in	rad

	non-overlapping deformation region	
$\varphi_{\mathrm{ERL}}(\theta)$	Expression of coordinate φ by coordinate θ in left part of elastic recovery region	rad
$\varphi_{\mathrm{ERR}}(\theta)$	Expression of coordinate φ by coordinate θ in right part of elastic recovery region	rad
S	Size of contact area	mm^2
$r_{\max}$	r coordinate of the maximum pressure position	mm
$\varphi_{\max}$	φ coordinate of the maximum pressure position	rad
$\theta_{\max}$	θ coordinate of the maximum pressure position	rad
p	Contact pressure	MPa
$p_{\max}$	Maximum contact pressure	MPa
d	Distance from the central position to the studied position in contact	mm
a	Radius of the circular contact region in contact	mm
$\bar{\sigma}$	Equivalent stress of sheet material	MPa
F	Forming force	N
N	Reciprocal of the strain hardening exponent	
S_{P}	Projected size of contact area	mm^2

P	Studied position in contact	
P_{max}	Maximum pressure position in contact	
P_b	Boundary position in contact	
d_b	Distance from maximum pressure position P_{max} to the contact boundary P_b via the studied position P	mm
λ	Correction factor on the reciprocal of strain hardening exponent in expression of contact pressure	
r_b	r coordinate of boundary position P_b	mm
φ_b	φ coordinate of boundary position P_b	rad
θ_b	θ coordinate of boundary position P_b	rad
P_1, P_2, P_3, P_4	Four points equally dividing the distance from the maximum pressure position to the boundary of contact region	
δ	Angle from the line between maximum pressure position and central position to the line between maximum pressure position and boundary position	rad
m	Number of equally divided parts from maximum pressure position to boundary position	

5.1 Introduction

In the study of ISF, investigations of deformation mechanism, fracture behaviour and tool wear are some of the key issues to promote the development of this promising manufacturing technology. As all the material deformation is driven by the local interaction, the study of local contact behaviour between forming tool and sheet material can be useful to reveal the above-mentioned issues. Moreover, the contact stress/ pressure distribution has an influence on the stress state and stress triaxiality under deformation. The prediction of contact pressure distribution can provide a fundamental insight into the fracture prediction.

In Chapter 4, an analytical model is developed to predict the forming force in ISF processes by looking into the deformation mechanism of ISF. Using the same approach established in Chapter 4, this chapter is focused on the analytical modelling and validation of the contact area and pressure distribution. By modelling the contact regions, the size of contact area, maximum contact pressure and pressure distribution, the local tool-sheet contact behaviour is investigated and predicted. The developed analytical model is validated by comparison with FE simulation for ISF of TA1 sheet and heat-assisted ISF of PEEK sheet. Based on the understanding of local tool-sheet contact in ISF, some aspects for further improvement of the analytical model are given.

5.2 Analytical model of the contact pressure distribution

5.2.1 Modelling of contact region

As investigated in Chapter 4, the contact regions in ISF can be divided into three different parts: OD, ND and ER regions, as illustrated in Figure. 5.1.

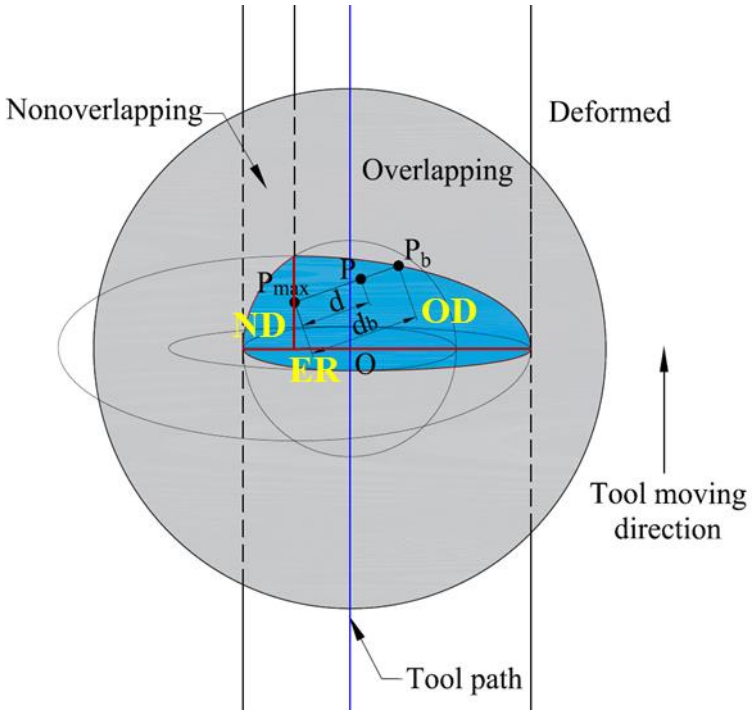


Figure 5.1 Contact region and maximum pressure position in ISF.

The boundaries of the OD region, ND region, right part of ER region (ERR) and left part of ER region (ERL) have the following expressions, respectively, as derived in Chapter 4:

$$\frac{(\sin\varphi\cdot cos\theta+\sin\beta_1)^2}{(\sin\alpha+\sin\beta_1)^2}+\frac{(\sin\varphi\cdot\sin\theta)^2}{(\sin\beta)^2-(\sin\beta_1)^2}=1 \tag{5.1}$$

$$\varphi=\beta \tag{5.2}$$

$$\frac{(\sin\varphi\cdot\cos\theta)^2}{(\sin\alpha)^2}+\frac{(r_{\text{tool}}\cdot\sin\varphi\cdot\sin\theta)^2}{r_{\text{tool}}{}^2-\left[\exp\left(\frac{\sqrt{3}}{2}\cdot\frac{\bar{\sigma}(\bar{\varepsilon}_c)}{E}\right)-1\right]^2\cdot\left[\frac{t_0\cdot(1-\cos\alpha)\cdot\beta}{\alpha+\beta}\right]^2}=1 \tag{5.3}$$

$$\frac{(\sin\varphi\cdot\cos\theta)^2}{(\sin\beta)^2}+\frac{(r_{\text{tool}}\cdot\sin\varphi\cdot\sin\theta)^2}{r_{\text{tool}}{}^2-\left[\exp\left(\frac{\sqrt{3}}{2}\cdot\frac{\bar{\sigma}(\bar{\varepsilon}_c)}{E}\right)-1\right]^2\cdot\left[\frac{t_0\cdot(1-\cos\alpha)\cdot\beta}{\alpha+\beta}\right]^2}=1 \tag{5.4}$$

where φ is the angle from studied position to the tool axis, θ is the angle from workpiece meridional cross-section to the studied position, r_{tool} is the radius of the forming tool, t_0 is the initial sheet thickness, α is the actual drawing angle and β is the indentation angle in circumferential direction as calculated by Equation (5.5), β_1 is the

angle induced by the meridional increment of the forming tool and the relationship between β and β_1 can be expressed as Equation (5.6), $\bar{\sigma}$ is the equivalent stress determined by the constitutive relationship and $\bar{\varepsilon}_c$ is the mean equivalent strain at the tool centre position as expressed by Equation (5.7):

$$\beta = \frac{1}{2} \cdot \left[\sqrt{\alpha^2 + \frac{8 \cdot t_0 \cdot (1 - \cos\alpha) \cdot [1 + \exp(5n-1)]}{\exp(5n-1)}} - \alpha \right] \tag{5.5}$$

$$\beta_1 = \arcsin\left(\sin\beta - \frac{\Delta z}{r_{\text{tool}} \cdot \tan\alpha} \right) \tag{5.6}$$

$$\bar{\varepsilon}_c = \frac{2}{\sqrt{3}} \cdot \ln \frac{t_0 \cdot \sqrt{r_{\text{tool}}}}{\left[t_0 - \frac{t_0 \cdot (1 - \cos\alpha) \cdot \beta}{\alpha + \beta} \right] \cdot \sqrt{r_{\text{tool}} + t_0 - \frac{t_0 \cdot (1 - \cos\alpha) \cdot \beta}{\alpha + \beta}}} \tag{5.7}$$

where, n is the material strain hardening exponent and Δz is the step size.

For different contact regions, by solving Equations (5.1) – (5.4), the coordinate φ can be expressed by the coordinate θ as: $\varphi_{\text{OD}}(\theta)$ when $0 \le \theta \le \arccos\left(-\frac{\sin\beta_1}{\sin\beta}\right)$; $\varphi_{\text{ND}}(\theta)$ when $\arccos\left(-\frac{\sin\beta_1}{\sin\beta}\right) \le \theta \le \pi$; $\varphi_{\text{ERL}}(\theta)$ when $\pi \le \theta \le \frac{3}{2} \cdot \pi$; $\varphi_{\text{ERR}}(\theta)$ when $\frac{3}{2} \cdot \pi \le \theta \le 2 \cdot \pi$. The size of contact area (S) can be calculated by performing integration with the use of $\varphi_{\text{OD}}(\theta)$, $\varphi_{\text{ND}}(\theta)$, $\varphi_{\text{ERL}}(\theta)$ and $\varphi_{\text{ERR}}(\theta)$:

$$S = \int_0^{\arccos\left(-\frac{\sin\beta_1}{\sin\beta}\right)} \frac{1}{2} \cdot [r_{\text{tool}} \cdot \varphi_{\text{OD}}(\theta)]^2 \, \mathrm{d}\theta + \int_{\arccos\left(-\frac{\sin\beta_1}{\sin\beta}\right)}^{\pi} \frac{1}{2} \cdot [r_{\text{tool}} \cdot \varphi_{\text{ND}}(\theta)]^2 \, \mathrm{d}\theta +$$

$$\int_{\pi}^{\frac{3}{2}\pi} \frac{1}{2} \cdot [r_{\text{tool}} \cdot \varphi_{\text{ERL}}(\theta)]^2 \, \mathrm{d}\theta + \int_{\frac{3}{2}\pi}^{2 \cdot \pi} \frac{1}{2} \cdot [r_{\text{tool}} \cdot \varphi_{\text{ERR}}(\theta)]^2 \, \mathrm{d}\theta \tag{5.8}$$

In the tool movement along the circumferential direction, as the maximum deformation happens at the intersection layer between OD and ND regions, the maximum pressure position is analysed to be located at this intersection. Meanwhile, referring to the fact that in spherical indentation, the maximum pressure is always observed at the central position, the midpoint of the intersection line between OD and ND regions is analysed

to be the maximum pressure position. As the interaction point between boundaries of OD and ND regions has the coordinates of $(r_{\text{tool}}, \beta, \arccos\left(-\frac{\sin\beta_1}{\sin\beta}\right))$, the coordinates of the maximum pressure position $(r_{\max}, \varphi_{\max}, \theta_{\max})$ are derived as:

$$r_{\max} = r_{\text{tool}} \tag{5.9}$$

$$\varphi_{\max} = \arcsin\sqrt{\frac{1}{4}\cdot(\sin\beta)^2 + \frac{3}{4}\cdot(\sin\beta_1)^2} \tag{5.10}$$

$$\theta_{\max} = \pi - \arctan\sqrt{\frac{1}{4}\cdot\left(\frac{\sin\beta}{\sin\beta_1}\right)^2 - \frac{1}{4}} \tag{5.11}$$

The derivation of contact boundaries, contact area size and maximum pressure position provides the fundamental of the modelling of contact pressure distribution.

5.2.2 Modelling of contact pressure distribution

Hertz contact theory [143] provides Equation (5.12) to calculate contact pressure p in spherical indentation of elastic rigid half-space.

$$p(d) = p_{\max}\cdot\left(1 - \frac{d^2}{a^2}\right)^{1/2} \tag{5.12}$$

where, $p_{\max}$ is the maximum contact pressure, d is the distance from the central position to the studied position, and a is the radius of the circular contact region as shown in Figure 5.2.

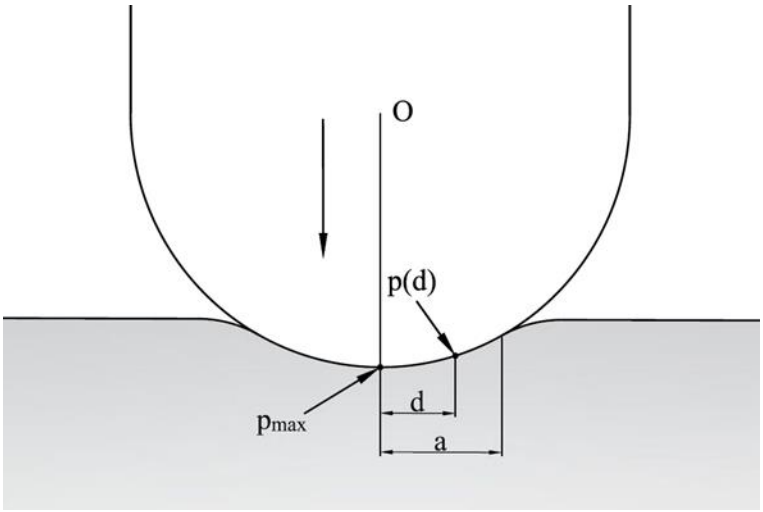


Figure 5.2 Illustration of contact between a rigid hemispherical tool and an elastic/ elastic-plastic half space.

Differently, the tool-sheet contact in ISF makes the material deformation in elastic-plastic regime rather than fully elastic regime. Meanwhile, the contact region in ISF has much more complicated shape rather than a simple circular shape. At last, the sheet material is relatively thin compared to the tool dimension and is in a free-standing condition when the forming tool comes into contact with the sheet. Therefore, the development of contact pressure expression in ISF should consider the above three differences.

For spherical indentation of a rigid half-space of strain hardening materials in elastic-plastic regime, the contact pressure distribution can be expressed by the following equation [144]:

$$p(d) = p_{\max} \cdot \left(1 - \frac{d^2}{a^2}\right)^{1/(2 \cdot N)} \tag{5.13}$$

where,

$$p_{\max} \approx \frac{2 \cdot N + 1}{2 \cdot N} \cdot 2.84 \cdot \bar{\sigma} \tag{5.14}$$

for fully plastic regime [145-147], or,

$$p_{\max} = \frac{2 \cdot N + 1}{2 \cdot N} \cdot \frac{F}{S_{\mathrm{P}}} \tag{5.15}$$

for elastic-plastic or fully plastic regimes [144, 148]. $\bar{\sigma}$ is the equivalent stress of sheet material, F is the forming force, N is the reciprocal of the strain hardening exponent n by $N = \frac{1}{n}$. $N = 1$ for fully elastic contact and $N = +\infty$ for perfectly plastic materials [144]. F and S_{P} in Equation (5.15) are the forming force and the projected size of contact area in the indentation direction, respectively. The first calculation method of maximum contact pressure by Equation (5.14) is an approximation equation while the second method by Equation (5.15) is based on the relationship with the mean contact pressure.

In the derivation of contact pressure in ISF, an assumption is made that the sheet material is under fully plastic deformation under tool-sheet contact. Referring to Equation (5.13), the pressure distribution between forming tool and sheet material in ISF may have the following equations:

$$p(d) = p_{\max} \cdot \left[1 - \left(\frac{d}{d_{\mathrm{b}}}\right)^2\right]^{1/(2 \cdot N)} \tag{5.16}$$

where, d_{b} is the distance from the maximum pressure position $\mathrm{P_{max}}$ to the contact boundary $\mathrm{P_b}$ via the studied position P as illustrated in Figure 5.1. As illustrated by Figure 5.3, according to the assumption, the sheet material under tool contact including to maximum pressure position is under fully plastic deformation, while other areas out of the contact region is under slight elastic deflection/ deformation. The calculation of maximum contact pressure $p_{\max}$ in ISF condition may follow Equation (5.14). In ISF condition, $\bar{\sigma}$ in Equation (5.14) is calculated as $\bar{\sigma}(\mathrm{P_{max}})$ by the constitutive relation and the equivalent strain at the maximum pressure position $\mathrm{P_{max}}$ based on the derivations of strain distribution in Chapter 4.

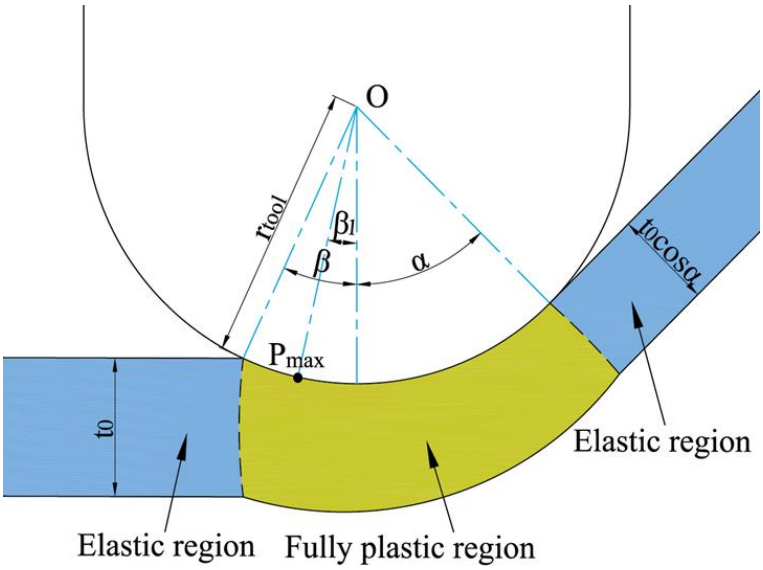


Figure 5.3 Illustration of elastic-plastic contact between forming tool and sheet material in ISF.

On the other hand, Equation (5.15) should be still applicable in fully plastic contact. However, the calculation of $p_{\max}$ with the above two methods show obvious difference, which may come from the nonuniform thickness distribution and the tool motion increment in circumferential and meridional directions. Therefore, an adaption of the calculation method based on mean contact pressure may be proposed with a correction factor λ on the reciprocal of strain hardening exponent and the following equation is obtained:

$$\frac{2\cdot N+1}{2\cdot N}\cdot 2.84\cdot \bar{\sigma}(\mathrm{P_{max}}) = \frac{2\cdot\lambda\cdot N+1}{2\cdot\lambda\cdot N}\cdot\frac{F}{S_\mathrm{P}} \tag{5.17}$$

where S_P in ISF can be calculated as the following equation:

$$S_\mathrm{P} = \int_0^{\arccos\left(-\frac{\sin\beta_1}{\sin\beta}\right)}\frac{1}{2}\cdot[r_{\mathrm{tool}}\cdot\sin\varphi_{\mathrm{OD}}(\theta)]^2\,\mathrm{d}\theta + \int_{\arccos\left(-\frac{\sin\beta_1}{\sin\beta}\right)}^{\pi}\frac{1}{2}\cdot[r_{\mathrm{tool}}\cdot \sin\varphi_{\mathrm{ND}}(\theta)]^2\,\mathrm{d}\theta + \int_{\pi}^{\frac{3}{2}\cdot\pi}\frac{1}{2}\cdot[r_{\mathrm{tool}}\cdot\sin\varphi_{\mathrm{ERL}}(\theta)]^2\,\mathrm{d}\theta + \int_{\frac{3}{2}\pi}^{2\cdot\pi}\frac{1}{2}\cdot[r_{\mathrm{tool}}\cdot \sin\varphi_{\mathrm{ERR}}(\theta)]^2\,\mathrm{d}\theta \tag{5.18}$$

By solving Equation (5.17), the correction factor may be calculated as following:

$$\lambda = \frac{F}{(2\cdot N+1)\cdot 2.84\cdot \bar{\sigma}(\mathrm{P_{max}})\cdot S_\mathrm{P} - 2\cdot N\cdot F} \tag{5.19}$$

Finally, the contact pressure distribution in ISF may be expressed as Equations (5.20) or (5.21):

$$p(d) = \frac{2\cdot\lambda\cdot N+1}{2\cdot\lambda\cdot N}\cdot\frac{F}{S_\mathrm{P}}\cdot\left[1-\left(\frac{d}{d_\mathrm{b}}\right)^2\right]^{1/(2\cdot\lambda\cdot N)} \tag{5.20}$$

$$p(d) = \frac{2\cdot N+1}{2\cdot N}\cdot 2.84\cdot\bar{\sigma}(\mathrm{P_{max}})\cdot\left[1-\left(\frac{d}{d_\mathrm{b}}\right)^2\right]^{1/(2\cdot\lambda\cdot N)} \tag{5.21}$$

5.2.3 Implementation method

Considering the complexity of the developed models for contact region, maximum pressure position and pressure distribution, point based method is used to implement the analytical model in MATLAB, the illustration of which is shown as Figure 5.4.

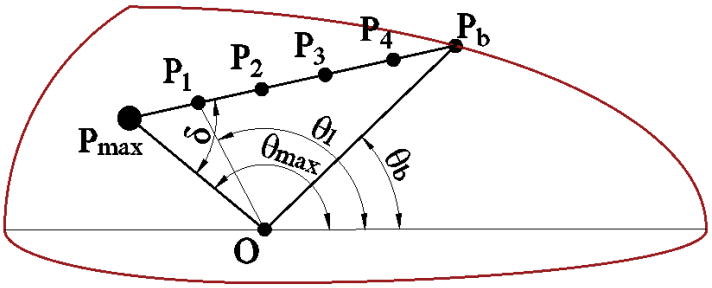


Figure 5.4 Illustration of implementation method of contact pressure distribution.

In the Figure 5.4, the coordinates of the boundary position P_b are: (r_b, φ_b, θ_b), among which r_b equals to r_{tool} and θ_b is interpolated as any angle from 0˚ to 360˚. The corresponding φ_b can be calculated using the already derived Equations (5.1) – (5.4) for the boundaries of different contact regions.

The distance from the maximum pressure position P_{max} to the boundary position P_b can be calculated as the following expression:

$$d_{\mathrm{b}} = \sqrt{(r_{\mathrm{tool}} \cdot \varphi_{\mathrm{b}})^2 + (r_{\mathrm{tool}} \cdot \varphi_{\max})^2 - 2 \cdot r_{\mathrm{tool}} \cdot \varphi_{\mathrm{b}} \cdot r_{\mathrm{tool}} \cdot \varphi_{\max} \cdot \cos(\theta_{\max} - \theta_b)} =$$

$$r_{\mathrm{tool}} \cdot \sqrt{{\varphi_{\mathrm{b}}}^2 + {\varphi_{\max}}^2 - 2 \cdot \varphi_{\mathrm{b}} \cdot \varphi_{\max} \cdot \cos(\theta_{\max} - \theta_{\mathrm{b}})} \quad (5.22)$$

If the distance from the maximum pressure position to the boundary is equally divided into 5 parts by 4 points (P_1, P_2, P_3, P_4), the distance from the maximum pressure position P_{max} to each point (d_1, d_2, d_3, d_4) can be calculated as follows:

$$d_1 = \frac{1}{5} \cdot r_{\mathrm{tool}} \cdot \sqrt{{\varphi_{\mathrm{b}}}^2 + {\varphi_{\max}}^2 - 2 \cdot \varphi_{\mathrm{b}} \cdot \varphi_{\max} \cdot \cos(\theta_{\max} - \theta_{\mathrm{b}})} \quad (5.23)$$

$$d_2 = \frac{2}{5} \cdot r_{\mathrm{tool}} \cdot \sqrt{{\varphi_{\mathrm{b}}}^2 + {\varphi_{\max}}^2 - 2 \cdot \varphi_{\mathrm{b}} \cdot \varphi_{\max} \cdot \cos(\theta_{\max} - \theta_{\mathrm{b}})} \quad (5.24)$$

$$d_3 = \frac{3}{5} \cdot r_{\mathrm{tool}} \cdot \sqrt{{\varphi_{\mathrm{b}}}^2 + {\varphi_{\max}}^2 - 2 \cdot \varphi_{\mathrm{b}} \cdot \varphi_{\max} \cdot \cos(\theta_{\max} - \theta_{\mathrm{b}})} \quad (5.25)$$

$$d_4 = \frac{4}{5} \cdot r_{\mathrm{tool}} \cdot \sqrt{{\varphi_{\mathrm{b}}}^2 + {\varphi_{\max}}^2 - 2 \cdot \varphi_{\mathrm{b}} \cdot \varphi_{\max} \cdot \cos(\theta_{\max} - \theta_{\mathrm{b}})} \quad (5.26)$$

Meanwhile, the angle δ illustrated in Figure 5.4, can be calculated using the cosine law as following:

$$\delta = \arccos\left[\frac{(r_{\mathrm{tool}} \cdot \varphi_{\max})^2 + {d_{\mathrm{b}}}^2 - (r_{\mathrm{tool}} \cdot \varphi_{\mathrm{b}})^2}{2 \cdot r_{\mathrm{tool}} \cdot \varphi_{\max} \cdot d_{\mathrm{b}}}\right] \quad (5.27)$$

According to the relationship in the triangle P_{max} OP_1, OP1 and $\angle P_{max}OP_1$ can be calculated as follows:

$$\mathrm{OP}_1 = \sqrt{(r_{\mathrm{tool}} \cdot \varphi_{\max})^2 + {d_1}^2 - 2 \cdot r_{\mathrm{tool}} \cdot \varphi_{\max} \cdot d_1 \cdot \cos\delta} \quad (5.28)$$

$$\angle \mathrm{P}_{\max}\mathrm{OP}_1 = \arccos\left[\frac{(\mathrm{r}_{\mathrm{tool}} \cdot \varphi_{\max})^2 + (\mathrm{r}_{\mathrm{tool}} \cdot \varphi_1)^2 - {d_1}^2}{2 \cdot {\mathrm{r}_{\mathrm{tool}}}^2 \cdot \varphi_{\max} \cdot \varphi_1}\right] \quad (5.29)$$

Therefore, the coordinates of P_1 can be expressed as follows:

$$r_1 = r_{\mathrm{tool}} \quad (5.30)$$

$$\varphi_1 = \sqrt{{\varphi_{\max}}^2 + \left(\frac{d_1}{\mathrm{r_{tool}}}\right)^2 - 2 \cdot \varphi_{\max} \cdot \frac{d_1}{\mathrm{r_{tool}}} \cdot \cos\delta} \tag{5.31}$$

$$\theta_1 = \theta_{\max} - \arccos\left[\frac{(\mathrm{r_{tool}} \cdot \varphi_{\max})^2 + (\mathrm{r_{tool}} \cdot \varphi_1)^2 - {d_1}^2}{2 \cdot {\mathrm{r_{tool}}}^2 \cdot \varphi_{\max} \cdot \varphi_1}\right] \tag{5.32}$$

Combining Equations (5.19) and (5.21), the corresponding contact pressure at $\mathrm{P_1}$ has the following expression:

$$p(\mathrm{P_1}) = \frac{2 \cdot n_{\mathrm{M}} + 1}{2 \cdot n_{\mathrm{M}}} \cdot 2.84 \cdot \bar{\sigma}(\mathrm{P_{max}}) \cdot \left[1 - \left(\frac{d_1}{d_{\mathrm{b}}}\right)^2\right]^{1/(2 \cdot \lambda \cdot n_{\mathrm{M}})} = \frac{2 \cdot n_{\mathrm{M}} + 1}{2 \cdot n_{\mathrm{M}}} \cdot 2.84 \cdot \bar{\sigma}(\mathrm{P_{max}}) \cdot \left(\frac{24}{25}\right)^{1/(2 \cdot \lambda \cdot n_{\mathrm{M}})} \tag{5.33}$$

Following the same procedure, the coordinates and contact pressure of $\mathrm{P_2}$, $\mathrm{P_3}$, $\mathrm{P_4}$ can be derived. The same, if the distance from the maximum pressure position to the boundary is equally divided into m parts by (m-1) points, the distance from the maximum pressure position to $\mathrm{P_{m-1}}$ can be calculated as the following equation:

$$d_{\mathrm{m-1}} = \frac{m-1}{m} \cdot r_{\mathrm{tool}} \cdot \sqrt{{\varphi_{\mathrm{b}}}^2 + {\varphi_{\max}}^2 - 2 \cdot \varphi_{\mathrm{b}} \cdot \varphi_{\max} \cdot \cos(\theta_{\max} - \theta_{\mathrm{b}})} \tag{5.34}$$

The coordinates of $\mathrm{P_{m-1}}$ can be expressed as follows:

$$r_{\mathrm{m-1}} = r_{\mathrm{tool}} \tag{5.35}$$

$$\varphi_{\mathrm{m-1}} = \sqrt{{\varphi_{\max}}^2 + \left(\frac{d_{\mathrm{m-1}}}{\mathrm{r_{tool}}}\right)^2 - 2 \cdot \varphi_{\max} \cdot \frac{d_{\mathrm{m-1}}}{\mathrm{r_{tool}}} \cdot \cos\delta} \tag{5.36}$$

$$\theta_{\mathrm{m-1}} = \theta_{\max} - \arccos\left[\frac{(\mathrm{r_{tool}} \cdot \varphi_{\max})^2 + (\mathrm{r_{tool}} \cdot \varphi_{\mathrm{m-1}})^2 - {d_{\mathrm{m-1}}}^2}{2 \cdot {\mathrm{r_{tool}}}^2 \cdot \varphi_{\max} \cdot \varphi_{\mathrm{m-1}}}\right] \tag{5.37}$$

And the corresponding contact pressure at $\mathrm{P_{m-1}}$ has the following expression:

$$p(\mathrm{P_{m-1}}) = \frac{2 \cdot n_{\mathrm{M}} + 1}{2 \cdot n_{\mathrm{M}}} \cdot 2.84 \cdot \bar{\sigma}(\mathrm{P_{max}}) \cdot \left[1 - \left(\frac{d_{\mathrm{m-1}}}{d_{\mathrm{b}}}\right)^2\right]^{1/(2 \cdot \lambda \cdot n_{\mathrm{M}})} = \frac{2 \cdot n_{\mathrm{M}} + 1}{2 \cdot n_{\mathrm{M}}} \cdot 2.84 \cdot \bar{\sigma}(\mathrm{P_{max}}) \cdot \left[1 - \left(\frac{m-1}{m}\right)^2\right]^{1/(2 \cdot \lambda \cdot n_{\mathrm{M}})} \tag{5.38}$$

With the expressions of points' coordinates and the corresponding contact pressure, the analytical model for the contact pressure distribution is implemented and visualized in MATLAB. It is noteworthy that the interpolating density of θ_b and the value of m have an important influence on the visualization resolution of contact pressure distribution.

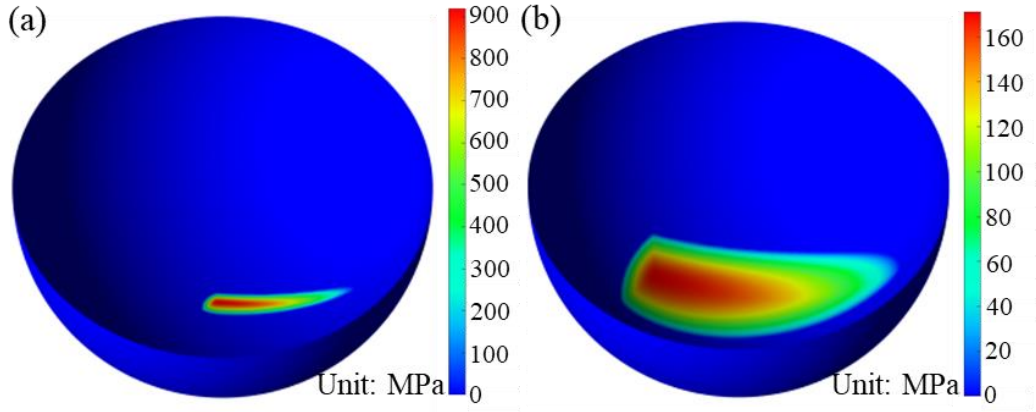


Figure 5.5 MATLAB visualization of contact pressure distribution on the forming tool in ISF of (a) TA1 sheet and (b) PEEK sheet.

5.3 Finite element simulation

5.3.1 ISF of TA1 sheet

ISF of TA1 sheet is used in FE simulation for validation. The FE simulations of ISF were conducted in ABAQUS software. The FE model for the ISF of TA1 sheet is given as Figure 5.6. The FE model is comprised of a squared TA1 sheet with dimensions of 140 × 140 × 0.7 mm and a forming tool with radius of 5 mm. The opening diameter of the designed shape is 90 mm, the depth 45 mm, and the drawing angle from 22° to 88°. Other ISF parameters can be found in Table 5.1. The blank holders for the plate are replaced with the setting of boundary condition to constrain the degree of freedom of the clamped sheet material. The helical tool path for the ISF process was generated in Autodesk Fusion 360 software to form a truncated cone shape. Motions in three directions are defined to apply the tool path on the forming tool. The contact type is set

as surface-to-surface contact. Penalty contact method is used for tangential contact behaviour and a value of 0.25 is set as the coefficient of friction, while "hard" contact is used for normal contact behaviour. Other material parameters used in the FE simulation can be found in Table 5.2 and Johnson-Cook model [101] was used to define the plasticity as shown in Figure 5.7. The 8-node brick element with reduced integration (C3D8R) is used in the mesh step. The general mesh strategy is to use structured fine mesh at the contact or deformation area, and to use free coarse mesh at the clamped area and the central non-contact area. As the elements would have severer deformation in the meridional and thickness directions with the increase of step size and drawing angle, it is necessary for the element sizes to keep suitable aspect ratio outside in. Therefore, the meshed elements have gradual changing sizes from 0.707 × 0.442 × 0.175 mm outside to 0.188 × 0.088 × 0.175 mm inside as shown in Figure 5.6. Time increment of 5×10^{-5} s is used in the simulation. An enhanced hourglass control and a distortion control with length ratio of 0.1 are used to reduce the element distortion.

Table 5.1 Parameters used in the FE simulation for ISF of TA1 and PEEK sheets.

Parameter	Temperature (°)	Step size (mm)	Spindle speed (rpm)	Feed rate (mm/min)	Tool radius (mm)	Initial sheet thickness (mm)
ISF of TA1	23	0.28	0	800	5	0.7
ISF of PEEK	130	1	100	2350	5	3

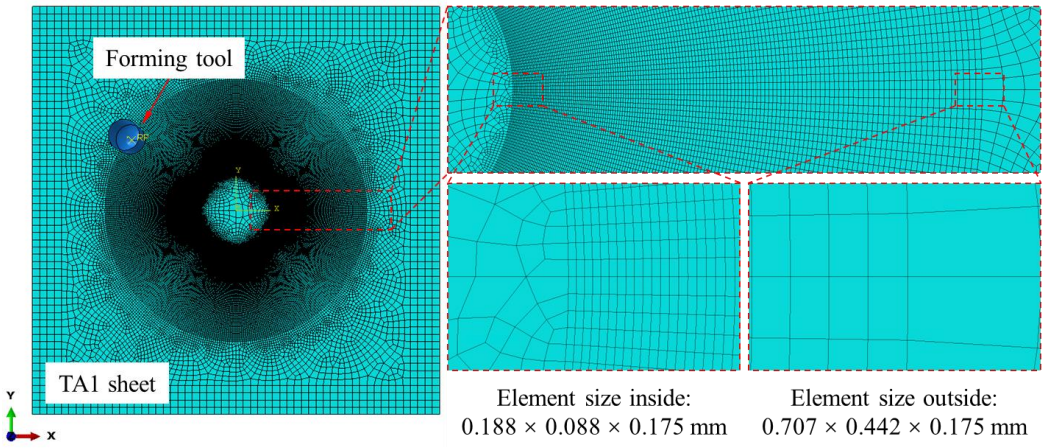


Figure 5.6 FE model and element mesh strategy of ISF of TA1 sheet.

Table 5.2 Parameters in FE simulation of ISF of TA1 sheet.

Parameter	Coefficient of friction	Density (kg/m^3)	Young's modulus (MPa)	Poisson's ratio
Value	0.25	4510	105000	0.32

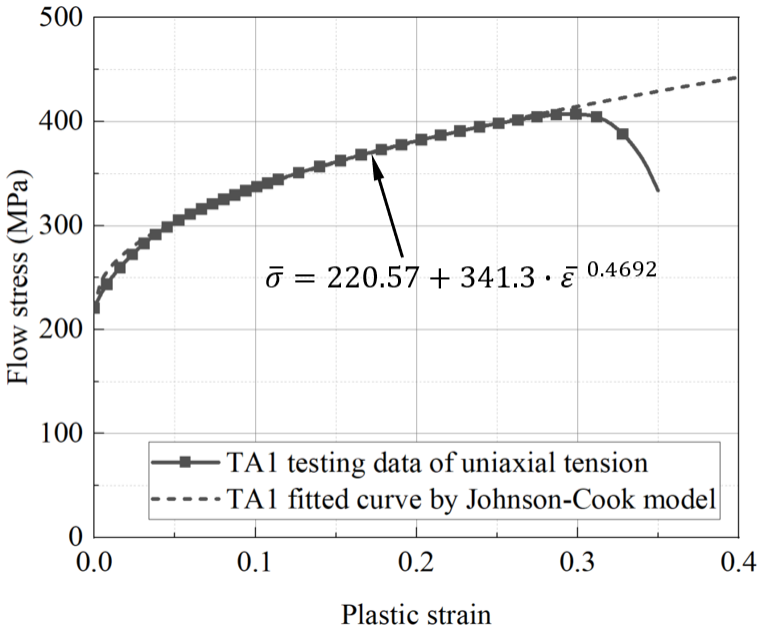


Figure 5.7 Data of quasi-static uniaxial tension and Johnson-Cook model for the plasticity definition in FE simulation.

5.3.2 Heat-assisted ISF of PEEK sheet

The FE model for heat-assisted ISF of PEEK sheet is similar to that for ISF of TA1

sheet. The PEEK sheet has a dimension of 240 × 240 × 3 mm, and the radius of the forming tool is still 5 mm. The opening diameter of the designed shape is 150 mm, the depth 64.91 mm, and the drawing angle from 30° to 80°. Other parameters are given in Table 5.1. To conduct thermomechanical simulation, thermal conductivity [149], specific heat capacity [150] and Young's modulus [151] at different temperatures were obtained from the literature and defined as given in Figure 5.8. Instead of using the original ZOP model to predict the true stress – strain curves in whole elastic-plastic deformation, the Modified ZOP model I [152, 153] as given in Appendix B is used to predict the flow stress – plastic strain curves of PEEK in only plastic deformation at high temperatures based on the testing results from Wang et al. [154], as shown in Figure 5.9. As the flow stress shift of PEEK below and above 130 °C shows different trends, two sets of model parameters were derived and are given in Table 5.3 without consideration of the strain rate effect. The data of the predicted curves are used in the FE model to define the plasticity property. The frictional coefficient and other material parameters are assumed constant with change of temperature, as given in Table 5.4, while 90 % of inelastic dissipation is defined to be used in calculation of the temperature rise. The initial temperature of the whole sheet is set as 130 °C and a sink temperature of 130 °C is defined on the bottom surface to provide continuous heat during forming process. Besides, the heat loss is defined by setting another sink temperature on all other surfaces, and a convective heat transfer coefficient of air is defined as 15 W/(m^2·°C) according to preliminary tests. Additionally, heat generation is considered in the contact setting. All the dissipated energy caused by friction is converted to heat, while half of the converted heat is distributed to the sheet material. The 8-node thermally coupled brick element with reduced integration (C3D8RT) is selected in the thermomechanical simulation. The element size gradually changes from 1.272 × 0.817 × 0.5 mm outside

to 0.317 × 0.163 × 0.5 mm inside. To give relatively stable simulation results, the time increment is set to be 4×10^{-5} s. The same as ISF simulation of TA1 sheet, an enhanced hourglass control and a distortion control are used in the case for PEEK sheet.

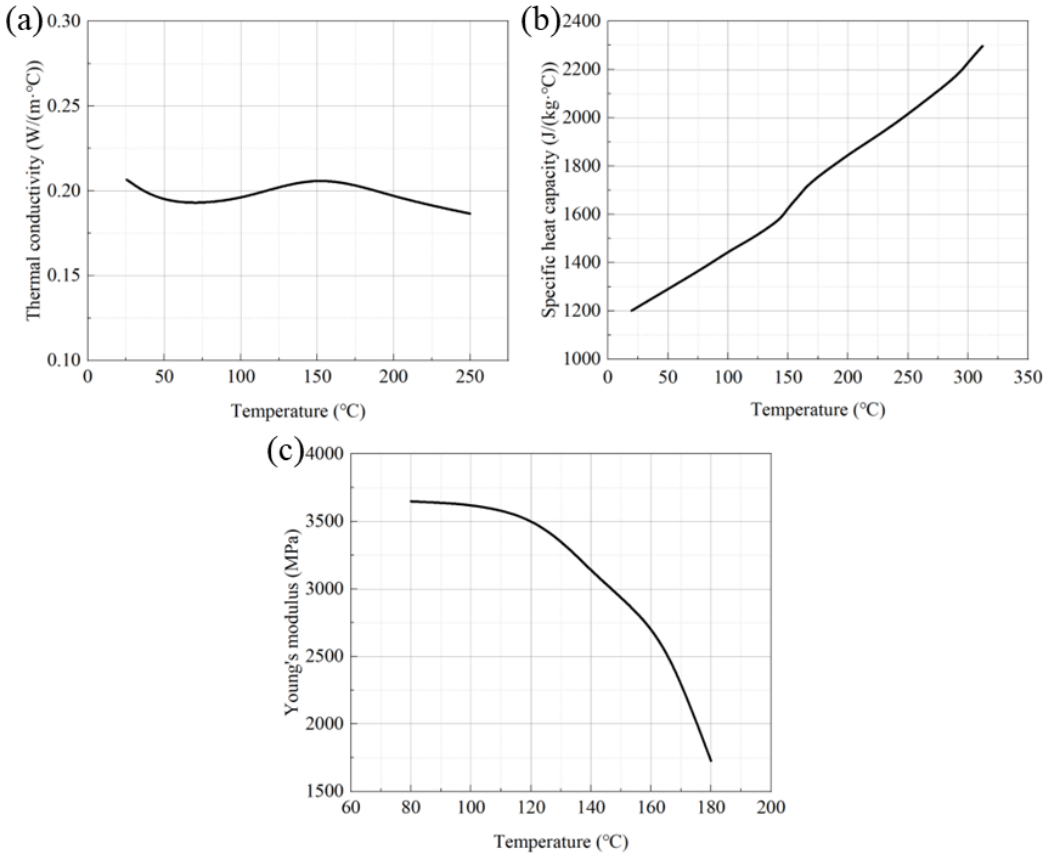


Figure 5.8 (a) Thermal conductivity [149], (b) specific heat capacity [150] and (c) Young's modulus of PEEK [151] at different temperatures.

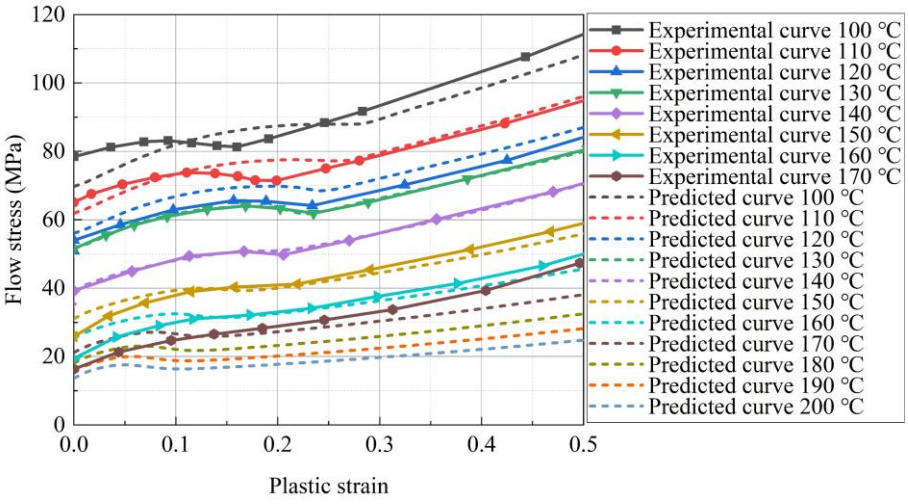


Figure 5.9 Flow stress data and constitutive prediction of PEEK at different high temperatures.

Table 5.3 Model parameters of Modified ZOP model I for PEEK at high temperatures.

Model parameters	**Below 130 °C**	**Above 130 °C**
$\boldsymbol{k}$	0.9822	0.9473
$\boldsymbol{w}$	131.1	68.75
$\boldsymbol{\lambda}$	28.36	11.99
$\boldsymbol{n}$	1.273	0.8509
$\boldsymbol{\mu}$	0.1446	0.4458
$\boldsymbol{C_1}$	-0.2575	-0.6403
$\boldsymbol{C_2}$	1.951	1.771
$\boldsymbol{\alpha}$	13.51	167.4
$\boldsymbol{K_1}$ **(MPa)**	382.1	78.65
$\boldsymbol{K_2}$ **(MPa)**	57.37	42.18
$\boldsymbol{m}$	—	—
$\boldsymbol{a}$	131	486.9
$\boldsymbol{B}$ **(MPa)**	51.54	39.24

Table 5.4 Parameters in FE simulation of ISF of PEEK sheet.

Parameter	Coefficient of friction	Density (kg/m^3)	Poisson's ratio
Value	0.05	1310	0.38

Figure 5.10 shows the temperature distribution in the FE simulation of heat-assisted ISF of PEEK, which indicates the workableness of the coupled thermomechanical simulation.

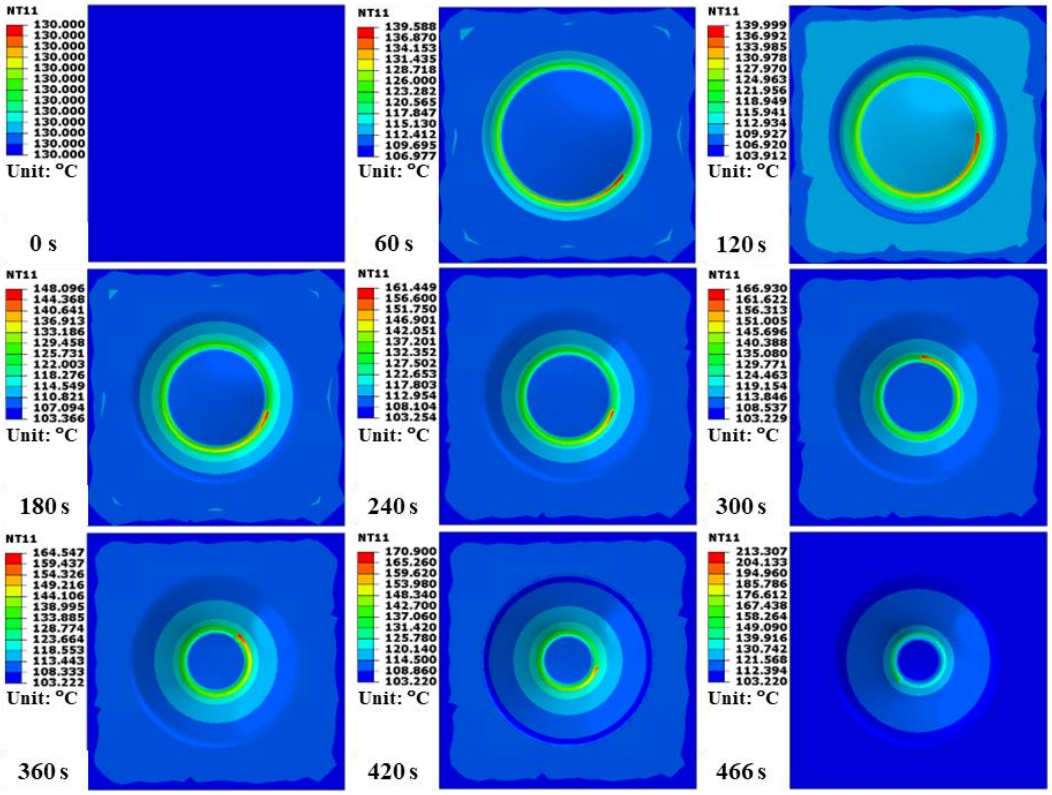


Figure 5.10 Temperature distribution in FE simulation of heat-assisted ISF of PEEK sheet.

5.4 Validation of analytical model with ISF of TA1 and PEEK

The measurement of contact area and pressure distribution is technically challenging. So, a practicable approach to validate the analytical model is to use FE simulation. This section is focused on the validation and comparison between the FE simulation and the analytical model in terms of the forming force variation, size of the contact area, the maximum contact pressure and the pressure distribution.

5.4.1 Comparison of forming force between analytical model and FE simulation

The comparison of forming force components between FE simulation and analytical results of ISF of 0.7 mm TA1 sheet is given in Figure 5.11. It can be observed that the trend of force variation shows good agreement between FE simulation and analytical prediction and the alternation of horizontal forces F_x and F_y is well described as shown

in detail by Figure 5.11(b). The continuously increasing vertical forming force F_v in FE simulation is in good accordance with the analytical model with the increase of forming time and drawing angle, while the peak horizontal forces F_x and F_y by analytical prediction are slightly higher than the results from FE simulation. This may result from the overestimation of the effect of material thinning on the tangential horizontal force and insufficient approximation of friction coefficient. It is noteworthy that compared with Figure 4.12, Figure 5.11 shows reduced agreement between the analytical results and the simulation result of F_x and F_y in ISF of TA1, although there is no change to the ISF condition. There are two reasons for this result. Firstly, the underestimation of forming force in FE simulation is a result of the insufficient material stiffness in FE simulation, which may be caused by using reduced integration element to save computing resources. Secondly, the mismatching of forming time is a result of the slight difference in tool moving coordinates along the tool path between FE simulation and the MATLAB implementation of analytical model.

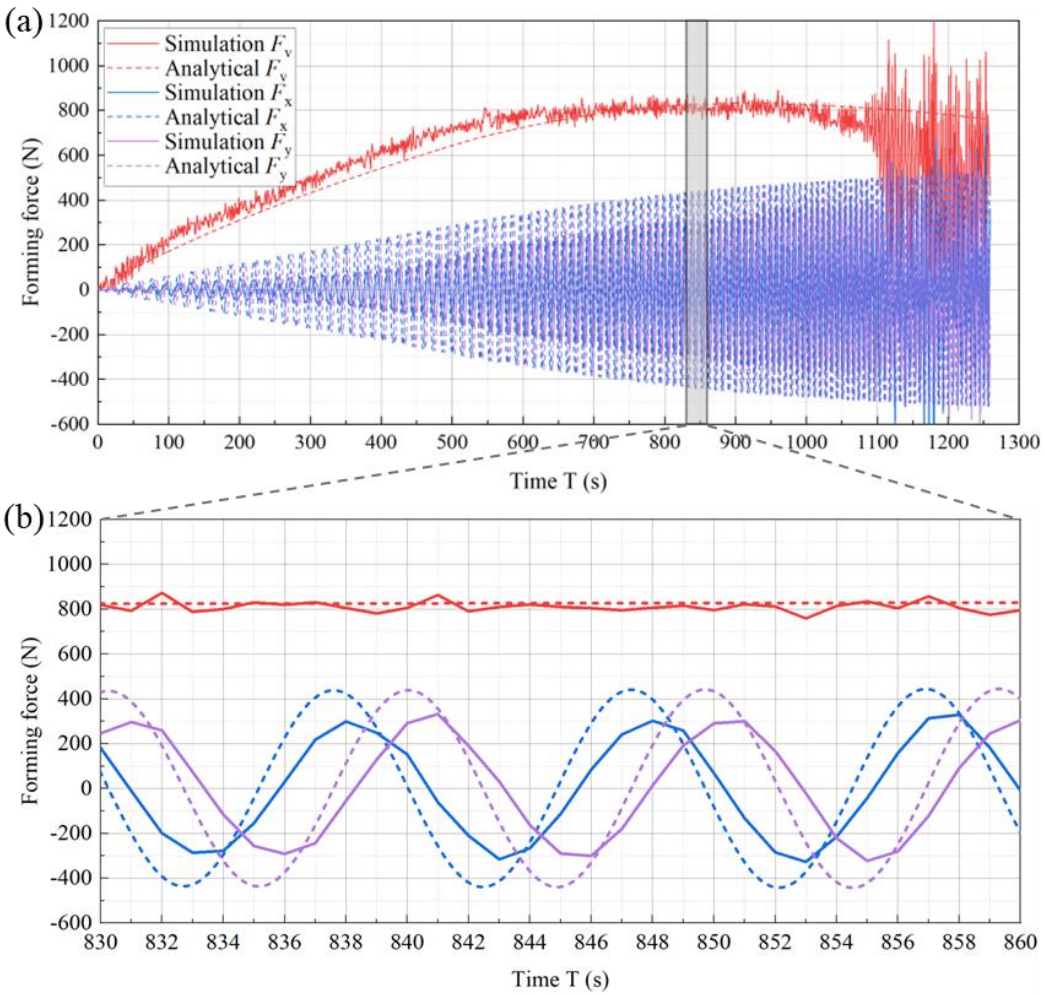


Figure 5.11 Comparison of forming force between FE simulation and analytical prediction in ISF of TA1. (a) Whole process comparison and (b) detailed comparison in an enlarged time range.

As shown in Figure 5.12(a), the comparison of vertical forming force F_v in ISF of PEEK sheet has relatively larger deviation in the beginning stage, while after this the consistency can be observed. The horizontal components F_x and F_y also show discrepancy in the first 300 s. The deviation between analytical and FE simulation results in all force components at the beginning of ISF may be caused by the difference in prediction of global bending effect due to the use of backing plate, which leads to the rapid rise of all force components. However, this global bending effect on the forming force can be neglected in ISF of TA1 sheet because no backing plate was used in this case.

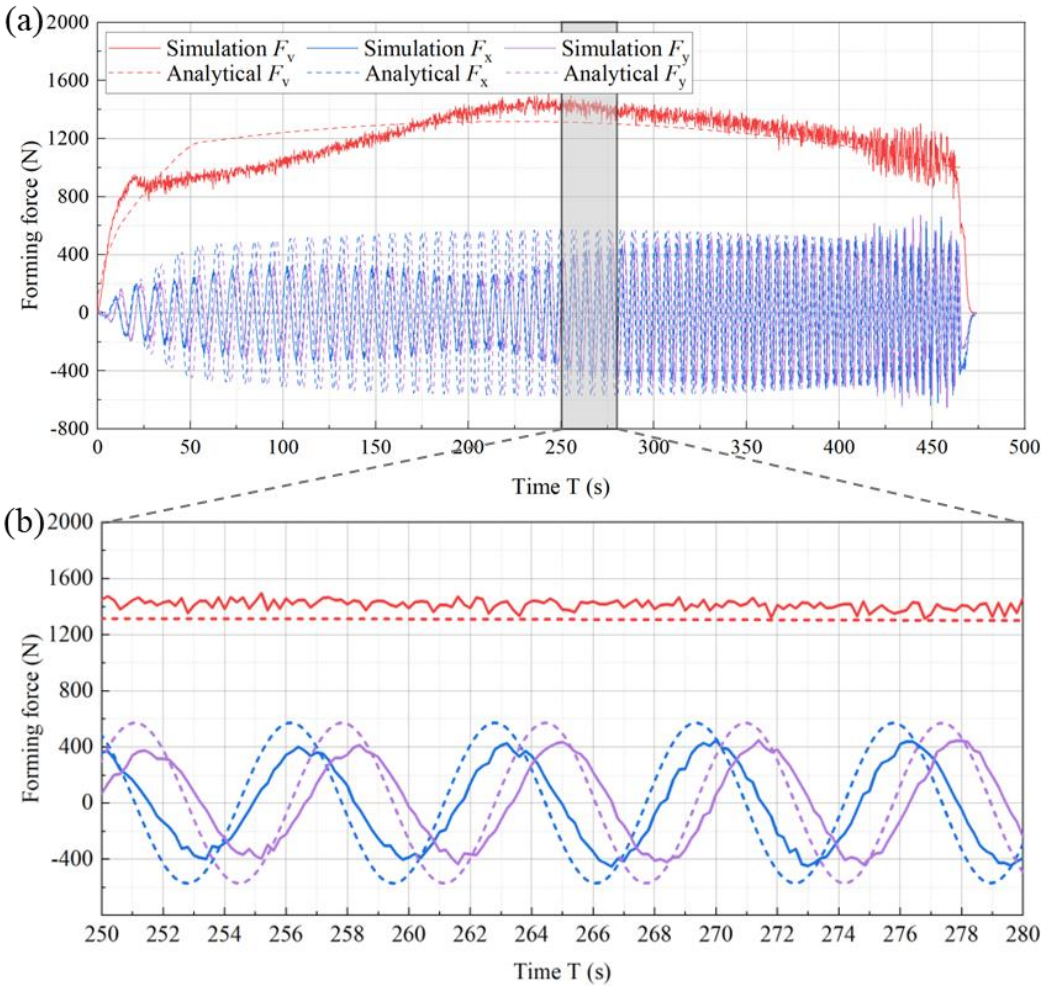


Figure 5.12 Comparison of forming force between FE simulation and analytical prediction in ISF of PEEK. (a) Whole process comparison and (b) detailed comparison in an enlarged time range.

5.4.2 Validation of the size of contact area

The data of contact area were obtained from the history output in ABAQUS as shown in Figure 5.13(a) for ISF of TA1 sheet and Figure 5.13(b) for ISF of PEEK sheet. The size of contact area in ISF simulation of TA1 sheet varies up to about 4 mm^2, which is much smaller than the maximum size of about 20 mm^2 in ISF simulation of PEEK sheet. This is a result of the much higher material rigidity of TA1 (with Young's modulus of about 105 GPa) than PEEK (with Young's modulus of about 3.6 GPa), and the much smaller step size of 0.28 mm in ISF of TA1 sheet compared to 1 mm in ISF of PEEK sheet. Lower material rigidity of PEEK causes more sheet material to be involved in

elastic deformation, and larger step size drives more material to undergo plastic deformation as well. The above two reasons explain why the contact area in ISF of PEEK sheet is larger than ISF of TA1 sheet.

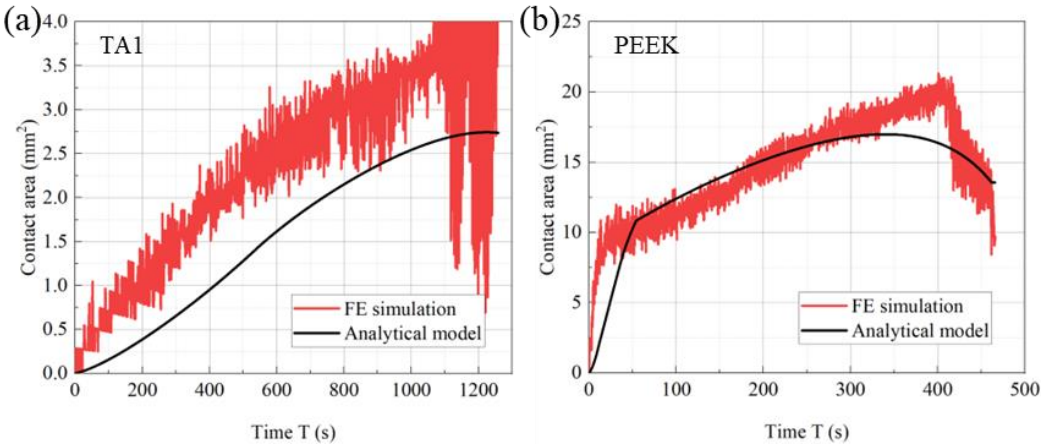


Figure 5.13 Comparison of the size of contact area between FE simulation and analytical prediction in ISF of (a) TA1 and (b) PEEK.

It is observed that the size variation of contact area in FE simulation of TA1 is more dispersed than that of PEEK sheet. As the size of contact area in ISF of TA1 is quite small, to capture the contact behaviour under tool-sheet contact, enough number of elements, i.e., small enough element size and corresponding small time increment are desired. In the current FE simulation, high performance computer with 40 computing cores was used and it took over 110 h to run the case. After different trials, the current FE model settings are found the most reasonable solution for the simulation. Even though, the disperse variation of contact area is still inevitable. However, the contact area in ISF of PEEK sheet is relatively large, and the requirement of element size is reduced to simulate the contact behaviour under forming tool. The data of contact area are relatively centrally distributed.

As demonstrated by the black curves in Figure 5.13(a) and (b), the analytical model is able to capture the change of contact area at different time. Figure 5.13(a) presents that

the analytically predicted size of contact area in ISF of TA1 sheet is smaller than the simulation result. This may be caused by the underestimation of contact area in the developed analytical model, but more importantly, it may be a result of the insufficient element size in FE simulation, which could cause overestimation of contact area. The effect of element size on the FE simulation result is discussed in the following Section 5.5.1. With satisfactory element size, the analytical model predicts well the size of contact area in ISF of PEEK sheet as compared with the FE simulation result.

5.4.3 Validation of the maximum contact pressure

The data maximum contact pressure in FE simulation were extracted from the field output in ABAQUS. As shown in Figure 5.14(a) and (b), the variation of maximum contact pressure shows only slight change after the sudden increase in the initial stage. The same as FE simulation, the analytical model captures the trend well. For ISF of TA1, the FE simulation results are presented smaller than the analytical results. This is an inevitable comparison result as the size of contact area in simulation is larger than that predicted by analytical model and the element size is not small enough to capture the contact behaviour. In terms of the ISF of PEEK sheet, the analytical model is able to capture the maximum contact pressure well as compared with the simulation results.

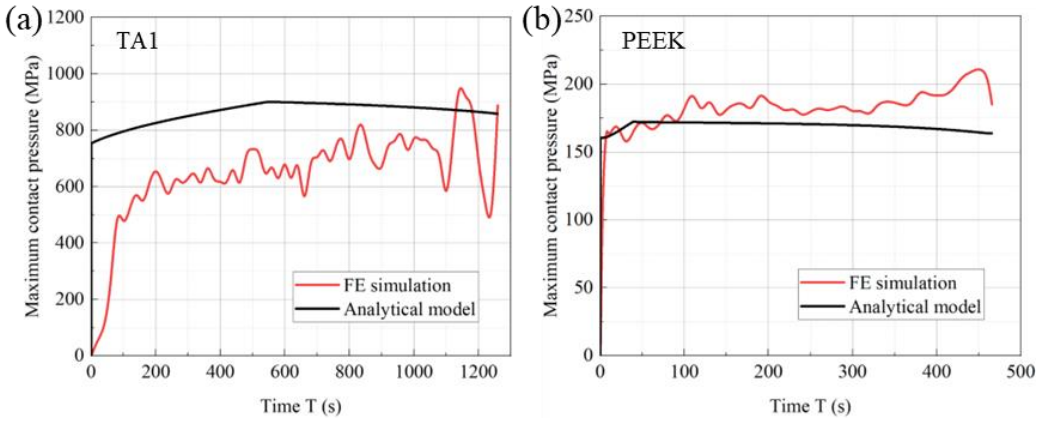


Figure 5.14 Comparison of the maximum contact pressure between FE simulation and analytical prediction in ISF of (a) TA1 and (b) PEEK.

5.4.4 Validation of contact pressure distribution

The comparison of contact pressure distribution between the FE simulation and analytical model of ISF of TA1 is given in Figure 5.15. For different drawing angles of 40°, 50° and 60°, the shape of the contact region is well predicted by the analytical model as compared to the FE simulation results. With the increase of drawing angle, both analytical model and FE simulation have obviously extended width of contact region but slightly shrinking length. This reflects the validity of the modelling process and confirms that, more sheet material falls into overlapping region and less is newly deformed when larger drawing angle is applied. In terms of contact region shape, the only difference is that the contact region produced by FE simulation is not as regular as analytical prediction with uneven boundaries. However, in analytical prediction of different drawing angles, the distribution trend is slightly different from FE simulation, that is, the pressure reduction from maximum pressure position to the contact boundary is slower than that in FE simulation, and the FE simulation shows steeper change of contact pressure.

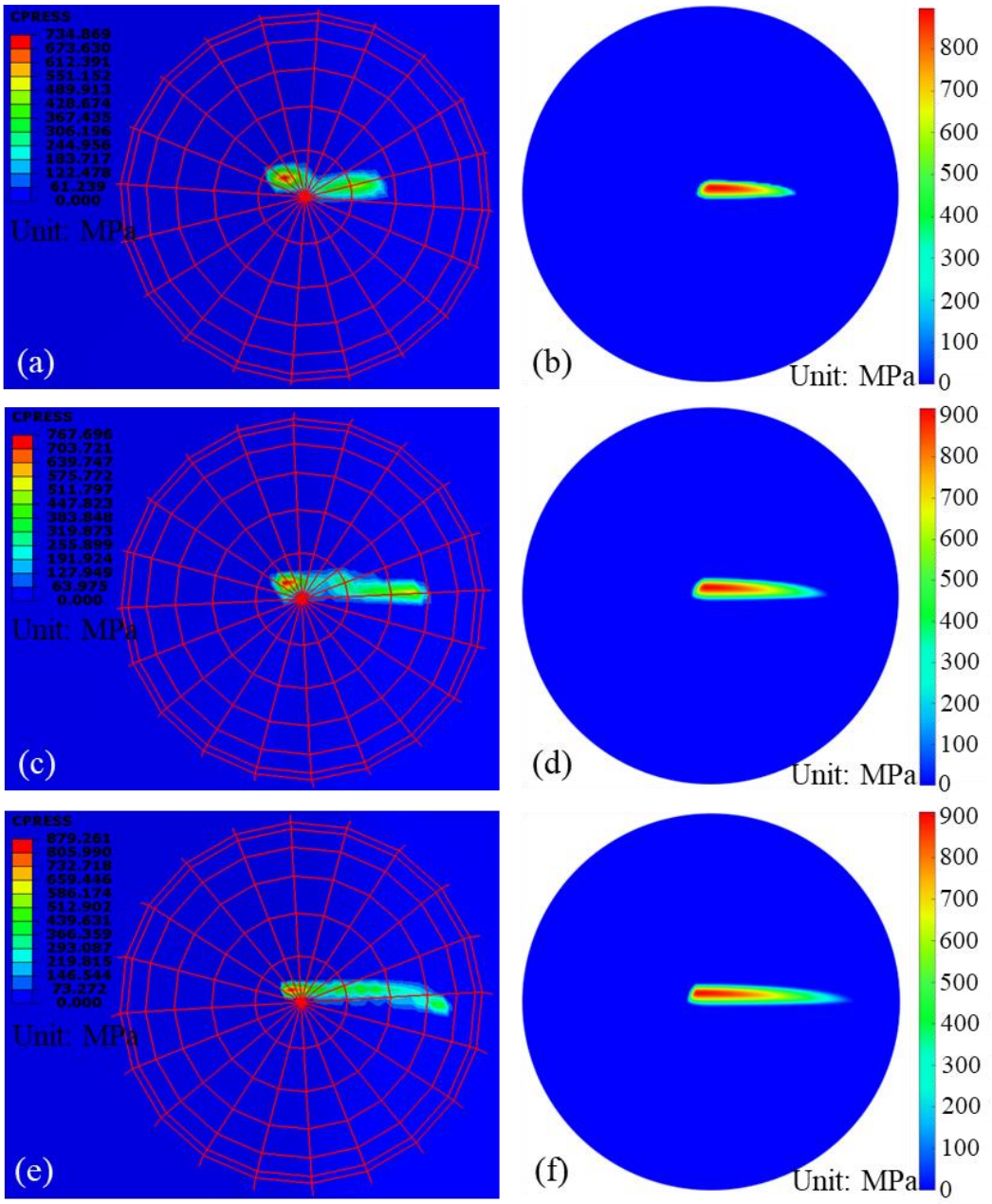


Figure 5.15 Comparison of contact pressure distribution between FE simulation (a), (c) and (e) and analytical prediction (b), (d) and (f) with different drawing angles in ISF of TA1. (a) and (b) 40°, (c) and (d) 50°, (e) and (f) 60°.

A quantitative comparison of the contact area and the maximum contact pressure between FE simulation and analytical result of ISF of TA1 is given in Figure 5.16. The relative error for contact area comparison is as large as 45.52% at drawing angle of 40°, but has a smaller value of 24.85% at drawing angle of 60°. While the relative errors for maximum pressure comparison show smaller values, 22.64% at drawing angle of 40°

and 3.47% at drawing angle of 60°. In conclusion, for ISF of TA1, the analytical result does not give a good agreement with FE simulation result, but a better prediction is achieved at higher drawing angles. In addition to the inaccuracy of the analytical model, more important reason for this is that even the highly refined FE mesh (smallest element size of 0.188 × 0.088 × 0.175 mm as shown in Figure 5.6) is still not sufficient to accurately capture the boundaries of the small contact area in ISF of TA1. On the other hand, the results from the analytical model give a clearly defined contact region. Smaller contact area, clearer boundaries and larger maximum contact pressure will be given by the FE simulation, and better comparison between the analytical and FE simulation results will be obtained, if much more refined mesh is applied. However, the current FE simulation took 40 computing cores and 110 h to complete, and an exponential increase in the demand of computing resources is necessary for more refined mesh. Therefore, the mesh density and prediction accuracy of FE simulation is limited by computing resources. This explains the limited prediction accuracy of FE simulation and the discrepancy between the analytical and FE results.

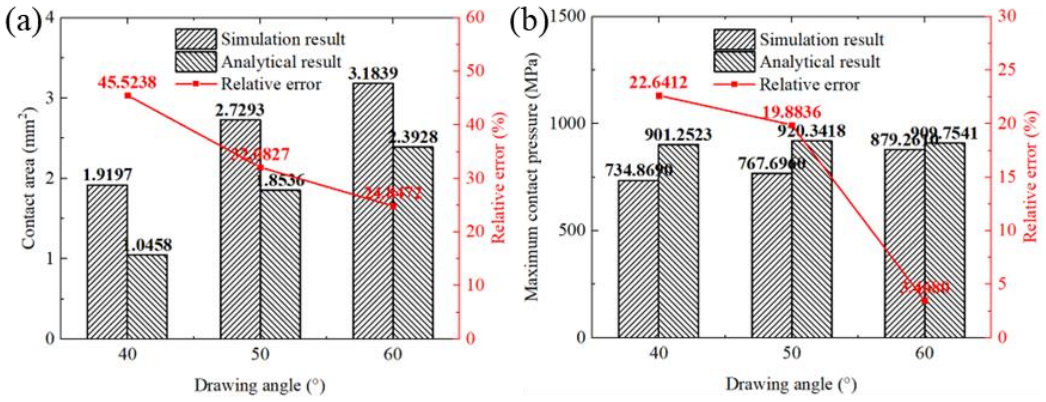


Figure 5.16 Quantitative comparison of (a) contact area and (b) maximum contact pressure between FE simulation and analytical prediction with drawing angles of 40°, 50° and 60° in ISF of TA1.

Clearly, there is a scope for improvement in the more precise prediction of contact area and maximum contact pressure. However, the developed analytical model presents a

comprehensive in-process evaluation of the complicated interfacial behaviour between the ISF tool and workpiece for the first time. A detailed understanding and insight of the interfacial behaviour would have a significant impact to a number of important areas of current ISF research including ISF thermomechanical behaviour, ISF workpiece surface finish and ISF tooling.

Figure 5.17 shows the comparison of contact pressure distribution in ISF of PEEK sheet from FE simulation and analytical model. It is clearly observed that the contact region is much larger than that in ISF of TA1 sheet, which is a result of lower material rigidity and larger step size. In FE simulation, the boundary of contact region is still not smooth compared with analytical prediction. The width extension and length shrink of contact region can be reflected by both FE simulation and analytical model. The analytical model can effectively predict the shape of contact region and the pressure distribution under tool-sheet contact in ISF of PEEK sheet, although there is slight discrepancy in the changing trend of contact pressure.

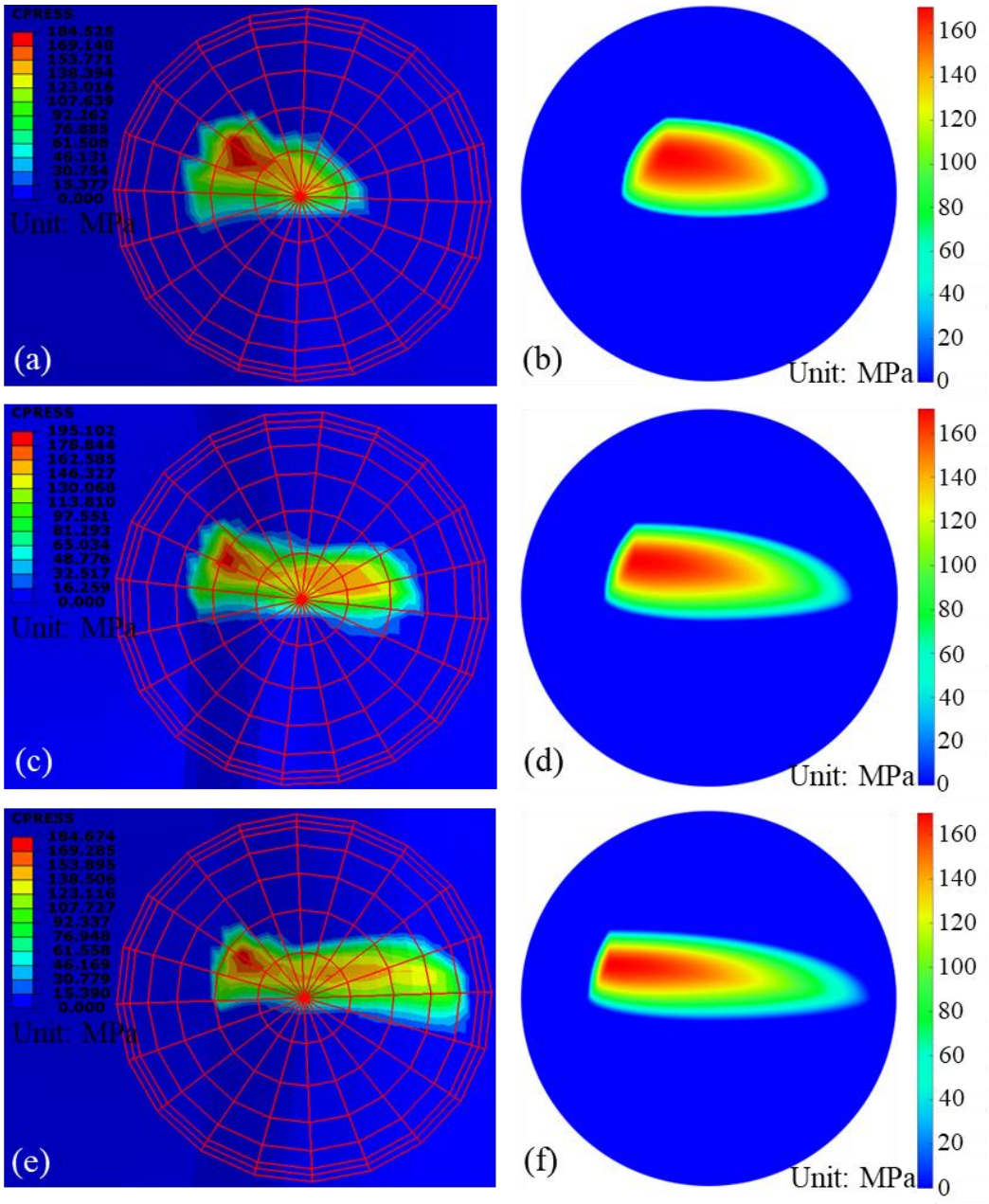


Figure 5.17 Comparison of contact pressure distribution between FE simulation (a), (c) and (e) and analytical prediction (b), (d) and (f) with different drawing angles in ISF of PEEK. (a) and (b) 40°, (c) and (d) 50°, (e) and (f) 60°.

Figure 5.18 shows the quantitative comparison of the contact area and the maximum contact pressure between the analytical result and FE simulation result of ISF of PEEK. Both contact area and maximum pressure have small relative errors. The maximum relative error for contact area is 5.29% at drawing angle of 40°, and for the maximum contact pressure it is 12.32% at drawing angle of 50°. The quantitative comparison

indicates good agreement between the analytical result and FE simulation result of ISF of heat-assisted PEEK. Different from ISF of TA1, the contact area in heat-assisted ISF of PEEK is much larger, and the element size in FE simulation is sufficient for accurate capture of the contact area. This leads to the better prediction from FE simulation and the small discrepancy between the analytical and FE results.

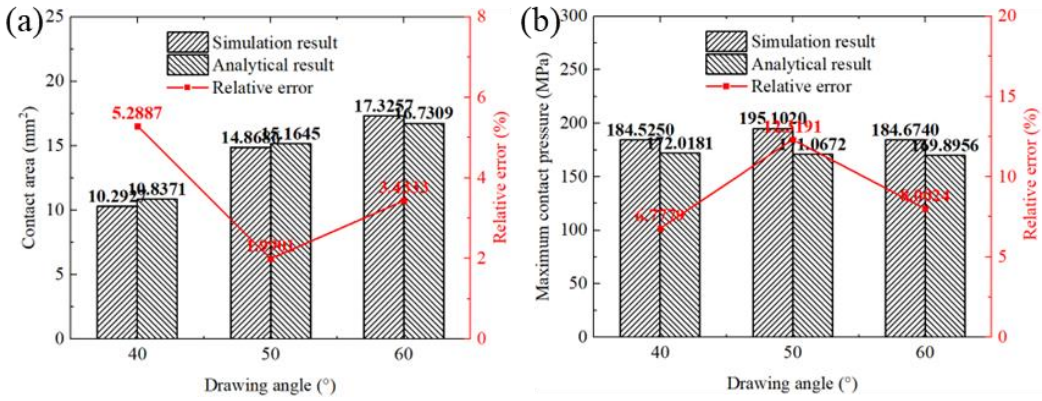


Figure 5.18 Quantitative comparison of (a) contact area and (b) maximum contact pressure between FE simulation and analytical prediction with drawing angles of 40°, 50° and 60° in ISF of PEEK.

5.5 Discussions

5.5.1 Effect of element size on the FE simulation results

As compared in Sections 5.4.2 and 5.4.3, in ISF of TA1 sheet, the size of contact area and the maximum contact pressure predicted by FE simulation and the developed model show obvious discrepancies. This may be a result of insufficiently small element size in the FE model, which is limited by computing resource. To confirm the explanation, two mesh strategies regarding to different element size were used to run the FE simulation: strategy I with element size from 0.707 × 0.442 × 0.175 mm outside to 0.188 × 0.088 × 0.175 mm inside, and strategy II with coarser element size from 1.414 × 0.883 × 0.175 mm outside to 0.377 × 0.177 × 0.175 mm inside. The comparison of predicted contact area and maximum contact pressure between these two mesh strategies is demonstrated

as shown in Figure 5.19. The coarser element size leads to larger size of contact area and smaller contact pressure in FE simulation, and the deviation from the analytical model becomes larger. The finer element size helps to increase the simulation accuracy and improve the capability to reflect the contact behaviour. This comparison verifies the reasonability of the explanation that the element size may have an influence on the large difference between FE simulation and analytical results of contact area and maximum contact pressure. The discrepancy may be eliminated if small enough element size is applied, but this should be conducted with consideration of reasonable use of computing resources.

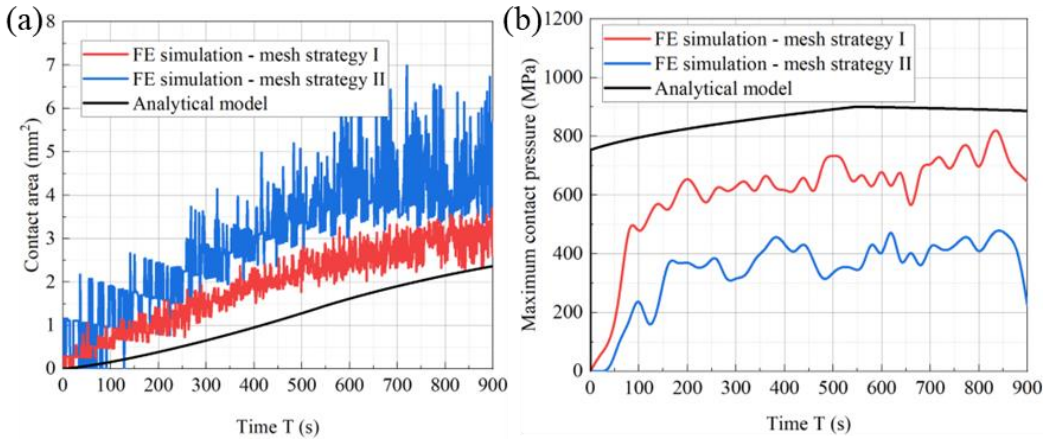


Figure 5.19 Effect of element size in ISF simulation of TA1 sheet on the comparison between FE simulation and analytical results. (a) Size of contact area and (b) the maximum contact pressure.

5.5.2 Potential improvement of the analytical model

In the current analytical model, the equation of contact pressure distribution is adapted from the equation for spherical indentation of an elastic-plastic half surface with a flat surface. Two aspects may be useful for the improvement of the analytical model: (1) In ISF, the thickness of sheet material is relatively small compared with the tool dimension, therefore the current distribution equation may cause the prediction inaccuracy although a correction factor is applied. Further improvement should consider the dimensional

effect between the forming tool and sheet material. (2) The pressure distribution equation should consider the existing curvature of preformed sheet surface in last tool-sheet contact, instead of simplifying the question the same to indentation on a flat surface.

5.6 Conclusions

The conclusions of this chapter can be drawn as follows:

(1) An analytical model for contact behaviour in ISF is developed with consideration of localised tool-sheet contact condition and the contact mechanics of elastic-plastic materials. Compared to FE simulation, the analytical modelling can help to understand the tool-sheet contact behaviour and provides an efficient method for contact prediction.

(2) By validation with ISF simulation of TA1 and PEEK sheets, the developed analytical model can predict the shape and size of contact region, the maximum contact pressure, and the pressure distribution, although there are some discrepancies as compared to FE simulation.

(3) The pressure reduction rate from the maximum pressure position to contact boundary shows slight deviation in comparison with FE simulation, and the pressure distribution equation still has a scope to improve by taking consideration of tool-sheet dimensional relationship and the preformed curvature change of the contact region.

Chapter 6 Heat-assisted Incremental Sheet Forming of PEEK and PMMA

Nomenclature

Symbol	Term	Unit
F_h	Horizontal force	N
F_{x}	Forming force in x direction	N
F_{y}	Forming force in y direction	N
t_0	Initial sheet thickness	mm
r_{tool}	Tool radius	mm
Ψ	Designed drawing angle	rad
α	Actual drawing angle	rad
R_{b}	Distance from the part centre/ symmetry axis to the edge of backing plate	mm
R	Distance from the part centre/ symmetry axis to the tool position	mm
r_{bending}	Bending radius	mm
h	Depth of tool position	mm
$r_{\mathrm{bending}}^{\Psi}$	Final bending radius without consideration of springback	mm

R_Ψ	Distance from the part centre/ symmetry axis to the tool position at the designed drawing angle Ψ	mm
h_Ψ	Depth of tool position at the designed drawing angle Ψ	mm
$\theta_{\text{bending}}^{\Psi}$	Final bending angle without consideration of springback	rad
E	Young's modulus of sheet material	MPa
$\bar{\sigma}_\Psi$	Equivalent stress of inner or outer surface	MPa
$\bar{\varepsilon}_\Psi$	Equivalent strain of inner or outer surface	
$r_{\text{bending}}^{\Psi*}$	Bending radius considering springback	mm
$\theta_{\text{bending}}^{\Psi*}$	Bending angle considering springback	rad
r	Distance from studied position to tool centre	mm
φ	Angle from studied position to tool axis	rad
θ	Angle from workpiece meridional cross-section to studied position	rad
σ_θ, σ_φ, σ_r	Stresses in θ, φ and r directions	MPa
f	Coefficient of friction between tool and sheet material	
$\bar{\sigma}$	Equivalent stress of sheet material	MPa

$\bar{\varepsilon}$	Equivalent strain of sheet material	
σ_{m}	Hydrostatic stress	MPa
η	Stress triaxiality	
t	Sheet thickness	mm
ξ	Twist angle	rad
γ	Shear angle	rad
d_{γ}	Measured normal deviation from the horizontal datum line	mm
R_0	R_0 distance from the original positions to the part central line	mm
θ^*	Angle from the original x axis to the studied position in the horizontal plane	rad
φ^*	Angle from the central axis of the part to the studied position	rad
r^*	Distance from the central axis of the part to the studied position	mm
l_{θ^*} , l_{φ^*}, t	Dimensions of the small element under contact	mm
σ_{φ^*}, σ_{θ^*}, σ_{r^*}	Stresses in φ^*, θ^* and r^* directions	MPa
σ'_{r^*}	Through thickness deviator stress	MPa
τ_{θ^*}	Circumferential shear stress	MPa

$\Delta\gamma_{\theta^*}$	Circumferential instant shear strain change	
$\Delta\varepsilon_{r^*}$	Through thickness instant strain change	
$\Delta\alpha$	Increment of actual drawing angle	rad
$\Delta\gamma$	Increment of shear angle	rad
$\Delta\xi$	Increment of twist angle	rad
F_t^{ls}, F_t^f	Tangential component of the localised shear force and the tangential friction force	N
x_n, y_n, z_n	Coordinates of tool positions	mm
γ_n, ξ_n	Total shear and twist angles at tool position (x_n, y_n, z_n)	rad
$F_{t\,i}^{ls}$, $F_{t\,i}^f$	Tangential component of localised shear force, tangential friction force at tool position (x_i, y_i, z_i)	N
α_i	Drawing angle at tool position (x_i, y_i, z_i)	rad
$\bar{\sigma}_i$	Equivalent stress at tool position (x_i, y_i, z_i)	MPa
α_{i-1}	Drawing angle at tool position $(x_{i-1}, y_{i-1}, z_{i-1})$	rad

6.1 Introduction

Currently ISF of metallic sheets have been tested widely. Different metals such as steel, aluminium alloy, magnesium alloy and titanium alloy show excellent response to ISF. In recent years, ISF of thermoplastics have drawn more attention and is found to have

promising application prospects in auto industry and medical field.

Among different kinds of thermoplastics, both PEEK and PMMA show excellent biocompatibility and are biomedical materials which can be used in medical implants. PEEK is a semi-crystalline thermoplastic with excellent mechanical and chemical properties. PMMA is also called organic glass and the brittleness at room temperature makes it difficult to process. The flexible and customised manufacture of these two materials can promote the medical applications such as cranioplasty.

This chapter aims to test the feasibility of using ISF to form high-performance PEEK and brittle PMMA sheets at elevated temperature. With design of heat-assisted ISF setup, the effect of spindle speed, feed rate and geometry on temperature distribution, forming force variation, forming accuracy and thickness distribution are investigated. A proper set of process parameters is obtained, and the research output is used to conduct the manufacture of cranial plate using ISF. According to the experimental results of heat-assisted ISF of PEEK and PMMA, some challenging issues including forming inaccuracy, fracture and twist behaviour are observed and discussed with theoretical models based on the constitutive, force and contact pressure prediction models developed in Chapters 3 – 5. The testing results are used to develop and validate the analytical models for the challenging issues, while the developed models help to explain and understand the mechanism of forming inaccuracy, fracture, and twist behaviour in heat-assisted ISF of thermoplastics.

6.2 Materials and methods

6.2.1 Material

Extruded PEEK 450G and clear PMMA sheets with thickness of 3 mm supplied by Rochling Group were used in this study. The glass transition temperature of these two

materials is 143 °C and 105 °C, respectively. PEEK and PMMA sheets were prepared by laser cutting with a size of 240 mm × 240 mm × 3 mm to be placed in the ISF fixture.

6.2.2 Heat-assisted ISF setup

As shown in Figure 6.1(a) and (b), the ISF fixture and the spherical forming tool was set up on a 5-axis Hermle CNC milling machine (model: C800U) according to the ISF test rig design in Figure 6.1(c). The fixture consisted of a frame, four clamping plates and backing plate. To form truncated cone and pyramid shapes, two different backing plates contained circular or squared orifices with 160 mm diameter or side length. A flat heater mat was placed covering the top surface to heat PEEK and PMMA sheets before starting the ISF process, while flexible silicone rubber heating tapes were used to heat the sheets during the whole process. The flexible heating tapes are able to move downwards along with the bottom surface of the formed part so that they can follow the shapes to continuously heat the sheets. Thermocouples were used for temperature measurement to control the heating process and capture temperature variation on the bottom surface of sheets with the use of LabVIEW software. Nearby the ISF fixture, an infrared camera (model: Flir E6) was set up to record the temperature distribution on the top surface of the sheets. Below the ISF fixture, a Kistler force transducer (type: 9367C) was placed to measure the 3-axis forming forces F_{x}, F_{y} and F_{z} during ISF process.

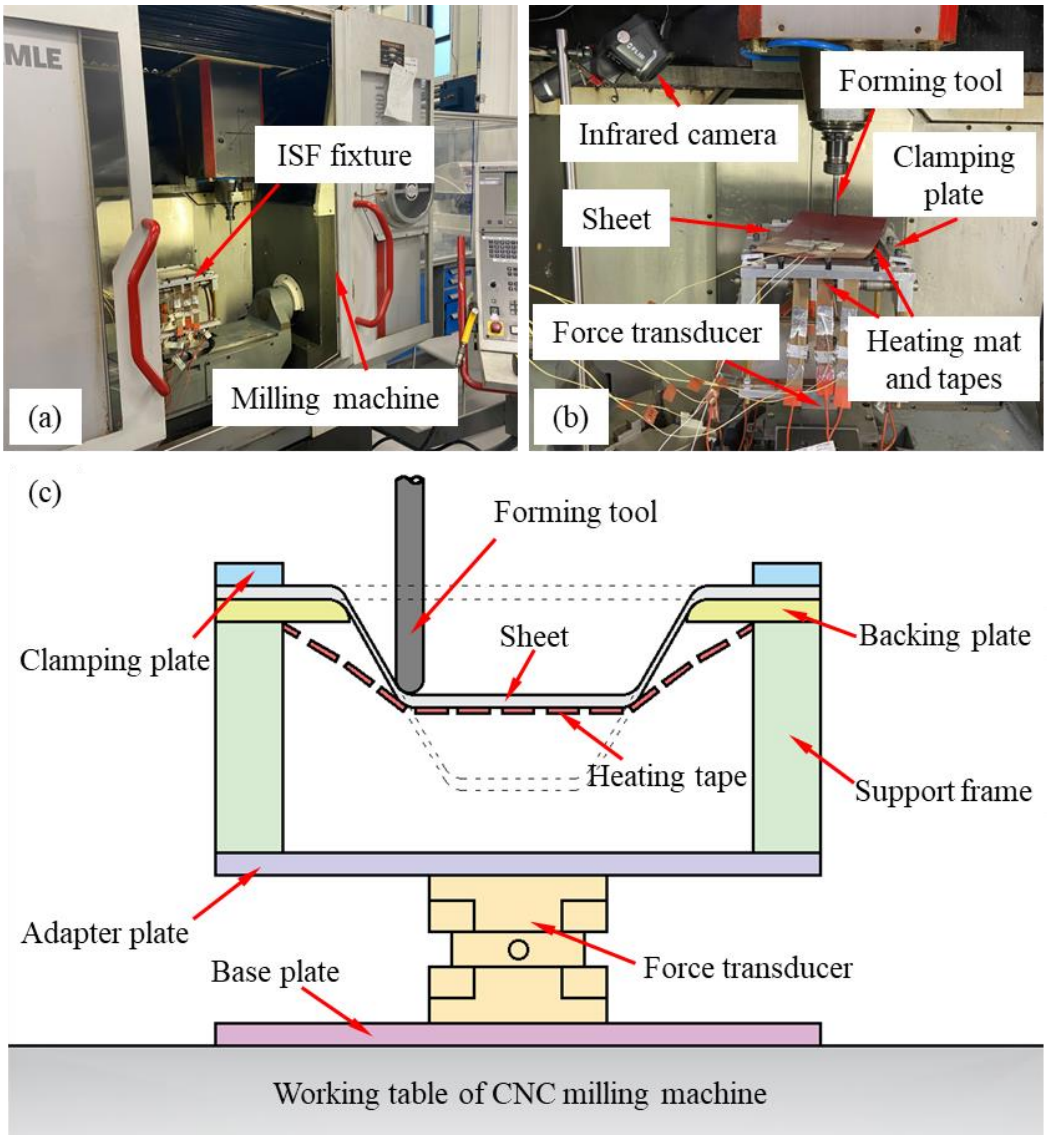


Figure 6.1 Experimental setup of heat-assisted ISF. (a) CNC milling machine, (b) ISF fixture, heating and measurement systems, and (c) schematic of the ISF test rig.

6.2.3 ISF experimental design

Truncated cone shape and truncated pyramid shape with varying drawing angle from 30° to 80° were designed to be formed by ISF process, both of which have the same profile. As shown in Figure 6.2, the initial diameter/ side length of the design shapes is 150 mm, and the designed final depth is 64.91 mm to reach the final drawing angle of 80°. The use of varying drawing angle makes it easy to show the formability as larger drawing angle produces larger strain, while the corner of the truncated pyramid shape

could give biaxial tension deformation condition, which is different from the plane strain condition for the finally deformed truncated cone shape.

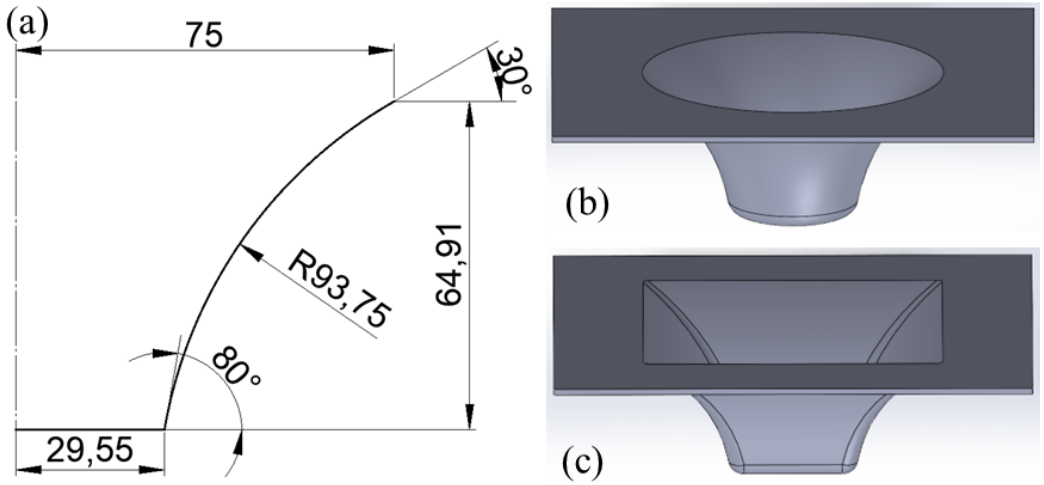


Figure 6.2 Designed shape of ISF tests: (a) Profile with varying drawing angles, (b) model truncated cone part and (c) model of truncated pyramid part.

Based on the designed forming shape, the experimental plan can be found as Table 6.1. In the plan, the effect of three process parameters, including spindle speed, feed rate and forming shape are compared for PEEK and PMMA sheet. The selection of the preheating temperature of 130 °C in ISF of PEEK sheets was guided by the glass transition temperature of around 143 °C to achieve a balance between the material formability and the elastic recovery. The selection for the preheating temperature for PMMA was based on both the glass transition temperature (around 114 °C) and preliminary test. Spindle speed of 100 rpm, feed rate of 2600 mm/min and step size of 1 mm were used in the preliminary tests, and an early fracture happened with a preheating temperature of 90 °C, while a preheating temperature of 100 °C led to well forming without fracture as shown in Figure 6.3. Therefore, 100 °C and 110 °C were used in the ISF processing of PMMA. In terms of other unlisted parameters, the ISF parts were manufactured by a hemi-spherical tool with radius of 5 mm and by the step

size of 1 mm. RTD COMPOUND lubricant was used in all test cases.

Table 6.1 Experimental parameters for ISF of PEEK and PMMA.

ID	Temperature (°C)	Spindle speed (rpm)	Feed rate (mm/min)	Step size (mm)	Shape
PEEK I	130	100	2350	1	Truncated cone
PEEK II	130	1000	2350	1	Truncated cone
PEEK III	130	100	1000	1	Truncated cone
PEEK IV	130	100	2350	0.5	Truncated cone
PEEK V	130	100	2350	1	Truncated pyramid
PMMA I	100	100	2600	1	Truncated cone
PMMA II	110	100	2600	1	Truncated cone
PMMA III	100	1000	2600	1	Truncated cone
PMMA IV	100	100	2600	1	Truncated pyramid

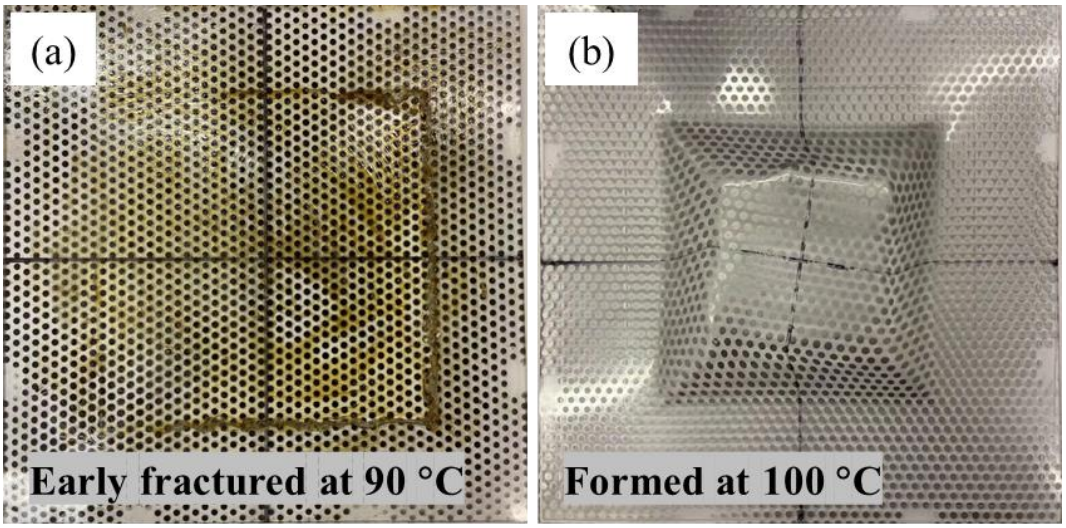


Figure 6.3 Preliminary ISF testing results of PMMA at (a) 90 °C and (b) 100 °C.

6.2.4 Model of cranial plate for ISF manufacture

As show in Figure 6.4(a), a skull model from a patient was obtained by computed tomography (CT) scan. By cutting and splitting the head model, a customised cranial plate was created as given in Figure 6.4(b). A spiral tool path was generated with a constant stepover of 1 mm to conduct the manufacture. Besides, a spindle speed of 100 rpm and a tool with radius of 5 mm was used for ISF of both PEEK and PMMA sheets. Feed rates of 2300 mm/min and 2000 mm/min, temperatures of 130 °C and 100 °C were used for PEEK and PMMA, respectively. Also, RTD COMPOUND was used as the lubricant.

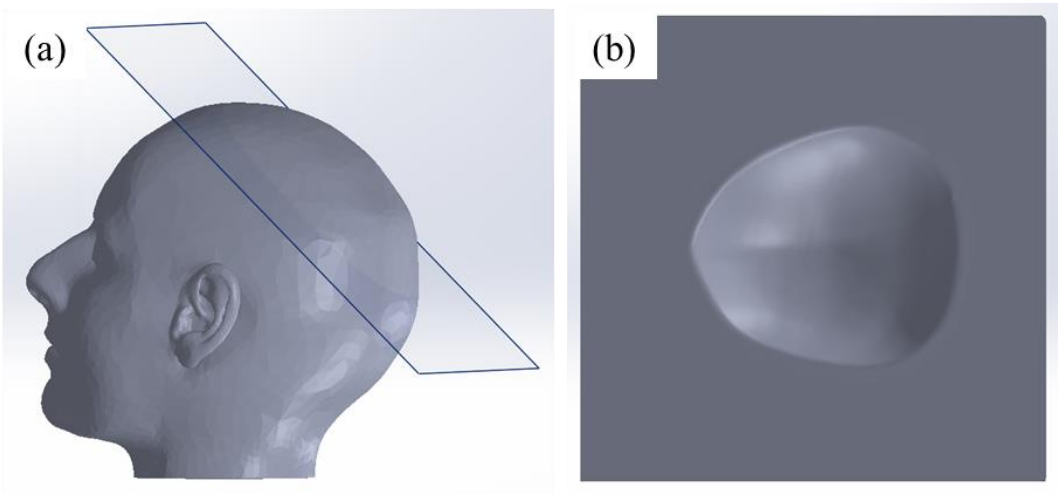


Figure 6.4 (a) Head model and (b) customised cranial plate for ISF manufacture.

6.2.5 Geometric and thickness measurement

The geometric shape was measured by a laser scanning system with the combination of Leica Absolute Tracker and Leica T-Scan 5, as shown in Figure 6.5. Both top and bottom surfaces were scanned and combined to form the whole part. The thickness distribution was produced by Spatial Analyzer software and the geometric deviation was obtained by comparing to the designed model.

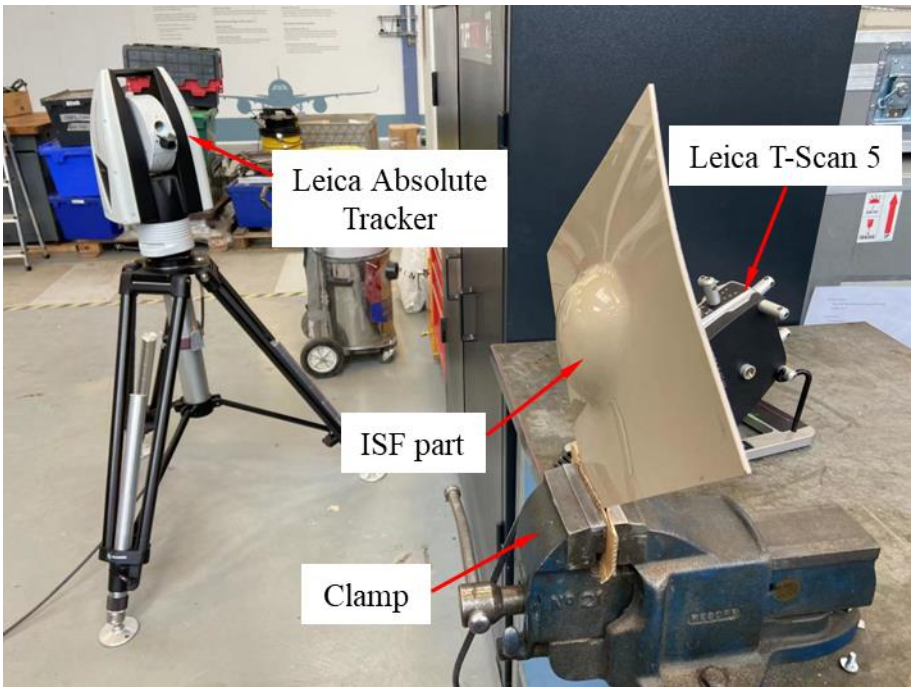


Figure 6.5 Laser scanning system for geometric shape measurement.

6.3 Results and discussions of heat-assisted ISF of PEEK

6.3.1 ISF formed parts

After heat-assisted ISF, the formed PEEK parts are shown in Figure 6.6. It is necessary to clarify that the dots on the formed parts were initially painted for observation of the strain distribution but do not work properly due to the wear by forming tool. From the formed parts, it is observed that all the parts were formed well without early fracture, which indicates the feasibility of ISF in forming of PEEK. However, although good formability of PEEK is shown in ISF, there are still some obvious defects such as twist in PEEK I, II, III and IV parts, and buckling in PEEK V part. The twist and buckling behaviour may be a result of the poor material rigidity of PEEK at high temperature and the corresponding discussion is given in Section 6.6.3.

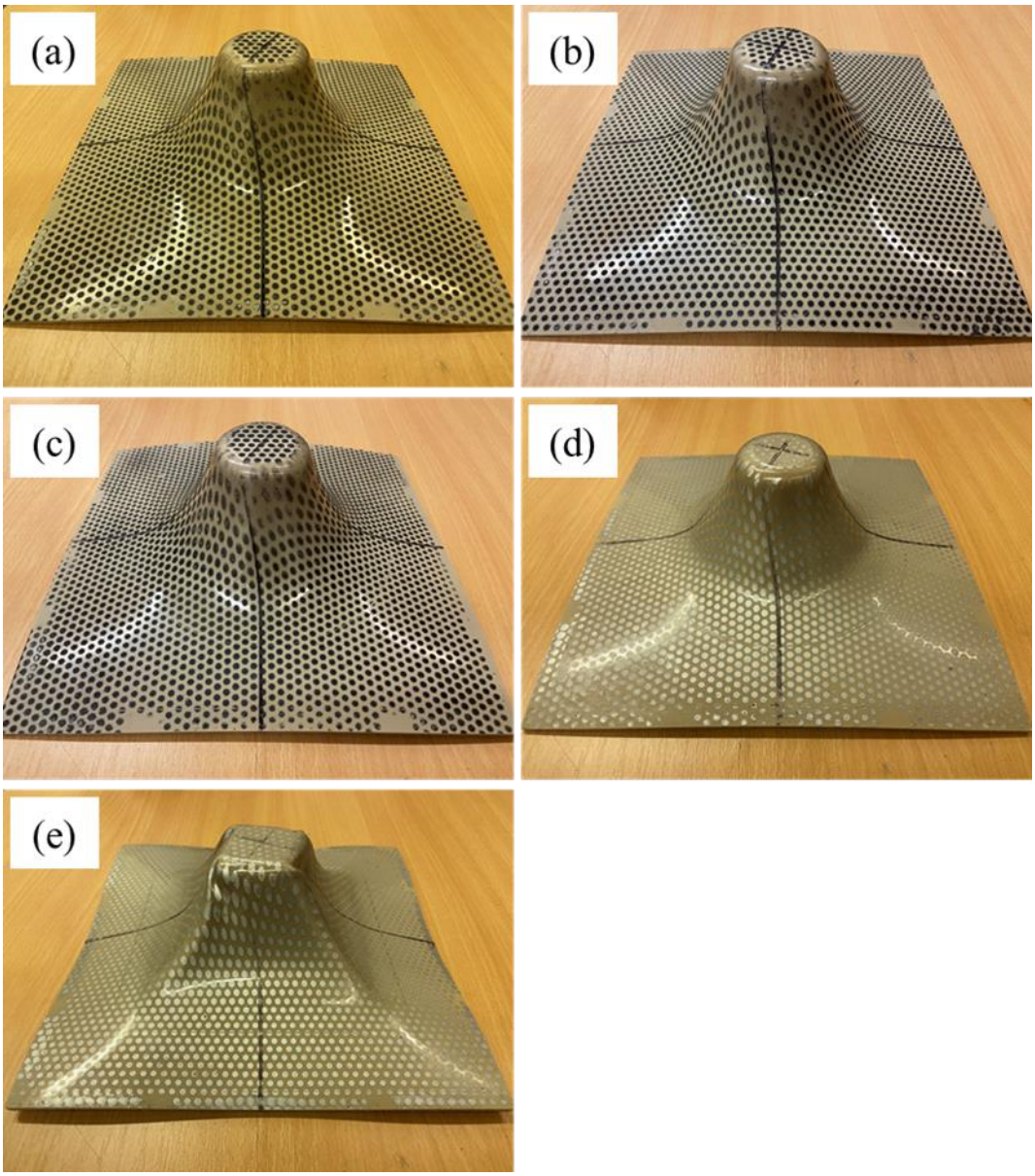


Figure 6.6 ISF formed parts of (a) PEEK I, (b) PEEK II, (c) PEEK III, (d) PEEK IV and (e) PEEK V.

6.3.2 Forming temperature

The temperature distribution during ISF of PEEK truncated cone and pyramid parts are depicted by Figures 6.7 and 6.8. At the beginning of ISF process, uniform temperature distribution can be observed for both shapes. However, as the process goes on, the distribution becomes nonuniform, with the highest temperature shown at the tool position and the adjacent area, no matter the shape is truncated cone or truncated pyramid. There are two sources for the temperature rise at the tool position during ISF:

(1) friction heat generated between the forming tool and sheet material; (2) heat converted from plastic work. Due to the tool-sheet contact and plastic deformation of the blank sheet in ISF process, the heat loss from the blank sheet away from tool motion and the accumulation of heat in the region of tool-sheet contact lead to localised peak temperature increases toward the end of the forming process.

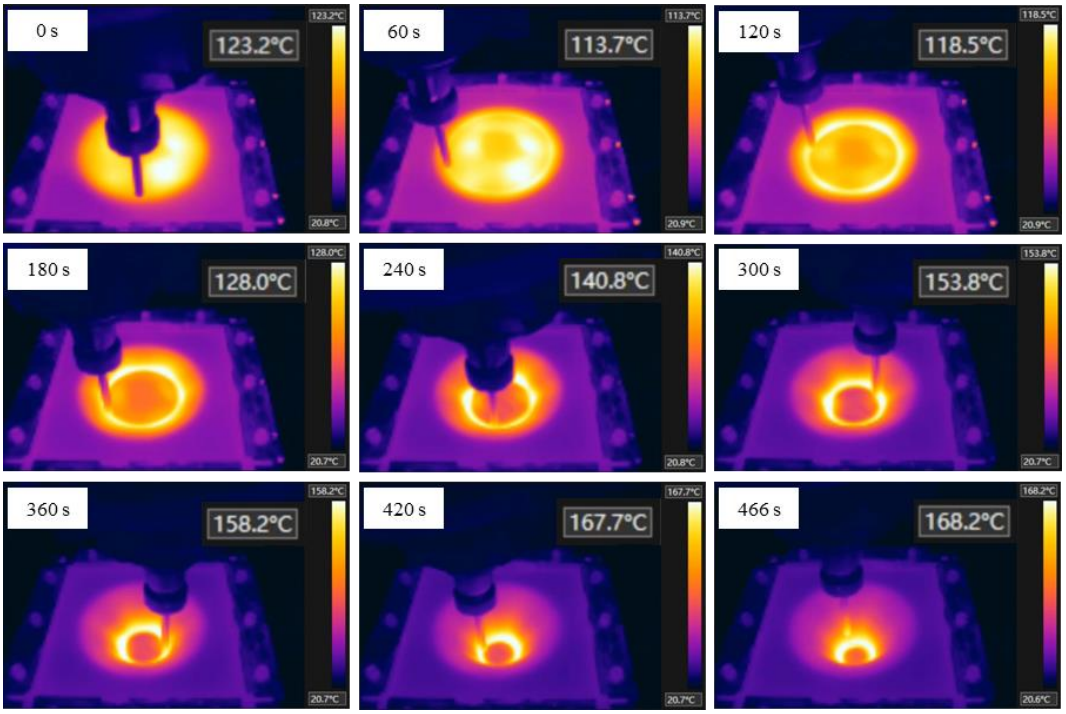


Figure 6.7 Temperature distribution during ISF of PEEK truncated cone part PEEK I.

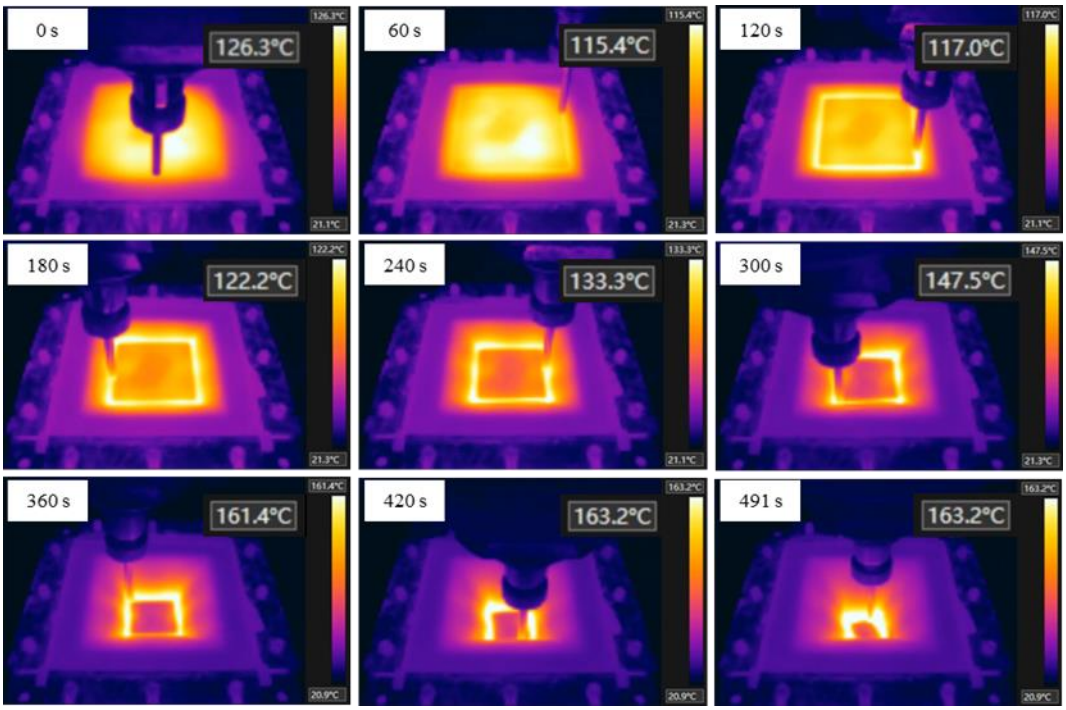


Figure 6.8 Temperature distribution during ISF of PEEK truncated pyramid part PEEK V.

The effect of different process parameters on temperature variation is shown in Figure 6.9. The temperature at the centre position on the bottom surface was measured by thermocouple and recorded in LabVIEW, while the highest temperature shown at the tool position and the adjacent area was automatically captured and recorded by the infrared camera. It is observed that at the beginning of ISF, the temperature on the bottom surface is gradually decreased because the heat loss after the removal of the flat heater mat. With the forming of parts, as the bottom surface approached to and even got in contact with the heating tapes below, a continuous temperature increase could be obtained. Differently, after the initial temperature decrease, the highest temperature on the top surface rises remarkably, which is mainly the result of heat generation from friction and plastic work.

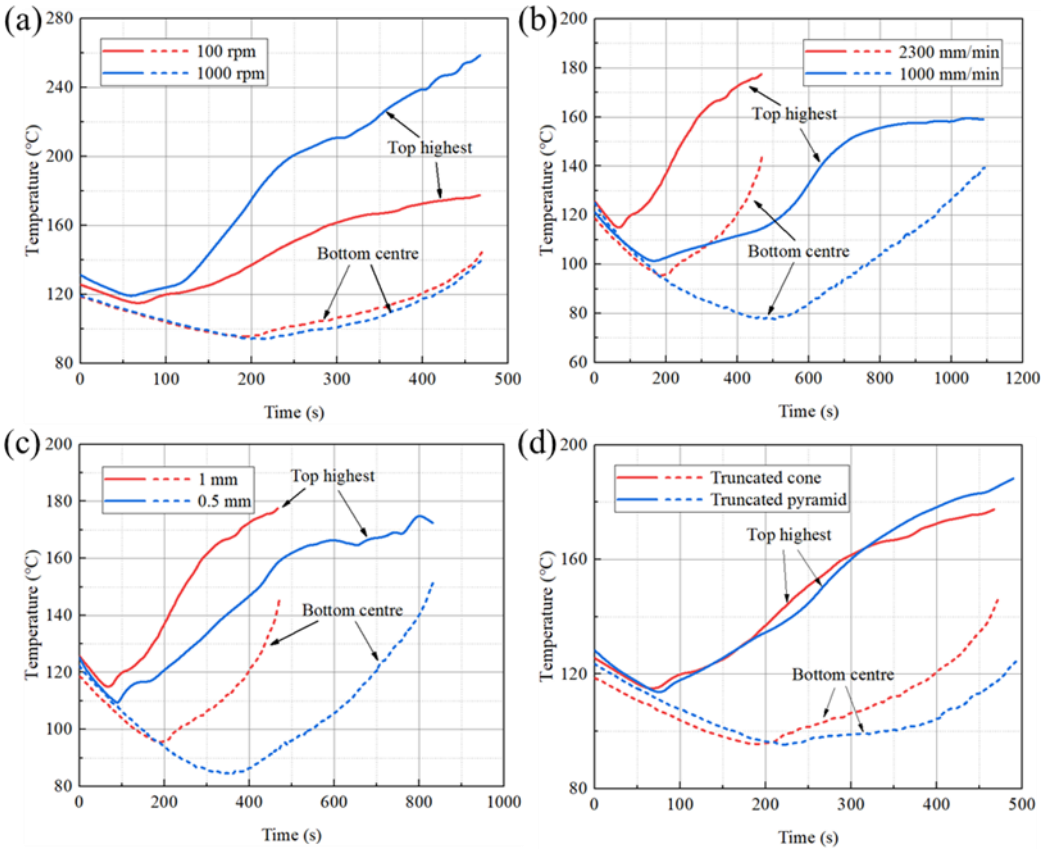


Figure 6.9 Comparison of temperature variation during ISF of PEEK. (a) Effect of spindle speed, (b) effect of feed rate, (c) effect of step size and (d) effect of forming shape.

As shown in Figure 6.9(a), it can be clearly observed that the spindle speed has significant influence on the highest temperature of the top surface and the influence becomes more obvious at later stage, while the temperature of the bottom centre remains the same. By the end of ISF process, the case with spindle speed of 100 rpm shows a temperature of 177.45 °C, while a higher spindle speed of 1000 rpm generated higher temperature up to 258.55 °C. As these two cases have the same forming shapes and therefore the same heat generation from plastic work, the temperature elevation mainly results from the more heat generation due to friction of forming tool.

As shown in Figure 6.9(b), feed rate has obvious influence on the highest temperature, although it is not as remarkable as the effect of spindle speed. Compared to the test with feed rate of 1000 mm/min, the use of a feed rate of 2300 mm/min could produce a

temperature increase of about 20 °C at tool position by the end of ISF. Two reasons contribute to the influence. Firstly, higher feed rate leads to less heat loss each cycle of tool movement, and secondly, more friction heat was generated due to faster relative movement. Feed rate also plays a role in the change of temperature variation at the sheet bottom centre. A minimum temperature of 95.65 °C with feed rate of 2300 mm/min is about 20 °C higher than that with feed rate of 1000 mm/min, while it was reached much earlier. This results from the accelerated increase of forming depth and the quicker approach of bottom surface to the heating tapes to reduce the heat loss.

Compared to the feed rate, similar effect is also observed from Figure 6.9(c), which shows temperature variations for different step sizes with a different mechanism. The temperature elevation for different step sizes came from more material deformation under the effect of tool contact. The increased material deformation could contribute to the increased heat generation from plastic work, and more friction heat because of the rising forming force, which is described in Section 6.3.3.

As shown in Figure 6.9(d), the forming shape also has an influence on the variation of highest temperature on the top surface of the sheet. The highest temperature, i.e., the temperature at the localised tool position, during ISF of truncated pyramid shape is higher than that of truncated cone shape. This can be explained by different deformation conditions in truncated pyramid and cone parts. It is well acknowledged that the final state of the material deformation is under plane strain condition in ISF of truncated cone part and at the straight edge part of truncated pyramid part, while it is under biaxial tension deformation condition at the corners of truncated pyramid part. At the corner of truncated pyramid part, the contact region between the forming tool and the sheet material becomes significantly larger than that in the linear part and subsequently there is more material deformation. This results in more heat generation from both plastic

work and tool-sheet friction, and therefore larger temperature rise at the corner of truncated pyramid parts compared with the straight edge position and truncated cone part.

6.3.3 Forming force

In the ISF tests, forming forces in x, y and z directions were measured and recorded. As shown in Figure 6.10, the vertical force is the same as the force in the z direction, while the horizontal force F_h is composed of the forces in both x and y directions using the following equation:

$$F_h = \sqrt{F_{\mathrm{x}}{}^2 + F_{\mathrm{y}}{}^2} \tag{6.1}$$

where F_{x} and F_{y} are the forming forces in the x and y directions, respectively. For all testing cases, the vertical force firstly increases sharply and then maintains at a stable level or even a slight reduction, while the horizontal force continuously increases until the end of process. For ISF with increasing drawing angle at room or constant high temperature, the vertical forming force trends to increase until the drawing angle reaches about 50 ° and decrease afterwards. However, in the case of heat-assisted ISF with tool rotation, the localised forming temperature would be increased significantly from the beginning to the end, which results in the material softening and subsequently the decrease of forming force.

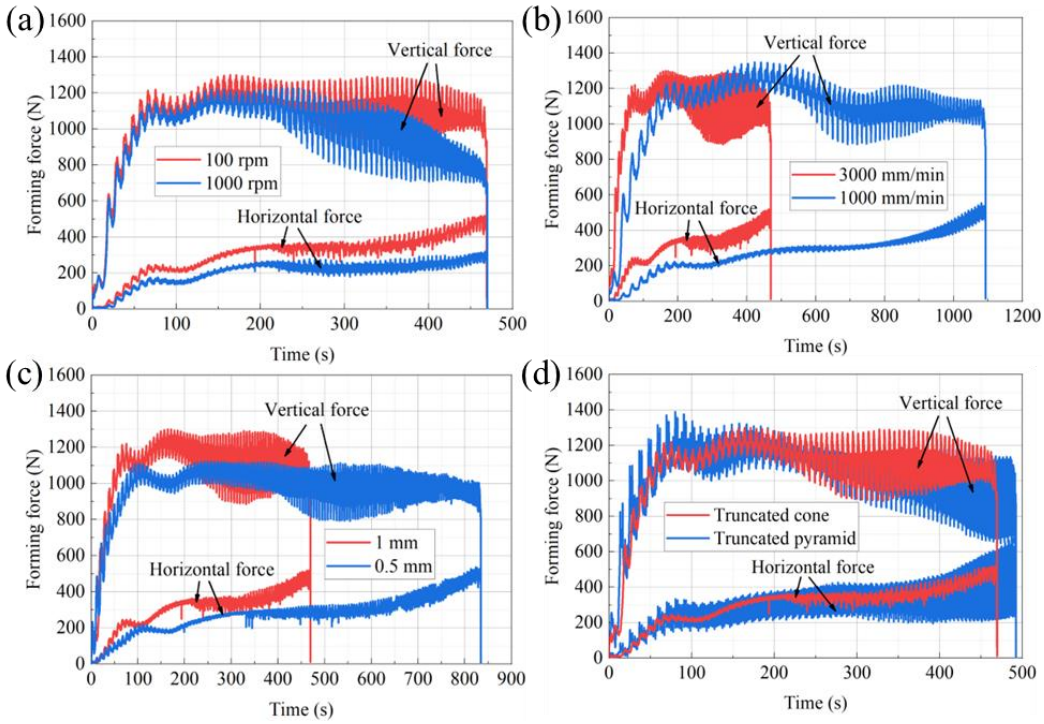


Figure 6.10 Comparison of vertical and horizontal forming forces in ISF of PEEK sheet. (a) Effect of spindle speed, (b) effect of feed rate, (c) effect of step size and (d) effect of forming shape.

As shown in Figure 6.10(a), higher spindle speed can reduce both the vertical and horizontal forming force effectively especially at the last stage of forming. This is a result of more material softening due to larger temperature rise, as illustrated in Figure 6.10(a). The comparison of forming forces for different feed rates are given in Figure 6.10(b) and it shows that only slight influence can be given by feed rate. Although material hardening would happen with larger strain rate, the temperature increase is also obtained, which leads to material softening. Therefore, a balance is reached between the effect of temperature and strain rate at a larger feed rate. As shown in Figure 6.10(c), larger step size can increase the vertical forming force because of more material deformation. Although slightly higher localised temperature is obtained to soften the material, it is not enough to offset the increased reaction force. Finally, the effect of forming shape, i.e., deformation condition, can be found in Figure 6.10(d). The forming force fluctuation during ISF of the truncated pyramid part is greatly larger than that of

the truncated cone part. At the initial stage, the temperature at the corner position is almost the same as other parts, so the larger contact region and more material deformation results in higher forming force. Therefore, the forming force would increase suddenly when the tool moves the corner position. However, at the later stage of forming, since higher temperature can be obtained at the corner position, the material softening leads to the reduced forming force, although there is enhanced tool-sheet contact and more material deformation at the corner. Therefore, each time when the tool moves to the corner of truncated pyramid part, the force would have a sudden drop, which is a totally different phenomenon compared to that at initial stage of the process.

In addition to the experimental study of the effect of ISF conditions on forming force variation, the measured forming force in heat-assisted ISF of PEEK is also used to validate the analytical model for force prediction and the FE simulation, which are developed and presented in Chapters 4 and 5. As shown in Figure 6.11, both the analytical model and FE simulation give effective prediction of vertical forming force, although the predicted results are slightly larger than the experimental result. However, the analytical model shows obvious overestimation in predicting horizontal forming force, while better prediction is given by FE simulation. The reason for a degree of discrepancy of the analytical prediction may be the lack of consideration of local temperature rise, inappropriate assumption of frictional coefficient and insufficient flexibility to respond the change of deformation behaviour with sheet thickness increase.

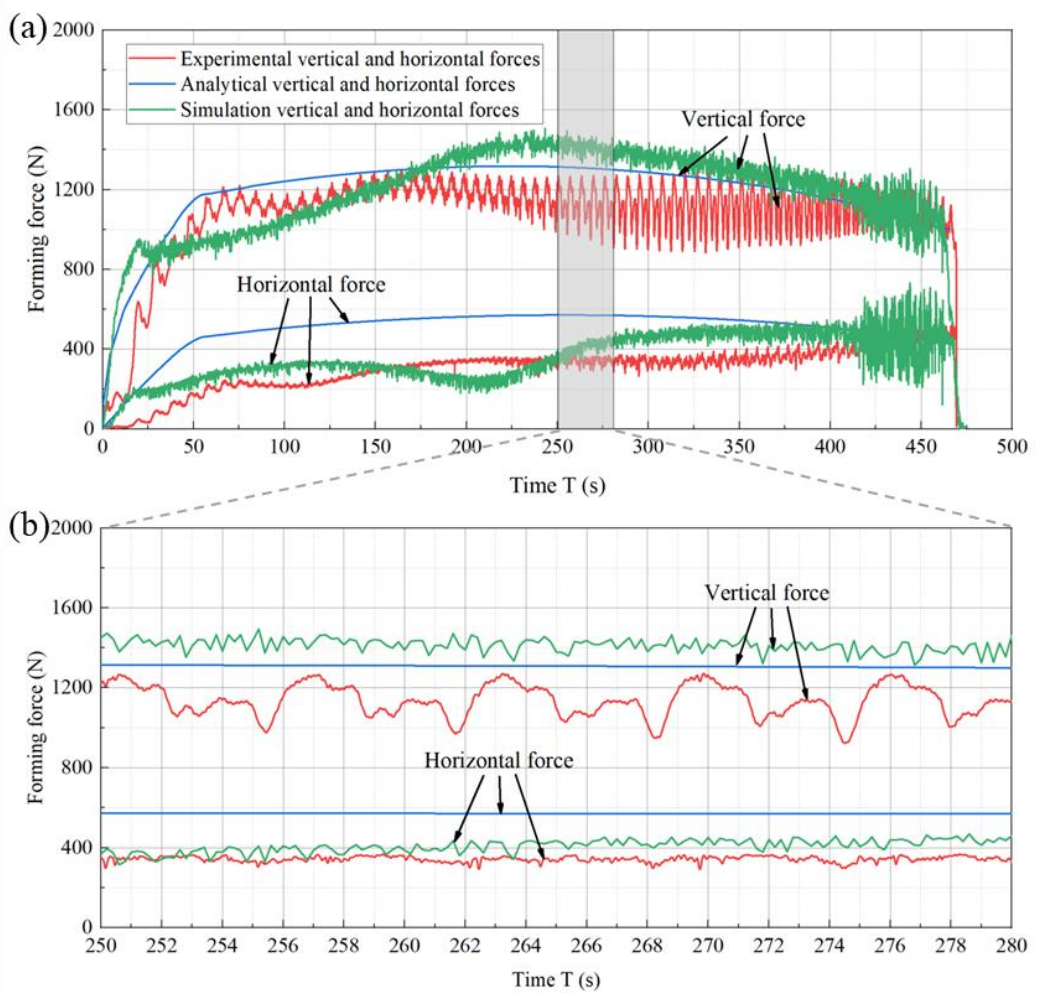


Figure 6.11 Comparison among experimental, analytical and simulation force components in ISF of truncated cone part of PEEK: (a) whole process comparison and (b) detailed comparison in an enlarged time range.

6.3.4 Geometric accuracy

The geometric accuracy of different cases is firstly evaluated by the deviation distribution map as shown in Figure 6.12. The deviation is calculated as the normal distance from the outer surface of formed part to the corresponding surface of the designed model. The formed parts and designed models were aligned at the boundary of the deformation area, which is also the boundary of backing plate. In the deviation map, the negative value of deviation indicates that the area was not sufficiently formed, where the formed sheet did not reach the designed shape because of the springback and thermal distortion.

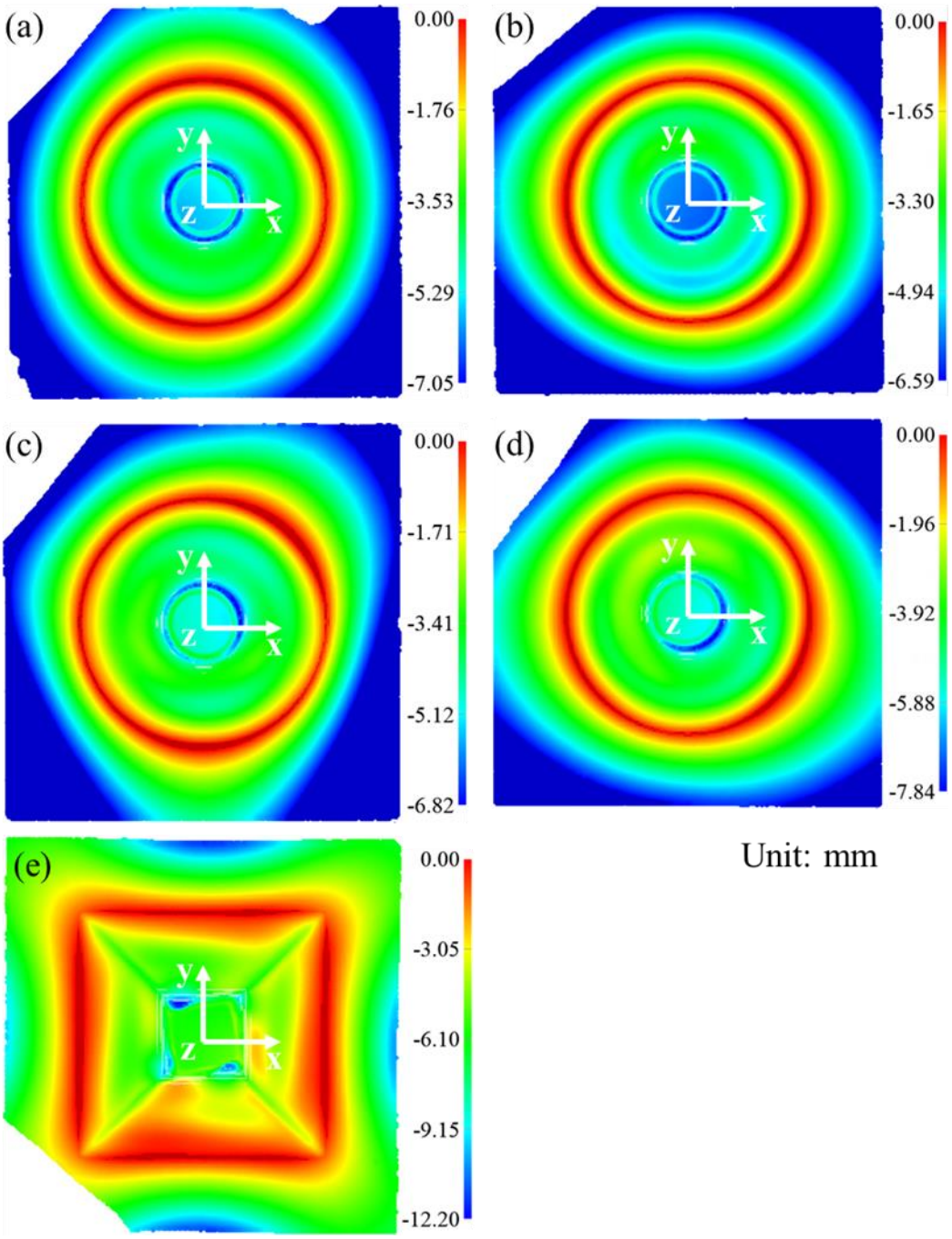


Figure 6.12 Deviation map of the formed PEEK parts as compared with the designed model: (a) PEEK I, (b) PEEK II, (c) PEEK III, (d) PEEK IV and (e) PEEK V.

All the five ISF cases of PEEK have the same variation trend of the geometric deviation. It is observed that the smallest deviation is located at the alignment position supported by the backing plate. Inside the boundary of backing plate, the distribution of deviation is relatively uniform but becomes larger gradually. In the deformation area, the largest deviation can be found at the bottom fillet position, where the sheet material is last

deformed and the springback and thermal distortion are most obvious. Outside the deformation area, severer deviation can be observed from the boundary of backing plate, which is a result of the combined effect of springback due to residual stress due to thermal stress after its removal from the blank holder. Different from the truncated cone part, the formed truncated pyramid part has obvious buckling, which has an obvious influence on the deviation distribution and can be observed in Figure 6.12(e). However, this does not necessarily mean that the truncated cone parts do not have any defect. The twist behaviour of truncated cone parts in heat-assisted ISF is discussed in Section 6.6.2.

To investigate the effect of different process parameters on the forming accuracy, the cross-section profiles from the outer surface of the different formed parts are compared as given in Figure 6.13. It is noteworthy that the designed model in Figure 6.13 is the profile of the outer surface, which is slightly different from the one given in Figure 6.2(a) of Section 6.2.3. All the cases show insufficient forming depth as compared with the designed profile because of the effect of springback and thermal distortion during and after heat-assisted ISF process. Lower spindle speed is observed effective in the improvement of forming accuracy. As shown in Figure 6.13(a), the goodness of fit between designed model and the formed part by 100 rpm spindle speed is better at the formed wall of the deformation area, and meanwhile, the final forming depth is larger than the formed part by 1000 rpm spindle speed. Larger spindle speed leads to higher local temperature as shown in Figure 6.13(a) and causes more obvious instant springback after deformation. Besides, feed rate and step size only have a minor influence on the forming accuracy, as show in Figure 6.13(b) and (c).

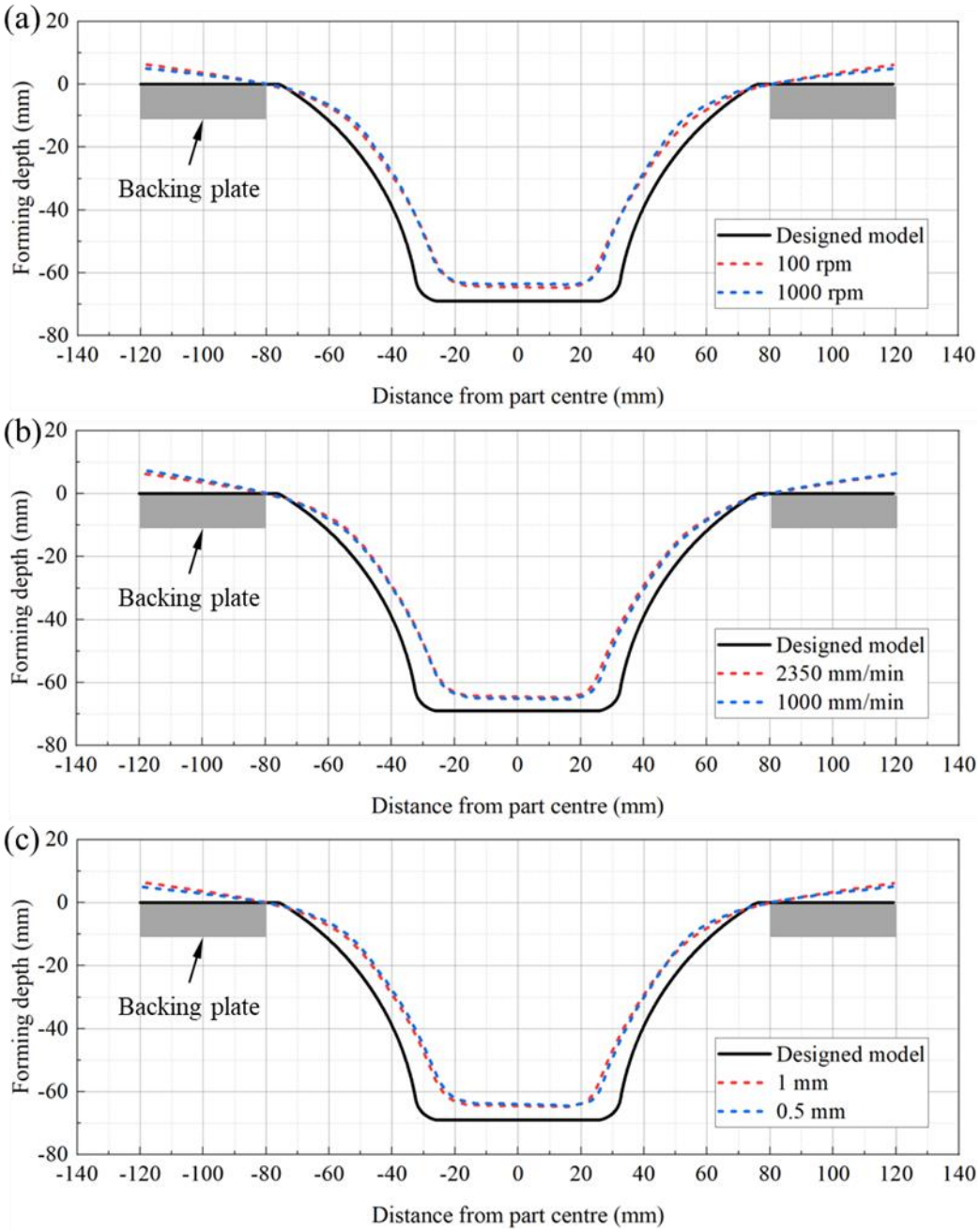


Figure 6.13 Profile comparison of formed truncated cone parts by heat-assisted ISF of PEEK sheet. (a) Effect of spindle speed, (b) effect of feed rate and (c) effect of step size.

For the truncated pyramid part, the profiles from cross-sections of the x-z plane and the digonal are compared in Figure 6.14. For both cross-sections, the difference from designed profile is very much the same when the depth is small. This indicates that the geometric features do not have obvious influence on the accuracy. However, the deviation becomes larger at the bottom fillet of the formed part, especially at the corner

position, because of the buckling due to sudden instability.

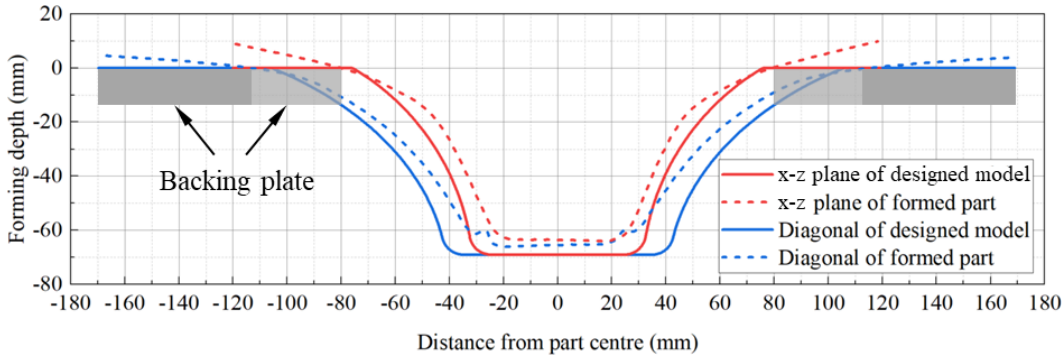


Figure 6.14 Profile comparison of formed truncated pyramid part by heat-assisted ISF of PEEK sheet from different cross-sections.

6.3.5 Thickness distribution

The thickness distribution of the formed PEEK parts is presented in Figure 6.15. The thickness is gradually reduced from the boundary of deformation area to the bottom of the parts. As shown in Figure 6.15(a), the minimum thickness of PEEK I part is 0.78 mm, which is larger than 0.53 mm calculated by the cosine law ($t_0 \cdot \cos\alpha$) as used in Chapter 4. In the cosine law for thickness estimation, t_0 is the initial sheet thickness, and α is the actual drawing angle. The larger thickness than cosine law estimation may be a result of the instant elastic recovery and the global bending effect at high temperature, which are more significant in heat-assisted ISF of thermoplastics than ISF of metal sheets. The material elastic recovery at high temperature increases the reduction of sheet thickness, while the global bending reduces the actual drawing angle α. Both lead to the larger measured thickness than the estimation by cosine law. The thickness distribution of truncated pyramid parts is given in Figure 6.15(e), where the thickness of corner position is much smaller than linear part. Twist and buckling defects can also be observed through the uneven thickness distribution and the large angle of deviation.

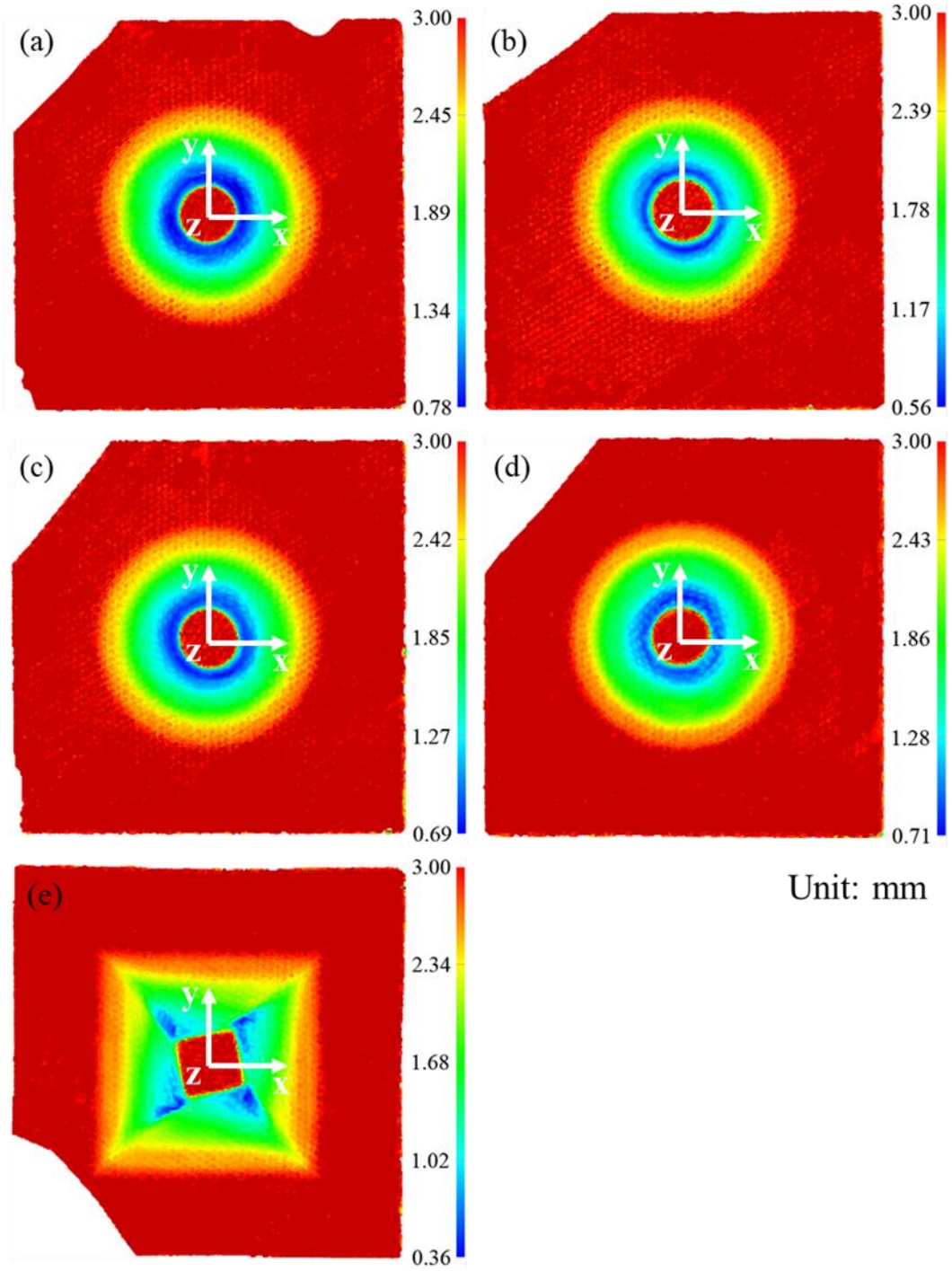


Figure 6.15 Thickness distribution of the formed PEEK parts: (a) PEEK I, (b) PEEK II, (c) PEEK III, (d) PEEK IV and (e) PEEK V.

The thickness distribution of cross-section can be found in Figure 6.16. It can be observed that the process parameters have different influences on the part thickness. The increase of the spindle speed can reduce the minimum thickness, which indicates that the higher local temperature rise causes more plastic flow under the tool-sheet contact.

Additionally, no obvious effect of feed rate and step size on the thickness distribution is observed. As shown in Figure 6.17, the thickness at the corner position of the truncated pyramid part has a reduction compared with other positions.

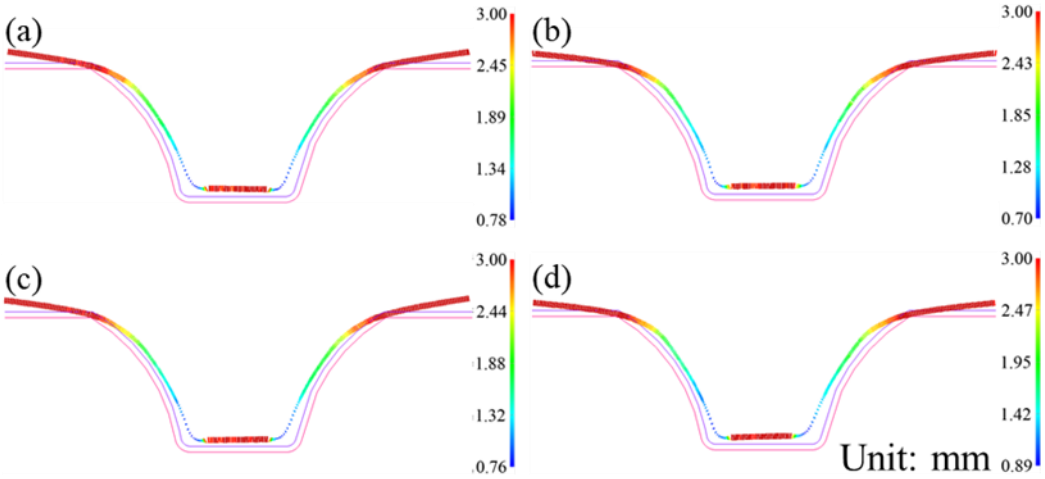


Figure 6.16 Thickness distribution from cross-section of formed PEEK truncated cone parts: (a) PEEK I, (b) PEEK II, (c) PEEK III and (d) PEEK IV.

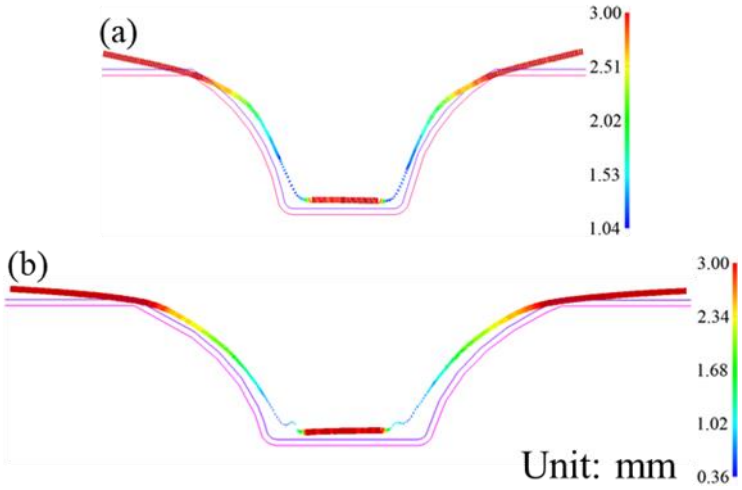


Figure 6.17 Thickness distribution from cross-section of formed PEEK truncated pyramid par: (a) From x-z plane and (b) from diagonal cross-section.

6.4 Results and discussion of heat-assisted ISF of PMMA

PMMA is a brittle material at room temperature. To test the formability of PMMA sheet in ISF, temperature elevation plays a most important role in ISF processing. The

findings of heat-assisted ISF of PEEK sheet in Section 6.3 clarifies that the spindle speed has the biggest influence on the forming temperature, forming force and geometric accuracy, as compared to the feed rate and step size. Therefore, different preheating temperatures and spindle speeds are used in ISF of PMMA sheet as detailed in Section 6.2.3. Also, different shapes including truncated cone and pyramid parts are tested.

6.4.1 ISF formed parts

As shown in Figure 6.18, the PMMA parts can be formed by heat-assisted ISF, but early fracture is observed, which is a result of the limited formability of PMMA even at high temperature. Twist and buckling also obviously exist in all the parts, which may reduce the forming accuracy.

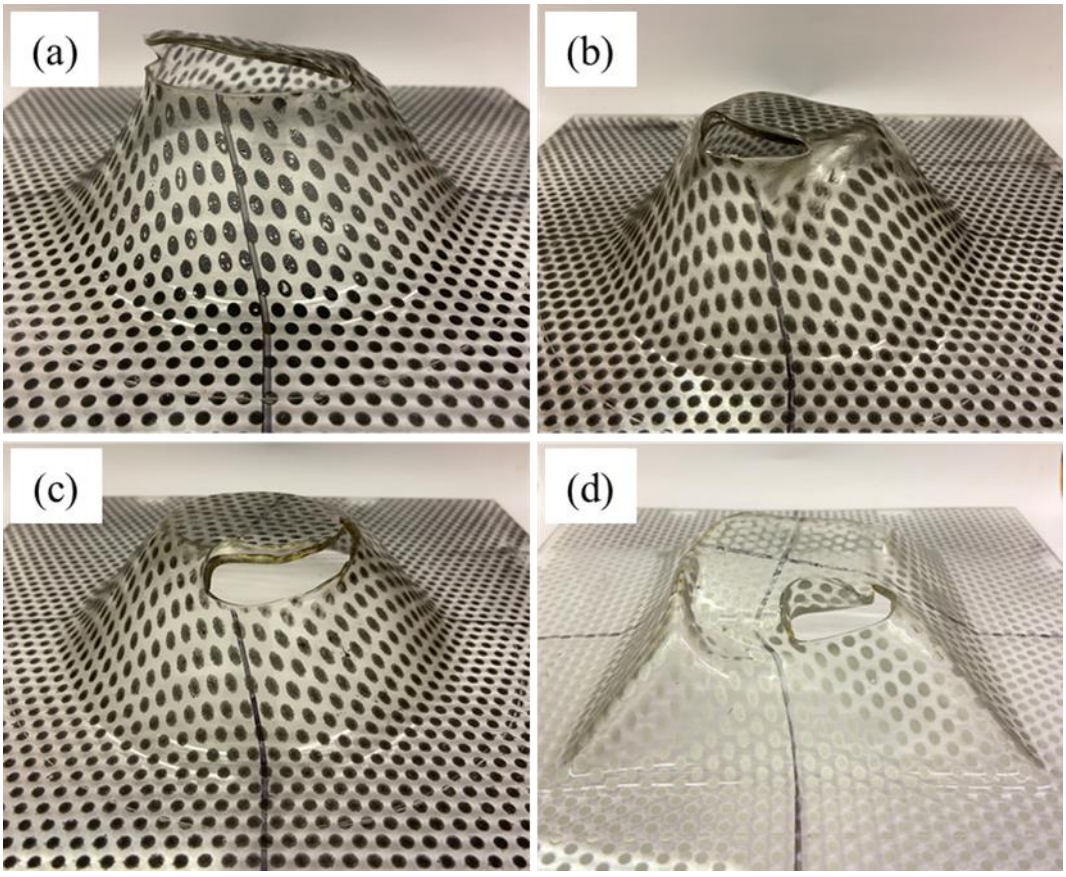


Figure 6.18 ISF formed parts of (a) PMMA I, (b) PMMA II, (c) PMMA III and (d) PMMA IV.

6.4.2 Forming temperature

In ISF testing of PMMA sheets, the temperature distribution on the top surface of truncated cone and pyramid parts are shown in Figures 6.19 and 6.20, respectively. The same as ISF of PEEK sheets, the highest temperature is distributed at the localised tool position. Also, a gradual increase of temperature can be observed from the tool position to the forming boundary, and a uniform temperature distribution is shown at the central region, i.e., the undeformed region of the sheets.

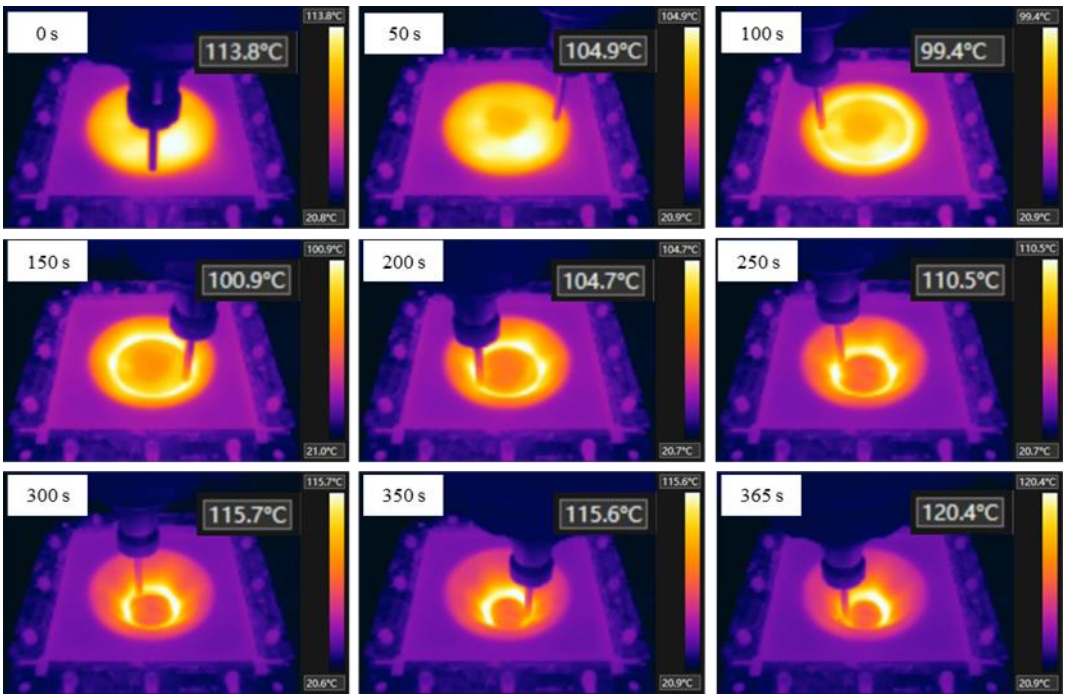


Figure 6.19 Temperature distribution during ISF of PMMA truncated cone part PMMA I.

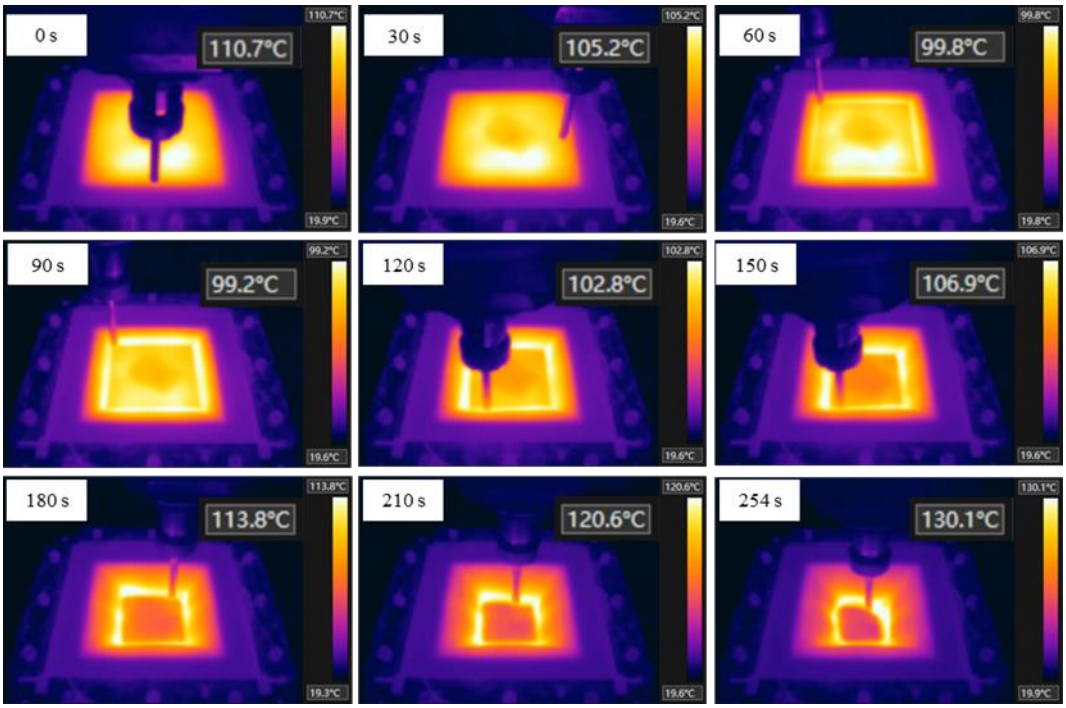


Figure 6.20 Temperature distribution during ISF of PMMA truncated pyramid part PMMA IV.

Figure 6.21 shows the effect of spindle speed, preheating temperature and forming shape on temperature variation during ISF process of PMMA sheets. The change of preheating temperature can affect the temperature on the bottom surface but has less influence on the highest temperature on the top surface. Compared to ISF of PEEK sheets, the effect of spindle speed is less obvious. As can be observed, a difference of about 20 °C is shown on the temperature of tool position at last stage of PMMA ISF, but a difference of 80 °C is given in ISF of PEEK. This is a result of the reduced forming force and less heat generation from friction, due to the less strength of PMMA as compared to PEEK, although PMMA has a smaller value of specific heat capacity. However, a more obvious influence on the temperature variation is given by different forming shape. The same as ISF of PEEK, the enhanced contact between forming tool and sheet material and increased forming force at the corner of truncated pyramid part leads to higher temperature rise.

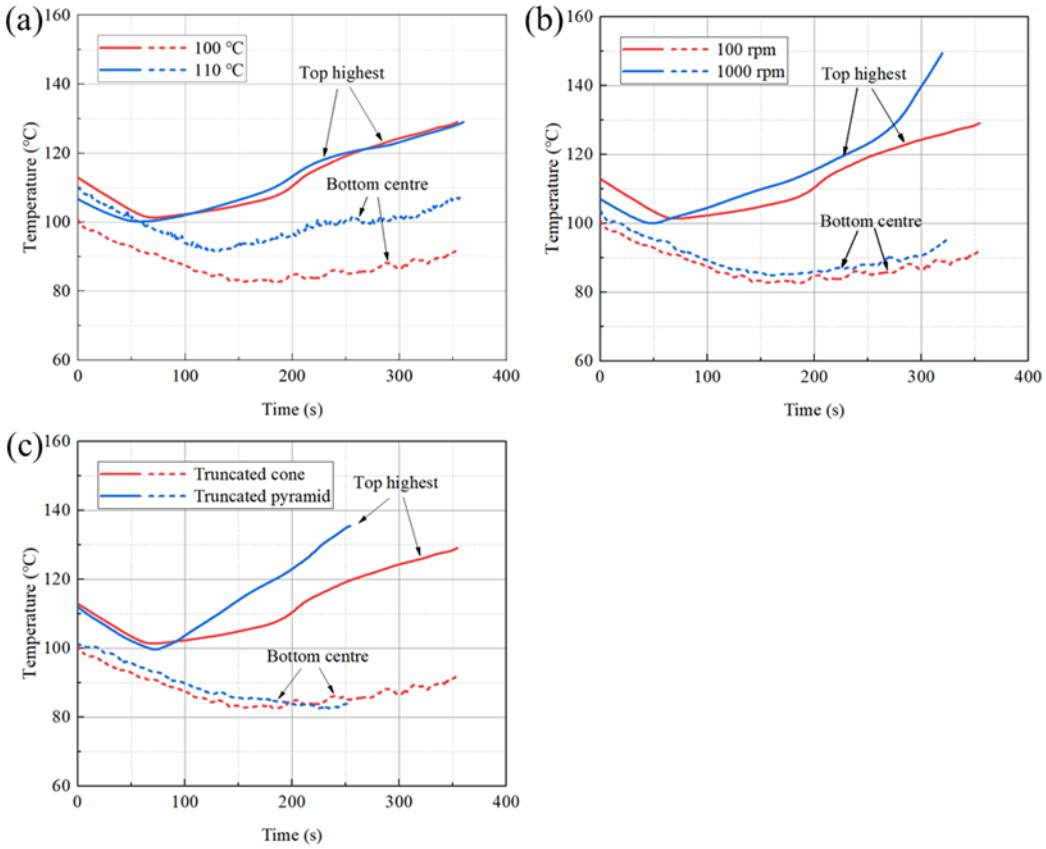


Figure 6.21 Comparison of temperature variation during ISF of PMMA sheet. (a) Effect of preheating temperature, (b) effect of spindle speed and (c) effect of forming shape.

6.4.3 Forming force

The effect of preheating temperature, spindle speed and forming shape on the vertical and horizontal forming forces is shown in Figure 6.22. Higher preheating temperature is found without obvious influence on the forming force because the localised temperature rise is more important to the local material under the forming tool. Higher spindle speed leads to slightly smaller forming force, but the influence is not as obvious as the effect in ISF of PEEK. PMMA has lower strength than PEEK and the forming force is much smaller. As the contact force has a positive effect on the friction generation between forming tool and sheet material, the local temperature rise by increased spindle speed in ISF of PMMA is smaller than ISF of PEEK, and consequently, the forming force has limited reduction. In terms of the effect of geometric feature, the same as ISF

of PEEK sheet, heat-assisted ISF of truncated pyramid PMMA part has larger force fluctuation than ISF of truncated cone part. This confirms again that the change of deformation state and contact condition exists in ISF of pyramid part.

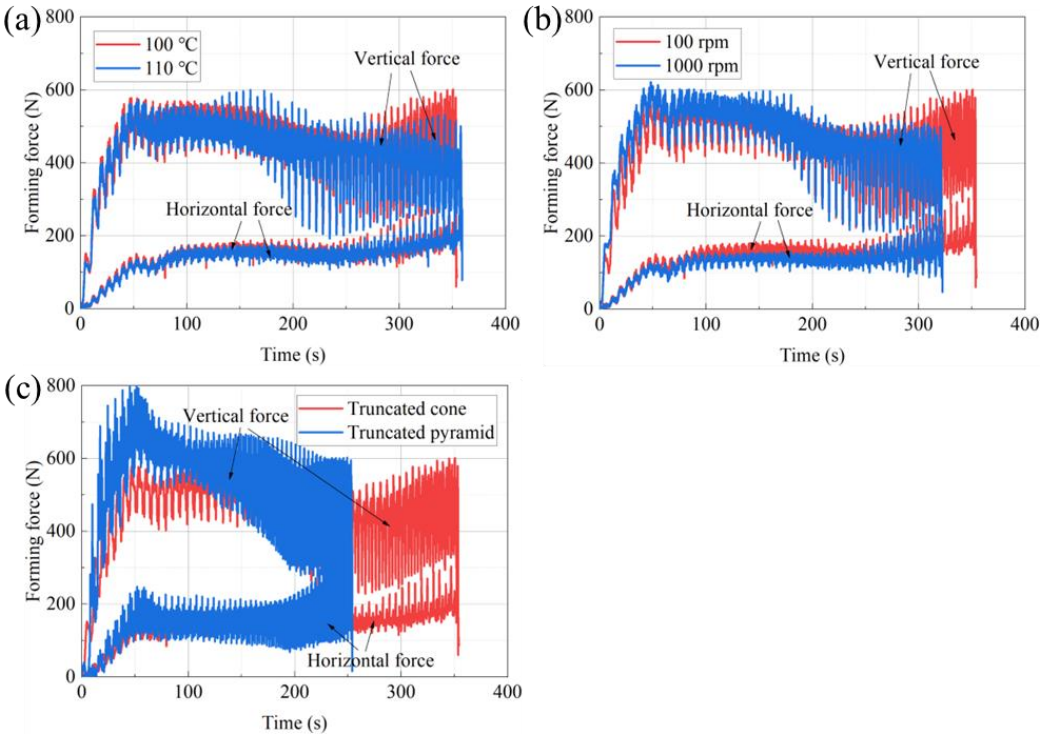


Figure 6.22 Comparison of vertical and horizontal forming forces in ISF of PMMA sheet. (a) Effect of preheating temperature, (b) effect of spindle speed and (c) effect of forming shape.

6.4.4 Geometric accuracy

The deviation distribution maps of different parts by ISF of PMMA are shown in Figure 6.23. The bottom of all the cases has extremely large deviation because of the early fracture during ISF process. The same as ISF of PEEK, the pyramid part of PMMA also shows clear twist and buckling defect as indicated by the nonuniform deviation distribution in circumferential direction.

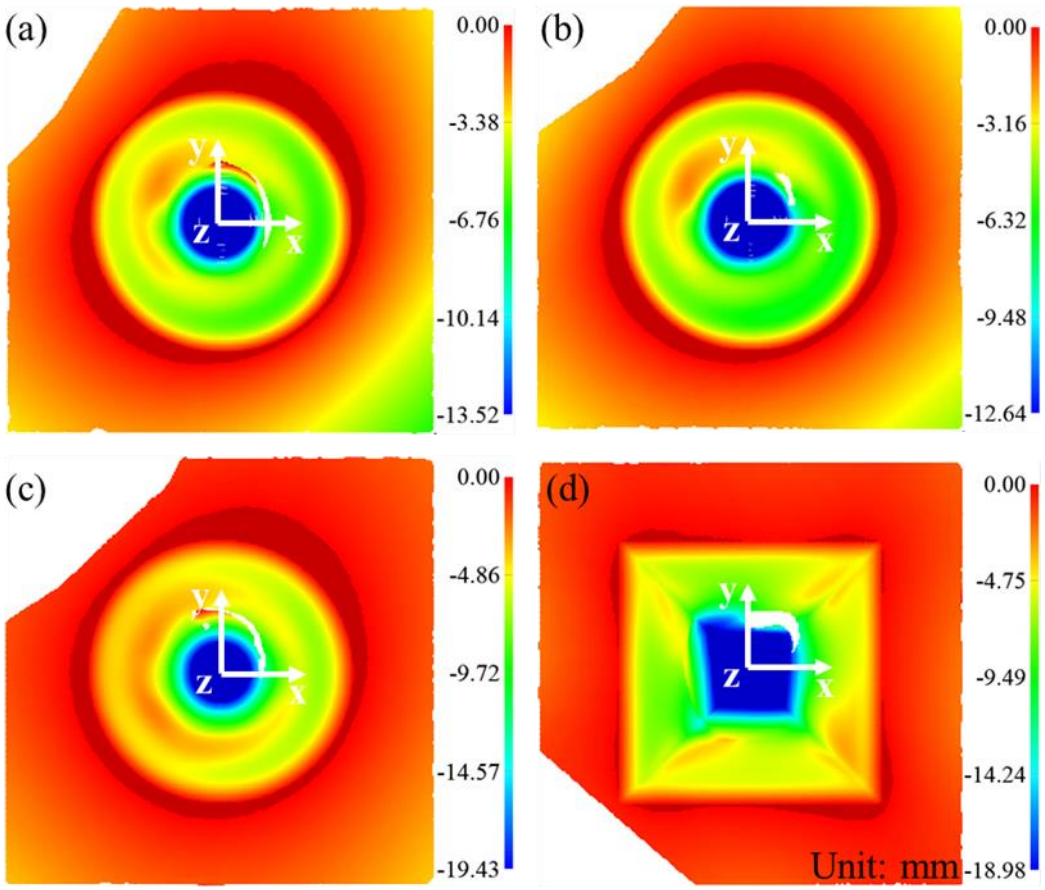


Figure 6.23 Deviation map of the formed PMMA parts as compared with the designed model: (a) PMMA I, (b) PMMA II, (c) PMMA III and (d) PMMA IV.

The effect of preheating temperature and spindle speed on the forming accuracy is presented by the comparison in Figure 6.24. From the cross-section profile of the formed parts, severe uneven deformation is observed, which is a clear indication of the additional stretch during deformation. This indicates that the stretch behaviour plays a vital role in the ISF process of PMMA, and the stretching force is an important part of the forming force. This stretch is analysed as a combined result of high springback, thermal distortion and low material strength of PMMA at high temperatures. The deformation of sheet material would have a severe recovery once the tool moves away, and there would be a stretching effect when the tool moves to this position again. Figure 6.24(a) shows that the increase in preheating temperature from 100 °C to 110 °C does not explicitly influence the accuracy. Although the initial/ preheating temperatures are

different, the difference of 10 °C may be eliminated by the heat loss after ISF process starts, which is the reason why no noticeable change in forming accuracy can be found. However, compared to preheating temperature, spindle speed has a more prominent effect on the geometric accuracy. As shown in Figure 6.24(b), the increase of spindle speed to 1000 mm/min causes earlier fracture and severer springback, and the formed part has a worse correlation to the designed model, especially in the forming depth. As the stretch behaviour due to thermal distortion is remarkable in heat-assisted ISF of PMMA, the material weakening could cause more advanced damage initiation under the increased spindle speed.

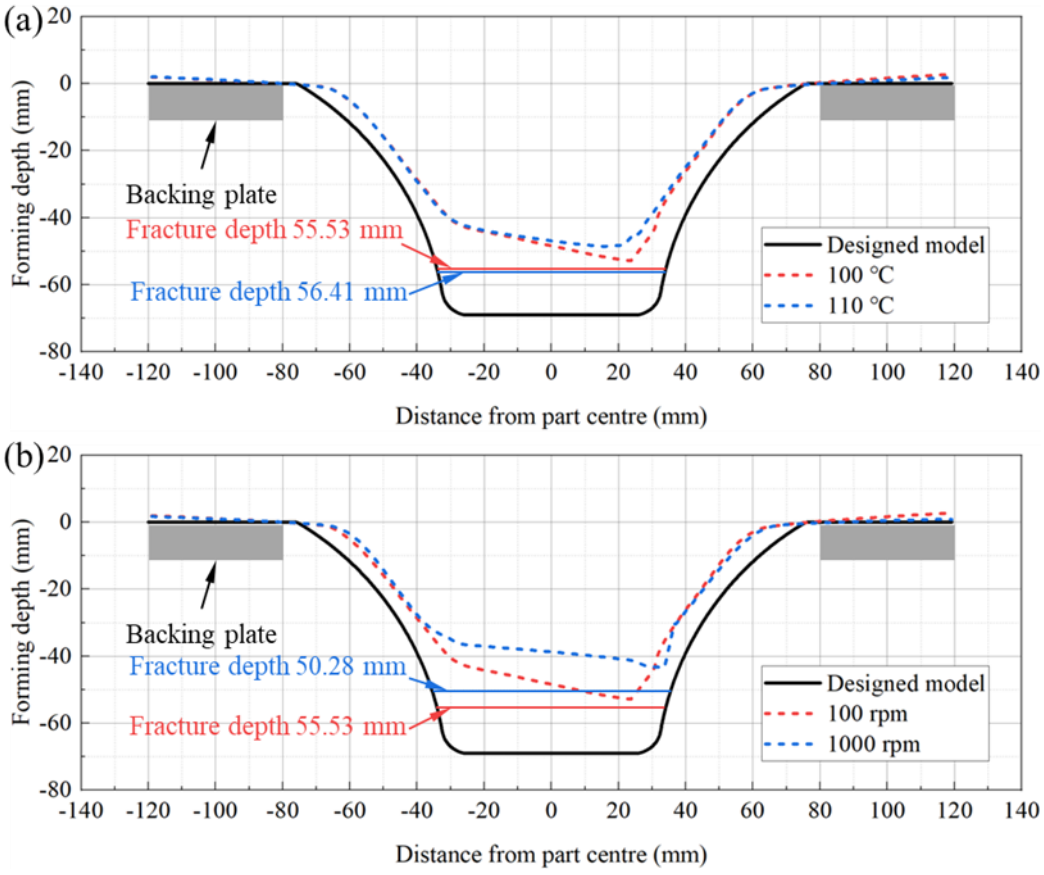


Figure 6.24 Profile comparison of formed truncated cone parts by heat-assisted ISF of PMMA sheet. (a) Effect of preheating temperature and (b) effect of spindle speed.

The same as ISF of PEEK, the effect of geometric features is insignificant as shown in Figure 6.25. The forming depth of truncated pyramid part is notably smaller than

truncated cone parts. The earlier fracture at corner position than at linear positions causes this observation.

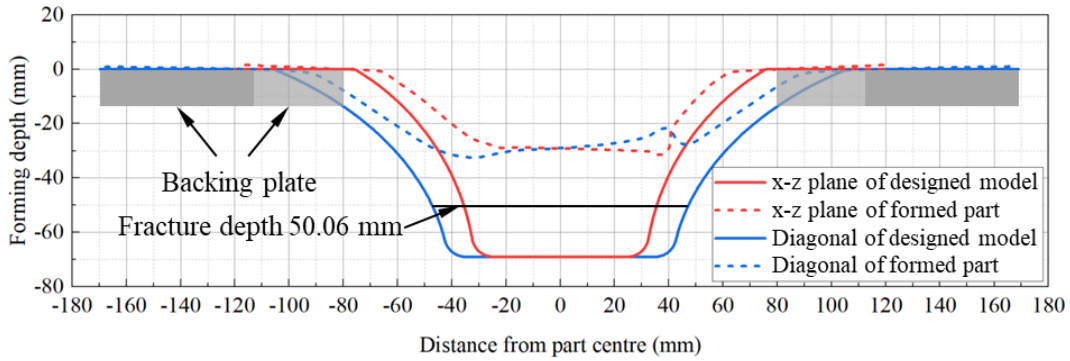


Figure 6.25 Profile comparison of formed truncated pyramid part by heat-assisted ISF of PMMA sheet from different cross-sections.

6.4.5 Thickness distribution

The thickness distribution of formed PMMA parts in different cases is given in Figure 6.26. The thickness reduction of the clamped undeformed area indicates that plastic flow happened in this area during ISF process. The stretch effect is a result of large forming force and low material strength of PMMA. In the deformed aera, the thickness gradually decreases outside with the increase of drawing angle.

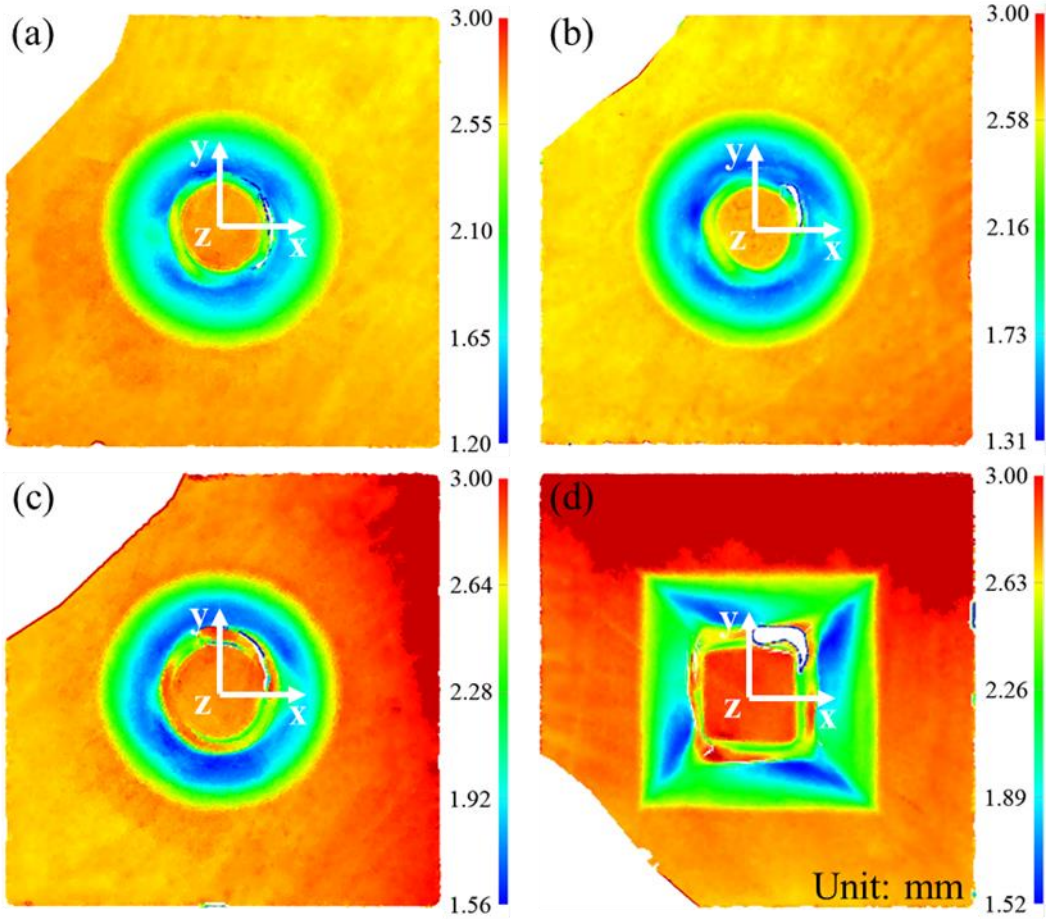


Figure 6.26 Thickness distribution of the formed PMMA parts: (a) PMMA I, (b) PMMA II, (c) PMMA III and (d) PMMA IV.

The minimum thickness of different parts can also indicate the forming depth with the change of process parameters. As shown in Figure 6.27, PMMA III part has the largest value of minimum thickness among all the truncated cone parts, and the forming depth of this part is the smallest. However, differently, the thickness distribution of PMMA IV part cannot be simply used as the indication of forming depth to compare with truncated cone parts. Although the thickness of the cross-sections shown in Figure 6.28 is much smaller than the truncated cone parts, which seems correlated to the forming depth, the minimum thickness of the whole part given in Figure 6.26(d) has a similar value to PMMA III part. Therefore, the relationship between the minimum thickness and the forming depth is invalid in the comparison between truncated cone and pyramid

parts. Combining the visible circumferential torsion, it can be concluded that the thickness reduction of the truncated pyramid part is a result of both deformation with increased drawing angle and the circumferential twist and buckling.

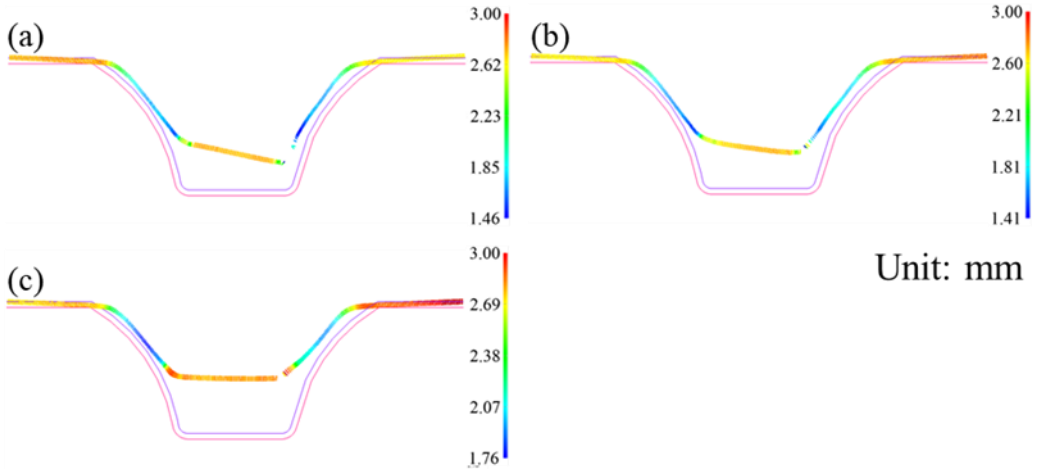


Figure 6.27 Thickness distribution from cross-section of formed PMMA truncated cone parts: (a) PMMA I, (b) PMMA II and (c) PMMA III.

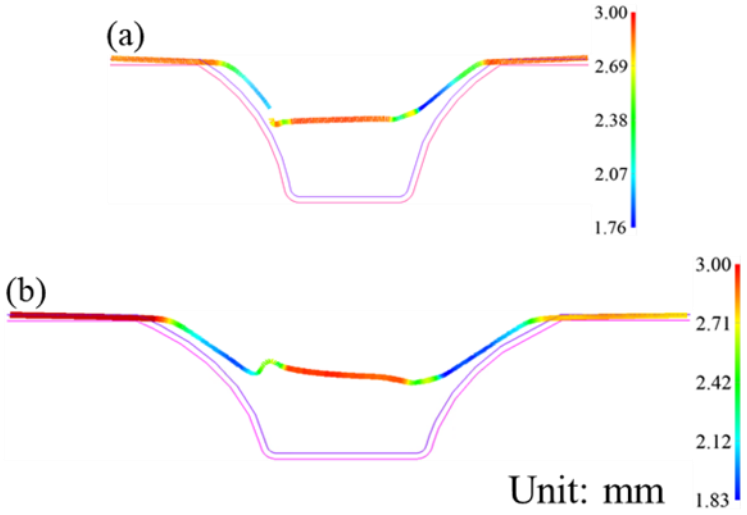


Figure 6.28 Thickness distribution from cross-section of formed PMMA truncated pyramid part: (a) From x-z plane and (b) from diagonal cross-section.

6.5 ISF-based manufacture of cranial plate

The possibility of heat-assisted ISF of PEEK and PMMA sheets is validated in Sections 6.3 and 6.4. Based on the study on the effect of different process parameters on the forming accuracy and thickness distribution, heat-assisted ISF of PEEK and PMMA

was tested for the medical application of cranial plate manufacture. The manufactured parts without fracture and other obvious defects are shown in Figure 6.29. This proves that the heat-assisted ISF can be a solution for the customised manufacture of PEEK and PMMA cranial plate.

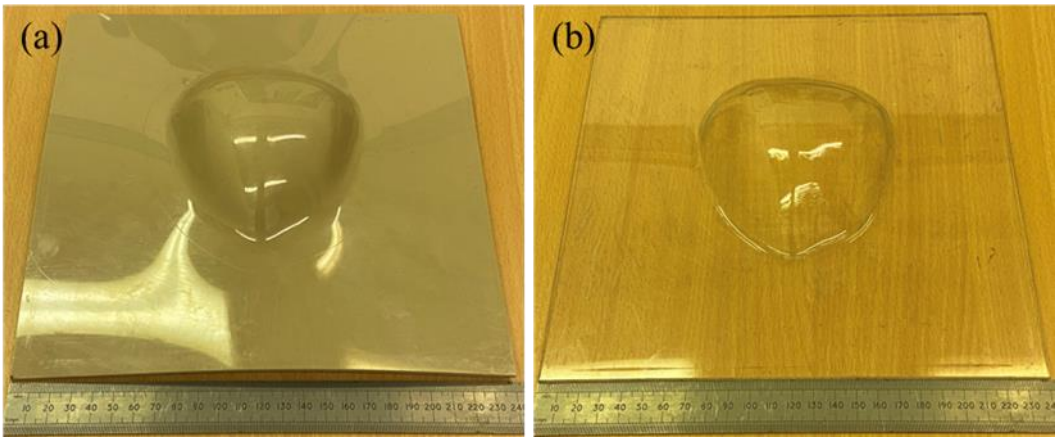


Figure 6.29 Heat-assisted ISF parts of (a) PEEK cranial plate and (b) PMMA cranial plate.

During the manufacture process, the temperature distribution was recorded as shown in Figures 6.30 and 6.31 for PEEK and PMMA parts, respectively. With the use of heating tapes and mat, the deformation area has higher temperature than the other area, where the backing plate has direct contact. The heat generation under the contact of forming tool can induce localised temperature rise to soften the sheet material. The above are the two reasons for the improved formability of PEEK and PMMA to complete the cranial plate manufacture.

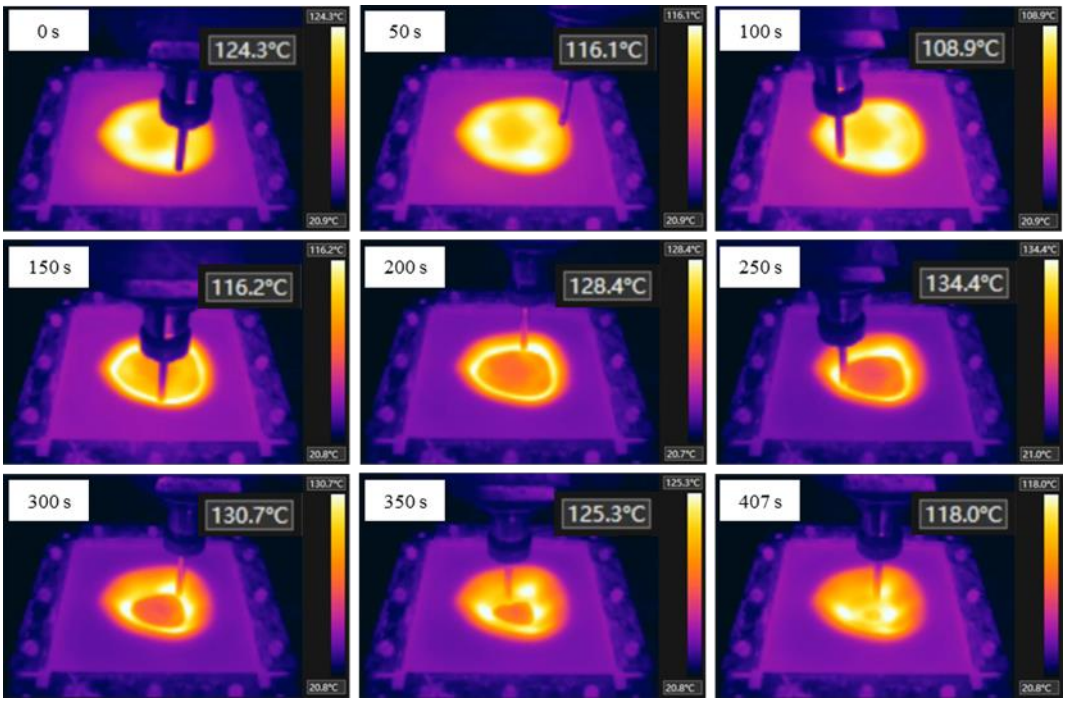


Figure 6.30 Temperature distribution during ISF-based manufacture of PEEK cranial plate.

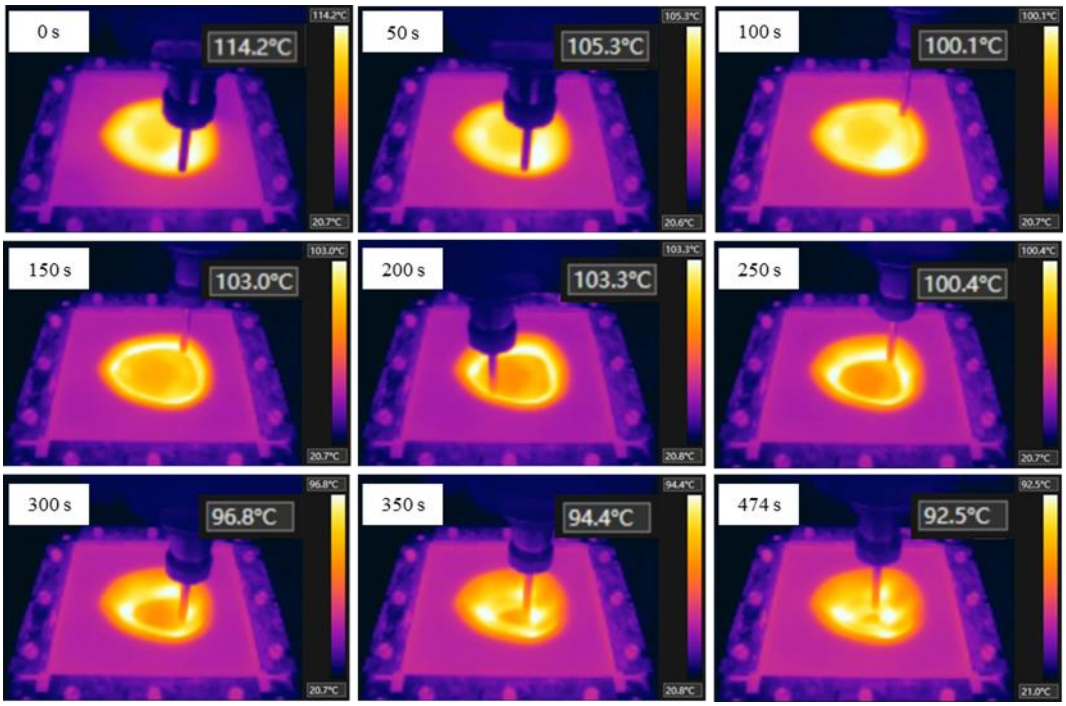


Figure 6.31 Temperature distribution during ISF-based manufacture of PMMA cranial plate.

The localised temperature rise can also be indicated by the difference between the maximum temperature of the top and bottom surfaces, as shown in Figure 6.32.

Different from ISF of truncated cone and pyramid parts, the maximum top temperature is gradually decreased after the significant rise. This temperature decrease on the top surface does not influence the forming process because of the relatively small drawing angle and the rising bottom temperature. At the end of the forming process, the significantly rising bottom temperature is a result of the fact that the heating tapes get in contact with the bottom surface of PEEK and PMMA parts.

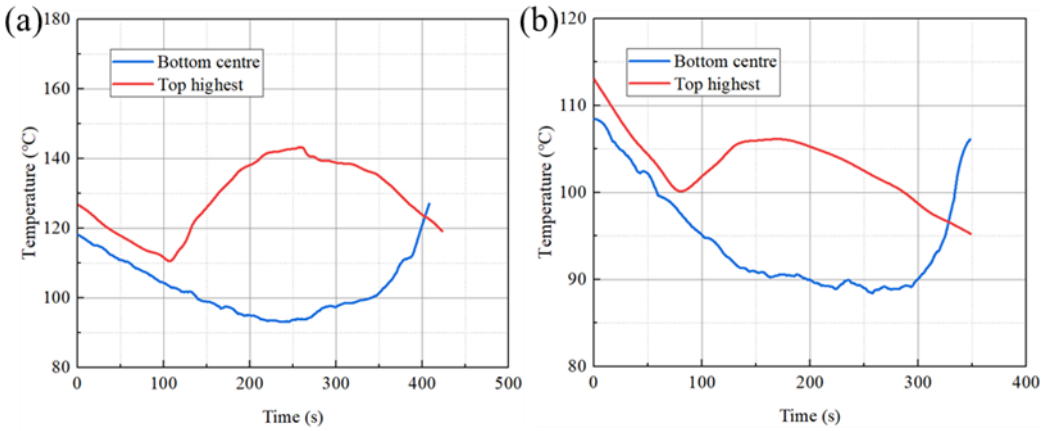


Figure 6.32 Temperature variation during ISF-based manufacture of (a) PEEK cranial plate and (b) PMMA cranial plate.

As shown in Figure 6.33, both vertical and horizontal forces in ISF of PMMA are smaller, although the preheating and localised temperatures are lower than ISF of PEEK. The variation trend of force components shows a quick increase to peak force and a gradual decrease afterwards. The high drawing angle at the beginning and the global bending effect due to the use of a backing plate contribute to the quick increase, as revealed in Chapter 4.

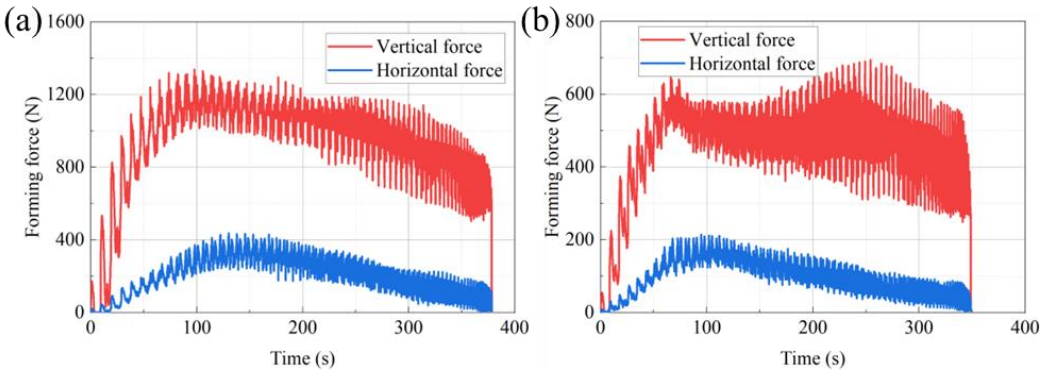


Figure 6.33 Vertical and horizontal forming forces in ISF-based manufacture of (a) PEEK cranial plate and (b) PMMA cranial plate.

The deviation between the manufactured cranial plates and the skull model is given in Figure 6.34. The results come from the comparison based on the alignment for best fit. In the deviation distribution map, the positive value represents that the area was formed beyond the designed model, while the negative value means that the area was not enough formed. Results show that the discrepancy mainly exists in the transition area from the peripheral to the central area, while the central area agrees well with the designed model. By comparison, ISF formed PMMA part has a maximum deviation of 4.19 mm, slightly better than the geometric accuracy of the PEEK part, the maximum deviation of which is 4.75. The better forming accuracy of PMMA part as compared with PEEK part can also be observed from cross-sections of y-z and x-z planes, as shown in Figure 6.35.

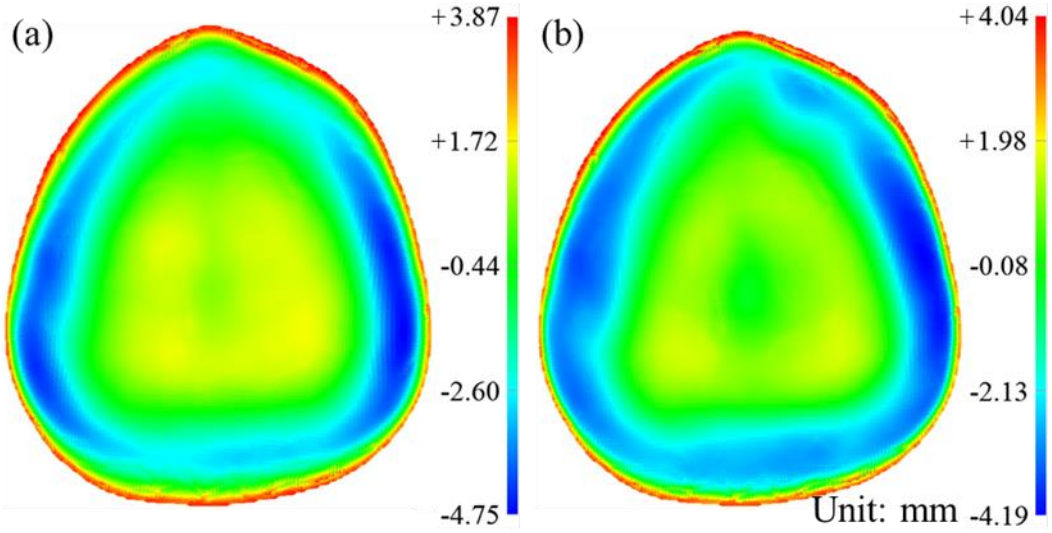


Figure 6.34 Deviation map of the formed cranial plate as compared with the designed model: (a) PEEK part and (b) PMMA part.

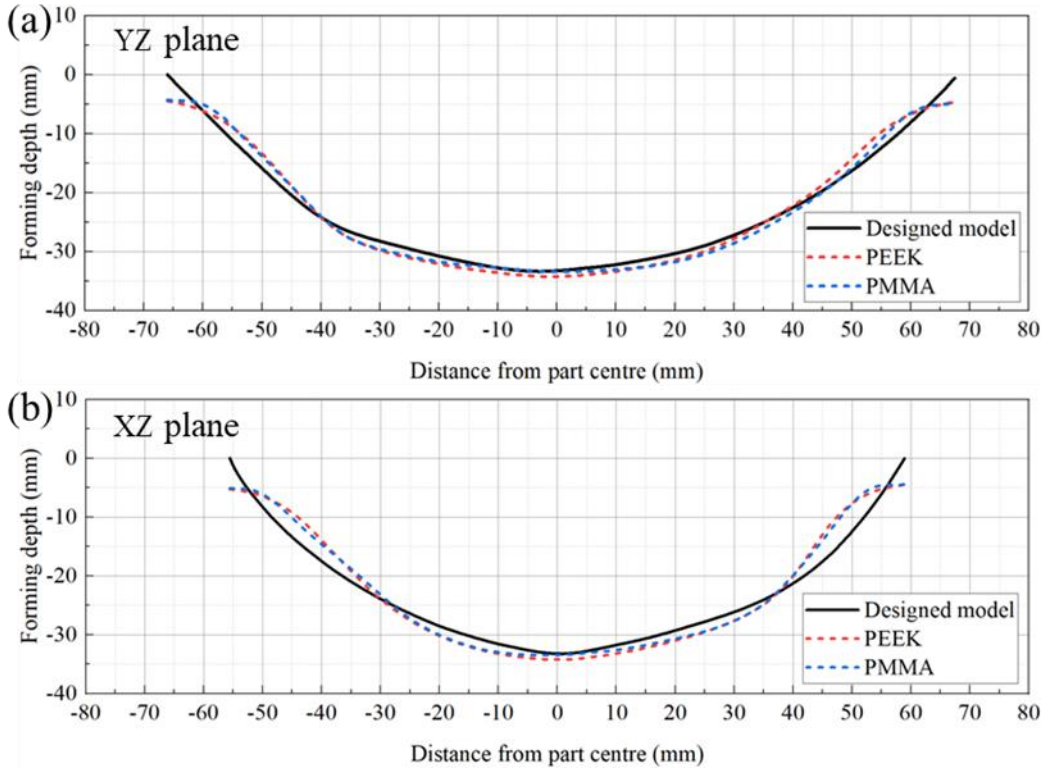


Figure 6.35 Profile comparison of formed cranial plates by heat-assisted ISF of PEEK and PMMA in cross-sections of (a) y-z plane and (b) x-z plane.

The thickness distribution of the PEEK and PMMA parts can be found in Figure 6.36(a) and (b), respectively. The minimum thickness is located in the transition area from the periphery to the central area, where the drawing angle is the largest. The thickness in

the edge and the central areas of the PEEK sheet is quite large and close to the initial thickness, while the thickness in these areas of PMMA sheet is smaller than the initial value, which results from the stretch behaviour during ISF of PMMA as described in Section 6.4.

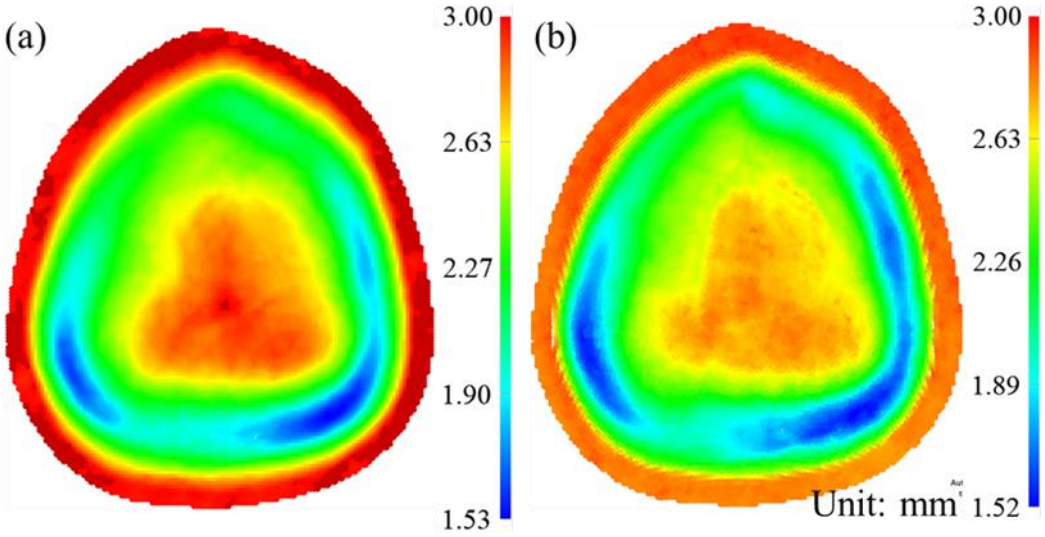


Figure 6.36 Thickness distribution of the formed cranial plate: (a) PEEK part and (b) PMMA part.

6.6 Discussions on the challenging issues in ISF of PEEK and PMMA

From the testing results in Sections 6.3, 6.4 and 6.5, it is found that the insufficient forming accuracy, fracture, and twist are key challenging issues in heat-assisted ISF of thermoplastics including PEEK and PMMA. This section gives a discussion on these three aspects. The developed model for forming accuracy considers the initial bending effect and springback in heat-assisted ISF of thermoplastics. The analytical model for fracture is developed by consideration of stress triaxiality and equivalent strain distribution of sheet thickness under the contact of forming tool. While the developed model for twist behaviour considers the continuous accumulation of twist along the tool path. These models are further validated by the testing results of heat-assisted PEEK and PMMA, and this leads to the conclusion that the above-mentioned models and

considerations are effective to explain and understand the mechanism behind the discussed challenging issues.

6.6.1 Forming accuracy

6.6.1.1 Theoretical analysis

As indicated by the experimental results in Sections 6.3.4 and 6.4.4, the formed shapes of PEEK and PMMA parts do not have good agreement with the designed model. As the backing plate has an orifice with a diameter of 160 mm for ISF of truncated cone parts or a side length of 160 mm for ISF of truncated pyramid parts, and there is a gap existing between the backing plate and the designed tool path, the discrepancy happens from the start of deformation area because of the bending behaviour, which causes the formed profile to shift from the designed model. Then, the springback would happen after tool removal due to the initial bending. Thermal stress due to the temperature rise would also cause the distortion after the clamp removal. Therefore, the geometric accuracy in heat-assisted PEEK and PMMA is mainly influenced by the initial bending effect, global springback and thermal distortion. However, the currently developed analytical framework in this thesis does not consider the localised temperature change and the global uneven temperature distribution. Meanwhile, the thermal distortion may only be assessed with FE simulation but is hard to be quantified with analytical method. Therefore, in the current work, the analytical model for the forming accuracy is developed with only consideration of the initial bending effect and the global springback but without the effect the thermal distortion. As shown in Figure 6.37, the initial bending condition in ISF is presented.

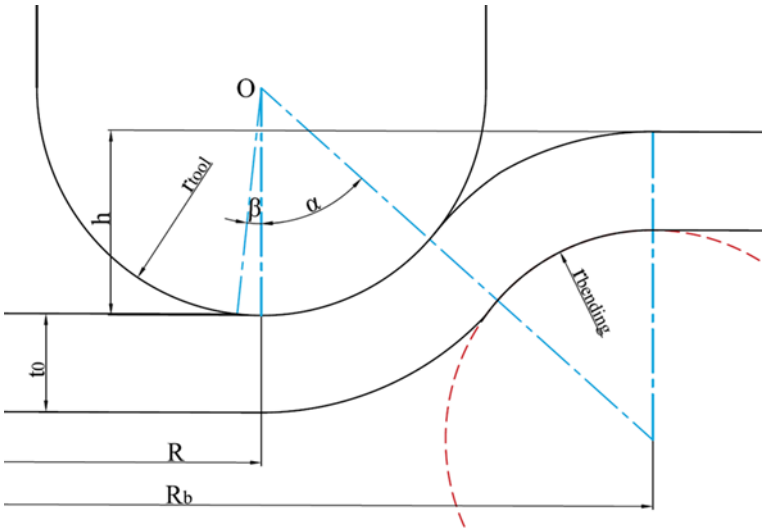


Figure 6.37 Illustration of the initial bending condition in ISF.

According to the geometry relationships, the following two equations can be given:

$$\left(r_{\text{bending}} + t_0 + r_{\text{tool}}\right) \cdot \sin\alpha = R_{\text{b}} - R \tag{6.2}$$

$$\left(r_{\text{bending}} + t_0\right) \cdot \cos\alpha + h - r_{\text{tool}} \cdot (1 - \cos\alpha) = r_{\text{bending}} + t_0 \tag{6.3}$$

where r_{tool} is the tool radius, R_{b} is the distance from the part centre/ symmetry axis to the edge of backing plate, R is the distance from the part centre/ symmetry axis to the tool position, r_{bending} is the bending radius and h is the depth of tool position. Under the bending effect, the actual drawing angle α is smaller than the designed drawing angle Ψ. The expression of α can be obtained from Equation (6.4) by solving Equations (6.2) and (6.3):

$$\alpha = 2 \cdot \tan^{-1}\left(\frac{h}{R_{\text{b}} - R}\right) \tag{6.4}$$

The actual drawing angle is calculated as Equation (6.4) initially and equals to Ψ after the designed value is reached. Therefore, as shown in Figure 6.38, the final bending radius $r_{\text{bending}}^{\Psi}$ without consideration of springback can be calculated by either of the following two equations:

$$r_{\text{bending}}^{\Psi} = \frac{R_{\text{b}} - R_{\Psi}}{\sin \Psi} - r_{\text{tool}} - t_0 \tag{6.5}$$

$$r_{\text{bending}}^{\Psi} = \frac{h_{\Psi}}{1 - \cos \Psi} - r_{\text{tool}} - t_0 \tag{6.6}$$

where R_{Ψ} and h_{Ψ} are the distance from the part centre/ symmetry axis to the tool position and the depth of tool position, respectively, when the actual drawing angle reaches the designed value Ψ. The final bending angle $\theta_{\text{bending}}^{\Psi}$ without consideration of springback equals to Ψ as well.

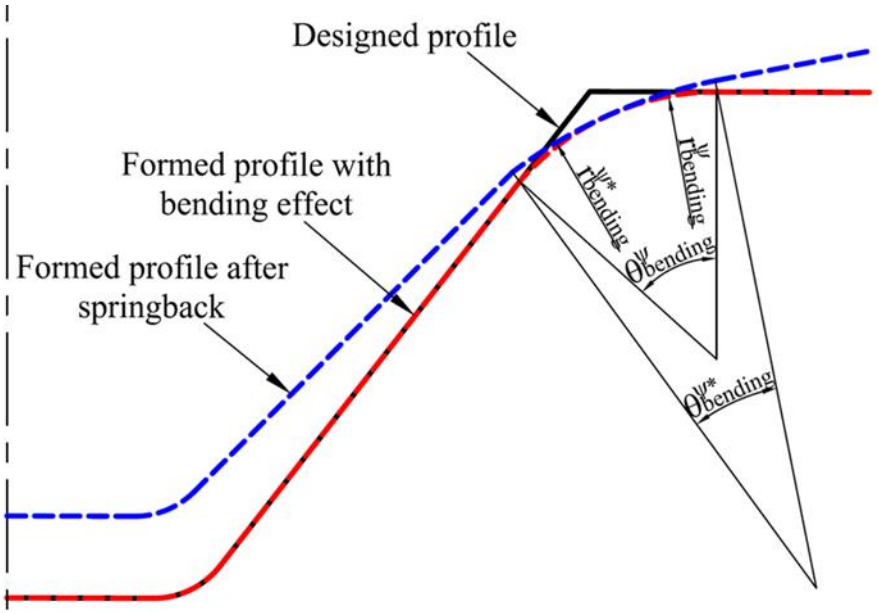


Figure 6.38 Illustration of the theoretical ISF formed profile with consideration of bending and distortion behaviours.

Considering the thermal distortion behaviour, the increase in the bending curvature $\Delta\left(1/r_{\text{bending}}^{\Psi}\right)$ and decrease in bending angle $\Delta\theta_{\text{bending}}^{\Psi}$ can be calculated by the following equations [140]:

$$\Delta\left(\frac{1}{r_{\text{bending}}^{\Psi}}\right) = -3 \cdot \frac{\bar{\sigma}_{\Psi}}{E \cdot t_0} \tag{6.7}$$

$$\Delta\theta_{\text{bending}}^{\Psi} \approx -3 \cdot \frac{\bar{\sigma}_{\Psi} \cdot r_{\text{bending}}^{\Psi}}{E \cdot t_0} \cdot \theta_{\text{bending}}^{\Psi} \tag{6.8}$$

where E is the Young's modulus and $\bar{\sigma}_{\Psi}$ is the equivalent stress of inner or outer surface, which is calculated by the constitutive model and the equivalent strain as given below:

$$\bar{\varepsilon}_{\Psi} = \frac{2}{\sqrt{3}} \cdot \ln \frac{r^{\Psi}_{\text{bending}} + t_0}{\sqrt{r^{\Psi}_{\text{bending}} \cdot \left(r^{\Psi}_{\text{bending}} + t_0\right)}} = \frac{1}{\sqrt{3}} \cdot \ln \frac{r^{\Psi}_{\text{bending}} + t_0}{r^{\Psi}_{\text{bending}}} \tag{6.9}$$

Therefore, after removal of forming tool and blank holder, as shown in Figure 6.39, the bending radius $r^{\Psi_*}_{\text{bending}}$ and bending angle $\theta^{\Psi_*}_{\text{bending}}$ considering springback behaviour is calculated as following:

$$r^{\Psi_*}_{\text{bending}} = \frac{1}{\frac{1}{r^{\Psi}_{\text{bending}}} - 3 \cdot \frac{\bar{\sigma}_{\Psi}}{E \cdot t_0}} \tag{6.10}$$

$$\theta^{\Psi_*}_{\text{bending}} = \theta^{\Psi}_{\text{bending}} - 3 \cdot \frac{\bar{\sigma}_{\Psi} \cdot r^{\Psi}_{\text{bending}}}{E \cdot t_0} \cdot \theta^{\Psi}_{\text{bending}} \tag{6.11}$$

It is clearly shown that without consideration of thermal distortion, the forming inaccuracy in ISF process is mainly influenced by the material constitutive response, Young's modulus, initial sheet thickness, tool radius, dimension of backing plate and the designed shape, which are all factors affecting the initial bending and the global springback.

6.6.6.2 Model validation

The developed analytical model was implemented by making corrections to the designed profile. The profile prediction can be achieved following three steps: profile drawn under design → profile corrected with bending effect → profile corrected with springback. As shown in Figure 6.39, the predicted formed profile was drawn according to the predicted bending radius and angle after springback, while the experimental result comes from the formed PEEK I part.

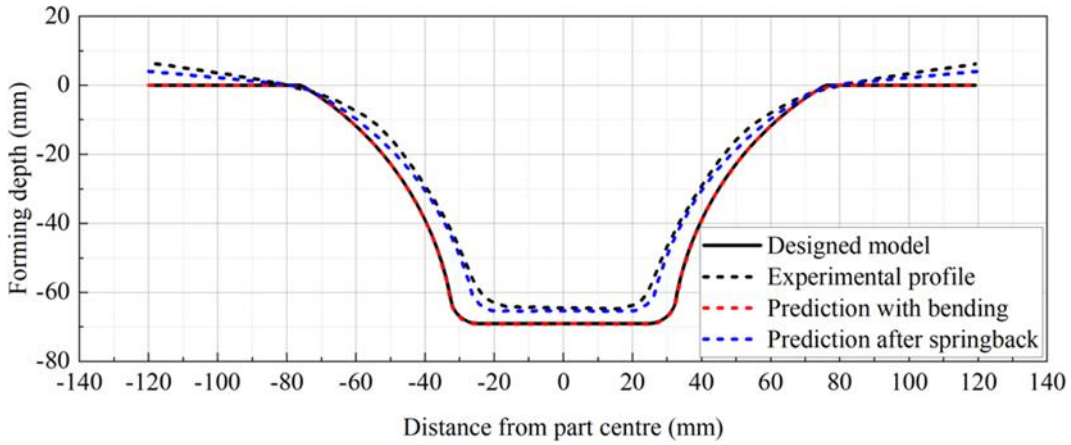


Figure 6.39 Comparison of the formed profile between the analytically prediction result and the experimental result.

The predicted result has good correlation with the measured part profile in terms of the forming depth, the deviation from designed model and the buckling behaviour of the undeformed area. The comparison indicates that the developed analytical model may be an effective method to predict the formed part profile in ISF process although the effect of thermal distortion is not considered in the derivation.

6.6.2 Fracture mechanism

6.6.2.1 Theoretical analysis

As indicated in literature [155-158], the stress triaxiality has significantly influence on the material fracture strain. In ISF process, the variation of stress triaxiality has been acknowledged. This section is focused on the stress triaxiality distribution and the equivalent strain distribution in ISF, which can help reveal the fracture mechanism in ISF.

The stress components can be derived by building up force equilibrium equations. The illustration of stress components on a small element are given in Figure 6.40. The illustration is drawn based on the local coordinate system proposed in Chapter 4. In the system, (r, φ, θ) are coordinates to identify the position of a small element, where r is

the distance from the studied position to the tool centre, φ is the angle between the position and the tool axis, and θ is the angle from the meridional cross-section to the position.

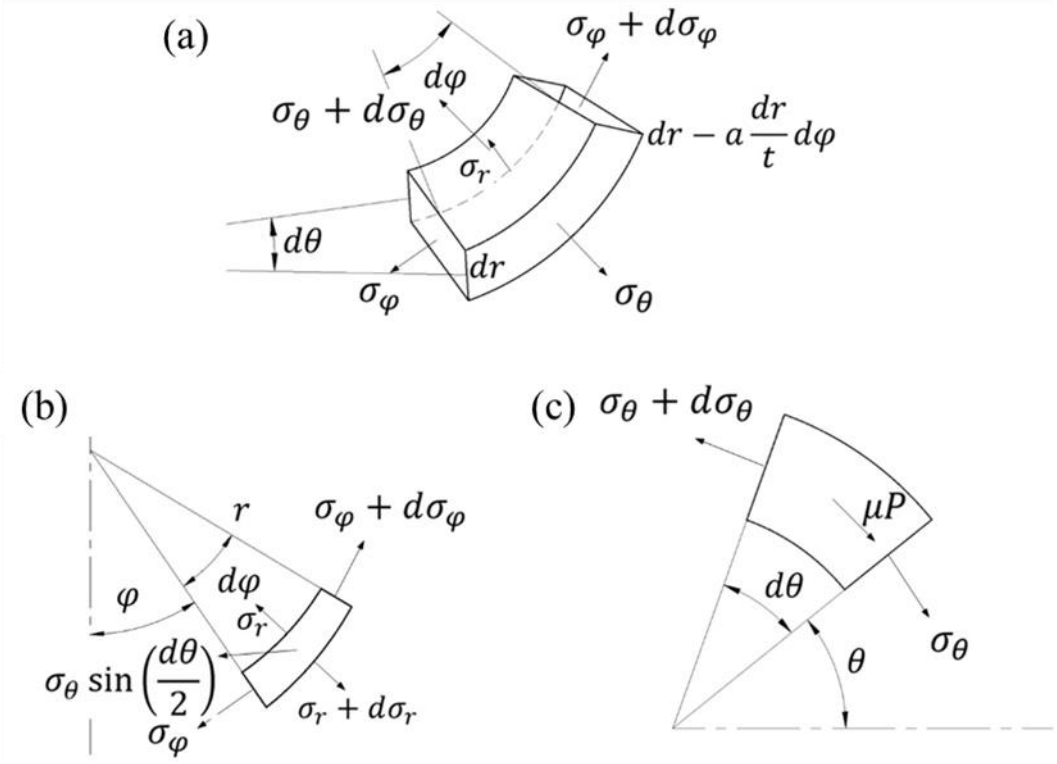


Figure 6.40 Illustration of stress components in a small element. (a) Stress components on a small element, (b) φ direction view and (c) θ direction view.

The force equilibrium equation along θ direction can be given as following:

$$\sigma_\theta \cdot r \cdot d\varphi \cdot \frac{1}{2} \cdot \left(t + t + \frac{dt}{2}\right) \cdot \cos\left(\frac{d\theta}{2}\right) + f \cdot \sigma_r \cdot r \cdot d\varphi \cdot r \cdot \sin\varphi \cdot d\theta = (\sigma_\theta + d\sigma_\theta) \cdot r \cdot d\varphi \cdot \frac{1}{2} \cdot \left(t + t + \frac{dt}{2}\right) \cdot \cos\left(\frac{d\theta}{2}\right) \quad (6.12)$$

where σ_θ, σ_φ and σ_r are the stresses in θ, φ and r directions, respectively, f is the coefficient of friction. By neglecting higher order terms, approximating $\cos\left(\frac{d\theta}{2}\right) \approx 1$ and assuming $r \cdot \sin\varphi \cdot d\theta \approx t$ [28], the equation can be simplified as following:

$$d\sigma_\theta = \mu \cdot \sigma_r \quad (6.13)$$

The force equilibrium equation along r direction can be given as following:

$$\sigma_{\mathrm{r}} \cdot r \cdot \mathrm{d}\varphi \cdot r \cdot \sin\varphi \cdot \mathrm{d}\theta + \sigma_{\theta} \cdot r \cdot \mathrm{d}\varphi \cdot \mathrm{d}r \cdot \sin\left(\frac{\mathrm{d}\theta}{2}\right) \cdot \sin\left(\varphi + \frac{1}{2} \cdot d\varphi\right) + (\sigma_{\theta} + \mathrm{d}\sigma_{\theta}) \cdot r \cdot \mathrm{d}\varphi \cdot \mathrm{d}r \cdot \sin\left(\frac{\mathrm{d}\theta}{2}\right) \cdot \sin\left(\varphi + \frac{1}{2} \cdot \mathrm{d}\varphi\right) + \sigma_{\varphi} \cdot r \cdot \sin\varphi \cdot \mathrm{d}\theta \cdot \mathrm{d}r \cdot \sin\left(\frac{\mathrm{d}\varphi}{2}\right) + \left(\sigma_{\varphi} + \mathrm{d}\sigma_{\varphi}\right) \cdot r \cdot \sin(\varphi + \mathrm{d}\varphi) \cdot \mathrm{d}\theta \cdot \mathrm{d}r \cdot \sin\left(\frac{\mathrm{d}\varphi}{2}\right) = (\sigma_{\mathrm{r}} + \mathrm{d}\sigma_{\mathrm{r}}) \cdot (r + \mathrm{d}r) \cdot \mathrm{d}\varphi \cdot r \cdot \sin\varphi \cdot \mathrm{d}\theta \tag{6.14}$$

By replacing $\mathrm{d}\sigma_{\theta}$ with Equation (6.13), neglecting higher order terms and approximating $\sin\left(\frac{\mathrm{d}\theta}{2}\right) \approx \frac{\mathrm{d}\theta}{2}$ and $\sin\left(\frac{\mathrm{d}\varphi}{2}\right) \approx \frac{\mathrm{d}\varphi}{2}$, Equation (6.14) can be simplified as following:

$$\frac{\mathrm{d}\sigma_{\mathrm{r}}}{\mathrm{d}r} = \frac{\sigma_{\theta} + \sigma_{\varphi} - \left(1 - \frac{1}{2} \cdot f\right) \cdot \sigma_{\mathrm{r}}}{r} \tag{6.15}$$

Although the final state of the deformed part by ISF is in plane strain condition, the sheet material undergoes equi-biaxial tension in the proposed coordinate system under the effect of forming tool. In equi-biaxial tension condition, the stress ratio equals to 1 and the following relationship can be obtained:

$$\sigma_{\theta} = \sigma_{\varphi} \tag{6.16}$$

The equivalent stress $\bar{\sigma}$ can be calculated as following:

$$\bar{\sigma} = \frac{1}{\sqrt{2}} \cdot \sqrt{\left(\sigma_{\mathrm{r}} - \sigma_{\varphi}\right)^2 + \left(\sigma_{\varphi} - \sigma_{\theta}\right)^2 + (\sigma_{\theta} - \sigma_{\mathrm{r}})^2} = \sigma_{\varphi} - \sigma_{\mathrm{r}} \tag{6.17}$$

where σ_{φ} is always larger than σ_{r} in ISF process. By combining Equations (6.15) – (6.17), the following Equation can be obtained:

$$\frac{\mathrm{d}\sigma_{r}}{\mathrm{d}r} = \frac{\left(1 + \frac{1}{2} \cdot f\right) \cdot \sigma_{\mathrm{r}} + 2 \cdot \bar{\sigma}}{r} \tag{6.18}$$

Integrating the above equation gives the following equation:

$$\sigma_{\mathrm{r}} = c_1 \cdot r^{1+\frac{1}{2}\cdot f} - \frac{4}{2+f} \cdot \bar{\sigma} \tag{6.19}$$

where c_1 is model parameter to be identified. To verify the correctness of the above integration, Equation (6.19) is substituted into both sides of Equation (6.18) as follows:

$$\frac{\mathrm{d}\sigma_r}{\mathrm{d}r} = c_1 \cdot \left(1 + \frac{1}{2} \cdot f\right) \cdot r^{\frac{1}{2}\cdot f} \tag{6.20}$$

$$\frac{\left(1+\frac{1}{2}\cdot f\right)\cdot\sigma_{\mathrm{r}}+2\cdot\bar{\sigma}}{r} = \frac{\left(1+\frac{1}{2}\cdot f\right)\cdot\left(c_1\cdot r^{1+\frac{1}{2}\cdot f}-\frac{4}{2+f}\cdot\bar{\sigma}\right)+2\cdot\bar{\sigma}}{r} = \frac{\left(1+\frac{1}{2}\cdot f\right)\cdot c_1\cdot r^{1+\frac{1}{2}\cdot f}-\left(1+\frac{1}{2}\cdot f\right)\cdot\frac{4}{2+f}\cdot\bar{\sigma}+2\cdot\bar{\sigma}}{r} =$$

$$\frac{\left(1+\frac{1}{2}\cdot f\right)\cdot c_1\cdot r^{1+\frac{1}{2}\cdot f}-\frac{2+f}{2}\cdot\frac{4}{2+f}\cdot\bar{\sigma}+2\cdot\bar{\sigma}}{r} = c_1 \cdot \left(1 + \frac{1}{2} \cdot \mu\right) \cdot r^{\frac{1}{2}\cdot f} \tag{6.21}$$

With Equations (6.20) and (6.21), the validity of Equation (6.19) can be confirmed.

As the bottom surface is free from any limit, the boundary condition can be given as: $r = r_{\mathrm{tool}} + t$, $\sigma_{\mathrm{r}} = 0$. Based on the boundary condition, the expression of σ_{r} is derived as Equation (6.22):

$$\sigma_{\mathrm{r}} = \frac{4\cdot\bar{\sigma}}{2+f} \cdot \left(\frac{r}{r_{\mathrm{tool}}+t}\right)^{1+\frac{1}{2}\cdot f} - \frac{4\cdot\bar{\sigma}}{2+f} \tag{6.22}$$

σ_{φ} and σ_{θ} can be calculated as following expressions:

$$\sigma_{\varphi} = \sigma_{\theta} = \frac{4\cdot\bar{\sigma}}{2+f} \cdot \left(\frac{r}{r_{\mathrm{tool}}+t}\right)^{1+\frac{1}{2}\cdot f} - \frac{(2-f)\cdot\bar{\sigma}}{2+f} \tag{6.23}$$

Then, the hydrostatic stress $\sigma_{\mathrm{m}} = \frac{1}{3} \cdot \left(\sigma_{\theta} + \sigma_{\varphi} + \sigma_{\mathrm{r}}\right)$ can be calculated as following:

$$\sigma_{\mathrm{m}} = \frac{4\cdot\bar{\sigma}}{2+f} \cdot \left(\frac{r}{r_{\mathrm{tool}}+t}\right)^{1+\frac{1}{2}\cdot f} - \frac{(8-2\cdot f)\cdot\bar{\sigma}}{6+3\cdot f} \tag{6.24}$$

And, the stress triaxiality η can be calculated by the following equation:

$$\eta = \frac{\sigma_m}{\bar{\sigma}} = \frac{4}{2+f} \cdot \left(\frac{r}{r_{tool}+t}\right)^{1+\frac{1}{2}\cdot f} - \frac{(8-2\cdot f)}{6+3\cdot f} \tag{6.25}$$

In the meridional cross-section, the thickness t can be calculated approximately as the following equation according to the assumption of linear distribution:

$$t = t_0 - \frac{t_0\cdot(1-\cos\alpha)\cdot(\beta+\varphi\cdot\cos\theta)}{\alpha+\beta} \tag{6.26}$$

And in equi-biaxial tension condition in the local coordinate system, the equivalent strain of meridional cross-section can be calculated by the following expression as derived in Chapter 4:

$$\bar{\varepsilon} = \frac{\sqrt{2}}{3} \cdot \sqrt{(\varepsilon_r - \varepsilon_\varphi)^2 + (\varepsilon_\varphi - \varepsilon_\theta)^2 + (\varepsilon_\theta - \varepsilon_r)^2} = \ln\frac{t_0\cdot r}{t\cdot\sqrt{r_{tool}\cdot(r_{tool}+t)}} \tag{6.27}$$

Based on Equations (6.25) and (6.27), the distribution of stress triaxiality and equivalent strain at the contact region can be implemented and visualised in MATLAB as shown in Figure 6.41. The displayed implementation results are the case of PEEK I.

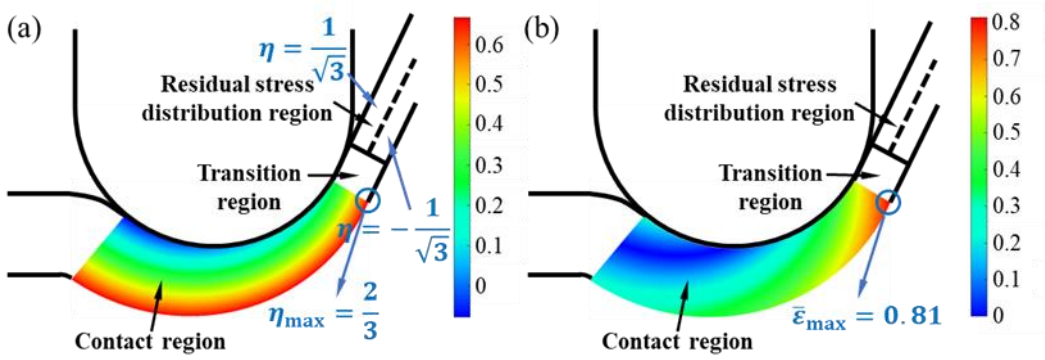


Figure 6.41 Illustration of the predicted results of (a) stress triaxiality distribution and (b) equivalent strain distribution in ISF with drawing angle of 60°, tool radius of 5 mm and sheet thickness of 3 mm.

The maximum stress triaxiality and the maximum equivalent strain take place at the same position, which is the outer surface of transition are between the inclined wall and the corner of formed part.

Outside the contact region, the residual stress distribution region and the transition region are already deformed area and under plane strain state. The residual stress distribution region exists because of the slight elastic recovery. The inner layer has compressive residual σ_φ stress, while the outer layer has tensile residual σ_φ stress. In this region, the three principal stresses have the following relationships in accordance with von-Mises flow rule:

$$\sigma_\theta = \frac{\sigma_\varphi + \sigma_r}{2} \tag{6.28}$$

where the through thickness stress σ_r equals to 0. The equivalent strain can be calculated as following:

$$\bar{\sigma} = \frac{1}{\sqrt{2}} \cdot \sqrt{(\sigma_r - \sigma_\varphi)^2 + (\sigma_\varphi - \sigma_\theta)^2 + (\sigma_\theta - \sigma_r)^2} = \frac{\sqrt{3}}{2} \cdot |\sigma_\varphi| \tag{6.29}$$

Therefore, the stress triaxiality of the inner layer of the residual stress distribution region can be derived as the following equation:

$$\eta = \frac{\sigma_m}{\bar{\sigma}} = \frac{(\sigma_\theta + \sigma_\varphi + \sigma_r)/3}{\bar{\sigma}} = \frac{1}{\sqrt{3}} \tag{6.30}$$

While the stress triaxiality of the outer layer of the residual stress distribution region is calculated as the following:

$$\eta = \frac{\sigma_m}{\bar{\sigma}} = \frac{(\sigma_\theta + \sigma_\varphi + \sigma_r)/3}{\bar{\sigma}} = -\frac{1}{\sqrt{3}} \tag{6.31}$$

As the stress triaxiality of the contact region and the residual stress distribution region are different, the sudden reverse change of stress triaxiality completes in the narrow transition region. The validity of the above deviation can be confirmed by the result of FE simulation of 3 mm PEEK sheet as shown in Figure 6.42.

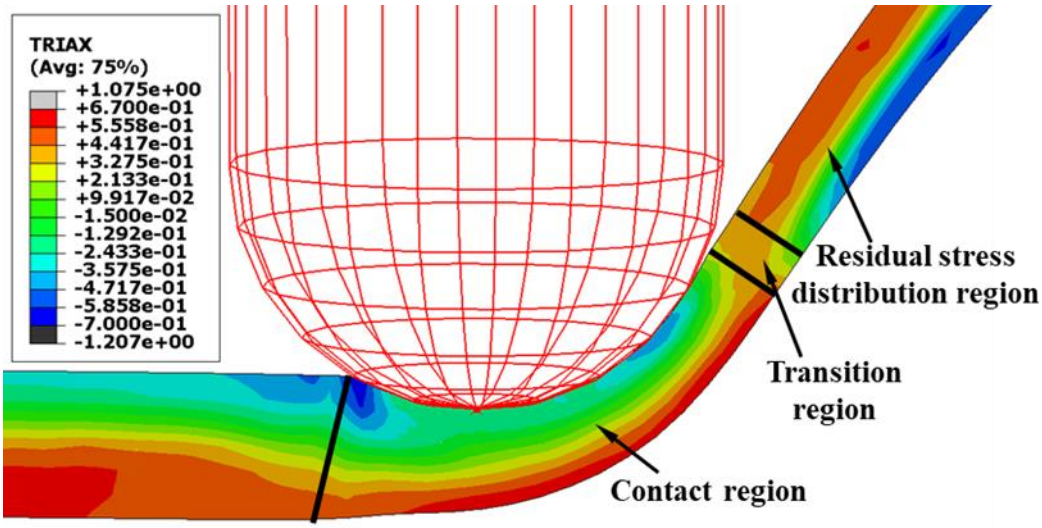


Figure 6.42 Simulation result of the stress triaxiality distribution of different regions under tool-sheet contact.

As the failure strain is mainly dependent on the stress triaxiality and there are two different trend of fracture locus with the increase of stress triaxiality when it is larger than 1/3. The first trend can be described as that there is always a declining trend of the failure strain with the increase of stress triaxiality. For this kind of failure strain – stress triaxiality relationship, the position of maximum stress triaxiality and equivalent strain would be the place with the most failure tendency. However, the second trend is that, instead of continuous reduction, the failure strain in equi-biaxial tension condition ($\eta = 2/3$) becomes larger, so the position of maximum stress triaxiality may not be prone to fail. For this kind of relationship, the narrow transition region between the contact region and the residual stress distribution region is where the sudden change of stress triaxiality happens (as large as from $2/3$ to $1/\sqrt{3}$ and even $-1/\sqrt{3}$), and this region still has the maximum equivalent strain. As a result, the transition region is analysed as the position where the failure is most prone to take place.

6.6.2.2 Experimental observation

Although current heat-assisted ISF parts of PEEK do not show fracture up to the

designed drawing angle of 80°, ISF parts of PMMA sheet have obvious fracture occurrence at the fillet region around the undeformed area, as shown in Figure 6.43.

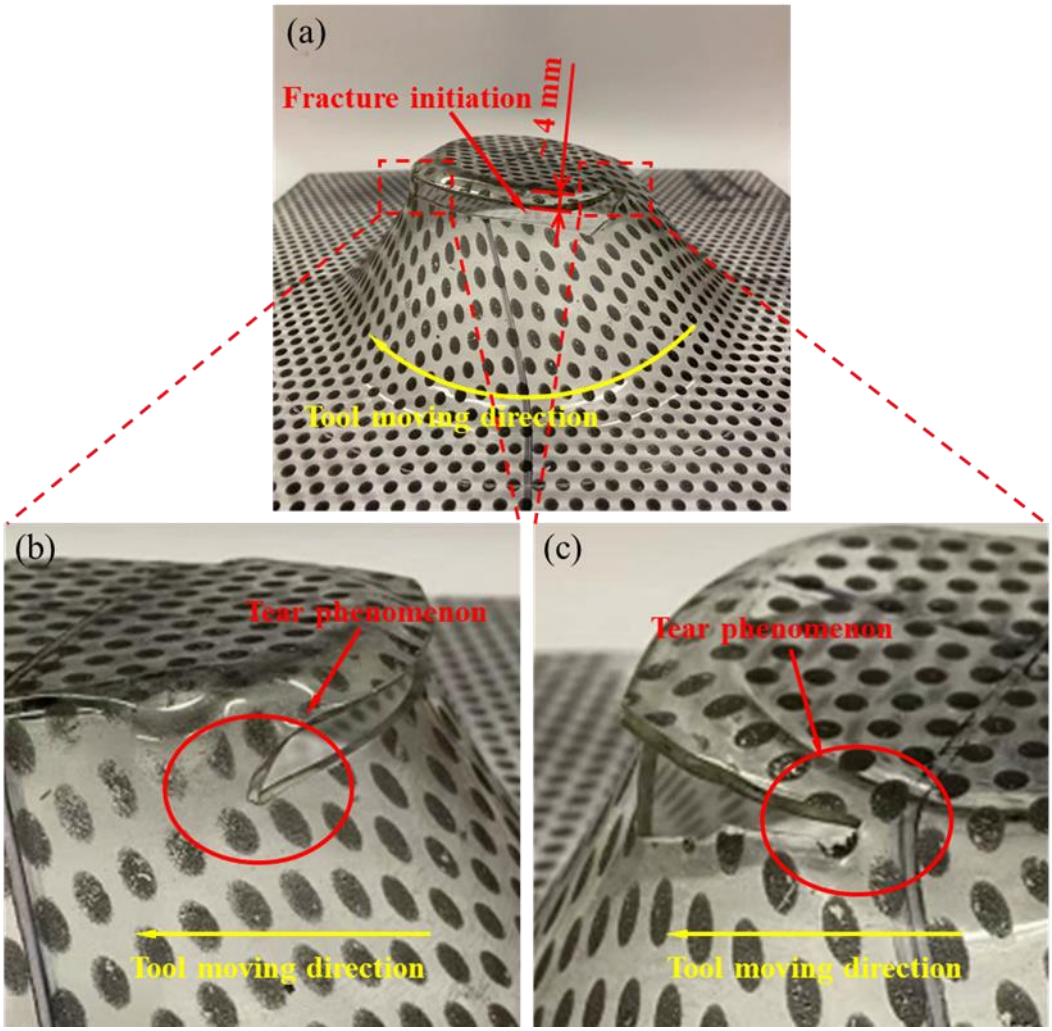


Figure 6.43 Fracture observation of ISF formed PMMA truncated cone part: (a) From the front view, (b) from the left view and (c) from the right view.

As shown in Figure 6.43(b) and (c), there is obvious tear phenomena at both ends of the fracture, which is a clear indication of the crack propagation. This can explain that the fracture was firstly initiated between the two ends and was propagated along and against the tool moving direction separately. The direct material stretch under the tool contact leads to the tear in tool moving direction, while the severe distortion of the sheet after fracture initiation causes the tear behaviour against tool moving direction. As shown in Figure 6.43(a), a distance of about 4 mm can be observed from the fracture position to

the bottom surface of the part. This indicates that the fracture did not happens under the tool contact but occurs at the transition region between the contact region and the residual stress distribution region, as analysed in Section 6.6.2.1.

6.6.3 Twist behaviour

6.6.3.1 Experimental observation

This section aims to discuss the observed twist behaviour of ISF formed truncated cones parts in Sections 6.3.1 and 6.4.1. As shown in Figure 6.44, in heat-assisted ISF of PEEK and PMMA sheets with truncated cone shape, the formed parts show more obvious twist behaviour than ISF of metal sheets because of worse material rigidity. The twist can be seen as a kind of defect affecting the geometric quality of the formed parts, and the evaluation of twist can be useful and fundamental for the geometric quality improvement.

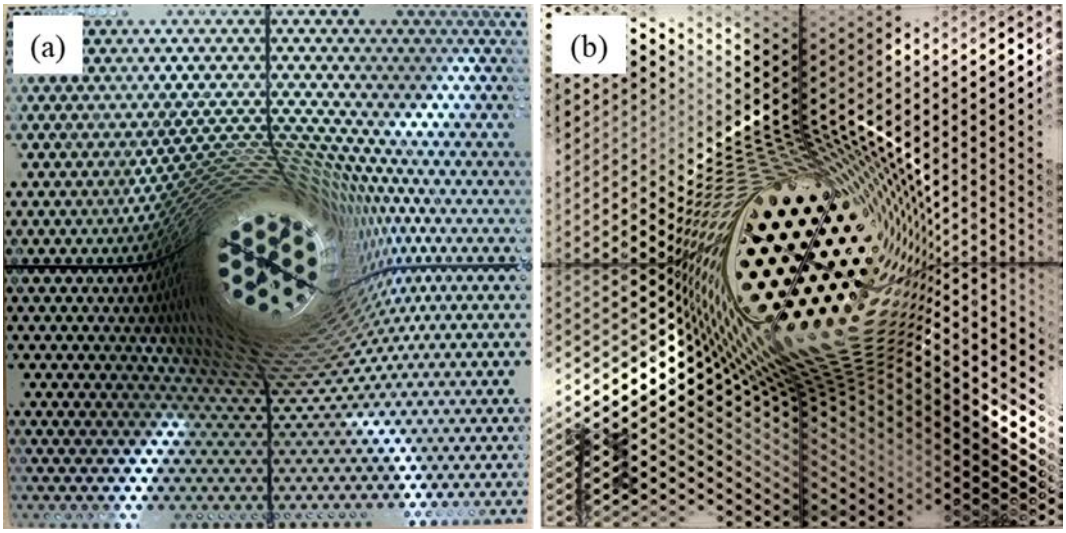


Figure 6.44 Observation of twist behaviour in ISF formed truncated cone parts: (a) PEEK part and (b) PMMA part.

From the formed part of PEEK and PMMA, it can be observed that the twist becomes more obvious from the deformation boundary to the part centre. To quantify the severity of the twist behaviour, two parameters are defined based on the experience in the twist

of shaft or tube. As shown in Figure 6.45(b), ξ is defined as the twist angle, which reflects the final angle on the bottom surface. While γ is defined as the shear angle, i.e., the shear strain, which reflects the evolution history of the torsion on the deformed area. The continuous increase of torsion along the tool path can be presented by the shear angle/ strain. It is noteworthy that γ is an angle on the curved surface obtained by conversion from the measured value in the top view with the following equation:

$$\gamma = \frac{\mathrm{d}\left[\arctan\left(\frac{d_\gamma}{R}\right)\cdot\sqrt{{d_\gamma}^2+R^2}\right]}{\mathrm{d}(R_0-R)} \tag{6.32}$$

where d_γ is the measured normal deviation from the horizontal datum line, R_0 and R are the distances from the original and current positions to the part central line, respectively.

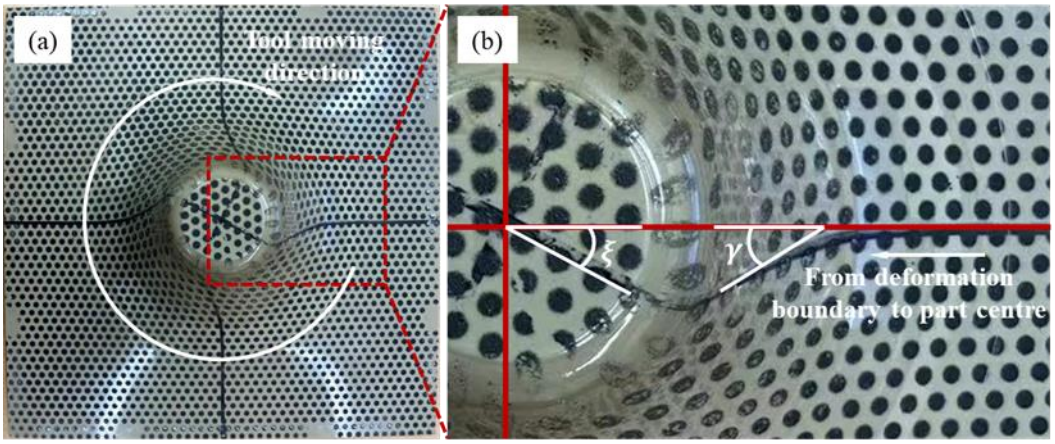


Figure 6.45 Definition of the twist angle and the shear stain/ angle of ISF formed truncated cone part: (a) Overview of the twisted PEEK part and (b) detailed definition.

6.6.3.2 Theoretical analysis

In ISF process, the local shear deformation accumulates the global twist/ torsion. Different from local coordinate system, a global coordinate system is proposed to evaluate the twist evolution as shown in Figure 6.46. In the coordinate system, θ^* is the angle from the original x axis to the studied position in the horizontal plane, φ^* is the

angle from the central axis of the part to the studied position and r^* is the distance from the central axis of the part to the studied position. For convenience, it is reasonable to assume the local contact area as a small element with size of $l_{\theta^*} \times l_{\varphi^*} \times t$ because it is much smaller compared to the whole part.

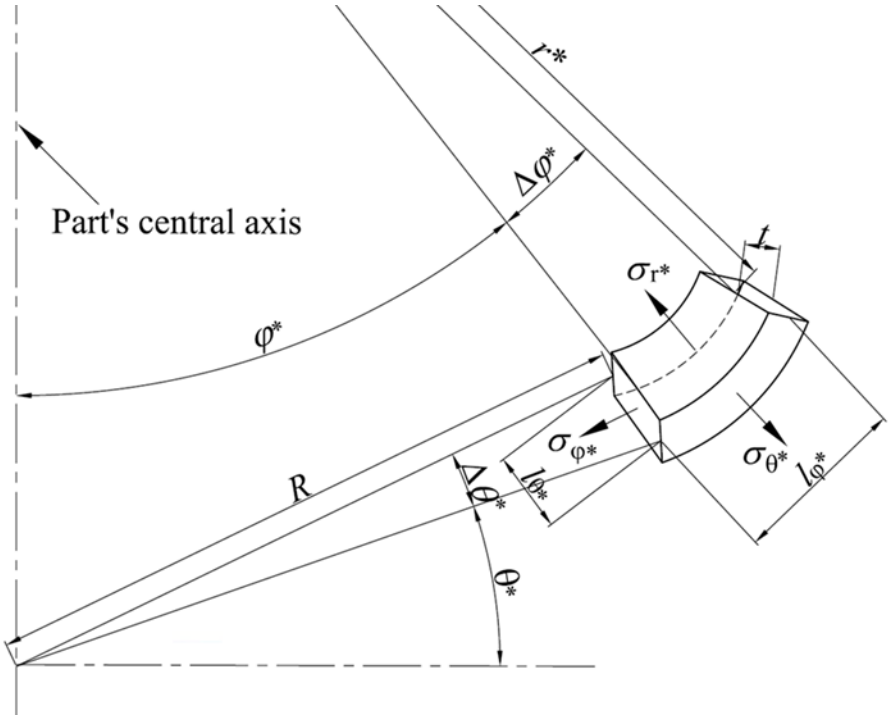


Figure 6.46 Global coordinate system and the principal stresses in ISF.

As the local contact is assumed to be a point contact, the deformation state can be seen as plane strain condition in the global system. The following relationships can be given by the Levy-Mises flow rule in plane strain condition:

$$\sigma_{\varphi^*} = \sigma_{r^*} + \frac{2}{\sqrt{3}} \cdot \bar{\sigma} \tag{6.33}$$

$$\sigma_{\theta^*} = \frac{\sigma_{\varphi^*} + \sigma_{r^*}}{2} \tag{6.34}$$

where, σ_{φ^*}, σ_{θ^*} and σ_{r^*} are the stresses in φ^*, θ^* and r^* directions. Accordingly, the through thickness deviator stress σ'_{r^*} is derived as following:

$$\sigma'_{r^*} = \sigma_{r^*} - \sigma_m = -\frac{1}{\sqrt{3}} \cdot \bar{\sigma} \tag{6.35}$$

In the studied small element, the following relationship between circumferential shear stress τ_{θ^*}, through thickness deviator stress σ'_{r^*}, circumferential instant shear strain change $\Delta\gamma_{\theta^*}$ and through thickness instant strain change $\Delta\varepsilon_{r^*}$ can be given according to the hypothesis of the Levy-Mises flow rule:

$$\frac{\tau_{\theta^*}}{\sigma'_{r^*}} = \frac{\Delta\gamma_{\theta^*}}{\Delta\varepsilon_{r^*}} \tag{6.36}$$

In the equation, the instant change of principal strain $\Delta\varepsilon_{r^*}$ can be calculated as following:

$$\Delta\varepsilon_{r^*} = \frac{t_0 \cdot \cos(\alpha - d\alpha) - t_0 \cdot \cos\alpha}{t_0 \cdot \cos\alpha} = \tan\alpha \cdot \Delta\alpha \tag{6.37}$$

where, $\Delta\alpha$ is the increment of actual drawing angle. The shear stress can be obtained as the following equation:

$$\tau_{\theta^*} = \sigma'_{r^*} \cdot \frac{\Delta\gamma_{\theta^*}}{\Delta\varepsilon_{r^*}} = -\bar{\sigma} \cdot \frac{\Delta\gamma}{\sqrt{3} \cdot \tan\alpha \cdot d\alpha} \tag{6.38}$$

where $\Delta\gamma$ is the increment of shear angle. As shown in Figure 6.47, according to the virtual work principle, the work applied by the torque on the small element equals to the shear strain energy as shown below:

$$\left(F_t^{ls} + F_t^{f}\right) \cdot \frac{R}{\sin\alpha} \cdot \Delta\xi \cdot \sin\alpha = \tau_{\theta^*} \cdot \Delta\gamma \cdot t \cdot l_\theta \cdot l_\varphi \tag{6.39}$$

where R is the distance from the tool position to the part centre and $\Delta\xi$ is the increment of twist angle. F_t^{ls} and F_t^{f} are the tangential component of the localised shear force and the tangential friction force, as defined in Chapter 4.

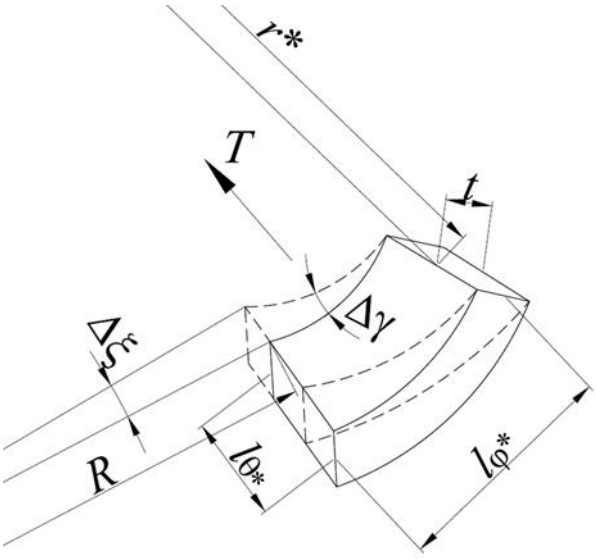


Figure 6.47 Illustration of the change of twist angel and shear strain/ angle in a small element.

According to Equations (6.38) and (6.39) combined with $R \cdot \Delta\xi = l_\varphi \cdot \Delta\gamma$, the change of shear strain $\Delta\gamma$ and twist angle $\Delta\xi$ can be calculated as follows:

$$\Delta\gamma = -\frac{\sqrt{3}\cdot\left(F_{\mathrm{t}}^{\mathrm{ls}}+F_{\mathrm{t}}^{\mathrm{f}}\right)\cdot\tan\alpha\cdot\Delta\alpha}{\bar{\sigma}\cdot t_0\cdot\cos\alpha\cdot l_\theta} \tag{6.40}$$

$$\Delta\xi = -\frac{\sqrt{3}\cdot\left(F_{\mathrm{t}}^{\mathrm{ls}}+F_{\mathrm{t}}^{\mathrm{f}}\right)\cdot\tan\alpha\cdot\Delta R\cdot\Delta\alpha}{\bar{\sigma}\cdot R\cdot t_0\cdot(\cos\alpha)^2\cdot l_\theta} \tag{6.41}$$

As a result, the total shear strain γ_n and the twist angle ξ_n at different tool position (x_n, y_n, z_n) can be calculated by accumulation of the shear strain increment and twist angle increment as the following equations:

$$\gamma_n = -\sum_{i=1}^{n}\frac{\sqrt{3}\cdot\left(F_{\mathrm{t}\,i}^{\mathrm{ls}}+F_{\mathrm{t}i}^{\mathrm{f}}\right)\cdot\tan\alpha_i\cdot(\alpha_i-\alpha_{i-1})}{\bar{\sigma}_i\cdot t_0\cdot\cos\alpha_i\cdot\sqrt{(x_i-x_{i-1})^2+(y_i-y_{i-1})^2+(z_i-z_{i-1})^2}} \tag{6.42}$$

$$\xi_n = -\sum_{i=1}^{n}\frac{\sqrt{3}\cdot\left(F_{\mathrm{t}\,i}^{\mathrm{ls}}+F_{\mathrm{t}i}^{\mathrm{f}}\right)\cdot\tan\alpha_i\cdot\left(\sqrt{{x_{i-1}}^2+{y_{i-1}}^2}-\sqrt{{x_i}^2+{y_i}^2}\right)\cdot(\alpha_i-\alpha_{i-1})}{\bar{\sigma}_i\cdot\sqrt{{x_i}^2+{y_i}^2}\cdot t_0\cdot(\cos\alpha_i)^2\cdot\sqrt{(x_i-x_{i-1})^2+(y_i-y_{i-1})^2+(z_i-z_{i-1})^2}} \tag{6.43}$$

where, $F_{\mathrm{t}\,i}^{\mathrm{ls}}$, $F_{\mathrm{t}\,i}^{\mathrm{f}}$, α_i and $\bar{\sigma}_i$ are the tangential component of localised shear force, tangential friction force, drawing angle, equivalent stress at the tool position (x_i, y_i, z_i), and α_{i-1} is the drawing angle at the tool position $(x_{i-1}, y_{i-1}, z_{i-1})$.

6.6.3.3 Model validation

The defined shear strain/ angle could show the evolution of twist during the forming process, so the validation of the shear strain/ angle would be more worth discussing. Following Equation (6.42), the shear strain/ angle from the outer boundary of the deformation area to the bottom fillet can be predicted as shown in Figure 6.48. It is noteworthy that the unit of the shear angle is radian, so it is omitted in Figure 6.48. The prediction and experimental results included in the comparison comes from the ISF of PEEK I part. In Figure 6.48, the outer boundary of deformation area is located at the first cycle of tool path.

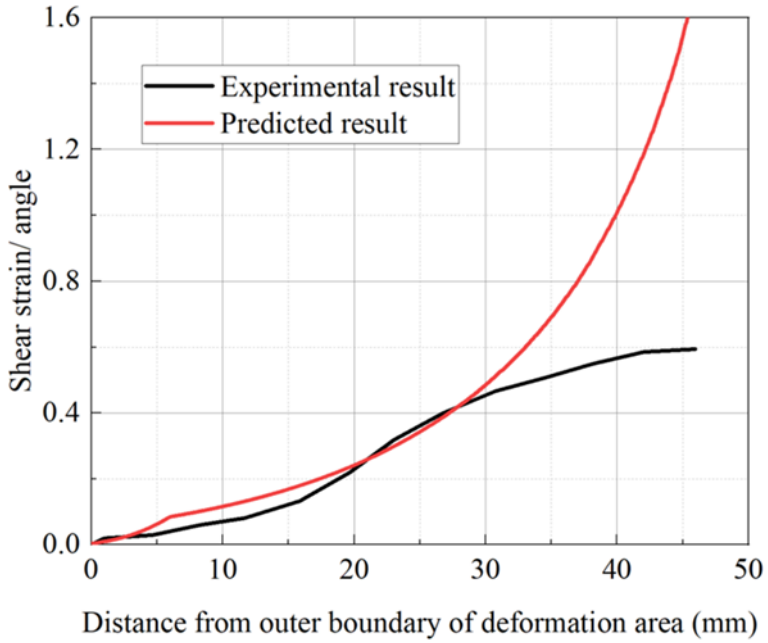


Figure 6.48 Comparison of the shear strain/ angle between analytically predicted result and experimental result.

The black solid curve represents the shear strain/ angle in experiment, while the red curve represents the predicted results with frictional coefficient of 0.25. It can be observed that the analytical model has good agreement with the experimental shear strain/ angle at the outer deformation area but overestimates the twist behaviour at the inner deformation area. This overestimation is a result of the higher predicted values of

horizontal force components by the force prediction model than experimental results. As shown in Figure 4.15, the predicted x and y forces are both higher than the experimental results. This may cause the larger shear strain increment $\Delta\gamma$ as well as the larger twisting angle increment $\Delta\xi$ as indicated by Figures 6.43 and 6.44. The accumulation of $\Delta\gamma$ leads to dramatic increase of the shear strain γ_n (as shown in Equation (6.42)) in the analytical model. The result shows that the developed analytical model may be a useful method to predict the evolution history of the twist and torsion, although there is a scope for improvement of the prediction accuracy of the tangential forming force.

6.7 Conclusions

The conclusions of this chapter are drawn as below:

(1) Heat-assisted ISF setup, force and temperature measurement systems have been developed and tested in conducting ISF of thermoplastics.

(2) With proper preheating temperature, spindle speed and feed rate, high-performance PEEK sheet and hard-to-form PMMA sheet can be processed by ISF. Heat-assisted ISF is considered to be an alternative to manufacture PEEK and PMMA cranial plate.

(3) Among all the studied process parameters, spindle speed has the most significant influence on the highest temperature, forming force and geometric accuracy in heat-assisted ISF of PEEK and PMMA sheet. Localised temperature rise due to friction heat generation and the plastic work explains the effect of spindle speed.

(4) Analytical models are developed to evaluate the insufficient forming accuracy, fracture and twist behaviour, which are main challenging issues in heat-assisted ISF of PEEK and PMMA based on the observation of experimental results. Effects of initial

bending and springback on the forming accuracy, effects of stress triaxiality and equivalent strain distribution on the fracture behaviour and twist accumulation along tool path are discussed and considered in the analytical models and validated by the testing results. Therefore, the developed models help to effectively explain and understand the generation mechanism of forming inaccuracy, fracture and twist in heat-assisted ISF of thermoplastics.

Chapter 7 Conclusions and Future Work

7.1 Introduction

The key conclusions on the constitutive modelling, analytical modelling of force and contact pressure based on the deformation mechanism and localised contact behaviour in ISF of metals and thermoplastics are summarised in this chapter. The exploration and discussions of heat-assisted ISF of PEEK and PMMA and the application in cranial plate manufacture are concluded as well. This leads to recommendations for future work following the current research.

7.2 Conclusions

In this thesis, a new phenomenological constitutive model for thermoplastics, new analytical models for force and contact pressure prediction are developed. The feasibility of heat-assisted ISF of PEEK and PMMA is explored, and some challenging issues, including forming inaccuracy, fracture and twist, are analysed. Validated by experimental tests, the analytical models are derived step by step and used for the discussion and understanding of the mechanism of the challenging issues observed from the experimental results of heat-assisted ISF processing of PEEK and PMMA. The main conclusions are summarised as follows:

(1) A new constitutive model with the use of novel piecewise and transition functions are developed to capture the complicated linear elasticity, yield, strain softening and hardening in deformation behaviour of thermoplastics.

(2) The developed constitutive model is used for compressive and tensile behaviours of PEEK and PC materials with better representation as compared with several commonly used models. This model and its modifications may also be used for hot deformation

behaviour of metallic materials.

(3) A new analytical model is developed with comprehensive consideration of local deformation state, tool-sheet interaction, thickness distribution under contact, local elastic recovery and global elastic bending/ deflection.

(4) The developed force prediction model is validated for the force prediction of different ISF conditions with different shapes (truncated cone, pyramid, and irregular cranial shape) and materials (TA1, AA3003 and PEEK). The change of deformation state and contact conditions in ISF with different geometric features can be reflected by the forming force and is predicted by the developed analytical model.

(5) An analytical model of contact pressure distribution in ISF is developed by revealing the contact mechanics of elastic plastic materials. A novel point-based method is used to implement the developed analytical model for visualisation.

(6) The shape and size of contact region, maximum contact pressure and pressure distribution are analytically predicted and have good agreement with FE simulation results of ISF of TA1 and PEEK sheets.

(7) Experimental investigation of heat-assisted ISF of PEEK and PMMA sheets are carried out with the setup of ISF fixtures under heating and the development of temperature and force measurement systems. Preheating temperature and spindle speed are two of the most important parameters in heat-assisted ISF.

(8) The main challenging issues in heat-assisted ISF of PEEK and PMMA are the forming accuracy, the fracture, and the twisting phenomenon, which may limit the application of ISF on thermoplastics. Theoretical analyses are given to discuss the observed defects.

7.3 Future work

The thesis investigates the deformation mechanism and contact behaviour in ISF process by developing a constitutive model, analytical models for force and contact pressure prediction. Experimental results are used to validate the developed models. Tests are carried out to demonstrate the feasibility of heat-assisted ISF of PEEK and PMMA, and discussions on the theoretical analysis of challenging issues are given. However, there are still some limitations of the current study and the recommendations for the future work are summarised as follows:

(1) As a phenomenological model, the new constitutive model can be used to describe the trend of flow stress, but it has limitations to reflect the material responses to largely different loading conditions, such as under low, intermediate, and high strain rate. A possible solution may be to add a functional term to describe the relationship and fill the gap between the low strain rate and the high strain rate behaviours. This would be a possible direction for the improvement of the new constitutive model.

(2) The current analytical model for force prediction is on the basis that the forming temperature keeps unchanged during the ISF process. This is acceptable for ISF without tool rotation. However, in ISF with tool rotation, frictional heat generation leads to the local temperature rise, and the prediction accuracy of the analytical model may become worse. Therefore, the analytical model for local temperature rise may be useful to improve the established analytical framework.

(3) The interaction between tool radius and sheet thickness plays an important role on the deformation behaviour and prediction effect of the analytical model. This may come from the slight change of indentation effect. For the next step, the reflection of the tool-sheet dimensional relationship may be considered to make the analytical model more

robust.

(4) The lubrication condition between forming tool and sheet material is essential to the horizontal forming force, but do not have obvious influence on the vertical force. An effective method to identify the friction coefficient in ISF process is of great significant in the force prediction by both analytical model and FE simulation.

(5) The use of a correction factor in the current analytical model is just an approximate method to reflect the effect of tool-sheet dimensional relationship on the contact pressure distribution. Further study is recommended to find a more accurate function to describe the effect, and FE simulation of thin sheet indentation may be a useful tool to carry out the investigation.

(6) Currently, the pressure distribution equation referring to the spherical indention into a half space with flat surface is used. This fails to reflect the existing curvature of the preformed sheet surface due to the feature of cyclic contact in ISF. It is recommended that a function considering the preformed curvature to be developed and used in the analytical model.

(7) The global bending, elastic springback and thermal distortion are the main reasons for the forming inaccuracy. Further analysis is recommended to quantify the thermal distortion in heat-assisted ISF of thermoplastics using both analytical method and FE simulation.

(8) The improvement of forming accuracy is essential to expand the practical application of ISF. Efforts such as adjustment of process parameters and development of novel ISF variants, are recommended to enable this improvement.

(9) The fracture still happens in ISF of PMMA even at high temperature, which limit the application of ISF manufacture of PMMA. While DSIF is a variant of ISF, which

could help to increase both forming accuracy and formability, because of the compressive effect between the forming tool and the support tool. The use of DSIF in PEEK and PMMA sheets is recommended for the future work.

(10) The temperature change in ISF with tool rotation is presented in this PhD work. The micromechanical damage model with consideration of temperature is recommended for more accurate prediction of failure initiation in ISF.

(11) The twist behaviour exists in both ISF of PEEK and PMMA because of the poor material rigidity at high temperature. Prevention of twist may be done from three different aspects: (A) To increase the stiffness of the sheets, such as with use of another layer of sheet or a damping system under the sheet; (B) To correct the twist, such as using bidirectional toolpath and multi pass toolpath; (C) To reduce the tangential force. Further research will be carried out to find a reasonable method to eliminate the twist.

(12) Excessive thinning of ISF formed parts is one of the reasons of fracture in ISF. Novel tooling strategy and hybrid process may be useful to reduce the trend of uneven thickness distribution.

(13) Poor surface quality is one of the weaknesses of ISF formed parts. Exploration of methods to improve the surface finish are of great value to the development and application of ISF.

References

[1] W. Emmens, G. Sebastiani, A.H. van den Boogaard, The technology of incremental sheet forming—a brief review of the history, Journal of Materials Processing Technology 210(8) (2010) 981-997.

[2] W.C. Emmens, A.H. van den Boogaard, An overview of stabilizing deformation mechanisms in incremental sheet forming, Journal of Materials Processing Technology 209(8) (2009) 3688-3695.

[3] D.R. Cooper, K.E. Rossie, T.G. Gutowski, The energy requirements and environmental impacts of sheet metal forming: An analysis of five forming processes, Journal of Materials Processing Technology 244 (2017) 116-135.

[4] P. Gupta, A. Szekeres, J. Jeswiet, Design and development of an aerospace component with single-point incremental forming, The International Journal of Advanced Manufacturing Technology 103(9) (2019) 3683-3702.

[5] D. Young, J. Jeswiet, Wall thickness variations in single-point incremental forming, Proceedings of the Institution of Mechanical Engineers, Part B: Journal of Engineering Manufacture 218(11) (2004) 1453-1459.

[6] Z. Cheng, Y. Li, C. Xu, Y. Liu, S. Ghafoor, F. Li, Incremental sheet forming towards biomedical implants: A review, Journal of Materials Research and Technology 9(4) (2020) 7225-7251.

[7] V.S. Le, A. Ghiotti, G. Lucchetta, Preliminary Studies on Single Point Incremental Forming for Thermoplastic Materials, International Journal of Material Forming 1 (2008) 1179-1182.

[8] V. Franzen, L. Kwiatkowski, P.A.F. Martins, A.E. Tekkaya, Single point

incremental forming of PVC, Journal of Materials Processing Technology 209(1) (2009) 462-469.

[9] D. Rajenthirakumar, R. Sridhar, Single point incremental sheet forming of polymer on Computer Numerically Controlled (CNC) milling machine tool, Key Engineering Materials, Trans Tech Publ, 2014, pp. 420-426.

[10] P.A.F. Martins, L. Kwiatkowski, V. Franzen, A.E. Tekkaya, M. Kleiner, Single point incremental forming of polymers, CIRP Annals - Manufacturing Technology 58(1) (2009) 229-232.

[11] V. Franzen, L. Kwiatkowski, J. Neves, P. Martins, A. Tekkaya, On the capability of single point incremental forming for manufacturing polymer sheet parts, ICTP2008, 9th International Conference on Theory of Plasticity, 2008.

[12] K. Thangavel, R. Duraiswamy, S. Nagarajan, S. Ramasamy, Influence of Roller Ball Tool in Single Point Incremental Forming of Polymers, Tehnički vjesnik 26(1) (2019) 171-176.

[13] R. Sridhar, D. Rajenthirakumar, Incremental Forming of Polymer-Numerical and Experimental Investigation, Polymers and Polymer Composites 24(7) (2016) 489-498.

[14] S.A. Yonan, M.B. Silva, P.A.F. Martins, A.E. Tekkaya, Plastic flow and failure in single point incremental forming of PVC sheets, Express Polymer Letters 8(5) (2014) 301-311.

[15] I. Bagudanch, M.L. Garcia-Romeu, G. Centeno, A. Elias-Zuniga, J. Ciurana, Forming force and temperature effects on single point incremental forming of polyvinylchloride, Journal of Materials Processing Technology 219 (2015) 221-229.

[16] G. Medina-Sánchez, E. Torres-Jimenez, R. Lopez-Garcia, R. Dorado-Vicente, R.

Cazalla-Moral, Temperature influence on Single Point Incremental Forming of PVC parts, Procedia Manufacturing 13 (2017) 335-342.

[17] M.P. Pradella, L.F. Folle, Study of incremental sheet forming process of PVC, Materia 21(4) (2016) 1094-1104.

[18] M.B. Silva, L.M. Alves, P.A.F. Martins, Single point incremental forming of PVC: Experimental findings and theoretical interpretation, European Journal of Mechanics A-Solids 29(4) (2010) 557-566.

[19] S.A. Yonan, C. Soyarslan, P. Haupt, L. Kwiatkowski, A.E. Tekkaya, A simple finite strain non-linear visco-plastic model for thermoplastics and its application to the simulation of incremental cold forming of polyvinylchloride (PVC), International Journal of Mechanical Sciences 66 (2013) 192-201.

[20] G. Centeno, D. Morales-Palma, B. Gonzalez-Perez-Somarriba, I. Bagudanch, J.J. Egea-Guerrero, L.M. Gonzalez-Perez, M.L. Garcia-Romeu, C. Vallellano, A functional methodology on the manufacturing of customized polymeric cranial prostheses from CAT using SPIF, Rapid Prototyping Journal 23(4) (2017) 771-780.

[21] I. Bagudanch, L.M. Lozano-Sánchez, L. Puigpinós, M. Sabater, L.E. Elizalde, A. Elías-Zúñiga, M.L. Garcia-Romeu, Manufacturing of Polymeric Biocompatible Cranial Geometry by Single Point Incremental Forming, Procedia Engineering 132 (2015) 267-273.

[22] G. Centeno, I. Bagudanch, D. Morales-Palma, M.L. García-Romeu, B. Gonzalez-Perez-Somarriba, A.J. Martinez-Donaire, L.M. Gonzalez-Perez, C. Vallellano, Recent Approaches for the Manufacturing of Polymeric Cranial Prostheses by Incremental Sheet Forming, Procedia Engineering 183 (2017) 180-187.

[23] I. Bagudanch, M.L. Garcia-Romeu, I. Ferrer, J. Ciurana, Customized cranial implant manufactured by incremental sheet forming using a biocompatible polymer, Rapid Prototyping Journal 24(1) (2018) 120-129.

[24] I. Bagudanch, G. Centeno, C. Vallellano, M.L. Garcia-Romeu, Towards the Manufacturing of Near Net Shape Medical Prostheses in Polymeric Sheet by Incremental Sheet Forming, Near Net Shape Manufacturing Processes, Springer2019, pp. 1-33.

[25] I. Bagudanch, M.L. García-Romeu, I. Ferrer, J. Ciurana, Customized cranial implant manufactured by incremental sheet forming using a biocompatible polymer, Rapid Prototyping Journal 24(1) (2018) 120-129.

[26] I. Bagudanch, L.M. Lozano-Sanchez, L. Puigpinos, M. Sabater, L.E. Elizalde, A. Elias-Zuniga, M.L. Garcia-Romeu, Manufacturing of polymeric biocompatible cranial geometry by single point incremental forming, in: J.M. Canela, I.B. Corral (Eds.), Mesic Manufacturing Engineering Society International Conference 2015, Elsevier Science Bv, Amsterdam, 2015, pp. 267-273.

[27] I.M. Ward, J. Sweeney, Mechanical properties of solid polymers, John Wiley & Sons2012.

[28] M.B. Silva, M. Skjoedt, P.A.F. Martins, N. Bay, Revisiting the fundamentals of single point incremental forming by means of membrane analysis, International Journal of Machine Tools and Manufacture 48(1) (2008) 73-83.

[29] J.R. Duflou, A.-M. Habraken, J. Cao, R. Malhotra, M. Bambach, D. Adams, H. Vanhove, A. Mohammadi, J. Jeswiet, Single point incremental forming: state-of-the-art and prospects, International Journal of Material Forming 11(6) (2018) 743-773.

[30] M.B. Silva, T.M. Martinho, P.A.F. Martins, Incremental Forming of Hole-Flanges in Polymer Sheets, Materials and Manufacturing Processes 28(3) (2013) 330-335.

[31] G. Ambrogio, F. Gagliardi, R. Conte, P. Russo, Feasibility analysis of hot incremental sheet forming process on thermoplastics, The International Journal of Advanced Manufacturing Technology 102(1-4) (2019) 937-947.

[32] Z. Yang, F. Chen, S. Gatea, H. Ou, Design of the novel hot incremental sheet forming experimental setup, characterization of formability behavior of polyether-ether-ketone (PEEK), The International Journal of Advanced Manufacturing Technology 106(11) (2020) 5365-5381.

[33] R. Conte, G. Ambrogio, D. Pulice, F. Gagliardi, L. Filice, Incremental Sheet Forming of a Composite Made of Thermoplastic Matrix and Glass-Fiber Reinforcement, Procedia Engineering 207 (2017) 819-824.

[34] R. Conte, F. Gagliardi, G. Ambrogio, F. Filice, P. Russo, Performance Analysis of the Incremental Sheet Forming on PMMA using a Combined Chemical and Mechanical Approach, in: D. Brabazon, S. Naher, I.U. Ahad (Eds.), Proceedings of the 20th International Esaform Conference on Material Forming, Amer Inst Physics, Melville, 2017.

[35] M. Okada, T. Kato, M. Otsu, H. Tanaka, T. Miura, Development of optical-heating-assisted incremental forming method for carbon fiber reinforced thermoplastic sheet-Forming characteristics in simple spot-forming and two-dimensional sheet-fed forming, Journal of Materials Processing Technology 256 (2018) 145-153.

[36] R. Sridhar, D. Rajenthirakumar, Polymer Sheet Hot Incremental Forming - An Innovative Polymer Forming Approach, Polymers & Polymer Composites 24(7) (2016) 447-453.

[37] T. Marques, M. Silva, P. Martins, On the potential of single point incremental forming of sheet polymer parts, The International Journal of Advanced Manufacturing Technology 60(1-4) (2012) 75-86.

[38] G. Hussain, A. Mahna, A. Iqbal, Response Surface Analysis of Cold Formability of Polymers in Incremental Sheet Forming: Effect of Parameters and Associated Thermal Softening, International Journal of Precision Engineering and Manufacturing 17(5) (2016) 613-621.

[39] I. Bagudanch, M. Vives-Mestres, M. Sabater, M.L. Garcia-Romeu, Polymer incremental sheet forming process: Temperature analysis using response surface methodology, Materials and Manufacturing Processes 32(1) (2017) 44-53.

[40] A. Formisano, M. Durante, A. Langella, F.M.C. Minutolo, Localized heat assisted incremental forming of polycarbonate sheets by tool rotation, AIP Conference Proceedings, AIP Publishing, 2019, p. 110002.

[41] S. Kulkarni, V.S.M. Sreedhara, G. Mocko, Asme, Heat assisted single point incremental forming of polymer sheets, Amer Soc Mechanical Engineers, New York, 2016.

[42] J. Jeswiet, E. Hagan, A. Szekeres, Forming parameters for incremental forming of aluminium alloy sheet metal, Proceedings of the Institution of Mechanical Engineers, Part B: Journal of Engineering Manufacture 216(10) (2002) 1367-1371.

[43] S. Gatea, H.G. Ou, G. McCartney, Review on the influence of process parameters in incremental sheet forming, The International Journal of Advanced Manufacturing Technology 87(1-4) (2016) 479-499.

[44] W.L. Edwards, T.J. Grimm, I. Ragai, J.T. Roth, Optimum Process Parameters for

Springback Reduction of Single Point Incrementally Formed Polycarbonate, Procedia Manufacturing 10 (2017) 329-338.

[45] M.A. Davarpanah, A. Mirkouei, X.Y. Yu, R. Malhotra, S. Pilla, Effects of incremental depth and tool rotation on failure modes and microstructural properties in Single Point Incremental Forming of polymers, Journal of Materials Processing Technology 222 (2015) 287-300.

[46] I. Bagudanch, M.L. Garcia-Romeu, M. Sabater, Incremental forming of polymers: process parameters selection from the perspective of electric energy consumption and cost, Journal of Cleaner Production 112 (2016) 1013-1024.

[47] M. Durante, A. Formisano, L. Boccarusso, A. Astarita, A. Langella, Single point incremental forming of cold-rolled polycarbonate sheets, AIP Conference Proceedings, AIP Publishing, 2019, p. 060007.

[48] M. Durante, A. Formisano, F. Lambiase, Incremental forming of polycarbonate sheets, Journal of Materials Processing Technology 253 (2018) 57-63.

[49] L.M. Lozano-Sánchez, I. Bagudanch, A.O. Sustaita, J. Iturbe-Ek, L.E. Elizalde, M.L. Garcia-Romeu, A. Elías-Zúñiga, Single-Point Incremental Forming of Two Biocompatible Polymers: An Insight into Their Thermal and Structural Properties, Polymers 10(4) (2018) 391.

[50] M. Sabater, M.L. Garcia-Romeu, M. Vives-Mestres, I. Ferrer, I. Bagudanch, Process Parameter Effects on Biocompatible Thermoplastic Sheets Produced by Incremental Forming, Materials 11(8) (2018) 15.

[51] G. Medina-Sanchez, A. Garcia-Collado, D. Carou, R. Dorado-Vicente, Force Prediction for Incremental Forming of Polymer Sheets, Materials 11(9) (2018) 1597.

[52] A. García-Collado, G. Medina-Sanchez, M. Kumar Gupta, R. Dorado-Vicente, Application of the Finite Element Method to the Incremental Forming of Polymer Sheets: The Thermomechanical Coupled Model and Experimental Validations, Polymers 12(8) (2020) 1715.

[53] T. McAnulty, J. Jeswiet, M. Doolan, Formability in single point incremental forming: A comparative analysis of the state of the art, CIRP Journal of Manufacturing Science and Technology 16 (2017) 43-54.

[54] L. Sevsek, T. Pepelnjak, The Review of the Achievements in the Field of Incremental Forming, Research and Science Today 17 (2019) 124.

[55] M.B. Silva, M. Skjoedt, N. Bay, P.A.F. Martins, Revisiting single-point incremental forming and formability/failure diagrams by means of finite elements and experimentation, The Journal of Strain Analysis for Engineering Design 44(4) (2009) 221-234.

[56] M.B. Silva, M. Skjoedt, A.G. Atkins, N. Bay, P.A.F. Martins, Single-point incremental forming and formability-failure diagrams, The Journal of Strain Analysis for Engineering Design 43(1) (2008) 15-35.

[57] I. Bagudanch, A. Elias-Zuniga, M.L. Garcia-Romeu, Evaluating material constitutive equations for the simulation of Incremental Sheet Forming applied to form thermoplastic materials, in: R.A. DeSousa, R. Valente (Eds.), Current State-of-the-Art on Material Forming: Numerical and Experimental Approaches at Different Length-Scales, Pts 1-3, Trans Tech Publications Ltd, Stafa-Zurich, 2013, pp. 1312-1319.

[58] I. Bagudanch, O. Martínez-Romero, A. Elías-Zúñiga, M.L. Garcia-Romeu, Identifying polymeric constitutive equations for incremental sheet forming modelling, Procedia Engineering 81 (2014) 2292-2297.

[59] L.V. Sy, N.T. Nam, A Numerical Simulation of Incremental Forming Process for Polymer Sheets, International Journal of Modelling and Simulation 32(4) (2012) 265-272.

[60] S.A. Yonan, P. Haupt, L. Kwiatkowski, V. Franzen, A. Brosius, A. Tekkaya, A viscoplastic material model based on overstress for the simulation of incremental sheet forming of thermoplastics, AIP Conference Proceedings, AIP, 2011, pp. 803-808.

[61] G.C. Zha, X. Zhou, C.K. Lu, W. Zhao, S. Sun, A.X. Yan, Z.K. Li, Experimental study on the limit test method of polypropylene sheet incremental forming, The International Journal of Advanced Manufacturing Technology 93(5-8) (2017) 2369-2374.

[62] M.A. Davarpanah, S. Bansal, R. Malhotra, Influence of Single Point Incremental Forming on Mechanical Properties and Chain Orientation in Thermoplastic Polymers, Journal of Manufacturing Science and Engineering-Transactions of the ASME 139(2) (2017) 9.

[63] M.A. Davarpanah, S. Bansal, R. Malhotra, Mechanical Properties and Chain Orientation in Single Point Incremental Forming of Semi-Crystalline Polyamide, ASME 2016 11th International Manufacturing Science and Engineering Conference, American Society of Mechanical Engineers Digital Collection, 2016.

[64] M. Durante, A. Formisano, F. Lambiase, Formability of polycarbonate sheets in single-point incremental forming, The International Journal of Advanced Manufacturing Technology (2019) 1-14.

[65] Z. Yang, F. Chen, Mechanism of twist in incremental sheet forming of thermoplastic polymer, Materials & Design (2020) 108997.

[66] M.B. Silva, P.S. Nielsen, N. Bay, P.A.F. Martins, Failure mechanisms in single-point incremental forming of metals, The International Journal of Advanced Manufacturing Technology 56(9-12) (2011) 893-903.

[67] S. Ai, B. Lu, J. Chen, H. Long, H. Ou, Evaluation of deformation stability and fracture mechanism in incremental sheet forming, International Journal of Mechanical Sciences 124 (2017) 174-184.

[68] V.A. Cristino, M.B. Silva, P.K. Wong, L.M. Tam, P.A. Martins, Hole–flanging of metals and polymers produced by single point incremental forming, International Journal of Materials and Product Technology 50(1) (2015) 37-48.

[69] I. Bagudanch, G. Centeno, C. Vallellano, M.L. Garcia-Romeu, Revisiting formability and failure of polymeric sheets deformed by Single Point Incremental Forming, Polymer Degradation and Stability 144 (2017) 366-377.

[70] J. Allwood, D. Shouler, A.E. Tekkaya, The increased forming limits of incremental sheet forming processes, Key Engineering Materials, Trans Tech Publ, 2007, pp. 621-628.

[71] X.B. Zhang, J. Wang, S.Q. Zhang, study on process parameters on single point incremental forming of PVC, Materials Science Forum, Trans Tech Publ, 2017, pp. 74-80.

[72] A. Formisano, L. Boccarusso, L. Carrino, F. Lambiase, F.M.C. Minutolo, Single Point Incremental Forming: Formability of PC Sheets, in: L. Fratini, R. DiLorenzo, G. Buffa, G. Ingarao (Eds.), Proceedings of 21st International Esaform Conference on Material Forming, Amer Inst Physics, Melville, 2018.

[73] G. Centeno, I. Bagudanch, A.J. Martinez-Donaire, M.L. Garcia-Romeu, C.

Vallellano, Critical analysis of necking and fracture limit strains and forming forces in single-point incremental forming, Materials & Design 63 (2014) 20-29.

[74] M.T. Shaw, W.J. MacKnight, Introduction to polymer viscoelasticity, John Wiley & Sons, 2018.

[75] D.K. Xu, W.C. Wu, R. Malhotra, J. Chen, B. Lu, J. Cao, Mechanism investigation for the influence of tool rotation and laser surface texturing (LST) on formability in single point incremental forming, International Journal of Machine Tools and Manufacture 73 (2013) 37-46.

[76] G. Buffa, D. Campanella, L. Fratini, On the improvement of material formability in SPIF operation through tool stirring action, The International Journal of Advanced Manufacturing Technology 66(9-12) (2013) 1343-1351.

[77] F. Maaß, S. Gies, A. Tekkaya, Deformation characteristics of thermoplastics in single point incremental forming, AIP Conference Proceedings, AIP Publishing, 2017, p. 050005.

[78] K.A. Al-Ghamdi, Spring back analysis in incremental forming of polypropylene sheet: An experimental study, Journal of Mechanical Science and Technology 32(10) (2018) 4859-4869.

[79] L.M. Lozano-Sanchez, A.O. Sustaita, M. Soto, S. Biradar, L. Ge, E. Segura-Cardenas, J. Diabb, L.E. Elizalde, E.V. Barrera, A. Elias-Zuniga, Mechanical and structural studies on single point incremental forming of polypropylene-MWCNTs composite sheets, Journal of Materials Processing Technology 242 (2017) 218-227.

[80] K. Branker, A study of energy, carbon dioxide emissions and economics in machining: milling and single point incremental forming, Queen's University, Canada,

2011.

[81] Z.B. Liu, Heat-assisted incremental sheet forming: a state-of-the-art review, The International Journal of Advanced Manufacturing Technology 98(9-12) (2018) 2987-3003.

[82] I.M. Ward, D.W. Hadley, An introduction to the mechanical properties of solid polymers, 1993.

[83] J.S. Bergstrom, Mechanics of solid polymers: theory and computational modeling, William Andrew, 2015.

[84] M. Biron, Thermoplastics and thermoplastic composites, William Andrew2018.

[85] M. Boyce, E. Arruda, An experimental and anaiytical investigation of the large strain compressive and tensile response of glassy polymers, Polymer Engineering & Science 30(20) (1990) 1288-1298.

[86] M.C. Boyce, E.M. Arruda, R. Jayachandran, The large strain compression, tension, and simple shear of polycarbonate, Polymer Engineering & Science 34(9) (1994) 716-725.

[87] K. Cao, Y. Wang, Y. Wang, Experimental investigation and modeling of the tension behavior of polycarbonate with temperature effects from low to high strain rates, International Journal of Solids and Structures 51(13) (2014) 2539-2548.

[88] P. Yu, X. Yao, Q. Han, S. Zang, Y. Gu, A visco-elastoplastic constitutive model for large deformation response of polycarbonate over a wide range of strain rates and temperatures, Polymer 55(25) (2014) 6577-6593.

[89] S. Hamdan, G. Swallowe, The strain-rate and temperature dependence of the mechanical properties of polyetherketone and polyetheretherketone, Journal of

materials science 31(6) (1996) 1415-1423.

[90] P. Rae, E. Brown, E. Orler, The mechanical properties of poly (ether-ether-ketone)(PEEK) with emphasis on the large compressive strain response, Polymer 48(2) (2007) 598-615.

[91] J. Millett, N. Bourne, G. Stevens, Taylor impact of polyether ether ketone, International Journal of Impact Engineering 32(7) (2006) 1086-1094.

[92] G.I. Taylor, The use of flat-ended projectiles for determining dynamic yield stress I. Theoretical considerations, Proceedings of the Royal Society of London. Series A. Mathematical and Physical Sciences 194(1038) (1948) 289-299.

[93] M. Nasraoui, P. Forquin, L. Siad, A. Rusinek, Influence of strain rate, temperature and adiabatic heating on the mechanical behaviour of poly-methyl-methacrylate: experimental and modelling analyses, Materials & Design 37 (2012) 500-509.

[94] G. Gurevich, P. Kobeko, A study of polymers. iii. technique of mechanical tests of vulcanizates of rubber and plastics, Rubber Chemistry and Technology 13(4) (1940) 904-917.

[95] R. Haward, The extension and rupture of cellulose acetate and celluloid, Transactions of the Faraday Society 38 (1942) 394-403.

[96] D.J. Senden, S. Krop, J. van Dommelen, L. Govaert, Rate - and temperature - dependent strain hardening of polycarbonate, Journal of Polymer Science Part B: Polymer Physics 50(24) (2012) 1680-1693.

[97] A. Mulliken, M. Boyce, Mechanics of the rate-dependent elastic–plastic deformation of glassy polymers from low to high strain rates, International Journal of Solids and Structures 43(5) (2006) 1331-1356.

[98] T. Ree, H. Eyring, Theory of non‐newtonian flow. i. solid plastic system, Journal of Applied Physics 26(7) (1955) 793-800.

[99] M.C. Boyce, D.M. Parks, A.S. Argon, Large inelastic deformation of glassy polymers. Part I: rate dependent constitutive model, Mechanics of materials 7(1) (1988) 15-33.

[100] E.M. Arruda, M.C. Boyce, Evolution of plastic anisotropy in amorphous polymers during finite straining, International Journal of Plasticity 9(6) (1993) 697-720.

[101] G.R. Johnson, W.H. Cook, A constitutive model and data for metals subjected to large strains, high strain rates, and high temperatures, Proceedings: 7th International Symposium on Ballistics, 1983, pp. 541-547.

[102] Y. Duan, A. Saigal, R. Greif, M. Zimmerman, A uniform phenomenological constitutive model for glassy and semicrystalline polymers, Polymer Engineering & Science 41(8) (2001) 1322-1328.

[103] F. Chen, H. Ou, S. Gatea, H. Long, Hot tensile fracture characteristics and constitutive modelling of polyether-ether-ketone (PEEK), Polymer Testing 63 (2017) 168-179.

[104] F. Chen, H. Ou, B. Lu, H. Long, A constitutive model of polyether-ether-ketone (PEEK), Journal of the Mechanical Behavior of Biomedical Materials 53 (2016) 427-433.

[105] D. Garcia-Gonzalez, A. Rusinek, T. Jankowiak, A. Arias, Mechanical impact behavior of polyether–ether–ketone (PEEK), Composite Structures 124 (2015) 88-99.

[106] C. G'sell, J. Jonas, Determination of the plastic behaviour of solid polymers at constant true strain rate, Journal of Materials Science 14(3) (1979) 583-591.

[107] J. Brooks, Processing wrought nickel and titanium superalloy, thermo-mechanical processing: theory, modeling and practice, A conference organized in celebration of the 75th anniversary of the Swedish Society for Material Technology, 1996.

[108] H. Wang, H. Zhou, Z. Huang, Y. Zhang, X. Zhao, Constitutive modeling of polycarbonate over a wide range of strain rates and temperatures, Mechanics of Time-Dependent Materials 21(1) (2017) 97-117.

[109] H. Zhu, H. Ou, A. Popov, Incremental sheet forming of thermoplastics: a review, The International Journal of Advanced Manufacturing Technology (2020) 1-23.

[110] B. Lu, Y. Fang, D.K. Xu, J. Chen, S. Ai, H. Long, H. Ou, J. Cao, Investigation of material deformation mechanism in double side incremental sheet forming, International Journal of Machine Tools and Manufacture 93 (2015) 37-48.

[111] K. Al-Ghamdi, G. Hussain, Threshold tool-radius condition maximizing the formability in SPIF considering a variety of materials: experimental and FE investigations, International Journal of Machine Tools and Manufacture 88 (2015) 82-94.

[112] K. Jackson, J. Allwood, The mechanics of incremental sheet forming, Journal of Materials Processing Technology 209(3) (2009) 1158-1174.

[113] B. Lu, Y. Fang, D.K. Xu, J. Chen, H. Ou, N.H. Moser, J. Cao, Mechanism investigation of friction-related effects in single point incremental forming using a developed oblique roller-ball tool, International Journal of Machine Tools and Manufacture 85 (2014) 14-29.

[114] Y.L. Li, W.J.T. Daniel, Z.B. Liu, H.B. Lu, P.A. Meehan, Deformation mechanics and efficient force prediction in single point incremental forming, Journal of Materials

Processing Technology 221 (2015) 100-111.

[115] T. Obikawa, S. Satou, T. Hakutani, Dieless incremental micro-forming of miniature shell objects of aluminum foils, International Journal of Machine Tools and Manufacture 49(12-13) (2009) 906-915.

[116] L. Filice, G. Ambrogio, F. Micari, On-line control of single point incremental forming operations through punch force monitoring, CIRP Annals-Manufacturing Technology 55(1) (2006) 245-248.

[117] J. Duflou, Y. Tunckol, A. Szekeres, P. Vanherck, Experimental study on force measurements for single point incremental forming, Journal of Materials Processing Technology 189(1-3) (2007) 65-72.

[118] G. Ambrogio, L. Filice, F. Micari, A force measuring based strategy for failure prevention in incremental forming, Journal of Materials Processing Technology 177(1-3) (2006) 413-416.

[119] R. Aerens, P. Eyckens, A. Van Bael, J.R. Duflou, Force prediction for single point incremental forming deduced from experimental and FEM observations, The International Journal of Advanced Manufacturing Technology 46(9-12) (2010) 969-982.

[120] J. Allwood, N. Houghton, K. Jackson, The design of an incremental sheet forming machine, Advanced Materials Research, Trans Tech Publ, 2005, pp. 471-478.

[121] Y.L. Li, Z.B. Liu, H.B. Lu, W.J.T. Daniel, S. Liu, P.A. Meehan, Efficient force prediction for incremental sheet forming and experimental validation, The International Journal of Advanced Manufacturing Technology 73(1-4) (2014) 571-587.

[122] A. Bansal, R. Lingam, S.K. Yadav, N.V. Reddy, Prediction of forming forces in single point incremental forming, Journal of Manufacturing Processes 28 (2017) 486-

493.

[123] Z. Chang, M. Li, J. Chen, Analytical modeling and experimental validation of the forming force in several typical incremental sheet forming processes, International Journal of Machine Tools and Manufacture 140 (2019) 62-76.

[124] G. Ambrogio, V. Cozza, L. Filice, F. Micari, An analytical model for improving precision in single point incremental forming, Journal of Materials Processing Technology 191(1-3) (2007) 92-95.

[125] J. Asghar, R. Lingam, E. Shibin, N.V. Reddy, Tool path design for enhancement of accuracy in single-point incremental forming, Proceedings of the Institution of Mechanical Engineers, Part B: Journal of Engineering Manufacture 228(9) (2014) 1027-1035.

[126] M. Durante, A. Formisano, A. Langella, Comparison between analytical and experimental roughness values of components created by incremental forming, Journal of Materials Processing Technology 210(14) (2010) 1934-1941.

[127] Z. Chang, J. Chen, Analytical model and experimental validation of surface roughness for incremental sheet metal forming parts, International Journal of Machine Tools and Manufacture 146 (2019) 103453.

[128] Y. Huang, J. Cao, S. Smith, B. Woody, J. Ziegert, M. Li, Studies of size effect on the formability of a domed part in incremental forming, International Manufacturing Science and Engineering Conference, 2008, pp. 645-654.

[129] Y. Fang, B. Lu, J. Chen, D.K. Xu, H. Ou, Analytical and experimental investigations on deformation mechanism and fracture behavior in single point incremental forming, Journal of Materials Processing Technology 214(8) (2014) 1503-

1515.

[130] Z. Chang, J. Chen, Analytical modeling of fracture strain and experimental validation in incremental sheet forming, Journal of Materials Processing Technology 294 (2021) 117118.

[131] J. Duflou, H. Vanhove, J. Verbert, J. Gu, I. Vasilakos, P. Eyckens, Twist revisited: Twist phenomena in single point incremental forming, CIRP annals 59(1) (2010) 307-310.

[132] H. Vanhove, J. Verbert, J. Gu, I. Vasilakos, J.R. Duflou, An experimental study of twist phenomena in single point incremental forming, International Journal of Material Forming 3 (2010) 975-978.

[133] Z. Chang, J. Chen, Mechanism of the twisting in incremental sheet forming process, Journal of Materials Processing Technology 276 (2020) 116396.

[134] P. Eyckens, A. Van Bael, R. Aerens, J. Duflou, P. Van Houtte, Small-scale Finite Element Modelling of the Plastic Deformation Zone in the Incremental Forming Process, International Journal Of Material Forming 1 (2008) 1159-1162.

[135] L. Xiaoqiang, H. Kai, S. Xu, W. Haibo, L. Dongsheng, L. Yanle, L. Qing, Experimental and numerical investigation on surface quality for two-point incremental sheet forming with interpolator, Chinese Journal of Aeronautics 33(10) (2020) 2794-2806.

[136] J. Joseph, Material Testing and Characterisation of PEEK Material, MSc Dissertation, Department of Mechanical, Materials and Manufacturing Engineering, University of Nottingham, Nottingham, UK, 2017.

[137] J.J. Park, Y.H. Kim, Fundamental studies on the incremental sheet metal forming

technique, Journal of Materials Processing Technology 140 (2003) 447-453.

[138] P.A.F. Martins, N. Bay, M. Skjoedt, M.B. Silva, Theory of single point incremental forming, CIRP Annals-Manufacturing Technology 57(1) (2008) 247-252.

[139] G. Hussain, L. Gao, A novel method to test the thinning limits of sheet metals in negative incremental forming, International Journal of Machine Tools and Manufacture 47(3-4) (2007) 419-435.

[140] J. Hu, Z. Marciniak, J. Duncan, Mechanics of sheet metal forming, Elsevier2002.

[141] B. Lu, H. Ou, S.Q. Shi, H. Long, J. Chen, Titanium based cranial reconstruction using incremental sheet forming, International Journal Of Material Forming 9(3) (2016) 361-370.

[142] E. Hagan, J. Jeswiet, Effect of wall angle on Al 3003 strain hardening for parts formed by computer numerical control incremental forming, Proceedings of the Institution of Mechanical Engineers, Part B: Journal of Engineering Manufacture 217(11) (2003) 1571-1579.

[143] H. Hertz, On the contact of elastic solids, Z. Reine Angew. Mathematik 92 (1881) 156-171.

[144] K.L. Johnson, K.L. Johnson, Contact mechanics, Cambridge University Press, 1987.

[145] P. Follansbee, G. Sinclair, Quasi-static normal indentation of an elasto-plastic half-space by a rigid sphere—I: Analysis, International Journal of Solids and Structures 20(1) (1984) 81-91.

[146] G. Sinclair, P. Follansbee, K. Johnson, Quasi-static normal indentation of an elasto-plastic half-space by a rigid sphere—II. Results, International Journal of Solids

and Structures 21(8) (1985) 865-888.

[147] M. Brake, An analytical elastic plastic contact model with strain hardening and frictional effects for normal and oblique impacts, International Journal of Solids and Structures 62 (2015) 104-123.

[148] H. Ghaednia, X. Wang, S. Saha, Y. Xu, A. Sharma, R.L. Jackson, A review of elastic–plastic contact mechanics, Applied Mechanics Reviews 69(6) (2017).

[149] B. Ghosh, F. Xu, X. Hou, Thermally conductive poly (ether ether ketone)/boron nitride composites with low coefficient of thermal expansion, Journal of Materials Science 56(17) (2021) 10326-10337.

[150] A. Stepashkin, D. Chukov, F. Senatov, A. Salimon, A. Korsunsky, S. Kaloshkin, 3D-printed PEEK-carbon fiber (CF) composites: Structure and thermal properties, Composites Science and Technology 164 (2018) 319-326.

[151] A. Drozdov, J. deClaville Christiansen, Thermo-Mechanical Behavior of Poly (ether ether ketone): Experiments and Modeling, Polymers 13(11) (2021) 1779.

[152] H. Zhu, H. Ou, A. Popov, A new phenomenological constitutive model for thermoplastics, Mechanics of Materials 157 (2021) 103817.

[153] H. Zhu, H. Ou, Constitutive modelling of hot deformation behaviour of metallic materials, Materials Science and Engineering: A 832 (2022) 142473.

[154] P. Wang, H. Yu, R. Ma, Y. Wang, C. Liu, C. Shen, Temperature-dependent orientation of poly (ether ether ketone) under uniaxial tensile and its correlation with mechanical properties, Journal of Thermal Analysis and Calorimetry 141(4) (2020) 1361-1369.

[155] Y. Bai, T. Wierzbicki, A new model of metal plasticity and fracture with pressure

and Lode dependence, International Journal of Plasticity 24(6) (2008) 1071-1096.

[156] Y. Bai, X. Teng, T. Wierzbicki, On the application of stress triaxiality formula for plane strain fracture testing, Journal of Engineering Materials and technology 131(2) (2009).

[157] Y. Bao, T. Wierzbicki, On fracture locus in the equivalent strain and stress triaxiality space, International Journal of Mechanical Sciences 46(1) (2004) 81-98.

[158] F. Chen, S. Gatea, H. Ou, B. Lu, H. Long, Fracture characteristics of PEEK at various stress triaxialities, Journal of the Mechanical Behavior of Biomedical Materials 64 (2016) 173-186.

[159] Y. Lin, X.-M. Chen, A critical review of experimental results and constitutive descriptions for metals and alloys in hot working, Materials & Design 32(4) (2011) 1733-1759.

[160] H.J. McQueen, N. Ryan, Constitutive analysis in hot working, Materials Science and Engineering: A 322(1-2) (2002) 43-63.

[161] A.S. Khan, S. Huang, Experimental and theoretical study of mechanical behavior of 1100 aluminum in the strain rate range 10^{-5}–$10^{4}s^{-1}$, International Journal of Plasticity 8(4) (1992) 397-424.

[162] B. Farrokh, A.S. Khan, Grain size, strain rate, and temperature dependence of flow stress in ultra-fine grained and nanocrystalline Cu and Al: synthesis, experiment, and constitutive modeling, International Journal of Plasticity 25(5) (2009) 715-732.

[163] D. Fields, W. Backofen, Determination of strain hardening characteristics by torsion testing, Proceedings of ASTM, 1957, pp. 1259-1272.

[164] A. Molinari, G. Ravichandran, Constitutive modeling of high-strain-rate

deformation in metals based on the evolution of an effective microstructural length, Mechanics of Materials 37(7) (2005) 737-752.

[165] U. Kocks, Laws for work-hardening and low-temperature creep, Journal of Engineering Materials and Technology 98 (1976) 76-85.

[166] H. Shi, A. McLaren, C. Sellars, R. Shahani, R. Bolingbroke, Constitutive equations for high temperature flow stress of aluminium alloys, Materials Science and Technology 13(3) (1997) 210-216.

[167] Y. Lin, G. Liu, A new mathematical model for predicting flow stress of typical high-strength alloy steel at elevated high temperature, Computational Materials Science 48(1) (2010) 54-58.

[168] F.J. Zerilli, R.W. Armstrong, Dislocation-mechanics-based constitutive relations for material dynamics calculations, Journal of Applied Physics 61(5) (1987) 1816-1825.

[169] D.L. Preston, D.L. Tonks, D.C. Wallace, Model of plastic deformation for extreme loading conditions, Journal of Applied Physics 93(1) (2003) 211-220.

[170] A. Rusinek, J. Klepaczko, Shear testing of a sheet steel at wide range of strain rates and a constitutive relation with strain-rate and temperature dependence of the flow stress, International Journal of Plasticity 17(1) (2001) 87-115.

[171] S. Bodner, Y. Partom, Constitutive equations for elastic-viscoplastic strain-hardening materials, Journal of Applied Mechanics 42 (1975) 385-389.

[172] Y. Lin, W.-Y. Dong, M. Zhou, D.-X. Wen, D.-D. Chen, A unified constitutive model based on dislocation density for an Al-Zn-Mg-Cu alloy at time-variant hot deformation conditions, Materials Science and Engineering: A 718 (2018) 165-172.

[173] K. Linka, M. Hillgärtner, K.P. Abdolazizi, R.C. Aydin, M. Itskov, C.J. Cyron,

Constitutive artificial neural networks: A fast and general approach to predictive data-driven constitutive modeling by deep learning, Journal of Computational Physics 429 (2021) 110010.

[174] G. Ji, F. Li, Q. Li, H. Li, Z. Li, A comparative study on Arrhenius-type constitutive model and artificial neural network model to predict high-temperature deformation behaviour in Aermet100 steel, Materials Science and Engineering: A 528(13-14) (2011) 4774-4782.

[175] Y. Hashash, S. Jung, J. Ghaboussi, Numerical implementation of a neural network based material model in finite element analysis, International Journal for Numerical Methods in Engineering 59(7) (2004) 989-1005.

[176] L. Niu, M. Cao, Z. Liang, B. Han, Q. Zhang, A modified Johnson-Cook model considering strain softening of A356 alloy, Materials Science and Engineering: A 789 (2020) 139612.

[177] H.Y. Li, X.F. Wang, J.Y. Duan, J.J. Liu, A modified Johnson Cook model for elevated temperature flow behavior of T24 steel, Materials Science and Engineering: A 577 (2013) 138-146.

[178] R. Bobbili, B.V. Ramudu, V. Madhu, A physically-based constitutive model for hot deformation of Ti-10-2-3 alloy, Journal of Alloys and Compounds 696 (2017) 295-303.

[179] Y. Lin, M.-S. Chen, J. Zhong, Constitutive modeling for elevated temperature flow behavior of 42CrMo steel, Computational Materials Science 42(3) (2008) 470-477.

[180] P. Geng, G. Qin, J. Zhou, Z. Zou, Hot deformation behavior and constitutive model of GH4169 superalloy for linear friction welding process, Journal of

Manufacturing Processes 32 (2018) 469-481.

[181] E. Voce, The relationship between stress and strain for homogeneous deformation, The Journal of the Institute of Metals 74 (1948) 537-562.

[182] A.S. Khan, R. Liang, Behaviors of three BCC metal over a wide range of strain rates and temperatures: experiments and modeling, International Journal of Plasticity 15(10) (1999) 1089-1109.

[183] A.S. Khan, H. Zhang, L. Takacs, Mechanical response and modeling of fully compacted nanocrystalline iron and copper, International Journal of Plasticity 16(12) (2000) 1459-1476.

[184] C. Zener, J.H. Hollomon, Effect of strain rate upon plastic flow of steel, Journal of Applied Physics 15(1) (1944) 22-32.

[185] C. Sellars, Modelling microstructural development during hot rolling, Materials Science and Technology 6(11) (1990) 1072-1081.

[186] F. Garofalo, Fundamentals of creep and creep-rupture in metals(Creep and creep rupture in metals and alloys, fundamental information for instruction and reference), New York, Macmillan Co., London, Collier-Macmillan, Ltd., 1965. 258 P (1965).

[187] Y. Lin, M.-S. Chen, J. Zhong, Effect of temperature and strain rate on the compressive deformation behavior of 42CrMo steel, Journal of Materials Processing Technology 205(1-3) (2008) 308-315.

[188] X. Peng, H. Guo, Z. Shi, C. Qin, Z. Zhao, Constitutive equations for high temperature flow stress of TC4-DT alloy incorporating strain, strain rate and temperature, Materials & Design 50 (2013) 198-206.

[189] H. McQueen, S. Yue, N. Ryan, E. Fry, Hot working characteristics of steels in

austenitic state, Journal of Materials Processing Technology 53(1-2) (1995) 293-310.

[190] H. Mirzadeh, J. Cabrera, J. Prado, A. Najafizadeh, Hot deformation behavior of a medium carbon microalloyed steel, Materials Science and Engineering: A 528(10-11) (2011) 3876-3882.

[191] F. Chen, Z. Cui, S. Chen, Recrystallization of 30Cr2Ni4MoV ultra-super-critical rotor steel during hot deformation. Part I: Dynamic recrystallization, Materials Science and Engineering: A 528(15) (2011) 5073-5080.

[192] A. Rudnytskyj, P. Simon, M. Jech, C. Gachot, Constitutive modelling of the 6061 aluminium alloy under hot rolling conditions and large strain ranges, Materials & Design 190 (2020) 108568.

[193] O. Bembalge, S. Panigrahi, Hot deformation behavior and processing map development of cryorolled AA6063 alloy under compression and tension, International Journal of Mechanical Sciences 191 (2021) 106100.

[194] S. Ding, S.A. Khan, J. Yanagimoto, Flow behavior and dynamic recrystallization mechanism of A5083 aluminum alloys with different initial microstructures during hot compression, Materials Science and Engineering: A 787 (2020) 139522.

[195] H.J. McQueen, S. Spigarelli, M.E. Kassner, E. Evangelista, Hot deformation and processing of aluminum alloys, CRC Press, 2011.

[196] Y. Lin, Y.-C. Xia, X.-M. Chen, M.-S. Chen, Constitutive descriptions for hot compressed 2124-T851 aluminum alloy over a wide range of temperature and strain rate, Computational Materials Science 50(1) (2010) 227-233.

[197] P. Prakash, D. Toscano, S.K. Shaha, M.A. Wells, H. Jahed, B.W. Williams, Effect of temperature on the hot deformation behavior of AZ80 magnesium alloy, Materials

Science and Engineering: A 794 (2020) 139923.

[198] J. Long, Q. Xia, G. Xiao, Y. Qin, S. Yuan, Flow characterization of magnesium alloy ZK61 during hot deformation with improved constitutive equations and using activation energy maps, International Journal of Mechanical Sciences 191 (2021) 106069.

[199] Y. Cai, C. Sun, Y. Li, S. Hu, N. Zhu, E.I. Barker, L. Qian, Phase field modeling of discontinuous dynamic recrystallization in hot deformation of magnesium alloys, International Journal of Plasticity 133 (2020) 102773.

[200] I. Balasundar, K. Ravi, T. Raghu, On the high temperature deformation behaviour of titanium alloy BT3-1, Materials Science and Engineering: A 684 (2017) 135-145.

[201] V. Balasubrahmanyam, Y. Prasad, Deformation behaviour of beta titanium alloy Ti–10V–4.5 Fe–1.5 Al in hot upset forging, Materials Science and Engineering: A 336(1-2) (2002) 150-158.

[202] C. Li, L. Huang, M. Zhao, S. Guo, J. Li, Hot deformation behavior and mechanism of a new metastable β titanium alloy Ti–6Cr–5Mo–5V–4Al in single phase region, Materials Science and Engineering: A 814 (2021) 141231.

[203] Y.-Q. Jiang, Y. Lin, G.-D. Pang, D.-G. He, N. Kotkunde, Constitutive model and processing maps for a Ti-55511 alloy in β region, Advanced Engineering Materials 22(2) (2020) 1900930.

[204] F. Chen, J. Liu, H. Ou, B. Lu, Z. Cui, H. Long, Flow characteristics and intrinsic workability of IN718 superalloy, Materials Science and Engineering: A 642 (2015) 279-287.

[205] P. Liu, R. Zhang, Y. Yuan, C. Cui, Y. Zhou, X. Sun, Hot deformation behavior

and workability of a Ni–Co based superalloy, Journal of Alloys and Compounds 831 (2020) 154618.

[206] L. Ouyang, R. Luo, Y. Gui, Y. Cao, L. Chen, Y. Cui, H. Bian, K. Aoyagi, K. Yamanaka, A. Chiba, Hot deformation characteristics and dynamic recrystallization mechanisms of a Co–Ni-based superalloy, Materials Science and Engineering: A 788 (2020) 139638.

[207] D.-X. Wen, Y. Lin, H.-B. Li, X.-M. Chen, J. Deng, L.-T. Li, Hot deformation behavior and processing map of a typical Ni-based superalloy, Materials Science and Engineering: A 591 (2014) 183-192.

[208] J. Xiao, D. Li, X. Li, T. Deng, Constitutive modeling and microstructure change of Ti–6Al–4V during the hot tensile deformation, Journal of Alloys and Compounds 541 (2012) 346-352.

[209] E. Puchi-Cabrera, M. Staia, J.-D. Guérin, J. Lesage, M. Dubar, D. Chicot, An experimental analysis and modeling of the work-softening transient due to dynamic recrystallization, International Journal of Plasticity 54 (2014) 113-131.

[210] R. Zeng, L. Huang, J. Li, H. Li, H. Zhu, X. Zhang, Quantification of multiple softening processes occurring during multi-stage thermoforming of high-strength steel, International Journal of Plasticity 120 (2019) 64-87.

[211] A. Iza-Mendia, A. Pinol-Juez, J. Urcola, I. Gutierrez, Microstructural and mechanical behavior of a duplex stainless steel under hot working conditions, Metallurgical and Materials Transactions A 29(12) (1998) 2975-2986.

[212] P. Wray, Onset of recrystallization during the tensile deformation of austenitic iron at intermediate strain rates, Metallurgical Transactions A 6(6) (1975) 1197-1203.

[213] E. Poliak, J. Jonas, A one-parameter approach to determining the critical conditions for the initiation of dynamic recrystallization, Acta Materialia 44(1) (1996) 127-136.

[214] G. Varela-Castro, J.-M. Cabrera, J.-M. Prado, Critical strain for dynamic recrystallisation. The particular case of steels, Metals 10(1) (2020) 135.

[215] C. Sellars, The physical metallurgy of hot working, Hot Working and Forming Processes, Sheffield, UK, 1979, pp. 3-15.

[216] C. Ouchi, T. Okita, Dynamic recrystallization behavior of austenite in Nb-bearing high strength low alloy steels and stainless steel, Transactions of the Iron and Steel Institute of Japan 22(7) (1982) 543-551.

[217] Y. Lin, M.-S. Chen, J. Zhong, Microstructural evolution in 42CrMo steel during compression at elevated temperatures, Materials Letters 62(14) (2008) 2132-2135.

Appendix A Identification of material parameters in the new constitutive model

In the new constitutive model developed in Chapter 3, there are twelve different parameters. To determine them, several steps should be followed. The procedure to derive these parameters is given by taking the tensile behaviour of PEEK as an example. The relevant experimental tests were carried out by Joseph [136] and the details are given in Section 3.3.1.

m:

At large strains, the stress $\sigma(\varepsilon, \dot{\varepsilon}, T)$ is defined as $g(\varepsilon, \dot{\varepsilon}, T)$ in Equation (3.4). At the same large strain ε, the value of flow stress σ is related to the strain rate $\dot{\varepsilon}$ and the temperature T. At constant temperature and large strain, some selected points are supposed to be (ε, σ_1), (ε, σ_2), (ε, σ_3) and $(\varepsilon, \sigma_\mathrm{i})$ at different strain rates $\dot{\varepsilon}_1$, $\dot{\varepsilon}_2$, $\dot{\varepsilon}_3$ and $\dot{\varepsilon}_\mathrm{i}$, respectively. At a reference strain rate, the reference stress can be obtained as follows:

$$\sigma_{\mathrm{ref}}(\varepsilon, \dot{\varepsilon}_{\mathrm{ref}}, T) = K_2 \cdot (e^{-C_1 \cdot \varepsilon} + \varepsilon^{C_2}) \cdot (1 - e^{-\alpha \cdot \varepsilon}) \cdot e^{a \cdot \left(\frac{1}{T} - \frac{1}{T_{\mathrm{ref}}}\right)} \tag{A.1}$$

Therefore, according to Equations (3.4) and (A.1), $\sigma(\varepsilon, \dot{\varepsilon}, T)$ can be expressed as:

$$\sigma(\varepsilon, \dot{\varepsilon}, T) = \sigma_{\mathrm{ref}} \cdot (\varepsilon, \dot{\varepsilon}_{\mathrm{ref}}, T) \cdot \left(\frac{\dot{\varepsilon}}{\dot{\varepsilon}_{\mathrm{ref}}}\right)^m \tag{A.2}$$

where, $\dot{\varepsilon}_{\mathrm{ref}}$ and $\sigma_{\mathrm{ref}}(\varepsilon, \dot{\varepsilon}_{\mathrm{ref}}, T)$ are selected and already known. m can be obtained by fitting the relationship between the flow stress and strain rate with Equation (A.2) as shown in Figure A.1(a). In the case of tensile behaviour of PEEK, a strain rate of 4.96×10^{-4} s^{-1} was chosen as the reference strain rate. The fitting is carried out in Curve Fitting Toolbox of MATLAB and the parameter m was calculated to be 0.0268 as shown in Table 3.1.

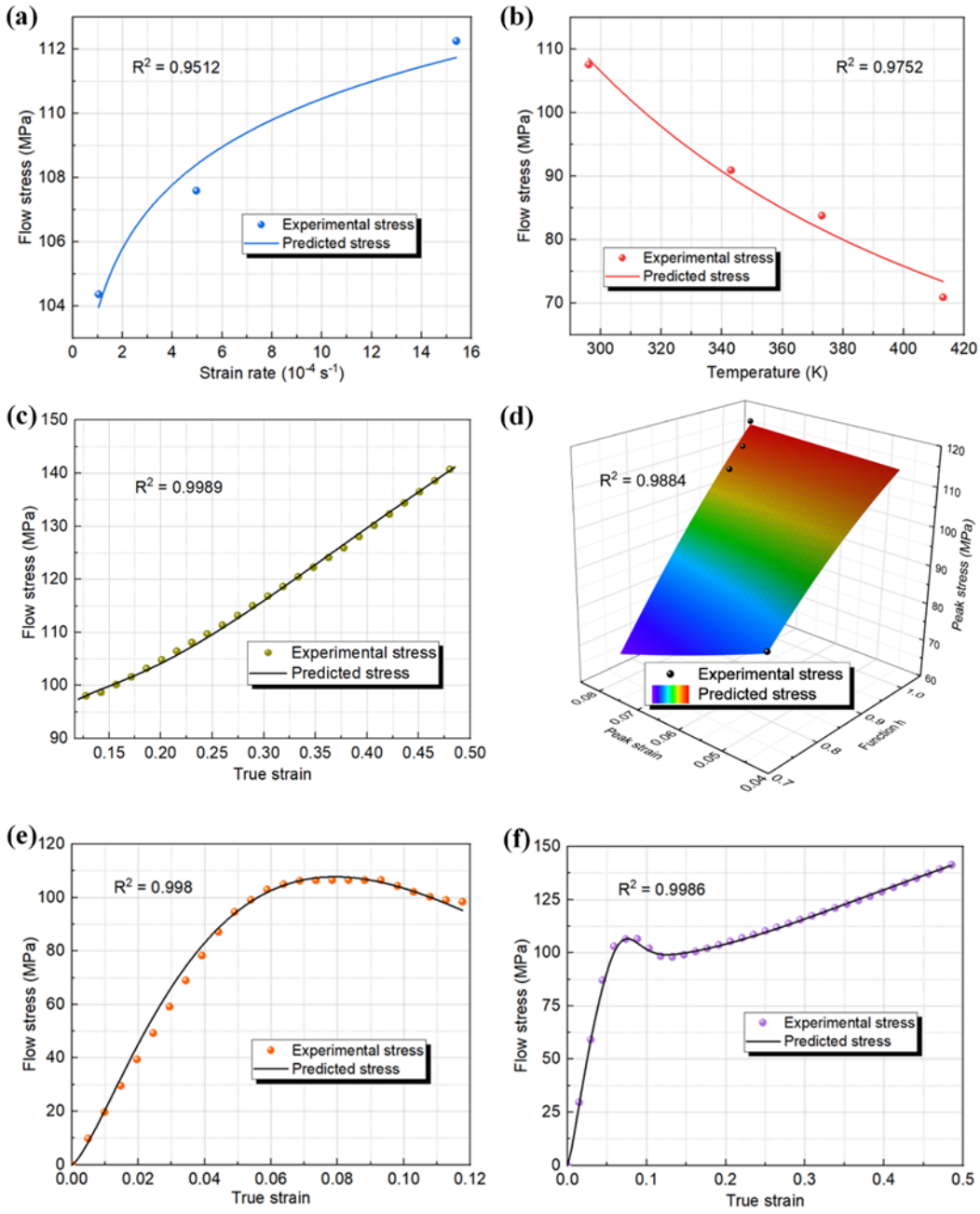


Figure A.1 Fitting and deviation process of (a) m, (b) a, (c) C_1, C_2, α and K_2, (d) μ, (e) n and (f) k, w, λ and K_1.

a:

At the same large strain ε, the value of flow stress σ is also related to the temperature T and the strain rate $\dot{\varepsilon}$. At constant strain rate, some selected points are supposed to be (ε, σ_1), (ε, σ_2), (ε, σ_3) and (ε, σ_i) at different temperatures, T_1, T_2, T_3 and T_i, respectively. At a reference temperature, the reference stress can be obtained as follows:

$$\sigma_{\mathrm{ref}}(\varepsilon, \dot{\varepsilon}, T_{\mathrm{ref}}) = K_2 \cdot (e^{-C_1 \cdot \varepsilon} + \varepsilon^{C_2}) \cdot (1 - e^{-\alpha \cdot \varepsilon}) \cdot \left(\frac{\dot{\varepsilon}}{\dot{\varepsilon}_{\mathrm{ref}}}\right)^m \quad \text{(A.3)}$$

Therefore, $\sigma(\varepsilon, \dot{\varepsilon}, T)$ can also be expressed as following based on Equations (3.4) and (A.3):

$$\sigma(\varepsilon, \dot{\varepsilon}, T) = \sigma_{\mathrm{ref}} \cdot (\varepsilon, \dot{\varepsilon}, T_{\mathrm{ref}}) \cdot e^{a \cdot \left(\frac{1}{T} - \frac{1}{T_{\mathrm{ref}}}\right)} \quad \text{(A.4)}$$

where, T_{ref} and $\sigma_{\mathrm{ref}}(\varepsilon, \dot{\varepsilon}, T_{\mathrm{ref}})$ are both selected and already known. In this case, a temperature of 296 K was selected as the reference temperature. The parameter a can be derived by fitting the relationship between the flow stress and temperature with Equation (A.4) as shown in Figure A.1(b) and a value of 408.4 was obtained for the tensile behaviour of PEEK as given in Table 3.1.

C_1, C_2, α and K_2:

C_1, C_2, α and K_2 can be obtained by fitting the intercepted curve with large strain range (larger than $\varepsilon_{\mathrm{critical}}$) from any stress-strain curve with Equation (3.4). The fitting result in the case of tensile behaviour of PEEK at a temperature of 296 K and a strain rate of 1.04×10^{-4} s^{-1} is presented in Figure A.1(c). As shown in Table 3.1, the calculated values are 11.77, 0.4707, 13.6 and 206.2, respectively.

μ:

As derived in Section 3.2.1.2, when $\varepsilon = \varepsilon_{\mathrm{peak}} = n \cdot \mu \cdot h(\dot{\varepsilon}, T)$, the peak stress can be determined as follows:

$$\sigma_{\mathrm{peak}} = K_1 \cdot \left[\frac{n \cdot \mu \cdot h(\dot{\varepsilon}, T)}{e}\right]^n = K_1 \cdot \left(\frac{\varepsilon_{\mathrm{peak}}}{e}\right)^n \quad \text{(A.5)}$$

At reference temperature and reference strain rate, the reference peak stress $\sigma_{\mathrm{peak}}^{\mathrm{ref}}$ can be obtained as follows:

$$\sigma_{\text{peak}}^{\text{ref}} = K_1 \cdot \left(\frac{\varepsilon_{\text{peak}}^{\text{ref}}}{e}\right)^n \tag{A.6}$$

Therefore, according to Equations (A.5) and (A.6), $\sigma(\varepsilon, \dot{\varepsilon}, T)$ can also be expressed as follows:

$$\sigma_{\text{peak}} = \sigma_{\text{peak}}^{\text{ref}} \cdot \left(\frac{\varepsilon_{\text{peak}}}{\varepsilon_{\text{peak}}^{\text{ref}}}\right)^n = \sigma_{\text{peak}}^{\text{ref}} \cdot \left(\frac{\varepsilon_{\text{peak}}}{\varepsilon_{\text{peak}}^{\text{ref}}}\right)^{\frac{\varepsilon_{\text{peak}}}{\mu \cdot h(\dot{\varepsilon}, T)}} \tag{A.7}$$

The peak stress points of each stress-strain curve are supposed to be $(\varepsilon_{\text{peak}}^1, \sigma_{\text{peak}}^1)$, $(\varepsilon_{\text{peak}}^2, \sigma_{\text{peak}}^2)$, $(\varepsilon_{\text{peak}}^3, \sigma_{\text{peak}}^3)$ and $(\varepsilon_{\text{peak}}^{\text{i}}, \sigma_{\text{peak}}^{\text{i}})$. The values of $h(\dot{\varepsilon}, T)$ for each case are supposed to be $h_1(\dot{\varepsilon}, T)$, $h_2(\dot{\varepsilon}, T)$, $h_3(\dot{\varepsilon}, T)$ and $h_{\text{i}}(\dot{\varepsilon}, T)$. As shown in Figure A.1(d), μ can be obtained by fitting the relationship between σ_{peak} and $\varepsilon_{\text{peak}}$ and $h(\dot{\varepsilon}, T)$ with Equation (A.7). In the example, the fitting result of μ was obtained to be 0.05976 as presented in Table 3.1.

n:

At small strains, the stress is defined as $f(\varepsilon, \dot{\varepsilon}, T)$ in Equation (3.2). As discussed earlier, the peak stress can be calculated as Equation (A.5). Therefore, K_1 can be expressed as:

$$K_1 = \sigma_{\text{peak}} \cdot \left(\frac{e}{\varepsilon_{\text{peak}}}\right)^n \tag{A.8}$$

Equation (3.2) can be rewritten as follows:

$$\sigma(\varepsilon, \dot{\varepsilon}, T) = \sigma_{\text{peak}} \cdot \left(\frac{e}{\varepsilon_{\text{peak}}}\right)^n \cdot \varepsilon^n \cdot e^{-\frac{\varepsilon}{\mu \cdot h(\dot{\varepsilon}, T)}} \tag{A.9}$$

n can be obtained by fitting the intercepted curve with small strain range (at least smaller than $\varepsilon_{\text{critical}}$ and larger than $\varepsilon_{\text{peak}}$) from any stress-strain curve with Equation (A.9). The fitting result is shown in Figure A.1(e) and the value of n was identified to be 1.382.

k, w, λ and K_1:

As three parameters related to the connection and transition between the defined expressions at small strains and large strains, k, w and λ can be derived by fitting any whole stress-strain curve with Equations (3.8), (3.1), (3.2), (3.4), (3.5) and (3.6). Figure A.1(f) shows the fitting result for the case of tensile behaviour of PEEK at a strain rate of 1.04×10^{-4} s^{-1} and temperature of 296 K. The parameter K_1 can also be obtained in the fitting process. As given in Table 3.1, in the case of tensile behaviour of PEEK, the values of k, w, λ and K_1 were computed to be 0.4538, 61.86, 3.945 and 12020, respectively.

It should be noted that in the identification process, different selections of ε, T, $\dot{\varepsilon}$, T_{ref}, and $\dot{\varepsilon}_{\mathrm{ref}}$ slightly affect the fitting results of model parameters. Minor changes in the obtained model parameters are possible but would not have much influence on the prediction effect of the constitutive model.

Appendix B Constitutive modelling of hot deformation behaviour of metallic materials

B.1 Introduction

As metallic materials are widely used for extensive engineering applications, different metal forming processes have been developed to manufacture raw metallic materials to various shapes and dimensions. The study of the deformation behaviour of metallic materials is of a vital importance to metal forming processes. The flow stress curves at high temperature show specific complexity as compared with ones at room temperature. It has been established that four stages of hot deformation of metallic materials can be summarised in the flow behaviour: work hardening (WH), transition, dynamic softening and steady state [159, 160]. The complex deformation behaviour makes it difficult to develop a constitutive model to predict the flow behaviour at high temperature. However, a proper constitutive model is of significance to the numerical simulation and sometimes analytical study of hot forming processes of metallic materials. Numerous researchers have worked on the development of effective constitutive models for the hot deformation behaviour of metals for decades and many excellent works have been carried out and reported. Generally, there are three main types of constitutive models [159]: phenomenological constitutive model [101, 161-167], physically based constitutive model [168-172] and neural network based constitutive model [173-175].

Among all the phenomenological models, the Johnson-Cook model [101] has been extensively used to predict the flow stress curves at different strains, strain rates and temperatures of metals. Its simple form and easy identification of model parameters make the Johnson-Cook model widely used for many metallic materials. However, at a given strain rate and temperature, although it is able to predict the trend of work

hardening (WH), the Johnson-Cook model is shown less robust in representing the softening in hot deformation of metals. This severely limits its applicability to hot deformation behaviours of metallic materials and many researchers have tried to make modifications considering the effect of strain softening [176, 177].

Not only the phenomenological Johnson-Cook model but also some physically based constitutive models like the Zerilli-Armstrong model [168] have the limitation to give a good representation of the complex deformation behaviour at high temperature including the hardening and softening behaviours in different strain ranges. To solve this problem, a number of researchers used high-order polynomials to predict the effect of stain on flow stress [178-180]. In many cases, high-order polynomials are able to give a good prediction of the strain hardening and softening behaviours, but the disadvantages are the requirements for many trials to determine too many parameters and there is no clear meaning for the prediction functions. Therefore, there is still a need to develop new constitutive models to predict the hardening-transition-softening-steady behaviour in the hot deformation of metallic materials.

In an earlier study by the authors, a new phenomenological constitutive model, the ZOP model was proposed to predict the tensile and compressive behaviour of thermoplastics at different temperatures and strain rates [152]. The similarity of the deformation behaviour between thermoplastics and metals at high temperatures is that both have initial hardening followed by softening stages. The only difference is that for thermoplastics, another hardening stage comes after the softening stage, whilst for hot deformation of metals, steady flow stress comes afterwards. However, the steady state could be considered as a zero hardening rate and the difference could be neglected. Therefore, the ZOP model has the potential to be used in the prediction of hot deformation behaviour in metallic materials.

The current work aims to test the applicability of the ZOP model in modelling the hot deformation behaviour in metallic materials and to modify the ZOP model for better prediction accuracy. In the following sections, the ZOP model is firstly introduced and used to predict the hot deformation behaviour of 42CrMo carbon alloy steel. Then three modified models are developed to achieve better prediction results. The development strategy and the comparison between different models are demonstrated. Discussions are given to show the applicability and advancement of the developed constitutive models and how the different parts of the constitutive models represent the microstructure evolution in the hot deformation of metals. Finally, the studied models are also used to predict the peak strain and DRX completion strain with the results and comparisons also given in the discussion section.

B.2 Constitutive modelling of hot deformation behaviour

B.2.1 ZOP model

The ZOP model was developed by Zhu et al. [152] using phenomenological equations to mathematically predict the stress of thermoplastics at different strains, strain rates and temperatures, an approach similar to some widely-used model such as Johnson-Cook model [101], Voce-Kocks model [165, 181] the models developed by Khan et al. [161, 162, 182, 183]. The prediction of deformation behaviour of this model is based on the concept of piecewise functions and transition functions. It can be considered to have four parts: 1) function to predict the effect of strain rate and temperature; 2) function to predict the initial hardening and transition and following dynamic softening stages; 3) function to predict the steady state or additional hardening stage; 4) functions to enable a smooth transition from small strain stage to large strain stage. Details are given in the following.

B.2.1.1 Effect of strain rate and temperature

In the hot deformation behaviour of metals, with the rise of strain rate and the decrease of temperature, the flow stress trends to be enhanced. As a result, in the ZOP model, the recognised G'Sell-Jonas model [106] is modified to predict the effect of strain rate and temperature as following:

$$h(\dot{\varepsilon}, T) = (\dot{\varepsilon}/\dot{\varepsilon}_{\mathrm{ref}})^{m} \cdot \exp[a \cdot (1/T - 1/T_{\mathrm{ref}})] \quad \text{(B.1)}$$

where $\dot{\varepsilon}$ is the strain rate, $\dot{\varepsilon}_{\mathrm{ref}}$ is the reference strain rate, T is the temperature, T_{ref} is the reference temperature, m is the model parameter related to the effect of strain rate and a is the parameter related to the effect of temperature. The use of reference strain rate and temperature gives the equation an explicit meaning of the change of flow stress when different strain rates and temperatures from reference ones are applied.

B.2.1.2 Initial hardening, transition and softening stages

The stress in the small strain range under initial hardening, transition and softening behaviours are predicted by the function $f(\varepsilon, \dot{\varepsilon}, T)$ as following:

$$f(\varepsilon, \dot{\varepsilon}, T) = K_1 \cdot \varepsilon^{n} \cdot \exp\{-\varepsilon/[\mu \cdot h(\dot{\varepsilon}, T)]\} \quad \text{(B.2)}$$

where ε is the true strain, K_1, n and μ are model parameters. In this function, $h(\dot{\varepsilon}, T)$ is used to reflect the effect of strain rate and temperature on the hardening, transition and softening stages. The mathematic illustration of $f(\varepsilon, \dot{\varepsilon}, T)$ at small strains can be found as the red curve in Figure B.1(a).

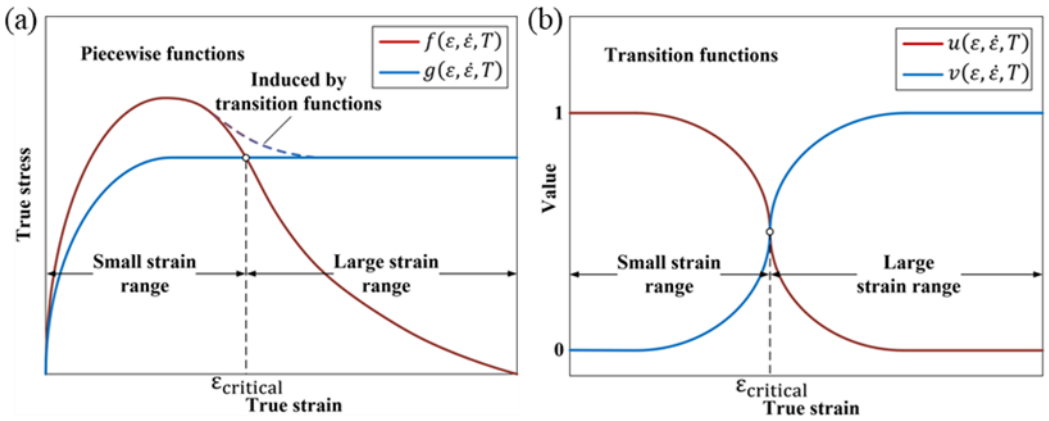


Figure B.1 Mathematic illustrations of (a) piecewise functions $f(\varepsilon,\dot{\varepsilon},T)$ and $g(\varepsilon,\dot{\varepsilon},T)$ and (b) transition functions $u(\varepsilon,\dot{\varepsilon},T)$ and $v(\varepsilon,\dot{\varepsilon},T)$

B.2.1.3 Steady state

The steady state can be treated as a hardening stage where the hardening rate is zero. Considering that a slight hardening behaviour may occur in this state, function $g(\varepsilon,\dot{\varepsilon},T)$ referring to the one in DSGZ model [102] is still applicable to predict the stress in large strain range. The function is given in the following expression:

$$g(\varepsilon,\dot{\varepsilon},T) = K_2 \cdot [\exp(-C_1 \cdot \varepsilon) + \exp C_2] \cdot [1 - \exp(-\alpha \cdot \varepsilon)] \cdot h(\dot{\varepsilon},T) \quad \text{(B.3)}$$

where K_2, C_1, C_2 and α are model parameters. Its mathematical meaning is illustrated as the blue curve in Figure B.1(a). This function is shown to be flexible to describe rising or steady curves at large strains.

B.2.1.4 Transition functions

As given above, the flow stress at small and large strains is predicted using two different functions. To achieve a smooth transition between the two functions at around a critical strain $\varepsilon_{critical}$, two transition functions are used in the ZOP model as follow:

$$u(\varepsilon,\dot{\varepsilon},T) = 1/\{1 + k \cdot \exp[w \cdot \varepsilon - \lambda \cdot h(\dot{\varepsilon},T)]\} \quad \text{(B.4)}$$

$$v(\varepsilon,\dot{\varepsilon},T) = 1/\{1 + \exp[\lambda \cdot h(\dot{\varepsilon},T) - w \cdot \varepsilon]\} \quad \text{(B.5)}$$

where k, w and λ are model parameters. The values of these functions stabilised at '1' and '0' with different strains, as shown in Figure B.1(b). The combination of the transition functions $u(\varepsilon, \dot{\varepsilon}, T)$ and $v(\varepsilon, \dot{\varepsilon}, T)$ contributes to the transition from the small strain stage to the large strain stage of the hot deformation behaviour. The expression of the ZOP model is given as the following control equation:

$$\sigma(\varepsilon, \dot{\varepsilon}, T) = f(\varepsilon, \dot{\varepsilon}, T) \cdot u(\varepsilon, \dot{\varepsilon}, T) + g(\varepsilon, \dot{\varepsilon}, T) \cdot v(\varepsilon, \dot{\varepsilon}, T) \quad \text{(B.6)}$$

A piecewise model can be given using the above expression, where the flow stress can be predicted using $f(\varepsilon, \dot{\varepsilon}, T)$ at small strain stage and using $g(\varepsilon, \dot{\varepsilon}, T)$ at large strain stage. In this model, there are twelve parameters including k, w, λ, n, μ, C_1, C_2, α, K_1, K_2, m and a, and reference strain and temperature should also be selected.

B.2.2 Modified model I

The ZOP model was initially proposed for the depiction of stress-strain curves of thermoplastics, which has a much smaller Young's modulus than metals. For thermoplastics, the transition from elasticity to the yield and plasticity is gradual and smooth because of the existence of non-linear elasticity, whilst in hot deformation of metals, a quicker transition from elastic to plastic deformation is acknowledged and it is less smooth than thermoplastics. Therefore, the modification of the ZOP model is to give a reasonable representation of the flow stress from the yield point instead of prediction from the zero-stress point.

The modification of the ZOP model is made in the expression of function $f(\varepsilon, \dot{\varepsilon}, T)$ and the modified function $f^*(\varepsilon, \dot{\varepsilon}, T)$ is expressed as below:

$$f^*(\varepsilon, \dot{\varepsilon}, T) = K_1 \cdot \varepsilon^n \cdot \exp\{-\varepsilon/[\mu \cdot h(\dot{\varepsilon}, T)]\} + B \cdot h(\dot{\varepsilon}, T) \quad \text{(B.7)}$$

where parameter B is used to enable the prediction starting from the yield point. With

the modification from $f(\varepsilon, \dot{\varepsilon}, T)$ to $f^*(\varepsilon, \dot{\varepsilon}, T)$, Modified model I may be given in the following equation:

$$\sigma(\varepsilon, \dot{\varepsilon}, T) = f^*(\varepsilon, \dot{\varepsilon}, T) \cdot u(\varepsilon, \dot{\varepsilon}, T) + g(\varepsilon, \dot{\varepsilon}, T) \cdot v(\varepsilon, \dot{\varepsilon}, T) \quad \text{(B.8)}$$

Thirteen parameters should be derived for Modified model I. Besides, selected reference strain rate and temperature should be given as well.

B.2.3 Modified model II

The modification made from the ZOP model to Modified model I is applied to improve the prediction accuracy of the original model at the initial small strain stage. Even though the ZOP model and Modified model I are both phenomenological constitutive models. They do not have any physical meaning to support the flow stress prediction and reflect the physical mechanism. To improve the prediction accuracy, physical method may also be used to modify ZOP model. For hot deformation of metals, the well-established Arrhenius equation can be used to predict the effect of strain rate and temperature related to the Zener-Hollomon (Z) parameter on the flow stress [184, 185], which is given as follows:

$$Z = \dot{\varepsilon} \cdot \exp[Q/(R \cdot T)] \quad \text{(B.9)}$$

$$\dot{\varepsilon} = F(\sigma_\mathrm{p}) \cdot \exp[-Q/(R \cdot T)] \quad \text{(B.10)}$$

where the function $F(\sigma_\mathrm{p})$ can be given in the form of a power function, exponential function or hyperbolic sine function as shown below [186]:

$$F(\sigma_\mathrm{p}) = \begin{cases} A' \cdot {\sigma_\mathrm{p}}^N & \alpha \cdot \sigma_\mathrm{p} < 0.8 \quad \text{(B.11)} \\ A'' \cdot \exp(\beta \cdot \sigma_\mathrm{p}) & \alpha \cdot \sigma_\mathrm{p} > 1.2 \quad \text{(B.12)} \\ A \cdot [\sinh(\gamma \cdot \sigma_\mathrm{p})]^N & for\ all\ \sigma_\mathrm{p} \quad \text{(B.13)} \end{cases}$$

where R is the universal gas constant (8.31 J·mol^{-1}·K^{-1}), T is the absolute temperature (K), Q is the activation energy of hot deformation (kJ·mol^{-1}), σ_p is the peak stress (MPa), A, A', A'', γ, β and N are the material constants, where $\gamma = \beta/N$.

Equation (B.13) is the most commonly used equation for all stress levels. From Equation (B.13), the following equation can be obtained:

$$\sigma_p = 1/\gamma \cdot \sinh^{-1}\{[\dot{\varepsilon} \cdot \exp(Q/(R \cdot T))/A]^{1/N}\} \quad \text{(B.14)}$$

Meanwhile, in the ZOP model, partial differentiation of $f(\varepsilon, \dot{\varepsilon}, T)$ of ε gives the following relationship:

$$\partial f(\varepsilon, \dot{\varepsilon}, T)/\partial \varepsilon = K_1 \cdot \varepsilon^{n-1} \cdot \exp\{-\varepsilon/[\mu \cdot h(\dot{\varepsilon}, T)]\} \cdot \{n - \varepsilon/[\mu \cdot h(\dot{\varepsilon}, T)]\} \quad \text{(B.15)}$$

From Equation (B.15), when the strain increases to a peak strain $\varepsilon_p = n \cdot \mu \cdot h(\dot{\varepsilon}, T)$ (defined as the strain where the peak stress appears), the peak stress is reached by using Equation (B.2):

$$\sigma_p = K_1 \cdot [n \cdot \mu \cdot h(\dot{\varepsilon}, T)/e]^n \quad \text{(B.16)}$$

Combining Equations (B.14) and (B.16), the following equation can be obtained:

$$1/\gamma \cdot \sinh^{-1}\{[\dot{\varepsilon} \cdot \exp(Q/(R \cdot T))/A]^{1/N}\} = K_1 \cdot [n \cdot \mu \cdot h(\dot{\varepsilon}, T)/e]^n \quad \text{(B.17)}$$

which leads to the following results for the expression of $h(\dot{\varepsilon}, T)$:

$$h(\dot{\varepsilon}, T) = e/(n \cdot \mu) \cdot [1/(\gamma \cdot K_1)]^{1/n} \cdot \{\sinh^{-1}[(Z/A)^{1/N}]\}^{1/n} \quad \text{(B.18)}$$

In Equation (B.18), the value of $e/(n \cdot \mu) \cdot [1/(\gamma \cdot K_1)]^{1/n}$ is constant. For simplification, the term $h(\dot{\varepsilon}, T)$ used in the constitutive model to predict the effect of strain rate and temperature can be replaced by the following expression without consideration of the term $e/(n \cdot \mu) \cdot [1/(\gamma \cdot K_1)]^{1/n}$:

$$h^*(\dot{\varepsilon},T)=\left\{\sinh^{-1}\left[(Z/A)^{1/N}\right]\right\}^{1/n}=\left\{\sinh^{-1}\left[(\dot{\varepsilon}\cdot\exp(Q/(R\cdot T))/A)^{1/N}\right]\right\}^{1/n} \quad \text{(B.19)}$$

Or it may be given in the following format:

$$h^*(\dot{\varepsilon},T)=\left\{\ln\left[(Z/A)^{1/N}+\left((Z/A)^{2/N}+1\right)^{1/2}\right]\right\}^{1/n} \quad \text{(B.20)}$$

With the modification from $h(\dot{\varepsilon},T)$ to $h^*(\dot{\varepsilon},T)$, Modified model II has the following formula:

$$\sigma(\varepsilon,\dot{\varepsilon},T)=f^{**}(\varepsilon,\dot{\varepsilon},T)\cdot u^*(\varepsilon,\dot{\varepsilon},T)+g^*(\varepsilon,\dot{\varepsilon},T)\cdot v^*(\varepsilon,\dot{\varepsilon},T) \quad \text{(B.21)}$$

where,

$$f^{**}(\varepsilon,\dot{\varepsilon},T)=K_1\cdot\varepsilon^n\cdot\exp\{-\varepsilon/[\mu\cdot h^*(\dot{\varepsilon},T)]\}+B\cdot h^*(\dot{\varepsilon},T)/h^*(\dot{\varepsilon}_{\mathrm{ref}},T_{\mathrm{ref}}) \quad \text{(B.22)}$$

$$g^*(\varepsilon,\dot{\varepsilon},T)=K_2\cdot[\exp(-C_1\cdot\varepsilon)+\exp C_2]\cdot[1-\exp(-\alpha\cdot\varepsilon)]\cdot h^*(\dot{\varepsilon},T) \quad \text{(B.23)}$$

$$u^*(\varepsilon,\dot{\varepsilon},T)=1/\{1+k\cdot\exp[w\cdot\varepsilon-\lambda\cdot h^*(\dot{\varepsilon},T)]\} \quad \text{(B.24)}$$

$$v^*(\varepsilon,\dot{\varepsilon},T)=1/\{1+\exp[\lambda\cdot h^*(\dot{\varepsilon},T)-w\cdot\varepsilon]\} \quad \text{(B.25)}$$

In the Modified model II, a total of fourteen parameters should be derived. The identification procedures of parameters k, w, λ, n, μ, C_1, C_2, α, K_1, K_2 and B are the same as the ZOP and the Modified model I. The parameters Q, A and N related to the effect of strain rate and temperature need to be determined first. Besides, the reference strain rate and temperature should also be determined prior to the identification of the model parameters.

B.2.4 Modified model III

From the prediction results of Modified model II as given in Section B.4, the Zener-Holloman parameter used in the constitutive model is not able to reflect the effect of strain rate and temperature with high prediction accuracy. Therefore, compensation for

either the strain rate or temperature should be used to enhance their effect on the flow stress. In this study, compensation for the strain rate in Z parameter is carried out via modifying the exponent of the strain rate in Z parameter. The modified Z parameter can be written in the following format [179]:

$$Z^* = \dot{\varepsilon}^M \cdot \exp[Q/(R \cdot T)] \tag{B.26}$$

And the modified term $h^{**}(\dot{\varepsilon}, T)$ can be expressed as follows:

$$h^{**}(\dot{\varepsilon}, T) = \left\{\sinh^{-1}\left[(Z^*/A)^{1/N}\right]\right\}^{1/n} = \left\{\ln\left[(Z^*/A)^{1/N} + \left((Z^*/A)^{2/N} + 1\right)^{1/2}\right]\right\}^{1/n} \tag{B.27}$$

Then the following expression is given as Modified model III:

$$\sigma(\varepsilon, \dot{\varepsilon}, T) = f^{***}(\varepsilon, \dot{\varepsilon}, T) \cdot u^{**}(\varepsilon, \dot{\varepsilon}, T) + g^{**}(\varepsilon, \dot{\varepsilon}, T) \cdot v^{**}(\varepsilon, \dot{\varepsilon}, T) \tag{B.28}$$

where,

$$f^{***}(\varepsilon, \dot{\varepsilon}, T) = K_1 \cdot \varepsilon^n \cdot \exp\{-\varepsilon/[\mu \cdot h^{**}(\dot{\varepsilon}, T)]\} + B \cdot h^{**}(\dot{\varepsilon}, T)/h^{**}(\dot{\varepsilon}_{\mathrm{ref}}, T_{\mathrm{ref}}) \tag{B.29}$$

$$g^{**}(\varepsilon, \dot{\varepsilon}, T) = K_2 \cdot [\exp(-C_1 \cdot \varepsilon) + \exp C_2] \cdot [1 - \exp(-\alpha \cdot \varepsilon)] \cdot h^{**}(\dot{\varepsilon}, T) \tag{B.30}$$

$$u^{**}(\varepsilon, \dot{\varepsilon}, T) = 1/\{1 + k \cdot \exp[w \cdot \varepsilon - \lambda \cdot h^{**}(\dot{\varepsilon}, T)]\} \tag{B.31}$$

$$v^{**}(\varepsilon, \dot{\varepsilon}, T) = 1/\{1 + \exp[\lambda \cdot h^{**}(\dot{\varepsilon}, T) - w \cdot \varepsilon]\} \tag{B.32}$$

In Modified model III, fifteen parameters are used, but only parameter M is required to be identified as other parameters are already given in Modified model II. Similarly, the reference strain rate and temperature are needed but this can be referred to as the ones used in Modified model II.

B.3 Identification of model parameters

To validate the developed constitutive models for deformation behaviour in hot deformation of metals, compression testing results of 42CrMo by Lin et al. [187] are used. The testing results are presented in true stress – strain curves with processing temperature from 850 ℃ to 1050 ℃ and strain rate from 0.01 s^{-1} to 50 s^{-1}. The identification of model parameters is performed based on the above testing results. It is noteworthy that the testing results at strain rate of 0.1 s^{-1} and different temperatures are not used in the parameter identification in order to test the real predictive capability of the developed models in Section B.4.

B.3.1 ZOP model

The identification procedures for the model parameters in the ZOP model can be found in detail in the previous work of Zhu et al. [152]. Six steps should be followed to determine all the twelve parameters, as summarised below. To derive the parameters for the hot compressive behaviour of 42CrMo, the reference strain and temperature are selected as 1 s^{-1} and 1050 °C, respectively.

Step 1:

By selecting points at the same large strain on curves at the same temperature but different strain rates, four values m_1, m_2, m_3 and m_4 can be calculated by fitting the relationship between the stress and strain rate with Equation (B.33) as shown in Figure B.2(a). m is identified to be 0.1081 by taking the average value of the above.

$$\sigma(\varepsilon, \dot{\varepsilon}, T) = \sigma_{\mathrm{ref}}(\varepsilon, \dot{\varepsilon}_{\mathrm{ref}}, T) \cdot (\dot{\varepsilon}/\dot{\varepsilon}_{\mathrm{ref}})^{m} \tag{B.33}$$

where $\sigma(\varepsilon, \dot{\varepsilon}, T)$ is the stress of selected points and $\sigma_{\mathrm{ref}}(\varepsilon, \dot{\varepsilon}_{\mathrm{ref}}, T)$ is the selected stress at the reference strain rate.

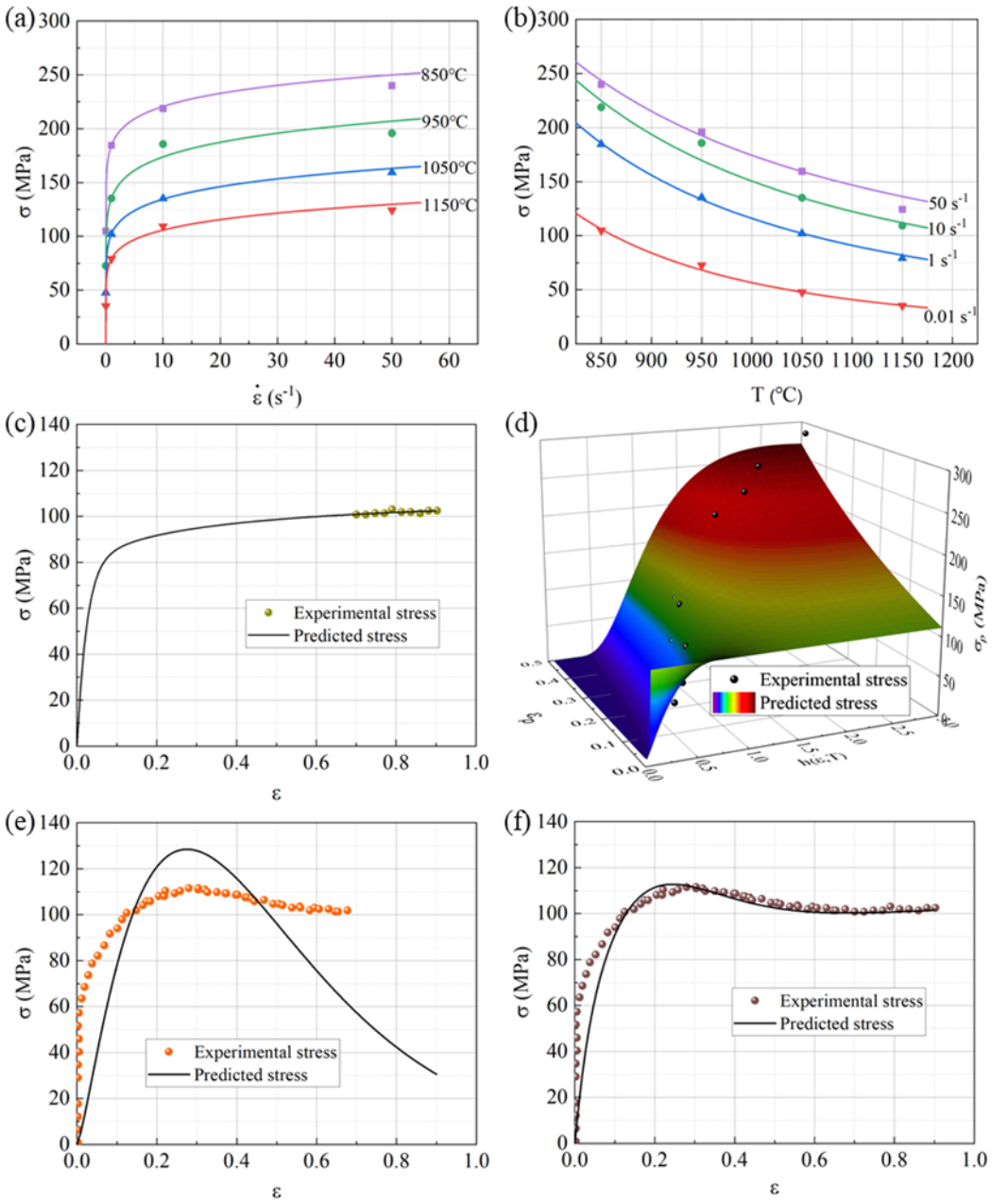


Figure B.2 Illustration of the fitting process of (a) m, (b) a, (c) C_1, C_2, α and K_2, (d) μ, (e) n and (f) k, w, λ and K_1.

Step 2:

Points are selected at the same large strain on curves at the same strain rate but different temperatures. Different values of a can be determined by fitting the relationship between the stress and temperature using Equation (B.34) as shown in Figure B.2(b). a is calculated as the average value and is identified as 2600.75.

$$\sigma(\varepsilon, \dot{\varepsilon}, T) = \sigma_{\mathrm{ref}}(\varepsilon, \dot{\varepsilon}, T_{\mathrm{ref}}) \cdot \exp[a \cdot (1/T - 1/T_{\mathrm{ref}})] \quad \text{(B.34)}$$

where $\sigma_{\mathrm{ref}}(\varepsilon, \dot{\varepsilon}, T_{\mathrm{ref}})$ is the selected stress at the reference temperature.

Step 3:

As shown in Figure B.2(c), by fitting the relationship between the stress and strain in the large strain range at reference strain rate and temperature with Equation (B.3), C_1, C_2, α and K_2 can be obtained as: 0.275, 0.2966, 46.14 and 58.52, respectively.

Step 4:

From all the flow stress curves, peak strains and stresses can be extracted, and the values of $h(\dot{\varepsilon}, T)$ at different conditions can be calculated. By fitting the relationship between σ_{p}, ε_{p} and $h(\dot{\varepsilon}, T)$ with Equation (B.35), μ can be identified to be 0.2076 as shown by Figure B.2(d).

$$\sigma_{\mathrm{p}} = \sigma_{\mathrm{p}}^{\mathrm{ref}} \cdot \left(\varepsilon_{\mathrm{p}}/\varepsilon_{\mathrm{p}}^{\mathrm{ref}}\right)^{\varepsilon_{\mathrm{p}}/[\mu \cdot h(\dot{\varepsilon}, T)]} \quad \text{(B.35)}$$

where $\varepsilon_{\mathrm{p}}^{\mathrm{ref}}$ and $\sigma_{\mathrm{p}}^{\mathrm{ref}}$ are peak strain and stress at reference strain rate and temperature.

Step 5:

After the identification of μ, by fitting the relationship between stress and strain in small strain range at reference strain rate and temperature with Equation (B.36), n is determined to be 1.327 as illustrated in Figure B.2(e).

$$\sigma(\varepsilon, \dot{\varepsilon}, T) = \sigma_{\mathrm{p}} \cdot \left(e/\varepsilon_{\mathrm{p}}\right)^{n} \cdot \varepsilon^{n} \cdot \exp\{-\varepsilon/[\mu \cdot h(\dot{\varepsilon}, T)]\} \quad \text{(B.36)}$$

Step 6:

Finally, as shown in Figure B.2(f), the fitting of the relationship between stress and strain in the whole range at reference strain rate and temperature with Equation (B.6)

gives the identification results of k, w, λ and K_1 as 0.6564, 4.524, 0 and 2681, respectively.

Following the above procedures, the model parameters of the ZOP model were derived and are given in Table B.1.

Table B.1 Parameters of the ZOP model for the hot compressive behaviour of 42CrMo.

ID	Model parameters	Value
1	k	0.6564
2	w	4.524
3	λ	0
4	n	1.327
5	μ	0.2076
6	C_1	0.275
7	C_2	0.2966
8	α	46.14
9	K_1 (MPa)	2681
10	K_2 (MPa)	58.52
11	m	0.1081
12	a	2600.75

B.3.2 Modified model I

The identification process of the parameters of Modified model I is almost identical to the ZOP model. The only difference is that parameter *B* is required to be identified during the fitting of the flow stress at small strains along with the identification process of parameter n. In the studied hot compressive behaviour of 42CrMo, the reference

strain rate is selected as 1 s^{-1} and reference temperature as 1050 °C. Given the above conditions, the parameters of Modified model I were identified according to the procedures and are listed in Table B.2.

Table B.2 Material parameters of Modified model I for the hot compressive behaviour of 42CrMo.

ID	Model parameters	Value
1	k	0.8285
2	w	2.842
3	λ	1.247
4	n	1.409
5	μ	0.2076
6	C_1	0.2805
7	C_2	0.2951
8	α	35.62
9	K_1 (MPa)	856.4
10	K_2 (MPa)	58.73
11	m	0.1081
12	a	2600.75
13	B (MPa)	74.28

B.3.3 Modified model II

The identification process of Modified model II is different as the effect of strain rate and temperature is predicted by function $h^*(\dot{\varepsilon}, T)$, which is given in Equations (B.19)

and (B.20). The following procedure is used to determine the parameters of Modified model II.

N:

From Equations (B.10) and (B.11), by taking the logarithm, the following equation can be obtained [187]:

$$\ln \dot{\varepsilon} = N \cdot \ln \sigma_{\mathrm{p}} + \ln A' - Q/(R \cdot T) \tag{B.37}$$

From the above equation, it can be clearly seen that the value of $1/N$ can be determined as the slope of $\ln \sigma_{\mathrm{p}}$ versus $\ln \dot{\varepsilon}$ curves in linear fitting, as shown in Figure B.3(a). N is calculated as 8.1755 MPa^{-1} by taking the average value of the ones obtained at different temperatures.

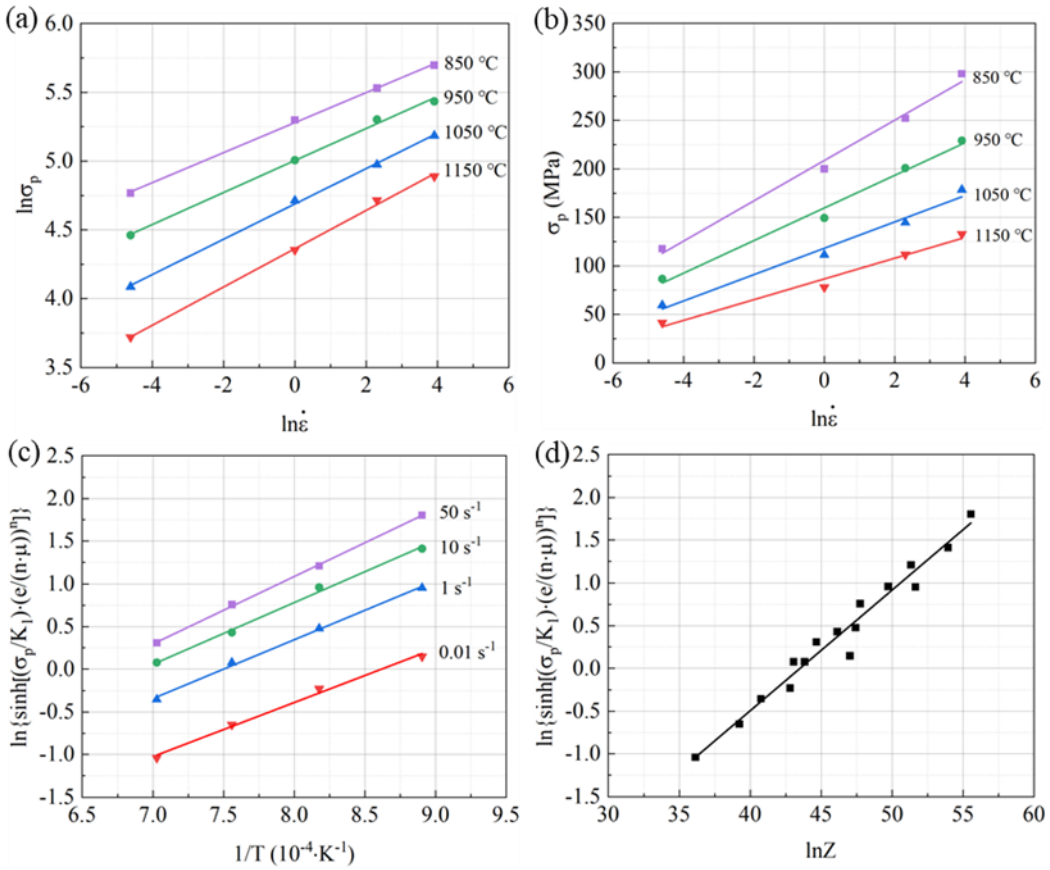


Figure B.3 Parameter calculation of $h^*(\dot{\varepsilon}, T)$ in Modified model II. Relationship between (a) $\ln \sigma_{\mathrm{p}}$ and $\ln \dot{\varepsilon}$, (b) σ_{p} and $\ln \dot{\varepsilon}$, (c) $\ln\{\sinh[\sigma_{\mathrm{p}}/K_1 \cdot (e/(n \cdot \mu))^n]\}$ and

$1/T$, and (d) $\ln\{\sinh[\sigma_p/K_1 \cdot (e/(n \cdot \mu))^n]\}$ and $\ln Z$.

β:

From Equations (B.10) and (B.12), by taking the logarithm, it gives [187]:

$$\ln \dot{\varepsilon} = \beta \cdot \sigma_p + \ln A'' - Q/(R \cdot T) \quad \text{(B.38)}$$

Therefore, by performing linear fitting, $1/\beta$ can be determined as the slope of σ_p versus $\ln \dot{\varepsilon}$ curves as shown in Figure B.3(b). β is calculated as 0.0687 MPa^{-1}, which is given by the average value of the ones at different deformation temperatures.

$K_1 \cdot (n \cdot \mu/e)^n$:

Substituting Equation (B.19) into Equation (B.16), the peak stress in Modified model II can be expressed as follows:

$$\sigma_p = K_1 \cdot (n \cdot \mu/e)^n \cdot \sinh^{-1}[(Z/A)^{1/N}] \quad \text{(B.39)}$$

Combining Equations (B.14) and (B.39), the value of $K_1 \cdot (n \cdot \mu/e)^n$ can be calculated as 119.0029 MPa using the following equation:

$$K_1 \cdot (n \cdot \mu/e)^n = 1/\gamma = N/\beta \quad \text{(B.40)}$$

Q:

From Equation (B.39), the following equation can be derived:

$$Q/T = R \cdot N \cdot \ln\{\sinh[\sigma_p/K_1 \cdot (e/(n \cdot \mu))^n]\} + R \cdot \ln A - R \cdot \ln \dot{\varepsilon} \quad \text{(B.41)}$$

Partially differentiating both sides of $1/T$ in Equation (B.41), it gives the following equation:

$$Q = R \cdot N \cdot \partial \ln\{\sinh[\sigma_p/K_1 \cdot (e/(n \cdot \mu))^n]\}/\partial(1/T) \quad \text{(B.42)}$$

And therefore:

$$\partial \ln\left\{\sinh\left[\sigma_{\mathrm{p}}/K_1 \cdot (e/(n \cdot \mu))^n\right]\right\}/\partial(1/T) = Q/(R \cdot N) \tag{B.43}$$

In the above equation, the value of $1/K_1 \cdot [e/(n \cdot \mu)]^n$, R and N are already known, therefore Q can be determined as the slope of the linearly fitted relationship between $\ln\left\{\sinh\left[\sigma_{\mathrm{p}}/K_1 \cdot (e/(n \cdot \mu))^n\right]\right\}$ and $1/T$ as shown in Figure B.3(c). By taking the average value of the ones for different strain rate conditions, the value of Q was calculated as 482.1344 kJ·mol^{-1}.

A:

From Equations (B.9) and (B.40), the following equations can be derived:

$$Z = \dot{\varepsilon} \cdot \exp[Q/(R \cdot T)] = A \cdot \left\{\sinh\left[\sigma_{\mathrm{p}}/K_1 \cdot (e/(n \cdot \mu))^n\right]\right\}^N \tag{B.44}$$

After taking the logarithm of both sides, the following relationship is obtained:

$$\ln\left\{\sinh\left[\sigma_{\mathrm{p}}/K_1 \cdot (e/(n \cdot \mu))^n\right]\right\} = \ln Z/N - \ln A/N \tag{B.45}$$

As given in Equation (B.45), $\ln A/N$ can be determined by the intercept of the linearly fitted $\ln\left\{\sinh\left[\sigma_{\mathrm{p}}/K_1 \cdot (e/(n \cdot \mu))^n\right]\right\}$ versus $\ln Z$ curve. Since the value of N has been identified in the above steps, A can be calculated as 6.37431×10^{21} s^{-1} from the linear fitting result as shown in Figure B.3(d).

From the above identification procedure, the parameters related to the effect of strain rate and temperature can be determined. Other parameters in Modified model II can be referred to the identification methods of the ZOP model and Modified model I. Before this, the reference strain rate and temperature need to be determined and they are selected as 1 s^{-1} and 1050 °C in the studied hot compressive behaviour of 42CrMo. Identified parameters of Modified model II are listed in Table B.3.

Table B.3 Material parameters of Modified model II for the hot compressive behaviour of 42CrMo

ID	Model parameters	Value
1	k	0.7939
2	w	3.971
3	λ	2.969
4	n	1.369
5	μ	0.3545
6	C_1	0.282
7	C_2	0.2965
8	α	45.67
9	K_1 (MPa)	973.4
10	K_2 (MPa)	106.3
11	N (MPa^{-1})	8.1755
12	Q ($kJ \cdot mol^{-1}$)	482.1344
13	A (s^{-1})	6.37431×10^{21}
14	B (MPa)	70.06

B.3.4 Modified model III

The identification process of Modified model III is based on the results of Modified model II. To determine the exponent of strain rate (M) for compensation of its effect on the flow stress, the following steps are followed.

With the modification from Z to Z^*, the expression of the peak stress is updated in the following:

$$\sigma_{\mathrm{p}} = K_1 \cdot (n \cdot \mu / e)^n \cdot \sinh^{-1}\left[(Z^*/A)^{1/N}\right] \tag{B.46}$$

After derivation, Equation (B.46) can be expressed as Equation (B.47).

$$\dot{\varepsilon}^M = A \cdot \left\{\sinh\left[\sigma_{\mathrm{p}}/K_1 \cdot (e/(n \cdot \mu))^n\right]\right\}^N \cdot \exp[-Q/(R \cdot T)] \tag{B.47}$$

By taking logarithm of both sides, the following equation can be derived in the following:

$$\ln\{\sinh[\sigma_p/K_1 \cdot (e/(n \cdot \mu))^n]\} = M/N \cdot \ln \dot{\varepsilon} - \ln A/N + Q/(N \cdot R \cdot T) \quad \text{(B.48)}$$

As shown in Equation (B.48), M/N can be identified as the slope of the linearly fitted relationship between the $\ln\{\sinh[\sigma_p/K_1 \cdot (e/(n \cdot \mu))^n]\}$ and $\ln \dot{\varepsilon}$. The relationships and linear fitting results at different deformation temperatures are given in Figure B.4. As N is already determined in the identification process of Modified model II, by taking the average value, M can be calculated as 1.4011.

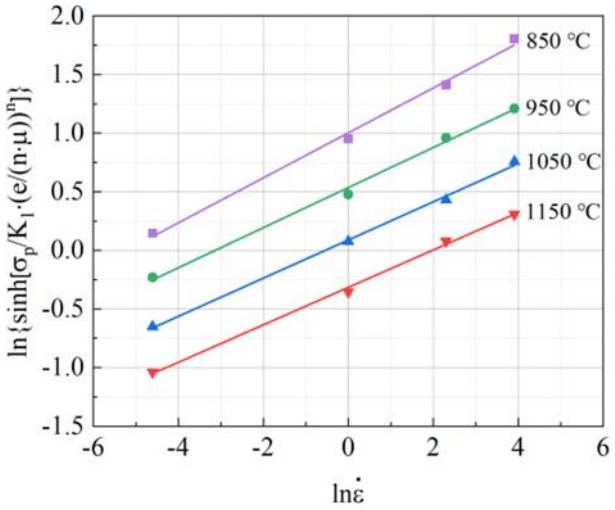


Figure B.4 Calculation of parameter M in Modified model III: the relationship between $\ln\{\sinh[\sigma_p/K_1 \cdot (e/(n \cdot \mu))^n]\}$ and $\ln \dot{\varepsilon}$.

The above proposed identification method of M is different from the trial-and-error method used in the studies of Lin et al. [179] and Peng et al. [188]. The advantage is obvious as an optimal solution of M can be obtained to achieve a higher prediction accuracy at the lower computing cost. The parameter of Modified model III can be found in Table B.4.

Table B.4 Material parameters of the modified model III for the hot compressive behaviour of 42CrMo.

ID	Model parameters	Value

1	k	0.7939
2	w	3.971
3	λ	2.969
4	n	1.369
5	μ	0.3545
6	C_1	0.282
7	C_2	0.2965
8	α	45.67
9	K_1 (MPa)	973.4
10	K_2 (MPa)	106.3
11	N (MPa^{-1})	8.1755
12	Q ($kJ \cdot mol^{-1}$)	482.1344
13	A (s^{-1})	6.37431×10^{21}
14	B (MPa)	70.06
15	M	1.4011

B.4 Validation of the developed constitutive models

The testing results of 42CrMo in the study of Lin et al. [187] are given as the solid curves in the figures (Figure B.5-B.8). From the testing results, the four stages of the stress-strain curves are presented clearly: work hardening, transition, dynamic softening and steady state. It also shows that with the increase of temperature and strain rate, the true stress of 42CrMo will be reduced and increased, respectively. The prediction results of the ZOP model, the modified models I, II and III are presented and validated in this section. The testing cases at 0.1 s^{-1} and different temperatures are also used in the

validation although they are not involved in the parameter identification. This is used to evaluate the predictive capability of the developed models.

B.4.1 Prediction and validation of ZOP model

Using the determined model parameters in Table B.1, the predicted flow stress curves at different strain rates and temperatures are depicted in Figure B.5. It is shown that the ZOP model represents well the flow stress at different strain ranges including hardening, transition, softening and steady state. More specifically, most predicted curves follow the experimental data to a high extent from the peak stress point, i.e., the transition point between the hardening and the softening stages. However, deficiency occurs at small strains. The predicted curves are not able to describe the sudden change of the slope where the elastic deformation completes and yielding happens. This is unavoidable for the ZOP model because it was originally proposed for thermoplastics, the small strain deformation of which has much smoother curves than metals. For the magnitude of flow stress curves, the ZOP model is capable to predict the effect of strain rate and temperature except from the curves of 1050 ℃ and 1150 ℃ at the strain rate of 0.01 s^{-1}, and the curve of 950 ℃ at the strain rate of 0.1 s^{-1}. This indicates the effectiveness of the strain rate and temperature related term $h(\dot{\varepsilon}, T)$ in the ZOP model but there is still scope for improvement to achieve better prediction for the shifting of the flow stress curves.

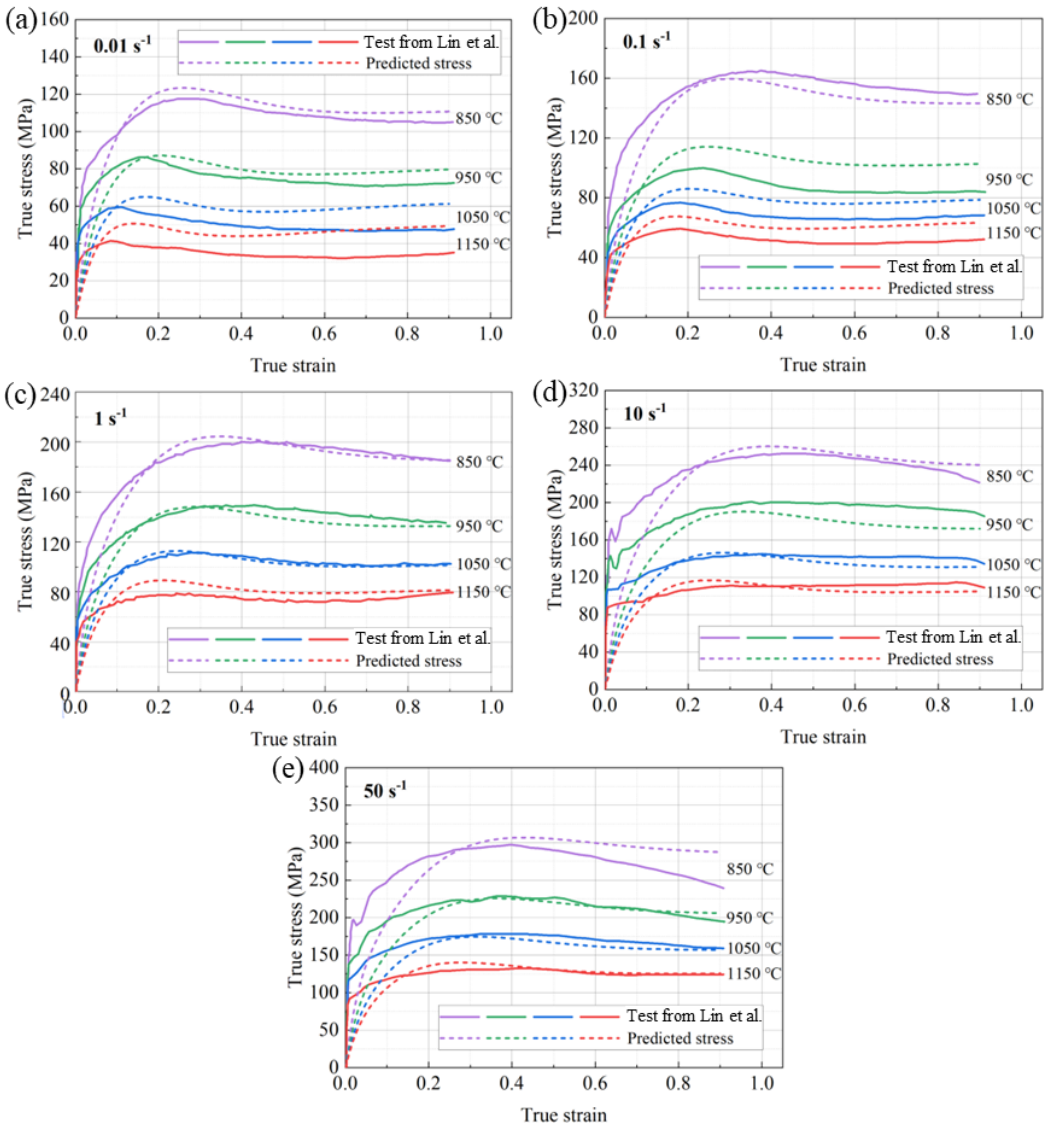


Figure B.5 Experimental true stress – strain curves of 42CrMo from Lin et al. [187] and prediction results of ZOP model at strain rate of (a) 0.01 s^{-1}, (b) 0.1 s^{-1}, (c) 1 s^{-1}, (d) 10 s^{-1} and (e) 50 s^{-1}.

B.4.2 Prediction and validation of Modified model I

The comparison between the experimental data and prediction results of Modified model I is depicted in Figure B.6. Modified model I shows a noted improvement on the prediction accuracy especially at the initial hardening and the following softening stages as compared with the ZOP model. It indicates that the proposed strategy works well in the prediction of the flow stress from the yield stress instead of from zero stress. It shows that the use of the piecewise functions and the transition functions is an effective way

to predict the effect of strain on the flow stress in hot deformation behaviour of metals. However, on the other hand, at the conditions of high temperature and low strain rate and the conditions of lower temperature and higher strain rate, the predicted curves are unable to follow the experimental curves well. The predicted results at temperature of 1150 ℃ and strain rate of 0.01 s^{-1} and at temperature of 950 ℃ and strain rate of 0.1 s^{-1} show considerable deviation from the testing result, which are shown by the red dotted curve in Figure B.6(a) and the green dotted curve in Figure B.6(b), respectively. The same observations are also presented at temperature of 850 ℃ and strain rate of 0.01 s^{-1} and some other conditions. This leads to conclusion that the term $h(\dot{\varepsilon}, T)$ lacks enough flexibility to give an accurate prediction of the effect of strain rate and temperature.

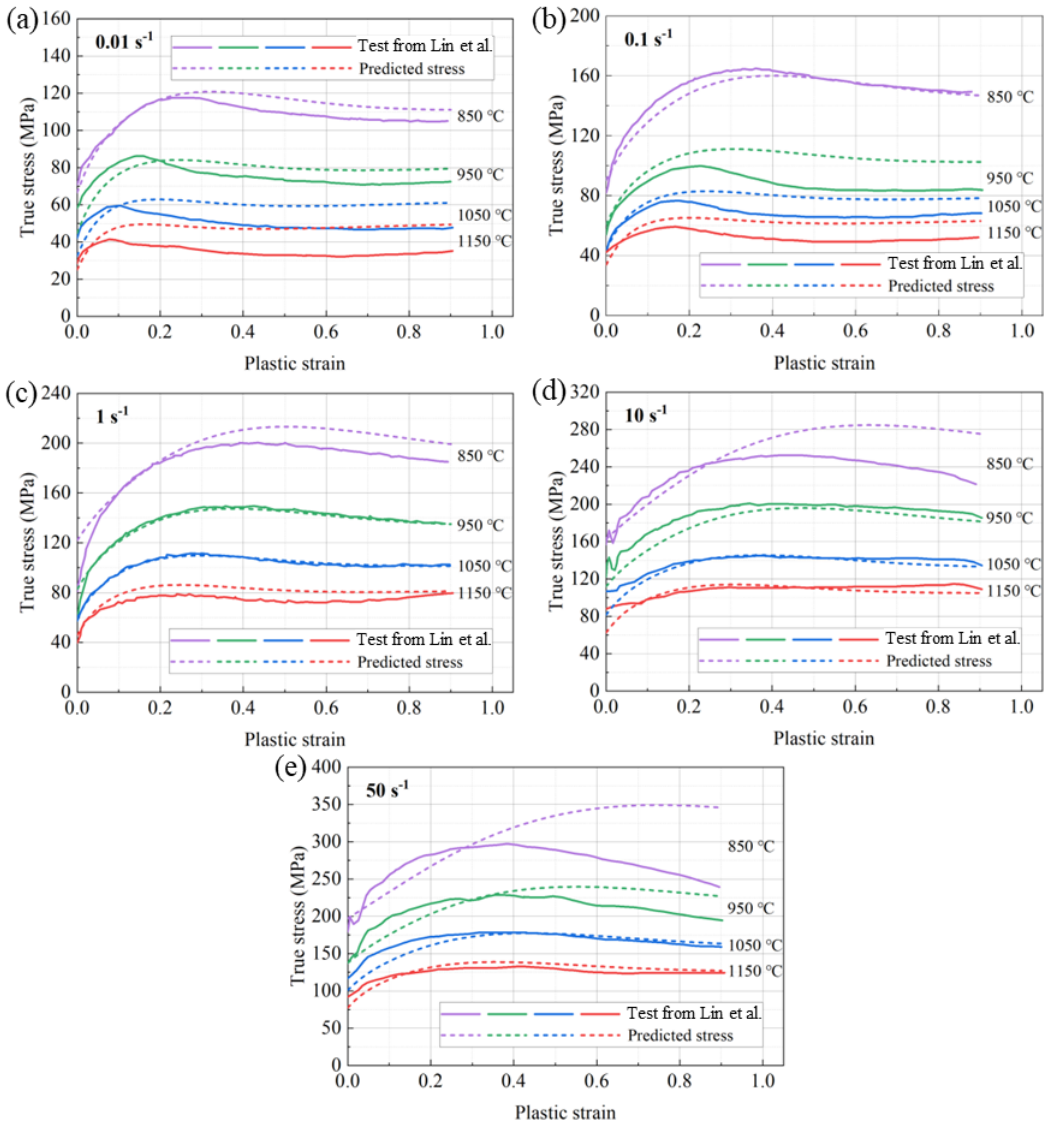


Figure B.6 Experimental true stress – strain curves of 42CrMo from Lin et al. [187] and prediction results of Modified model I at strain rate of (a) 0.01 s^{-1}, (b) 0.1 s^{-1}, (c) 1 s^{-1}, (d) 10 s^{-1} and (e) 50 s^{-1}.

B.4.3 Prediction and validation of Modified model II

The same as Modified model I, Modified model II also starts the prediction from the yield point, as shown in Figure B.7, which shows a good agreement of the overall shape of the flow stress curves. Especially at different temperature conditions at strain rates of 1 s^{-1} and 10 s^{-1}, the prediction curves follow the experimental curves very well. However, at strain rates of 0.01 s^{-1}, 0.1 s^{-1} and 50 s^{-1}, the predicted and experimental curves do not match up sufficiently well. In another word, the modified term $h^*(\dot{\varepsilon}, T)$ in Modified

model II is unable to predict the effect of strain rate and temperature with satisfactory accuracy, especially at small strain rate such as 0.01 s^{-1}, as shown in Figure B.7(a). At the strain rate of 0.01 s^{-1}, the deviation between the predicted and the experimental results becomes larger with the decrease of deformation temperature. Even if the trend and shape of the predicted flow stress curves have a good agreement with the experimental results, the inaccuracy could be improved. The above observation indicates that the use of the function $h^*(\dot{\varepsilon}, T)$ is still insufficiently robust for Modified model II to accurately predict the effect of strain rate and temperature in a wide range, even though its original format has been used widely with metallic materials.

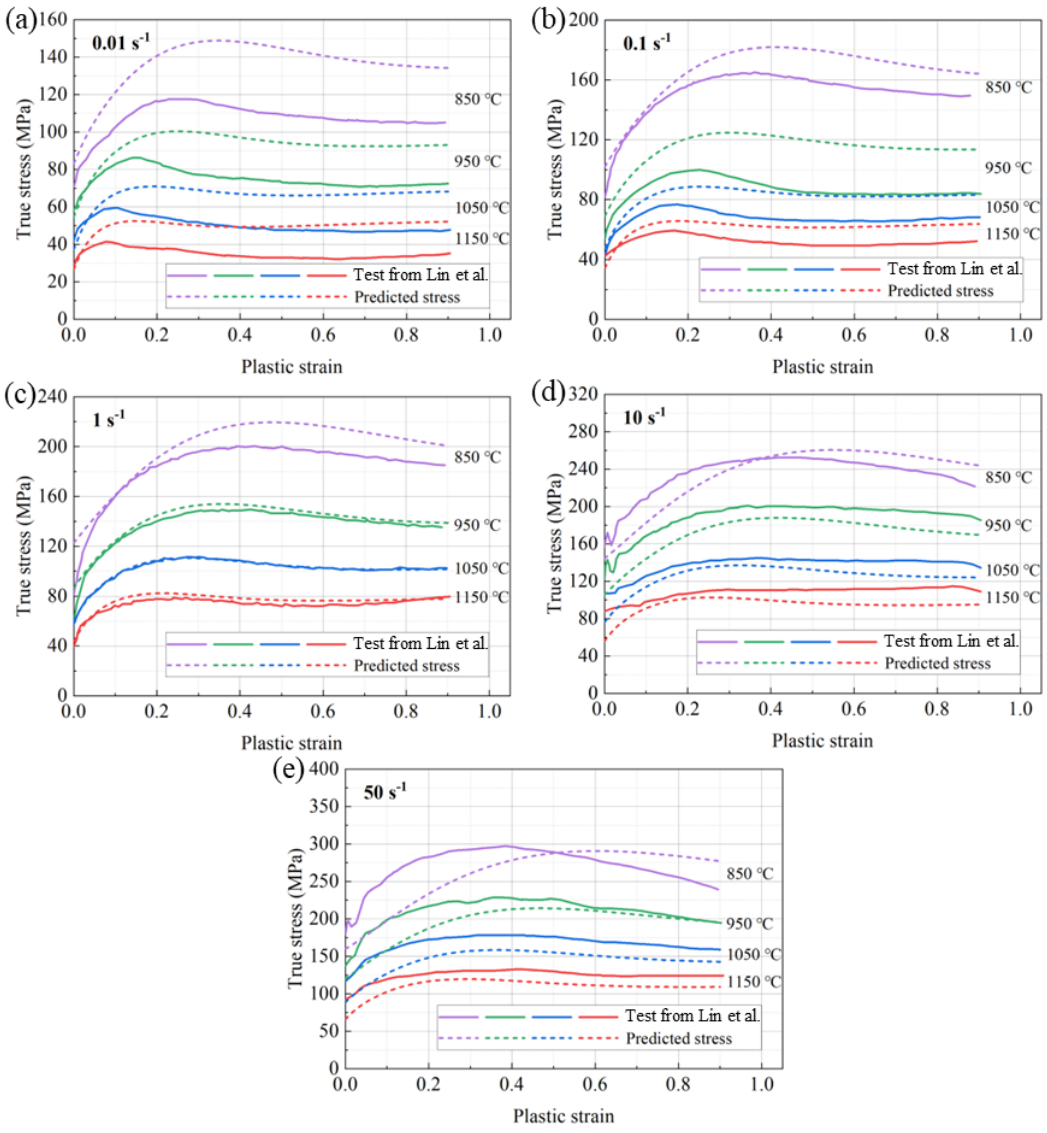


Figure B.7 Experimental true stress – strain curves of 42CrMo from Lin et al. [187] and prediction results of Modified model II at strain rate of (a) 0.01 s^{-1}, (b) 0.1 s^{-1}, (c) 1 s^{-1}, (d) 10 s^{-1} and (e) 50 s^{-1}.

B.4.4 Prediction and validation of Modified model III

To further improve Modified model II, the modified term $h^{**}(\dot{\varepsilon}, T)$ is used to predict the effect of strain rate and temperature with the addition of the exponent of strain rate in the Z parameter to compensate for the effect of strain rate. The prediction results of Modified model III are shown in Figure B.8 and a clearly improved prediction can be observed. Different deformation stages in hot deformation are predicted and presented properly due to the use of piecewise and transition functions and the change of prediction starting point at yield point instead of the zero-stress point. In the meantime, the shifting of the flow stress curves due to the change of strain rate and temperature is given satisfactorily because of the compensation for the effect of strain rate and the optimal identification of the exponent M. Although at the conditions of 0.1 s^{-1} at 950 ℃ and 50 s^{-1} at 850 ℃, the predicted curves deviate from the experimental ones to a degree, the capability of Modified model III to predict the effect of a wide range of strain rate and temperature is enhanced significantly as compared to Modified model II. Overall, Modified model III presents better prediction effect than the ZOP model and the other two modified models for the hot deformation behaviour of 42CrMo steel.

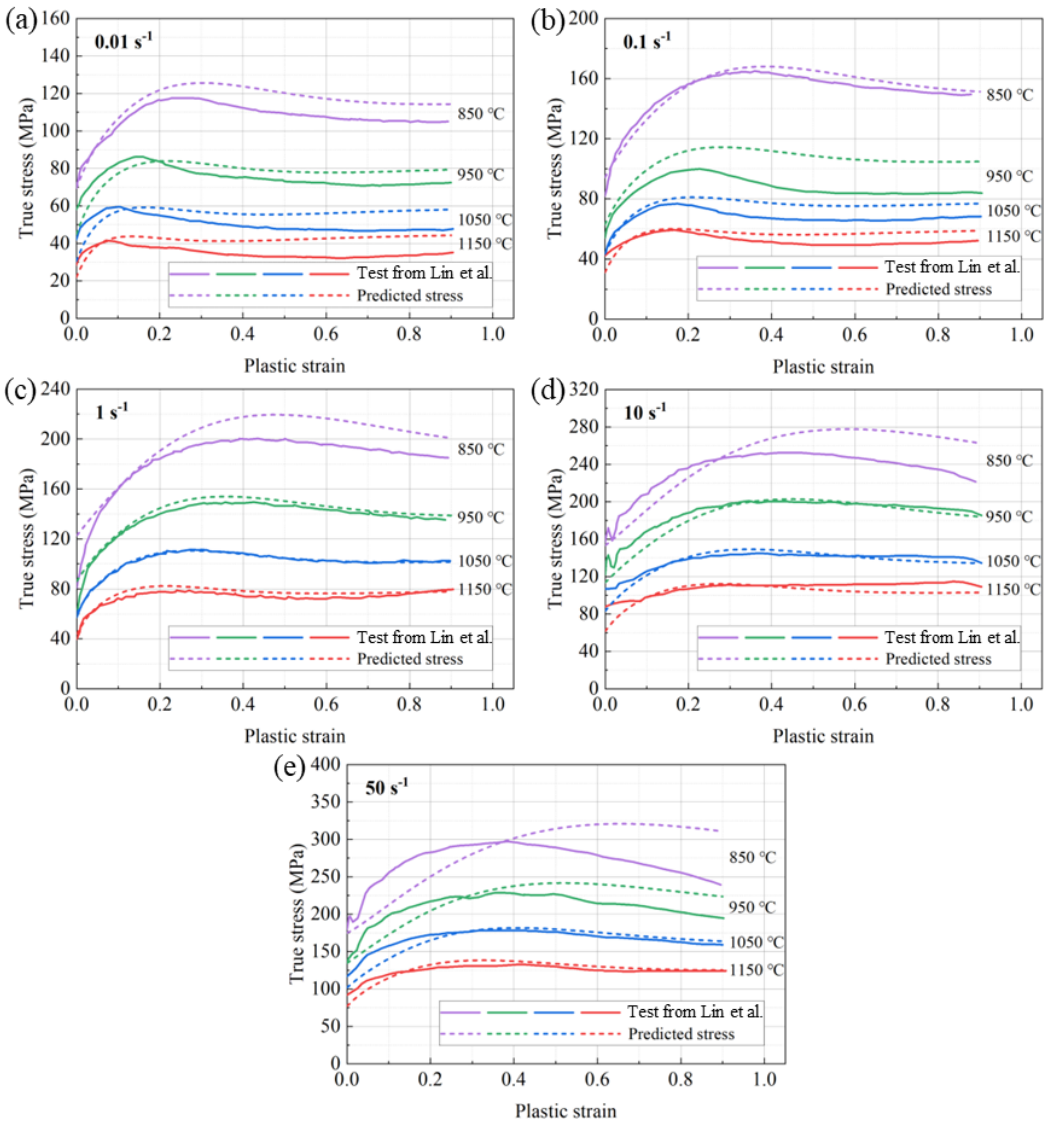


Figure B.8 Experimental true stress – strain curves of 42CrMo from Lin et al. [187] and prediction results of Modified model III at strain rate of (a) 0.01 s^{-1}, (b) 0.1 s^{-1}, (c) 1 s^{-1}, (d) 10 s^{-1} and (e) 50 s^{-1}.

B.4.5 Prediction of peak and yield stresses

The comparison of the peak stress at different strain rates from experiment data and prediction by the ZOP model, Modified models I, II and III is given in Figure B.9. In general, all models are able to predict the varying trend of the peak stress with the change of temperature and strain rate. The ZOP model gives accurate predictions of the peak stresses as compared with experimental results at different strain rates and temperatures. Modified model I is able to give favourable predictions in most conditions,

while deviation becomes larger at the strain rate of 10 s^{-1} and 50 s^{-1} and temperature of 850 ℃. Similarly, Modified model II works quite well in most cases except in the case of 0.01 s^{-1} strain rate. Finally, Modified model III shows a noted improvement as compared with Modified model II, and at all conditions, in predicting the peak stress with a high degree of accuracy. From the above observations, the ZOP model and Modified model III has a better capability in the prediction of the peak stress.

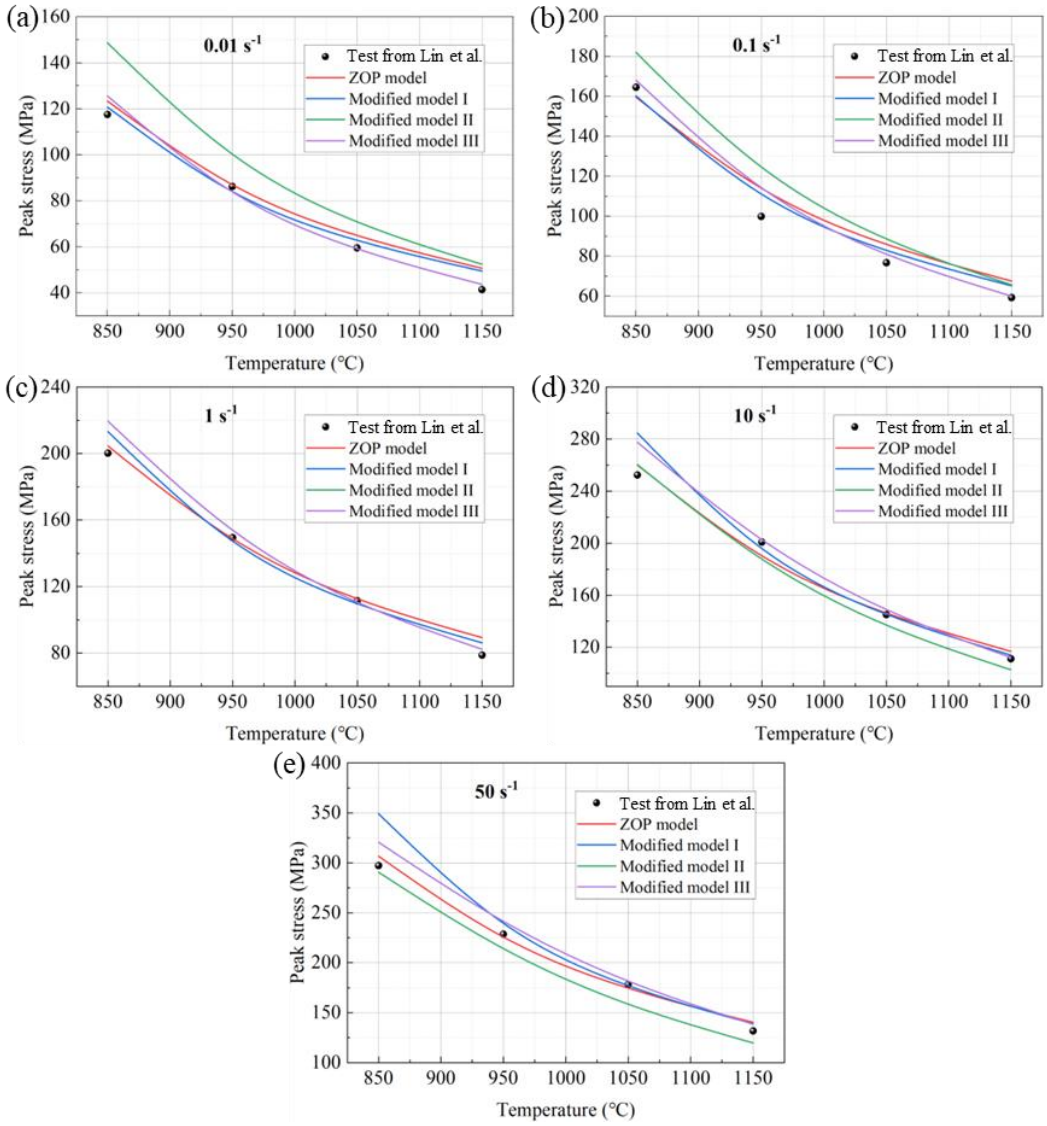


Figure B.9 Comparison of peak stress obtained from experimental results by Lin et al. [187] and predicted results from the ZOP model, Modified models I, II and III at deformation strain rate of (a) 0.01 s^{-1}, (b) 0.1 s^{-1}, (c) 1 s^{-1}, (d) 10 s^{-1} and (e) 50 s^{-1}.

The predicted yield stresses are compared with the experimental results as shown in

Figure B.10. In the figure, the predicted yield stress is identified to be the flow stress when a plastic strain of "0" is applied in Modified model I, II and III. The ZOP model is not included in this comparison because it starts the prediction from the zero-stress point and the predicted yield stress is unable to determine accurately by observation. Although the studied models can predict the general trend of the yield stress variation and give a reasonable prediction at deformation strain rates of 0.01 s^{-1}, 0.1 s^{-1} and 50 s^{-1}, deviation between the experimental data and predicted results is noticeable, especially in the conditions of 1 s^{-1} strain rate at temperature of 850 ℃ and 950 ℃, and of the case 10 s^{-1} strain rate at temperature of 1050 ℃ and 1150 ℃. This may be due to the inaccuracy in the extraction of the yield stress from the experimental data. Secondly, Modified models I, II and III may not be sufficiently suitable to predict the single yield stress in hot deformation of the 42CrMo steel, even though they are modified to start prediction from the yield point.

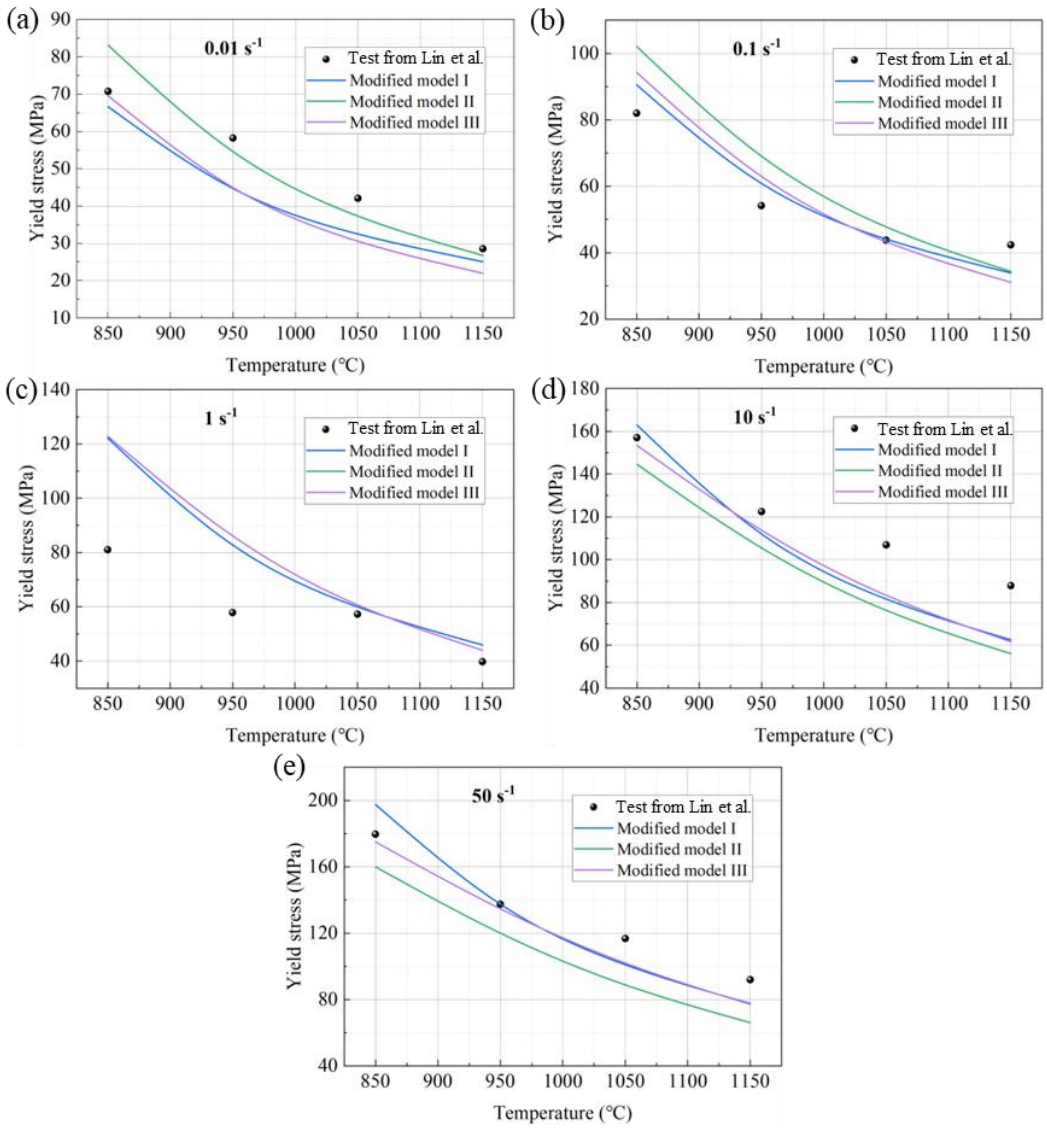


Figure B.10 Comparison of yield stress obtained from experimental results by Lin et al. [187] and predicted results from Modified models I, II and III at deformation strain rate of (a) 0.01 s^{-1}, (b) 0.1 s^{-1}, (c) 1 s^{-1}, (d) 10 s^{-1} and (e) 50 s^{-1}.

B.4.6 Evaluation and comparison of prediction accuracy

The prediction accuracy of each model is evaluated by the relative error δ, coefficient of determination (R^2) and root mean square error ($RMSE$).

Figure B.11 gives the relative error distribution between the experimental stress and predicted results of the studied constitutive models. It is clearly shown that the ZOP model provides better prediction at the later stage of deformation, while at small strain range, the predicted stress of the ZOP model shows a large deviation from the

experimental stress. This is because the ZOP model is unable to describe the elastic deformation of metals, Young's modulus of which is normally large. In terms of Modified models I, II and III, better prediction is usually given in the initial stage of deformation, which benefits from the prediction at the start point of yield point instead of the zero-stress point. As shown in Figure B.11(b) and (c), a comparison between Modified models I and II indicates that the original $h(\dot{\varepsilon}, T)$ is more efficient than the modified function $h^*(\dot{\varepsilon}, T)$ on the prediction of the effect of strain rate and temperature, even if $h^*(\dot{\varepsilon}, T)$ is a function with the use of the Arrhenius type equation and Z parameter, which are widely used in metallic materials. However, after further modification of the Z parameter on the compensation of strain rate effect, the modified function $h^{**}(\dot{\varepsilon}, T)$ gives a much better prediction accuracy than $h(\dot{\varepsilon}, T)$ and $h^*(\dot{\varepsilon}, T)$, as shown in Figure B.11(d). The improvement in prediction results is due to not only the additional exponent of the strain rate but also the optimal solution of parameter M introduced in this study.

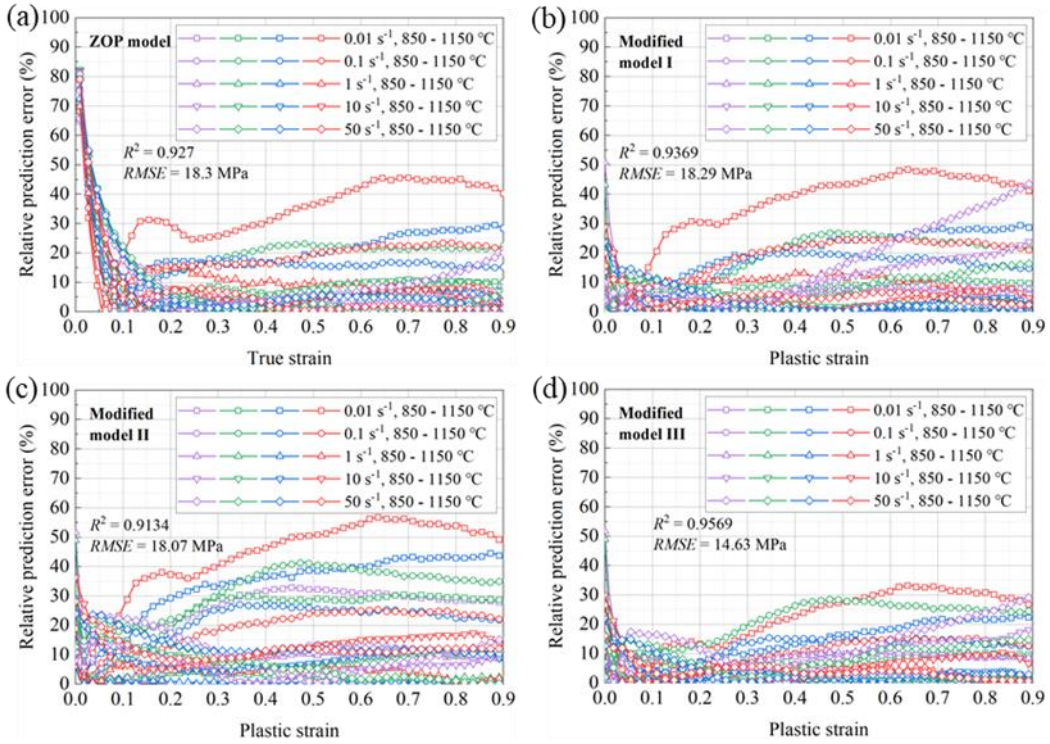


Figure B.11 Comparison between the experimental stress and predicted stress by (a) the ZOP model, (b) Modified model I, (c) Modified model II and (d) Modified model III.

With the use of R^2 and $RMSE$ calculated by Equations (B.50) and (B.51), the quantitative evaluation shows that among all four models, Modified model III is able to predict the flow stress with the highest degree of accuracy, and meanwhile, the predicted results of the ZOP model and Modified model II show least prediction accuracy in comparison. The R^2 value of Modified model III reaches 0.9569 and the $RMSE$ value is only 14.63 MPa, which means a great improvement from the original ZOP model after several steps of modification.

B.5 Discussion

B.5.1 Applicability of developed constitutive models

The present work demonstrates the applicability of the ZOP model and the modified models in predicting the hot deformation behaviour of 42CrMo. Results indicate that after several steps of modification, Modified model III is capable of predicting the flow stress under different strain, strain rate and temperature conditions with a high degree of accuracy. Although only the flow stress of 42CrMo is used to validate and compare the prediction accuracy, its testing results are representative and typical for the hot deformation behaviour of most metals. In the published literature, most metallic materials, such as steel [160, 187, 189-191], aluminium alloys [192-196], magnesium alloys [197-199], titanium alloys [200-203], superalloys [204-207], are similar in flow stress curves and variation trends under tension [193, 208], compression [209, 210] and torsion [160, 211] at hot deformation when DRX occurs. The typical representation of the hot deformation behaviour of metals at a certain temperature and strain rate can be summarised in Figure B.12. In the illustration, the blue curve represents the true stress

– true strain relationship under the effect of work hardening (WH) and dynamic recovery (DRV), and the red curve under the additional effect of dynamic recrystallization (DRX). As shown by the red curve, four different stages can be found including initial hardening or work hardening, transition, dynamic softening and steady state. The developed models are effective in dealing with this shape of flow stress curves by using the introduced piecewise functions and transition function as modelling tools. In terms of the hot deformation where only WH and DRV happen, the stress – strain behaviour has a much simpler shape as given by the blue curve in Figure B.12. The difference between the blue and red curves is that there is no softening stage before the achievement of steady state. Representation of this kind of curves can be achieved by the transition functions to allow a smooth stress change once the peak value is reached in small strain range. Therefore, the ZOP model and its modified models developed in this study, especially Modified model III, can be used to predict the hot deformation behaviour of many metallic materials.

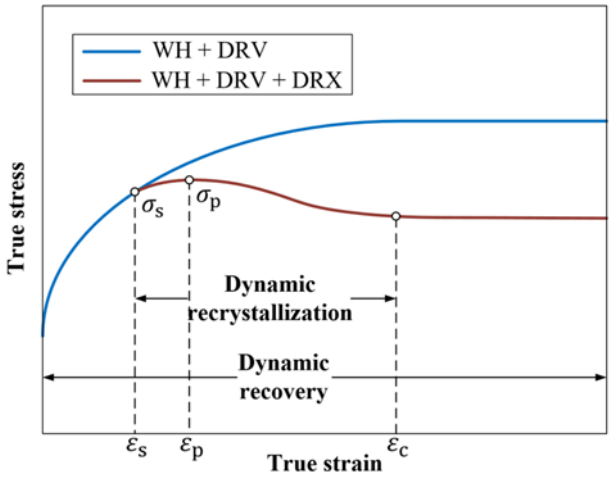


Figure B.12 Typical hot deformation behaviour of metals.

Meanwhile, the improvement of the ZOP and the modified models is obvious in the prediction of flow stress in hot deformation of metals. Although the effect of strain rate and temperature on the flow stress can be predicted effectively, the effect of strain is

mainly predicted by fitting high-order polynomials [178-180]. In comparison, the ZOP model and the modified models developed in this study show a clear degree of simplification and applicability. The piecewise functions used in the models provide a good level of accuracy in both small and large strain ranges, whilst the transition functions enable a smooth transition between small and large strain deformation behaviours and the flexibility to reflect accumulated effects of WH, dynamic recovery (DRV) and dynamic recrystallization (DRX).

B.5.2 Physical meanings of the developed constitutive models

The validity of the developed constitutive models is confirmed in Section B.4 and the applicability is discussed in Section B.5.1. It is worthwhile to discuss the underlining mechanism and the relationship between the developed models and microstructure evolution under hot deformation conditions. It is well established that WH, DRV and DRX exist in metal deformation at high temperatures, as shown in Figure B.12. At the initial stage of deformation, WH dominates the flow stress increase, and this is followed by the softening behaviour due to DRX. More specifically, WH exists throughout the whole deformation process, while the work hardening rate is reduced because of the existence of DRV. With the increase of deformation strain, when a critical value of strain (defined as ε_s) is reached, DRX starts and dominates the material behaviour. In completion of DRX, a balance between WH, DRV and DRX is achieved, and this leads to the steady state of flow stress curves. In the ZOP model and the modified models, piecewise functions are used to predict the flow stress at small and large strains separately, and the transition functions are used to enable a smooth shifting between different prediction parts. Taking Modified model III as an example, $f^{***}(\varepsilon, \dot{\varepsilon}, T)$ is responsible for the prediction of small strain deformation behaviour before ε_c, while $g^{**}(\varepsilon, \dot{\varepsilon}, T)$ is applied to predict larger strain deformation behaviour after ε_c. Obviously,

the predicted parts given by the function $f^{***}(\varepsilon, \dot{\varepsilon}, T)$ include the initial work hardening, transition and dynamic softening stages. If DRX continues even in large strains, the dynamic softening will continue as shown in the red curve in Figure B.1. However, the occurrence of DRX must have an endpoint. With the completion of DRX, the steady state appears, and the prediction may be given by function $g^{**}(\varepsilon, \dot{\varepsilon}, T)$. On this account, the completion strain of DRX (defined as ε_c) can be approximated as the critical strain $\varepsilon_{\text{critical}}$. In the process, transition functions $u^{**}(\varepsilon, \dot{\varepsilon}, T)$ and $v^{**}(\varepsilon, \dot{\varepsilon}, T)$ play an important role to approach smooth shifting from dynamic softening to the steady state, i.e., from DRX dominated deformation towards the steady state of flow stress. Also, the change of DRX completion strain at different strain rates and temperatures can be reflected by the transition functions because they provide flexibility in the change of the critical strain due to the involvement of strain rate and temperature related function $h^{**}(\dot{\varepsilon}, T)$ in $u^{**}(\varepsilon, \dot{\varepsilon}, T)$ and $v^{**}(\varepsilon, \dot{\varepsilon}, T)$. The above discussions show the meanings of different parts of the developed constitutive models and their relationship with microstructural evolution in hot deformation of metallic materials. This is a useful rationality for the use of the ZOP model and the modified models in flow stress prediction in hot deformation of metals. This also gives physical meanings to the developed constitutive models and even makes it possible to predict the occurrence and completion of DRX.

It has been revealed that DRX initially starts before the peak stress point, and the strain at the start of DRX is related to a minimum amount of energy [212, 213], so the discussion of the strain at the start of DRX is not easy and out of the scope of the developed constitutive models. Even though, the peak strain ε_p is available to determine using the constitutive models and it is an important tool to study the behaviour and the strain at the start of DRX because these two important strains have a close relationship

in which the starting strain of DRX is proportional to the peak strain [214] and could be approximated as $0.8 \cdot \varepsilon_{\mathrm{p}}$ as studied by Sellar [215] and Ouchi and Okita [216]. Meanwhile, the completion strain of DRX ε_{c} can be approximated as the critical strain $\varepsilon_{\mathrm{critical}}$ between the transition of the piecewise functions for small and large strain ranges, as at this point the flow stress curves enter into the steady state as discussed earlier. As a result, the peak strain ε_{p} and the completion strain of DRX ε_{c} are discussed below and predicted by the developed constitutive models.

Taking the ZOP model as an example, from Equations (B.14) and (B.15), the result of the partial differentiation indicates that the peak strain ε_{p} can be predicted by the following function:

$$\varepsilon_{\mathrm{p}} = n \cdot \mu \cdot h(\dot{\varepsilon}, T) \tag{B.49}$$

Meanwhile, the combination of $f(\varepsilon, \dot{\varepsilon}, T)$ and $g(\varepsilon, \dot{\varepsilon}, T)$ expressed by Equations (B.2) and (B.3) gives the following equation:

$$K_1 \cdot \varepsilon^n \cdot \exp\{-\varepsilon/[\mu \cdot h(\dot{\varepsilon}, T)]\} = K_2 \cdot [\exp(-C_1 \cdot \varepsilon) + \exp C_2] \cdot [1 - \exp(-\alpha \cdot \varepsilon)] \cdot h(\dot{\varepsilon}, T) \tag{B.50}$$

Solution of Equation (B.50) leads to the critical strain $\varepsilon_{\mathrm{critical}}$ or the completion strain of DRX ε_{c}. The prediction results of the peak strain ε_{p} and the completion strain of DRX ε_{c} and the comparison with experimental data are given in Figures B.13 and B.14, respectively.

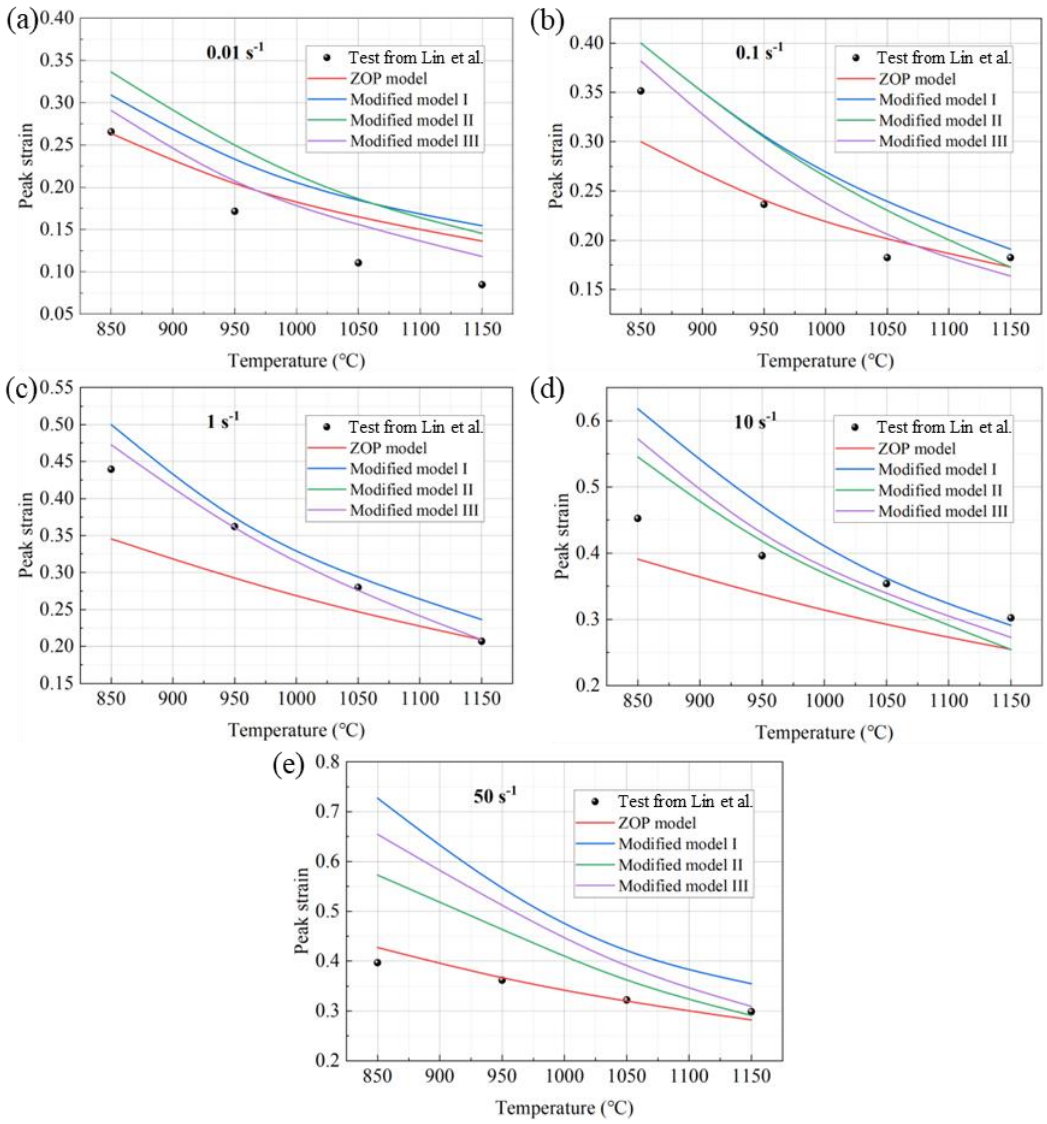


Figure B.13 Comparison of peak strain obtained from experimental results by Lin et al. [187] and predicted results from the ZOP model, Modified models I, II and III at deformation strain rate of (a) 0.01 s^{-1}, (b) 0.1 s^{-1}, (c) 1 s^{-1}, (d) 10 s^{-1} and (e) 50 s^{-1}.

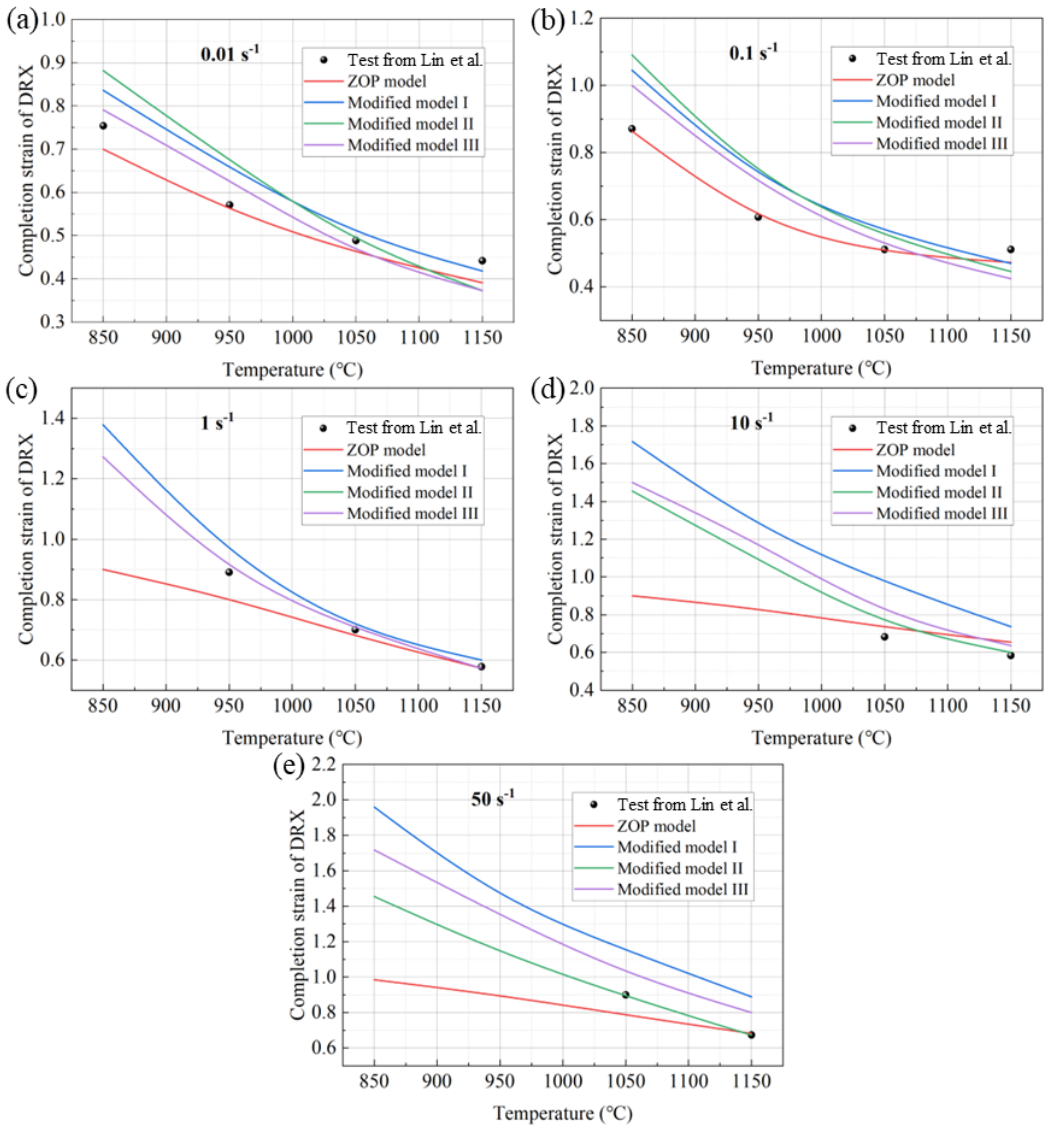


Figure B.14 Comparison of the completion strain of DRX obtained from experimental results by Lin et al. [187] and predicted results from the ZOP model, Modified models I, II and III at deformation strain rate of (a) 0.01 s^{-1}, (b) 0.1 s^{-1}, (c) 1 s^{-1}, (d) 10 s^{-1} and (e) 50 s^{-1}.

As shown in Figures B.13 and B.14, from experimental testing at the same strain rate, with the elevation of temperature, both the peak strain and the completion strain of DRX show a decreasing trend; while with the decrease of strain rate, the studied strains show a decreasing trend. This was confirmed by microstructure observation in the study of Lin et al. [217]. At higher temperatures, the grain sizes were observed larger at a constant deformation degree, which indicates larger degree of DRX, because the start and completion of DRX process are accelerated while at low temperatures, more time

is needed to complete DRX. At lower strain rates, although larger grain sizes were observed, it is a result of increased DRV rate. However, the required deformation time is longer at lower strain rates, so the DRX happens and completes at smaller strain than that at higher strain rates. In Figure B.13, the comparison between the experimental and predicted results shows that the developed constitutive models are capable of predicting the peak strain with comparable results. Among all four studied models, Modified model III gives the most favourable prediction of the peak strain compared with experimental ones despite that the deviations at 50 s^{-1} are observed to become larger at lower deformation temperature. In Figure B.14, the completion strains of DRX are predicted by the developed models. All the developed models, especially Modified models II and III, give effective prediction results of the DRX completion strains extracted from experimental flow stress curves. The success in predicting the peak strain and the completion strain of DRX shows that the developed constitutive models can be used as a useful tool to study the DRX process and microstructural evolution in the hot deformation of metallic materials.

B.6 Conclusions

This study demonstrates that the ZOP model and its modifications can be used to represent in hot deformation behaviour of metallic materials. The prediction results of the ZOP model and its modified models are investigated and presented, followed by a discussion of the applicability and physical meanings of these models in hot deformation of metals. The main conclusions can be drawn as below.

(1) The ZOP model shows less prediction accuracy in the initial hardening stage but works well at later deformation stages. In comparison, Modified models I, II and III give a better prediction of the flow stress from the yield stress.

(2) The ZOP model can be modified to predict the hot deformation behaviour of metals at different temperatures, strain rates and strains. The most favourable prediction is given by Modified model III, in which Arrhenius type equation and modified Zener-Holloman parameter are used to predict the effect of strain rate and temperature.

(3) In Modified model III, the Zener-Holloman parameter is modified to strengthen the effect of strain rate. Unlike random attempts in previous studies, the determination method of the exponent of strain rate is given by linear curve fitting of the relationship between the $\ln\{\sinh[\sigma_p/K_1 \cdot (e/(n \cdot \mu))^n]\}$ and $\ln \dot{\varepsilon}$. This is useful to obtain an optimum M value to achieve improved prediction accuracy.

(4) All of the developed models are able to predict the peak stress effectively. Among them, the ZOP model and Modified model III give better prediction accuracy than the others. However, the prediction of the yield strain could only be given by Modified models I, II and III and there is still scope for improvement in terms of prediction accuracy.

(5) The piecewise functions enable the prediction of flow stress curves in different strain ranges, while the transition functions are used to shift the two piecewise functions smoothly from one to the other. In terms of physical meaning, the DRX induced softening behaviour is shifted to a steady state among WH, DRV and DRX via the developed transition functions.

(6) The peak strain and DRX completion strain can be predicted effectively by the developed models, especially Modified model III. This is of significant meaning to the study of the occurrence and completion of DRX in the hot deformation of metals.